NASA CR-1150

NASA CONTRACTOR
REPORT

NASA CR-1150

NASA CR-1150

RECUPERATOR FOR SOLAR BRAYTON CYCLE SYSTEM

by A. F. Anderson

Prepared by
GARRETT CORPORATION
Los Angeles, Calif.
for Lewis Research Center

NATIONAL AERONAUTICS AND SPACE ADMINISTRATION • WASHINGTON, D. C. • AUGUST 1968

RECUPERATOR FOR SOLAR BRAYTON CYCLE SYSTEM

By A. F. Anderson

Distribution of this report is provided in the interest of
information exchange. Responsibility for the contents
resides in the author or organization that prepared it.

Prepared under Contract No. NAS 3-2793 by
AIRESEARCH MANUFACTURING DIVISION
Garrett Corporation
Los Angeles, Calif.

for Lewis Research Center

NATIONAL AERONAUTICS AND SPACE ADMINISTRATION

FOREWORD

The research described herein, which was conducted by the AiResearch Manufacturing Division of the Garrett Corporation, was performed under NASA Contract NAS 3-2793. Mr. G. N. Kaykaty, Space Power Systems Division, NASA-Lewis Research Center, was the Project Manager.

CONTENTS

v

CONTENTS (Continued)

APPENDICES

ILLUSTRATIONS

ILLUSTRATIONS (Continued)

ILLUSTRATIONS (Continued)

x

ILLUSTRATIONS (Continued)

ILLUSTRATIONS (Continued)

TABLES

SECTION I

INTRODUCTION AND SUMMARY

The purpose of this report is to present the results of all analytical and test work conducted during a program for the development of a recuperator to be utilized in a closed Brayton cycle space power system that uses solar energy as a heat source and argon as the working fluid. This report concludes the program performed by the AiResearch Manufacturing Division of The Garrett Corporation, Los Angeles, California, under National Aeronautics and Space Administration Contract NAS3-2793. The initial phase of the work was a parametric design study to determine the optimum recuperator operating conditions for the Brayton cycle. The study was followed by analysis and testing that was directed towards determining the final design configuration. The final phase of this program included fabrication and testing of a recuperator that was delivered to the NASA Lewis Research Center. The entire program is summarized at the back of the report.

PARAMETRIC DESIGN STUDY

The parametric design study was conducted to provide sufficient data to permit optimum recuperator operating conditions to be selected for the Brayton cycle. The study covered a recuperator effectiveness range from 0.75 to 0.95 and a range of $(\Delta P/P)_{TOTAL}$ of from 1/2 to 8 percent for both hot and cold flows. The analysis employed the specified Brayton cycle boundary conditions and gas flows shown below.

	Cold Inlet	Hot Inlet
Temperature, °R	801	1560
Pressure, psia	13.8	6.73
Argon flow rate, lb per min	36.69	36.69

In addition to selecting the optimum recuperator pressure drop and effectiveness, the parametric study also selected the type of heat exchanger to be used. During the study, four types of heat exchangers were examined; plate-fin multipass cross-counterflow, plate-fin pure counterflow, tubular multipass cross-counterflow and tubular pure counterflow. For each type, an AiResearch digital computer program was used to obtain a series of designs over a wide range of problem conditions. From this series of heat exchanger designs, curves were prepared to show the change in heat exchanger weight and dimensions for varying effectiveness and pressure drops. The curves included results for the heat exchanger cores only and also for the manifolded and packaged cores. Various packaging configurations which could be used for the different types of core were considered. The results of this parametric study were presented to NASA in an AiResearch report (L-9372) and from the curves, NASA selected the final recuperator configuration and specified an effectiveness of 0.9 and a $(\Delta P/P)_{TOTAL}$ of 2 percent. The selected configuration is pure counterflow plate-fin type. The numerous parametric curves generated during the study are discussed in Section 2. The selection of the final operating condition and heat exchanger type is presented in Section 3.

1

Also, during the parametric study, three specific areas of investigation were conducted; axial conduction (longitudinal heat flow) in pure counterflow heat exchangers, the determination of basic test data for gas flow outside and parallel to, tube bundles and the preparation of a computer program to design counterflow tubular heat exchangers. Each of these three specific areas of study is presented as Appendix A, B and C, respectively, of this report.

FINAL DESIGN INVESTIGATIONS

With the selection of the pure counterflow plate-fin configuration for the final recuperator design, several specific problem areas required investigation. In a pure counterflow configuration, both fluids enter and leave the heat exchanger from the same face and in plate-fin designs this requires the use of triangular-shaped end sections. These end sections contribute little to the heat transfer performance of the recuperator but produce parasitic pressure losses. In order to optimize the end section design, a large number of geometries were investigated. AiResearch, to facilitate this task, wrote a computer program to determine the pressure losses in these triangular end sections. The assemptions used, and the method of calculation employed by this program, together with some typical results, are shown in Appendix D of this report. The results obtained from this program and the overall influence of the triangular end sections or the recuperator are discussed in Section 4.

During the parametric study phase of this program, analytical techniques for determining the effect of axial conduction in pure counterflow heat exchangers indicated that one of the major areas of difficulty is the determination of the effective conduction path through a plate-fin matrix. AiResearch, therefore, conducted a series of tests to determine an effective conduction parameter (KA/L) for the type of matrix being considered for this application. The results of this axial conduction testing are presented in Section 5.

Another problem area that was investigated thoroughly during the final design phase of this contract is flow distribution. During the initial stages of the parametric design study, it was believed that flow distribution would not provide any serious problem in the pure counterflow plate-fin type of heat exchanger. However, results obtained from other design and development programs being conducted by AiResearch indicated that losses in heat transfer performance and increases in overall pressure drop could be encountered due to nonuniform flow distribution through the heat exchanger. When the nonuniformities and flow distribution are known, their effect on heat exchanger performance and pressure drop may be readily calculated. However, the determination of the nonuniformities resulting from any specific geometry are less easily determined and AiResearch, therefore, conducted a small test program to provide the necessary information experimentally. The results of this program led to the finally-selected heat exchanger configuration. Results of both analytical and test procedures that were used during this phase of the contract to determine the effect of flow distribution on the manifolds and the core of the selected unit are presented in Section 6.

The test configuration resulted in satisfactory heat transfer performance but indicated higher than anticipated pressure losses. Various methods of

2

decreasing overall pressure losses to the required $\Delta P/P$ of 2 percent were evaluated. The results of this evaluation are presented and discussed in Section 8.

Section 7 of this report presents some details of the mechanical design and fabrication methods. In this section, the manufacturing limitations of the present design are discussed, together with the stress analysis that verified the structural integrity of the selected recuperator configuration. Further stress calculations with respect to system integration and component mounting are presented in Appendix E.

The final task of the program was a limited performance test of the final full scale recuperator configuration. The results of this test are reported and discussed in detail in Section 9 of this report. The heat transfer data obtained from this test indicates that the design effectiveness was achieved. The limited pressure loss information from this test was inconclusive and therefore the more extensive testing performed on the small scale test core as discussed in Section 6 is considered to be the more valid basis for evaluating pressure losses on the full scale unit.

At various stages throughout the two-year study period, AiResearch conducted some additional tasks which did not directly effect the final recuperator configuration. These tasks included the determination of meteoroid protection requirements for the recuperator, the determination of specific recuperator designs to fit around the anticipated solar absorber, an investigation of a change in working fluids and a preliminary analysis of a gas-to-liquid heat sink heat exchanger. Further information on these additional tasks is presented in Appendix F.

SECTION 2

HEAT TRANSFER MATRIX PARAMETRIC ANALYSIS

The object of the parametric analysis was to determine the optimum heat exchanger design for the solar Brayton Cycle recuperator problem conditions specified by NASA. The operating conditions and range of variables to be examined are shown in the introduction section of this report. In order to determine the optimum heat exchanger design for this entire range of operating conditions, AiResearch considered four types of fixed boundary heat exchangers. The four types of heat exchangers considered were: (1) cross counter-flow tubular, (2) pure counter-flow tubular, (3) cross counter-flow plate and fin, (4) pure counter-flow plate and fin. As there is no single, unique heat exchanger which is optimum for satisfying all the specified operating conditions for the recuperator, it was necessary to examine each of the four matrixes being considered in detail over at least a part of the specified range. A very large number of matrix geometries were analyzed for each of the four types of heat exchangers. The design and analysis of each type of heat exchanger were conducted by utilizing IBM digital computer programs written by AiResearch specifically to design heat exchangers.

MULTIPASS CROSS COUNTERFLOW TUBULAR HEAT EXCHANGERS

In order to design cross counterflow tubular heat exchangers for the full range of specified cycle conditions, a large number of heat transfer matrixes were considered. Matrix variables that were considered, included different tube diameters, different tube spacings and both plain and ring dimpled tubes. The use of ring dimpled tubes increases the heat transfer on the inside surface of the tubes, but also yields an increase in friction factor. In some heat exchanger designs, however, this type of turbulence promotion can be beneficial. Throughout the analysis, all heat exchangers were assumed to be fabricated from stainless steel and the tube wall thickness was held constant at 0.004 inches.

The initial survey consisted of taking the specified problem conditions and obtaining heat exchanger cores from the IBM computer program. During this initial survey, the total available pressure drop was assumed to occur in the heat exchanger core only. The results obtained from these computer runs are shown in Figures 1, 2 and 3. Figure 1 shows how the weight and core dimensions of this type of heat exchanger vary with effectiveness. Curves are shown for three different pressure drop levels. The pressure drop values utilized in Figure 1 were $(\Delta P/P)_{TOTAL}$ of 1 percent, 4 percent and 8 percent. At each different effectiveness, a different number of passes was utilized. The number of passes associated with each particular effectiveness is shown on the curve. As the effectiveness is increased, the number of passes increases because the detrimental effect of no interpass mixing becomes more substantial. At the very high effectiveness (greater than 0.9) even the use of as many passes as 12 does not approach the idealized condition of pure counterflow. Figures 2 and 3
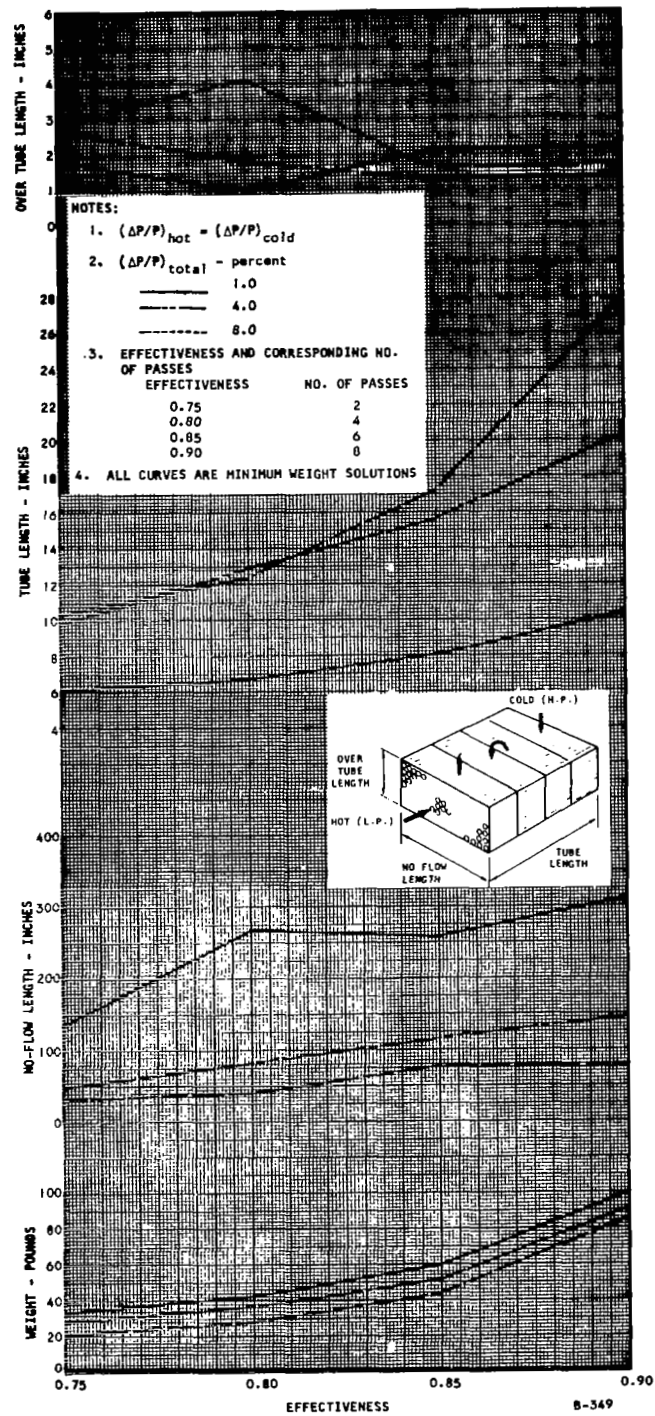
Figure 1. Tubular Multipass Cross Counterflow Core
Parameters Versus Effectiveness
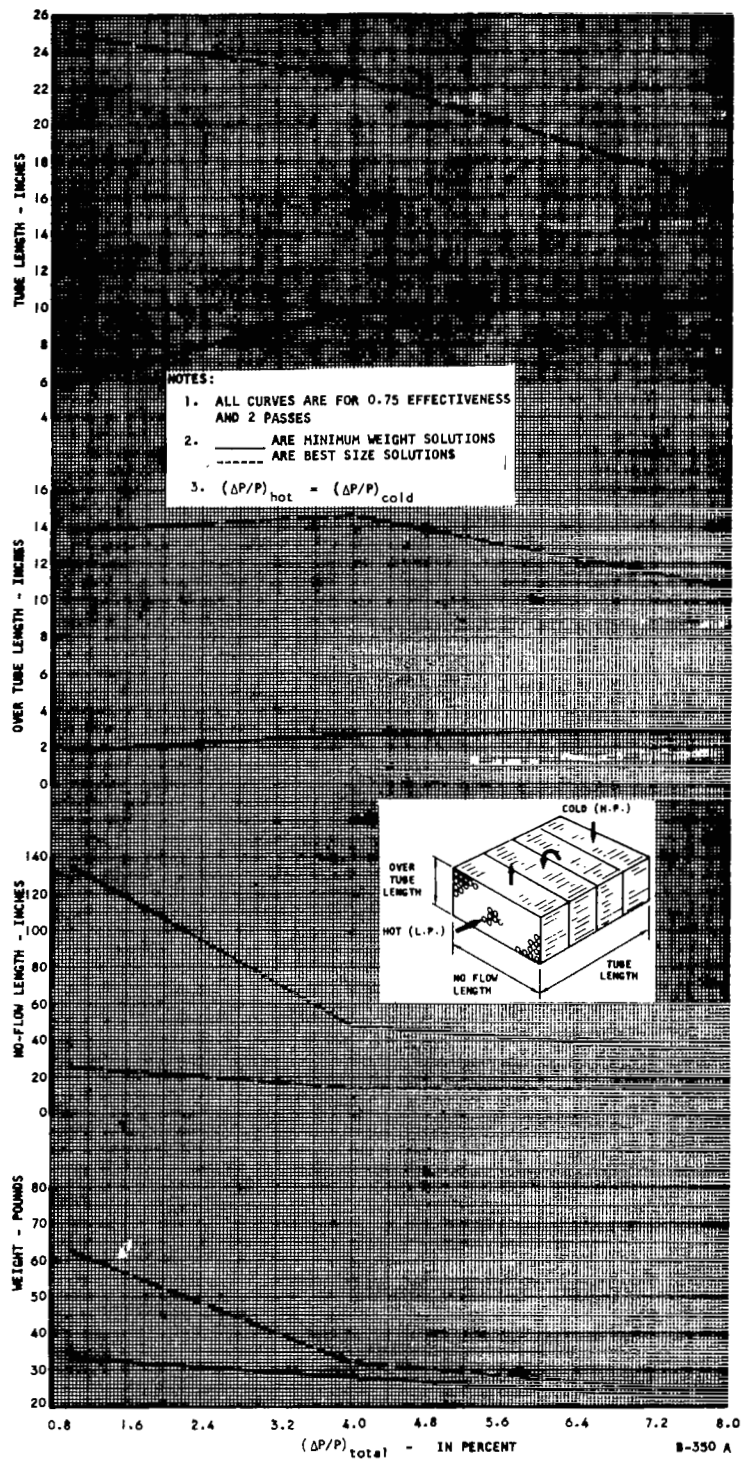
Figure 2. Tubular Multipass Cross Counterflow Core
Parameters Versus Percent Pressure Drop
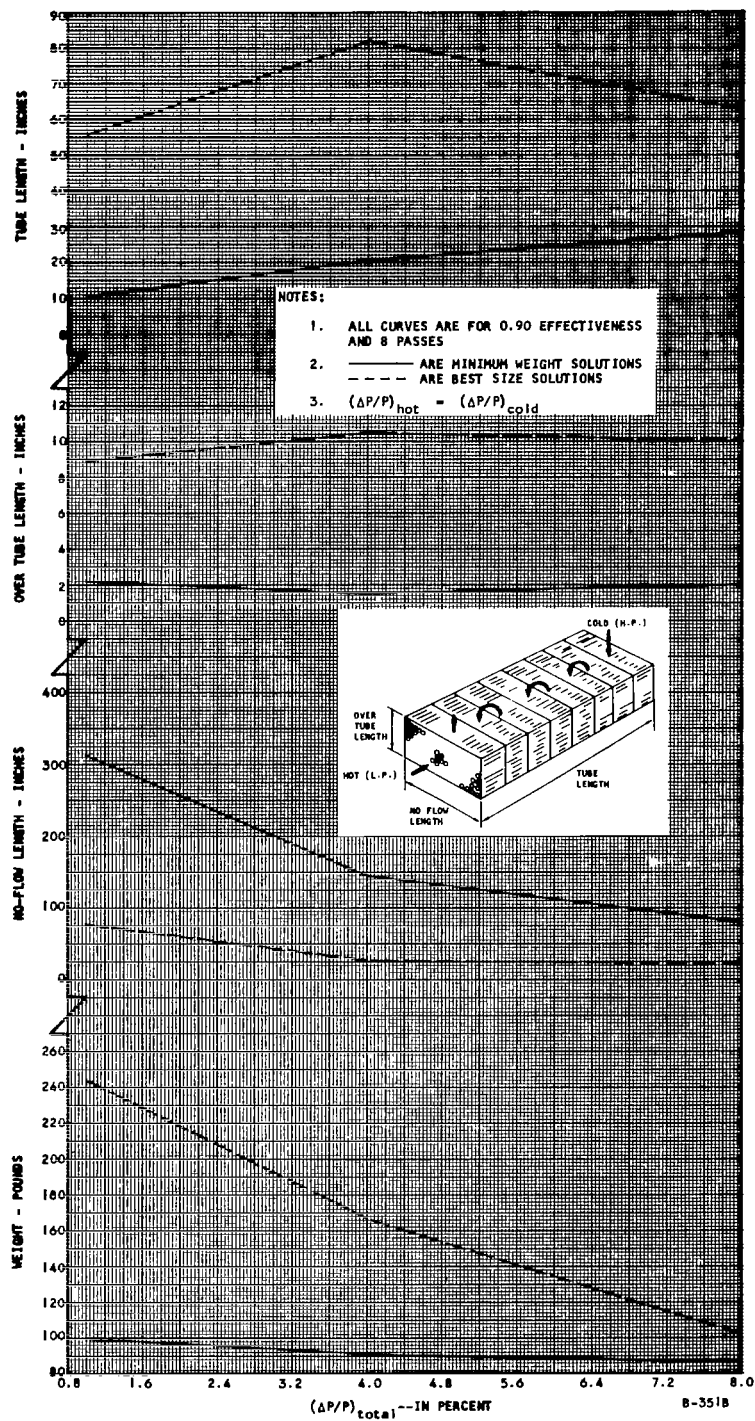
Figure 3. Tubular Multipass Cross Counterflow Core
Parameters Versus Percent Pressure Drop

show the effect on weight and core dimensions of varying pressure drops for heat exchanger effectivenesses of 0.75 and 0.90 respectively. On both these figures, curves are shown for minimum weight solutions and best size solutions. Minimum weight solutions disregard core dimensions while best size solutions take into account dimensional conventionality such as a rectangular tube bundle. In almost all cases the best size solution resulted in a substantially heavier core than the minimum weight solution. This is particularly true at high effectiveness and low pressure drop. At this end of the range of operating conditions, even the best size solutions result in very long no flow lengths.

The curves utilized in the study, Figures 1, 2 and 3, that show the effect of either effectiveness or pressure drop on heat exchanger core weight and dimensions, connect the computer design cases with straight lines. This particular method of presenting the data was used because interpolation between the actual data points is not strictly permissible. This is particularly true of the parameter, tube length. If the curves were prepared utilizing the same matrix geometry throughout, then both core geometry and core weight would give smooth curves for varying effectiveness and pressure drop. However, the same matrix geometry does not always yield either minimum weight or best size solutions and smooth curves are not obtained. If it is desirable to select a core operating at some intermediate condition, the curves shown in Figures 1, 2 and 3 give a very good indication of the expected dimensions and weight, but cannot be utilized to determine exact dimensions and weight.

The second phase of the study of this particular type of heat transfer matrix consisted of examining the various possible packaging methods and re-evaluating pressure losses in the heat exchangers to account for the necessary manifolding. For this particular type of heat exchanger a large number of packaging concepts are available, all of them yielding different effects on heat exchanger weight and performance. Early investigations into the effect of manifold pressure loss indicated that with almost all of the promising configurations a pressure drop split of approximately 85 percent in the heat exchanger core and 15 percent in the manifolds resulted in the most satisfactory solution. As this reduction of 15 percent in the pressure drop for the heat exchanger cores causes only a slight change in dimensions and weight of the cores, no new designs were made but the pressure drop in the existing designs increased. The designs shown in the following figures include manifolds that require 15 percent of the core drop; the overall pressure drop in these designs has, therefore, been increased by 15 percent on both sides.

At the low effectiveness and reasonably high pressure drop conditions, all heat exchangers, derived utilizing this type of core matrix had dimensions close to those of typical liquid to liquid tubular heat exchangers. As the computer program generates a rectangular bundle of tubes, the simplest possible packaging is to put this bundle of tubes into a rectangular box. Figure 4 illustrates how a heat exchanger with an effectiveness of 0.75 and a total core pressure drop $(\Delta P/P)$ of 4 percent could be packaged in this manner. A disadvantage of this type of

EFFECTIVENESS = 0.75
(ΔP/P) OVERALL = 4.6 PERCENT
OVERALL WEIGHT = 57.7 LB
OVERALL INCLUDES MANIFOLDS
FOR BOTH WEIGHT AND PRESSURE
DROP

TUBE LENGTH
30.4 IN.

HOT
ARGON
OUT

14.3 IN.
NO FLOW
LENGTH

COLD
ARGON
IN

HOT
ARGON
IN

COLD
ARGON
OUT

24.0 IN.
OVERTUBE
LENGTH
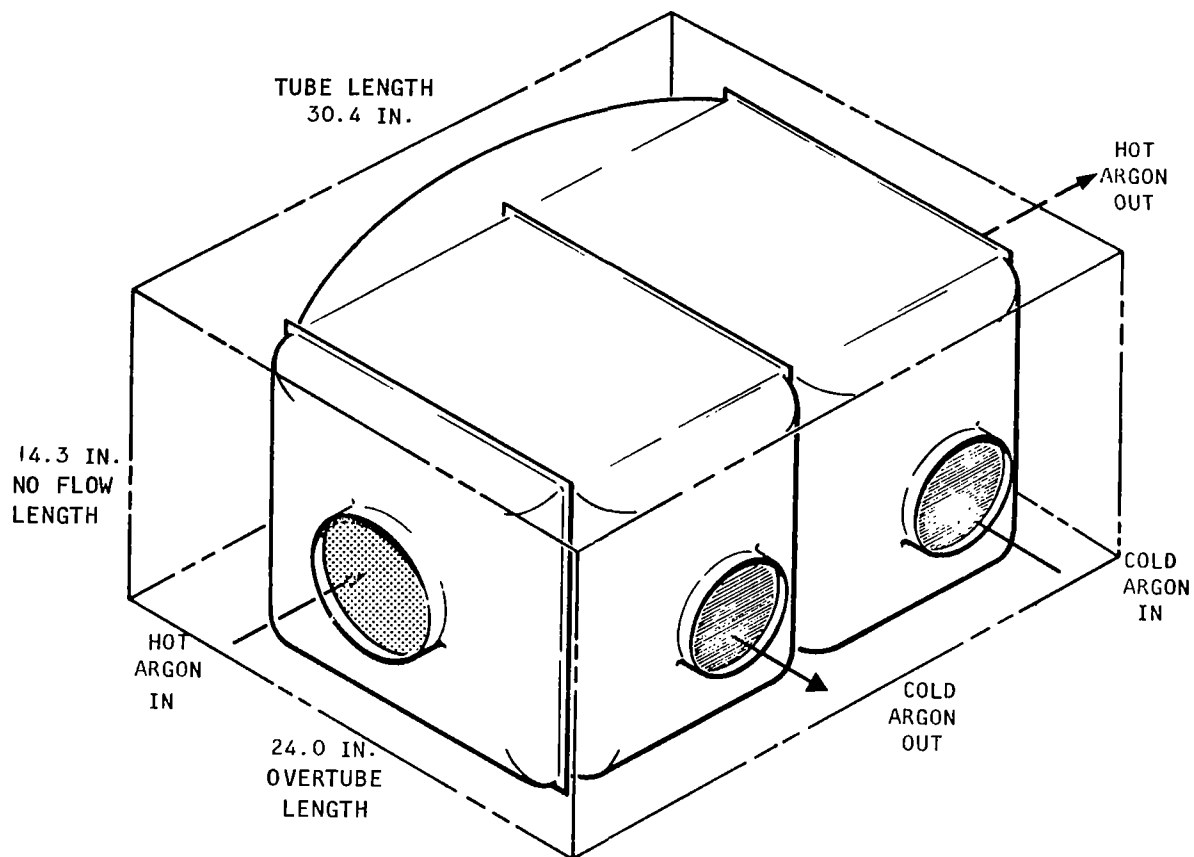
A-4371

Figure 4.   Simple Packaging of Tubular Cross Counterflow Heat Exchanger

packaging are the large, flat, unsupported faces that appear on the top and bottom of the heat exchanger. These faces should either be built from honey-combed structure or have supports or stiffeners provided in order to contain the low operating pressures of the Brayton Cycle System. The preferred configuration for this simple type of rectangular tube bundle is shown in Figure 5. This configuration is identical to that of a typical liquid to liquid heat exchanger. The low pressure fluid flows through the tubes and the high pressure fluid makes two passes across the tube bundle. The design shown in Figure 5 is also for an effectiveness of 0.75 and a total pressure drop of 4 percent. The core selected in this case is of slightly different geometry from that used in Figure 4, to conform more readily to this type of packaging. It can be seen from the weights shown on the two figures that not only does Figure 5 represent a better pressure vessel, but it also yields a lighter weight solution. As effectiveness increases so does heat exchanger size. Figure 6 illustrates how a heat exchanger with an effectiveness of 0.8 would appear if packaged in the simplest possible manner. Figure 7 illustrates how a package of this type may be changed to minimize the one long dimension. In this case the tubes are merely put into two bundles side by side rather than end to end, however, as can be seen from the weights on these two figures, the reduction in maximum length is also accompanied by an increase in weight. In all the four illustrations described so far, the packaging concepts utilized have applied primarily to the best size solutions of Figure 1, 2 and 3. In all cases there are solutions available that have substantially lighter weights. The problem of packaging these minimum weight solutions requires a different technique than the very simple one illustrated thus far. The main packaging problem arises from the large no flow lengths that accompany the tight, restrictive, transfer surfaces that yield the minimum weight solutions. By far the most attractive packaging concept for this type of heat exchanger core is the use of multiple concentric rings. A typical configuration for a heat exchanger utilizing this concept and designed for an effectiveness of 0.85 and a total pressure drop of 2.5 percent is shown in Figure 8. The core weight for this particular design was 59.0 lbs while the final wrapped up weight as shown on the figure, was 91.3 lbs. It is of interest to note that the best size core for these operating conditions had a core weight of 104 lbs. This weight is in excess of the total wrapped weight of the minimum weight core. As effectiveness increases and pressure drop decreases, the benefits of this particular type of packaging are increased. Even at the low effectiveness and high pressure drop conditions, the use of a single ring design, generally yields the most satisfactory solution. Figure 9 shows a typical single ring design.

This annular concept of packaging was, therefore used for all cores of this type. From the very large number of heat exchanger cores designed by the computer program, designs were selected for effectiveness of 0.75, 0.80, 0.85 and 0.90 and for core pressure drops of 1.0, 2.5, 4.0, 6.0 and 8.0. The cores selected for each of these points were then packaged in the concentric ring concept discussed above and overall dimensions and weight calculated. A chart of all these results was prepared and is shown in Figure 10. No redesign of the heat exchanger cores was made to allow for the 15 percent manifold pressure losses. The actual pressure losses in the heat exchangers are, therefore, a little in excess of the above core values. A table showing both the core and overall pressure drops for each of the curves shown is included in Figure 10. As in the previous figures, the actual data points As in the previous figures, the actual data points

EFFECTIVENESS = 0.75
(ΔP/P) OVERALL = 4.6 PERCENT
OVERALL WEIGHT = 53.4 LB
OVERALL INCLUDES THE MANIFOLDS
FOR BOTH WEIGHT AND PRESSURE
DROP

COLD ARGON
IN

COLD ARGON
OUT

HOT ARGON
OUT

22.3
IN.

HOT
ARGON
IN

26.8 IN.

22.3 IN.
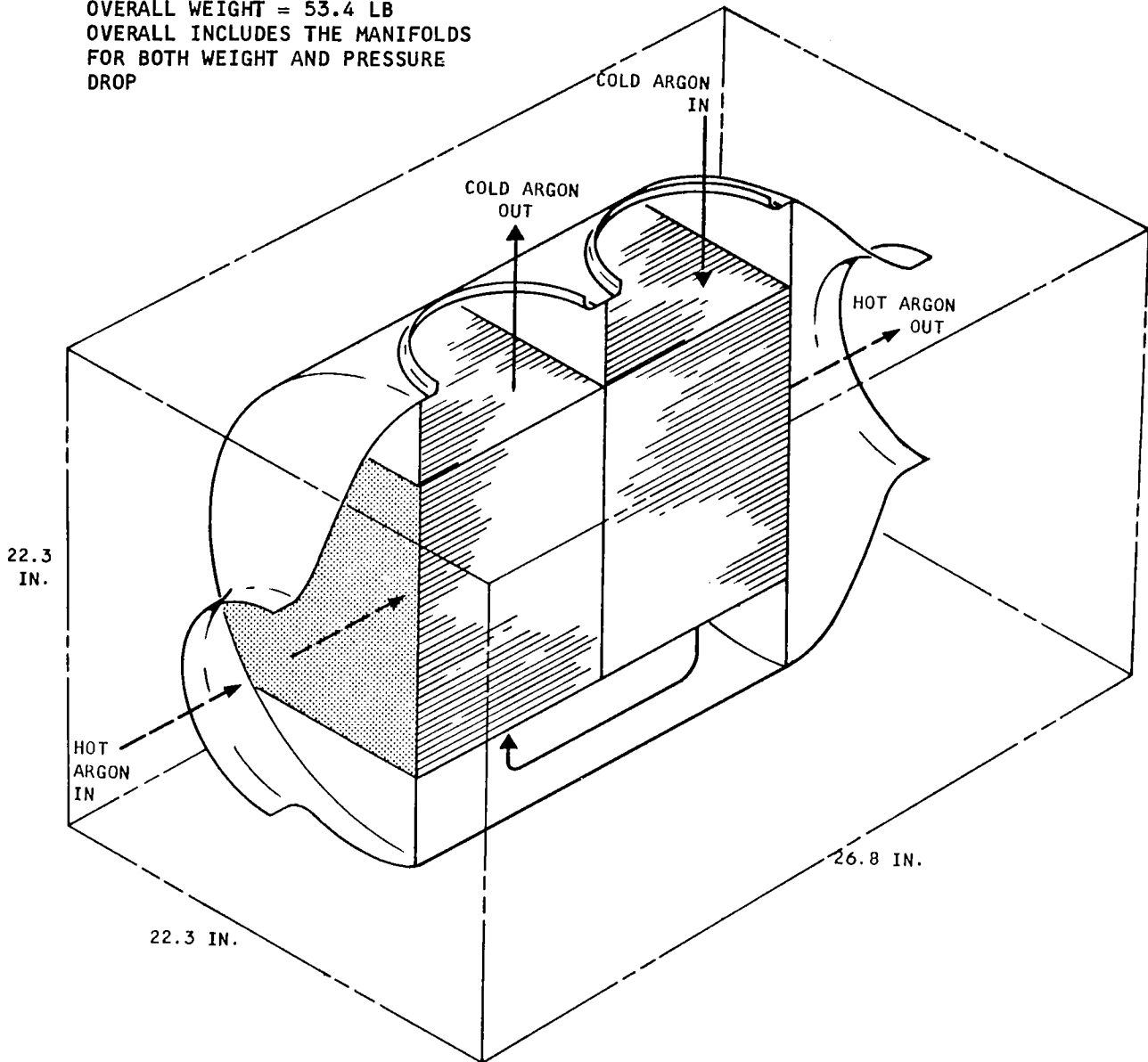
A-4369

Figure 5. Conventional Packaging for Tubular Cross Counterflow Heat Exchanger

11

EFFECTIVENESS = 0.80
(ΔP/P) OVERALL = 4.6 PERCENT
OVERALL WEIGHT = 114.3 LB
OVERALL INCLUDES MANIFOLDS FOR
BOTH WEIGHT AND PRESSURE DROP

HOT ARGON
OUT

COLD
ARGON
IN

17.0 IN.

60.0 IN.

HOT
ARGON
IN

COLD
ARGON
OUT

21.0 IN.
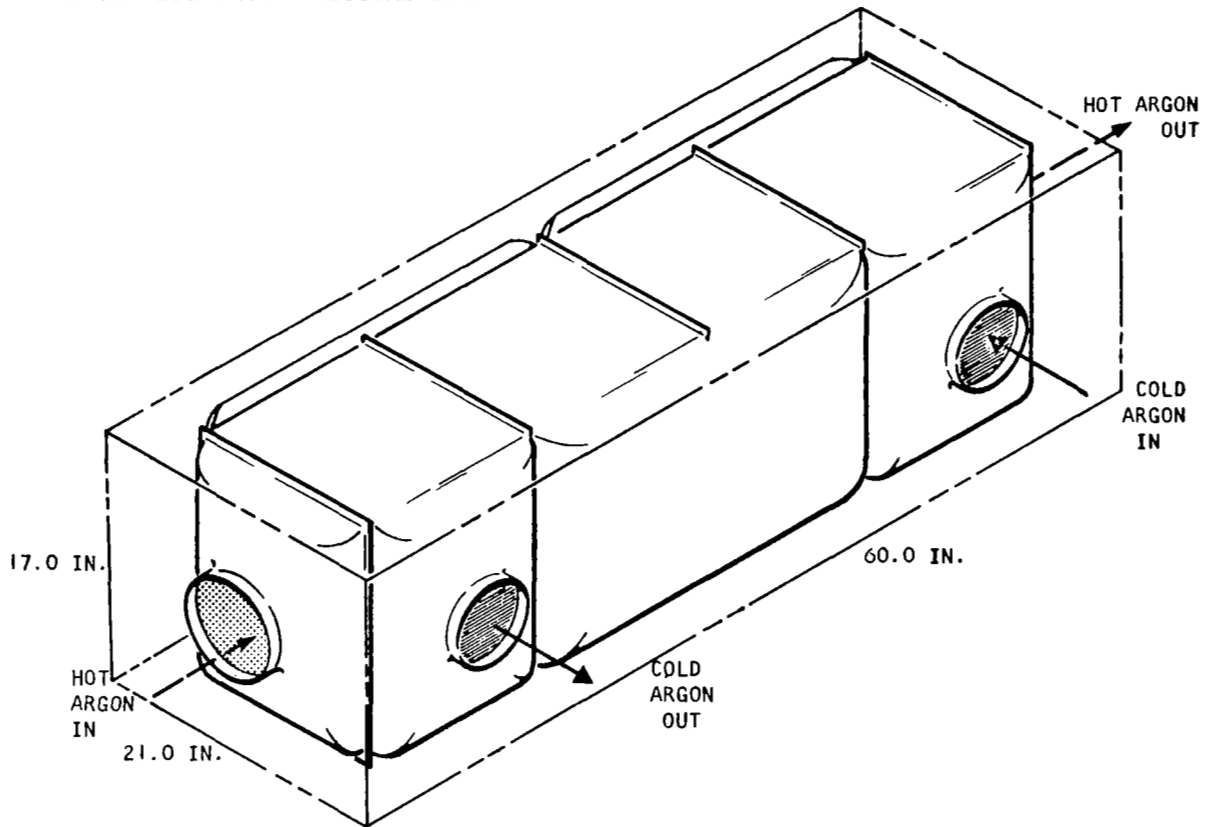
A-4365

Figure 6. Typical Packaging for Tubular Cross Counterflow Heat Exchanger

EFFECTIVENESS = 0.80
(ΔP/P) OVERALL = 4.6 PERCENT
OVERALL WEIGHT = 128.0 LB
OVERALL INCLUDES MANIFOLDS
FOR BOTH WEIGHT AND PRESSURE
DROP

COLD ARGON
OUT

COLD
ARGON
IN

21.0 IN.

HOT
ARGON
IN

33.2 IN.

HOT
ARGON
OUT

29.0 IN.
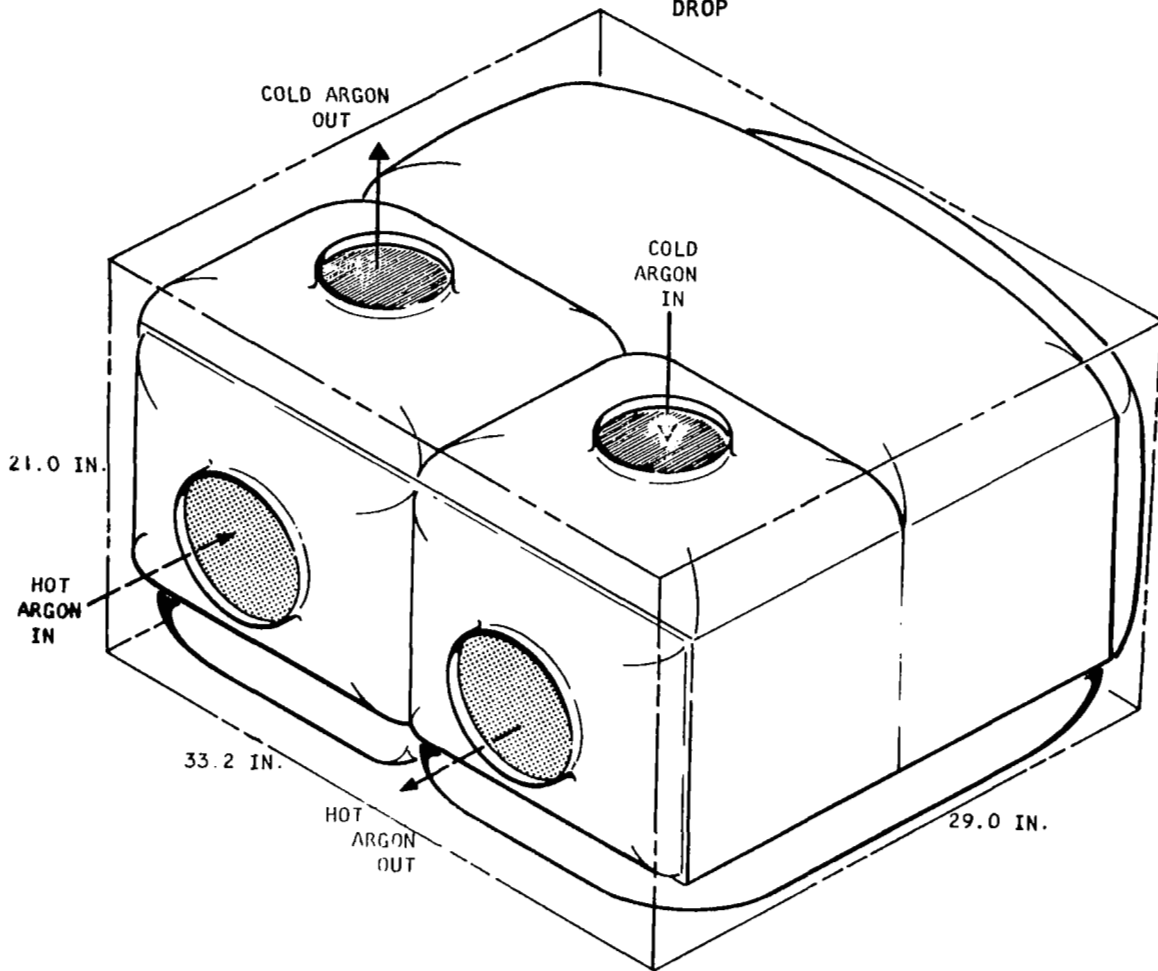
A-4366

Figure 7. Alternate Packaging for Tubular Cross Counterflow Heat Exchanger

13

COLD ARGON
IN

HOT ARGON
OUT

HOT
ARGON
IN

23.4 IN.

COLD
ARGON
OUT

21.4 IN.

23.4 IN.

EFFECTIVENESS = 0.85
ΔP/P OVERALL = 2.8 PERCENT
OVERALL WEIGHT = 91.3 LB

OVERALL INCLUDES MANIFOLDS
AND BAFFLES FOR BOTH WEIGHT
AND PRESSURE DROP.

B-416
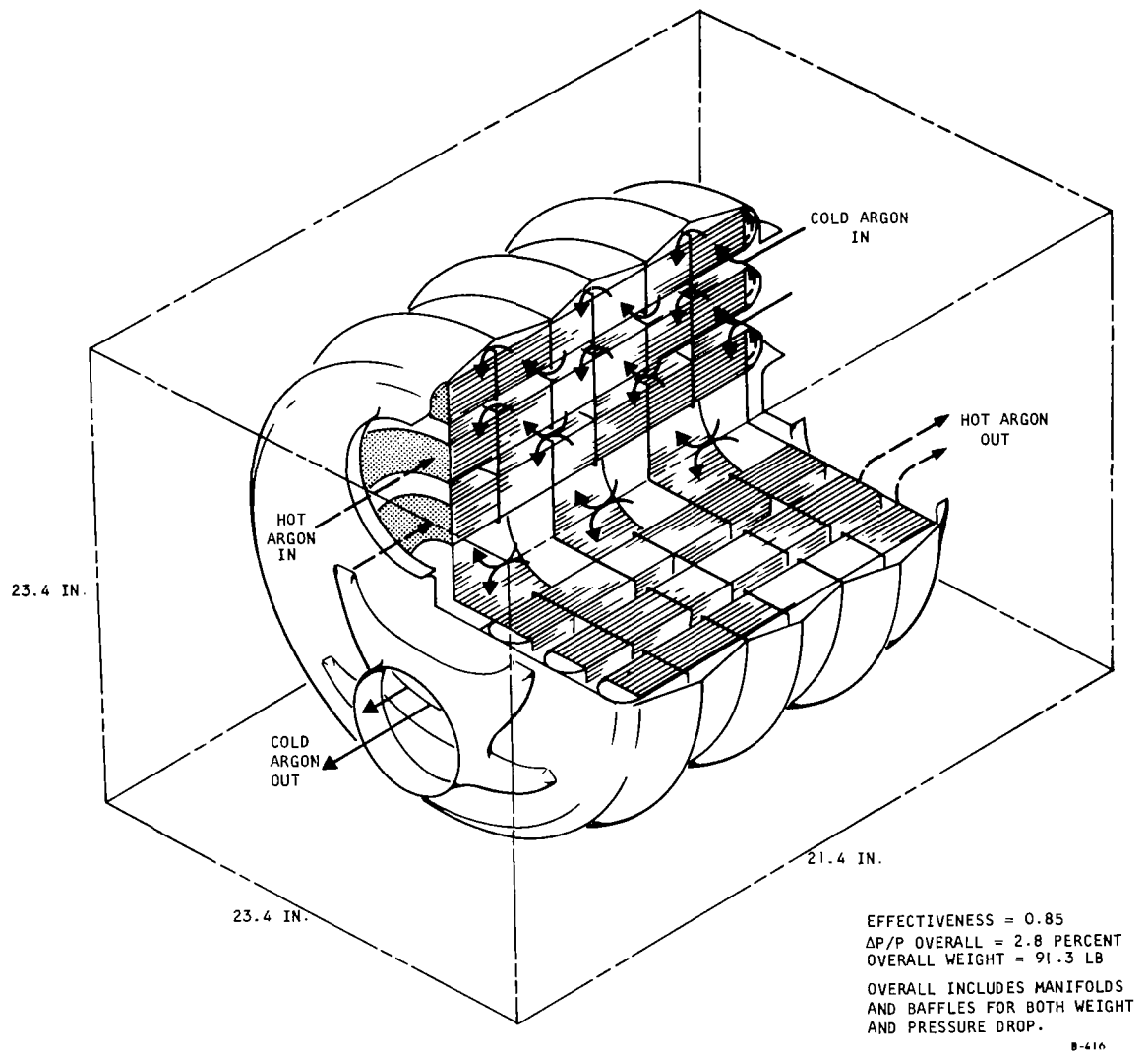
Figure 8. Multiconcentric Ring Packaging of Tubular
Cross Counterflow Heat Exchanger

HOT
ARGON
OUT

COLD
ARGON
IN

23.2 IN.

COLD
ARGON
OUT

50.8 IN.

EFFECTIVENESS = 0.90
ΔP/P OVERALL = 6.9 PERCENT
OVERALL WEIGHT = 156.2 LB

HOT
ARGON
IN

23.2 IN.
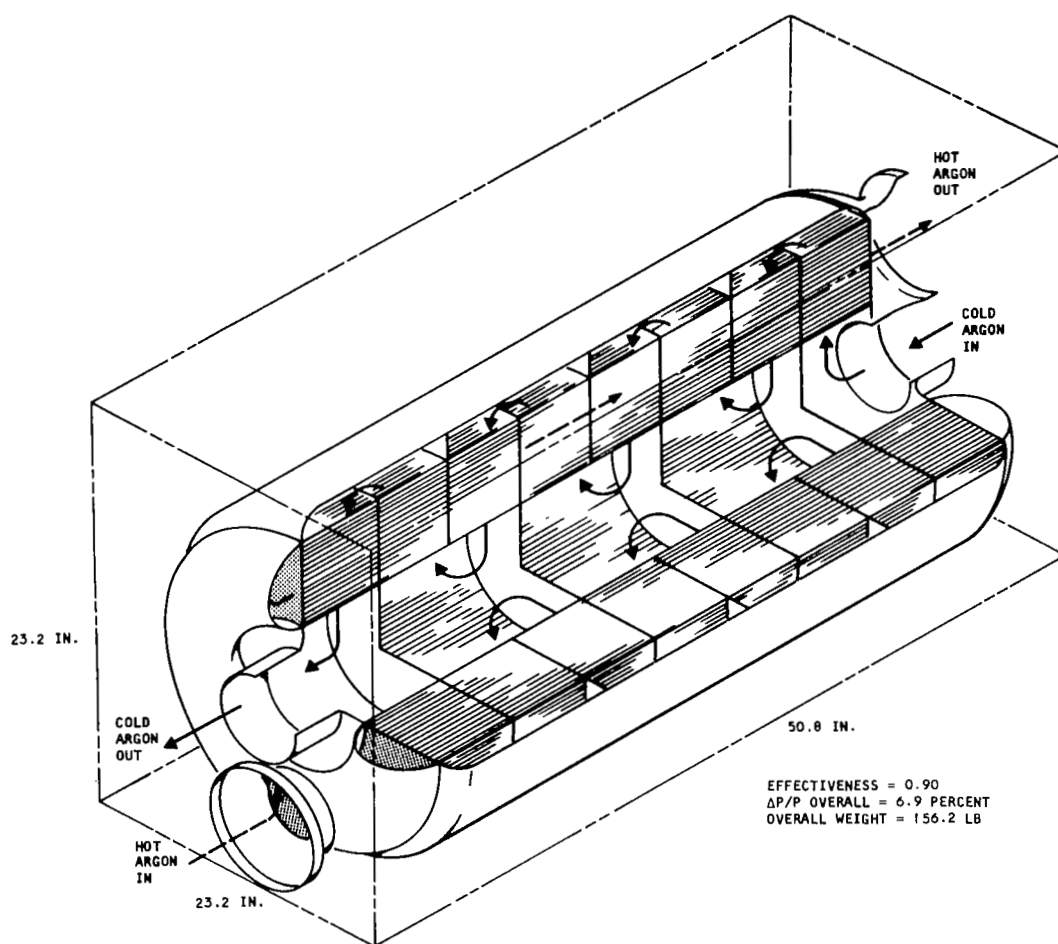
B-415

Figure 9. Single Ring Packaging of Tubular Cross
Counterflow Heat Exchanger
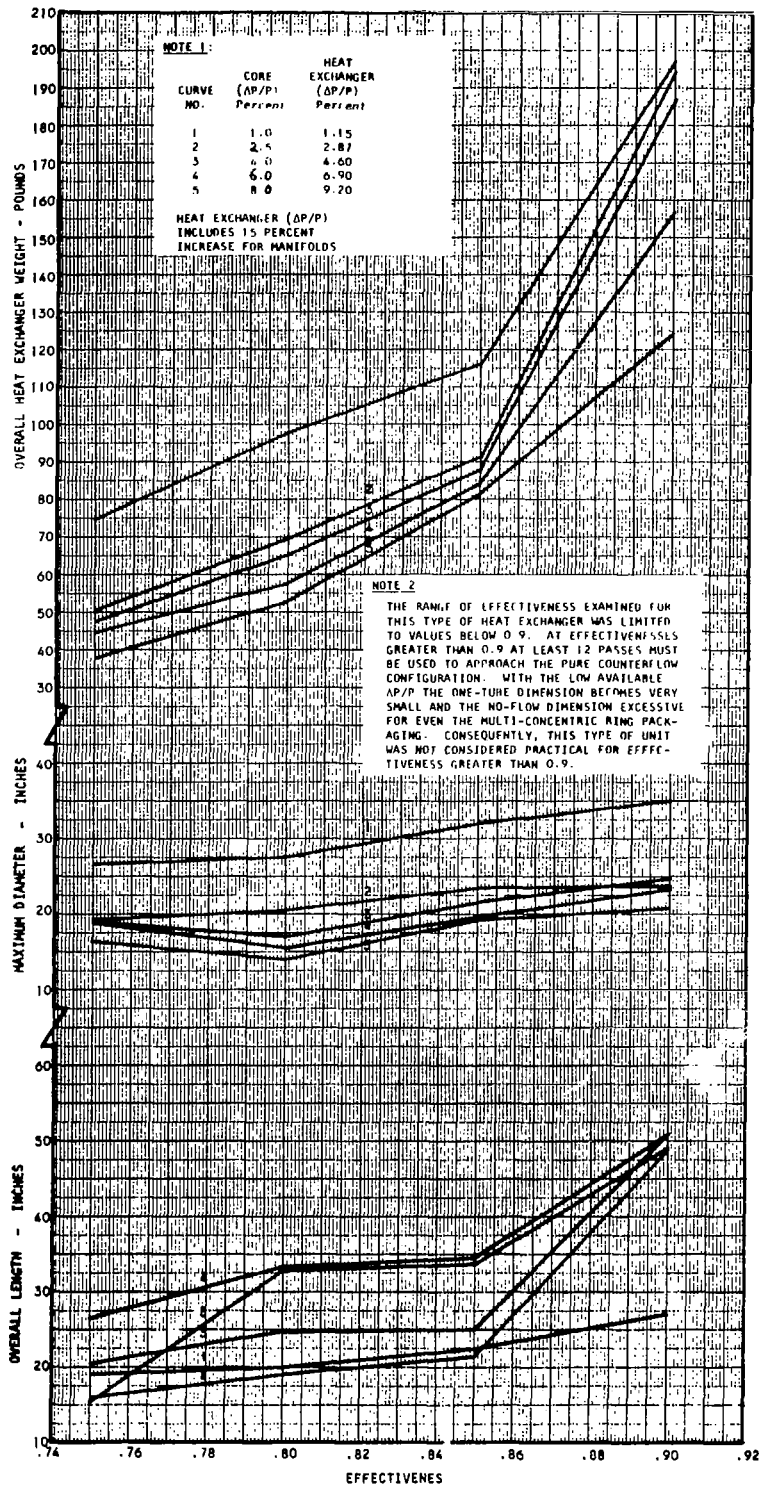
Figure 10. Tubular Multipass Cross Counterflow Heat
Exchanger Parameters Versus Effectiveness

16

quoted are connected by a series of straight lines. Also, as before, the absence of smooth curves and easy interpolation is due to the fact that as problems conditions change, the optimum matrix geometry also changes. These curves of Figure 10 do, however, illustrate clearly the effect of both effectiveness and total pressure drop on recuperators designed utilizing the multipass, cross counterflow tubular heat exchanger design concept.

MULTIPASS CROSS-COUNTERFLOW PLATE FIN HEAT EXCHANGERS

As with the multipass tubular heat exchanger solutions, a large number of matrix geometries were considered for the full range of problem conditions. The construction of all plate and fin matrices considered in this section of the study utilized 0.004 in. thick, nickel fins and 0.006 in. thick, stainless steel plates throughout. The nickel fins are preferred to stainless steel because of the higher thermal conductivity of nickel thereby increasing the contribution of the extended surface. Figures 11, 12 and 13 summarize representative weights and sizes obtained from the computer program used to design the plate fin multipass cross-counterflow heat exchangers. The results shown in these figures are for the heat transfer matrix only; no allowance was included for packaging or manifolding. Also the full available pressure drop is used within the core and, as with the cross-counterflow tubular solutions, Figure 11 shows the weight and the three basic dimensions of the heat transfer matrix plotted against effectiveness for three different pressure drop levels. As effectiveness increases, so does the number of passes and the number of passes actually utilized at each effectiveness is shown on the figure. Figures 12 and 13 show the effect of changing total pressure drop on heat exchangers with effectiveness of 0.75 and 0.90 respectively. In all cases with this type of heat transfer matrix, even at the lowest effectiveness and highest pressure drop, the no-flow dimension of the core is very large when compared to the other two dimensions. This very long no-flow dimension introduces packaging an and manifolding problems and even in the cases of the so-called best size solutions, careful attention must be paid to packaging in order to obtain reasonable overall dimensions.

Utilizing the simplest form of packaging for this type of core, that is, leaving the no-flow dimension as a single length, a core of the type illustrated in Figure 14 is evolved. This type of design is obviously unacceptable from the flow distribution standpoint as the manifold lengths are so great that a large part of the heat transfer matrix would be starved of flow. The very awkward appearance of this core is considerably emphasized by the inlets and outlets shown. The duct diameters of 8 in. on the low pressure side and 6 in. on the high pressure side were arbitrarily selected and are utilized on most figures shown in the parametric study. These duct sizes appear compatible with maintaining the very low pressure drop throughout the system. The particular heat exchanger shown in Figure 14 was designed for an effectiveness of 0.8 and a total pressure drop of 4 percent. Even at these fairly modest operating conditions and utilizing the "best size" type of solution, the overall package dimensions, using the simplest form of packaging are not acceptable. At a slightly higher pressure drop level (6 percent) and the same effectiveness and utilizing a form of packaging which divides the no-flow length into two equal portions, a somewhat improved form of packaging may be obtained as illustrated in Figure 15. For the range of operating conditions for the solar
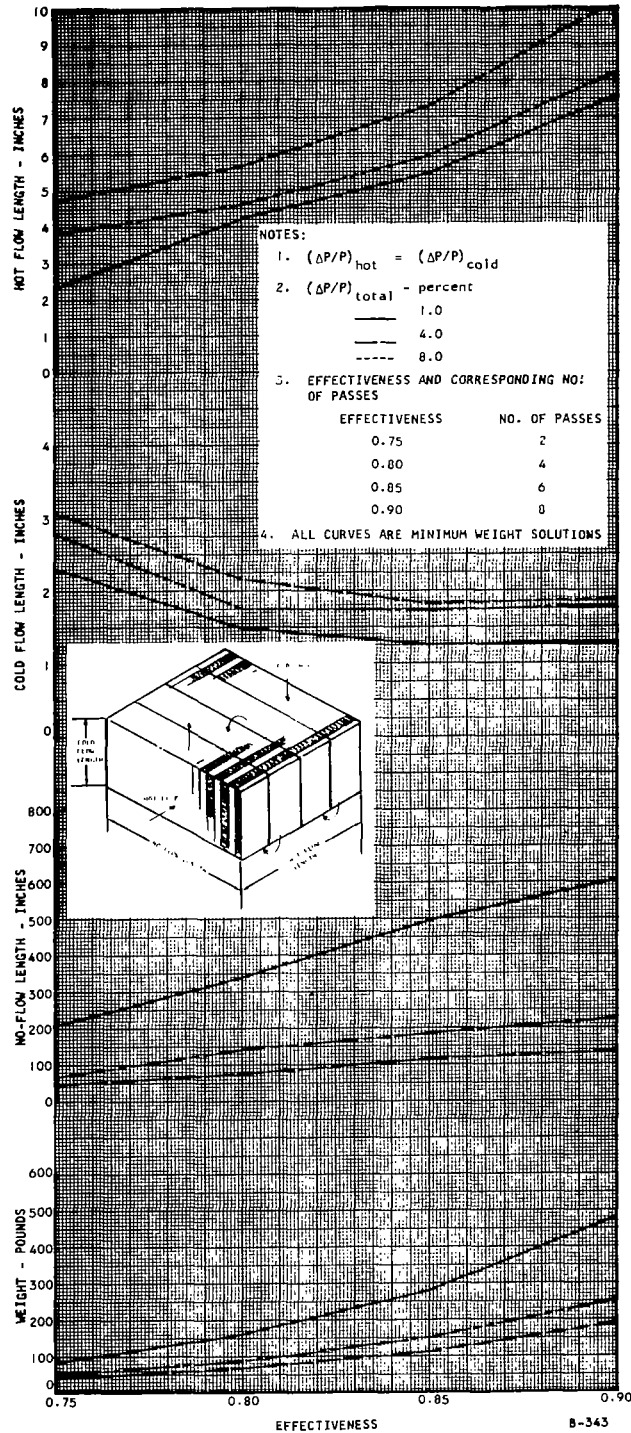
Figure 11. Plate-Fin Multipass Cross Counterflow Core
Parameters Versus Effectiveness

NOTES:
1. ALL CURVES ARE FOR 0.75 EFFECTIVENESS AND 2 PASSES
2. ———— ARE MINIMUM WEIGHT SOLUTIONS
   - - - - ARE BEST SIZE SOLUTIONS
3. $(\Delta P/P)_{hot} = (\Delta P/P)_{cold}$
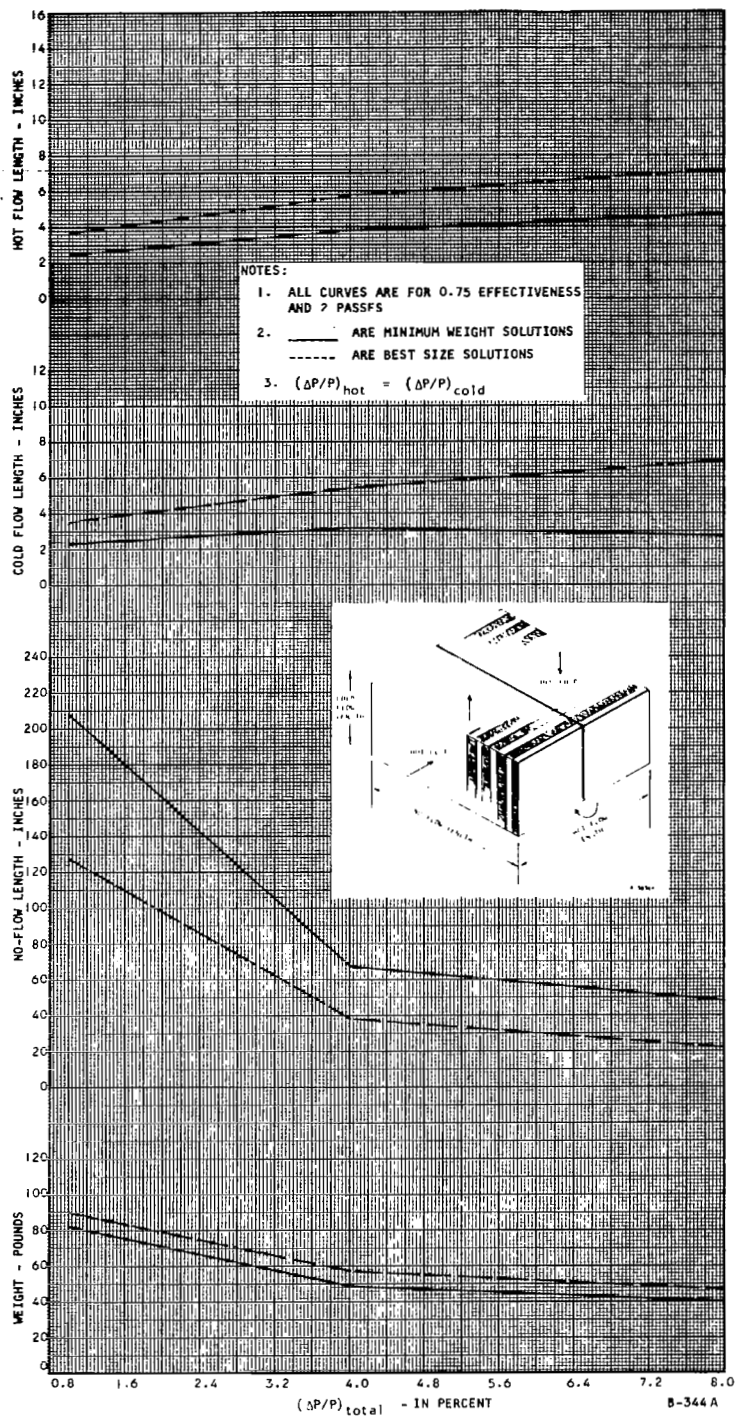
Figure 12.   Plate-Fin Multipass Cross Counterflow Core Parameters Versus Percent Pressure Drop
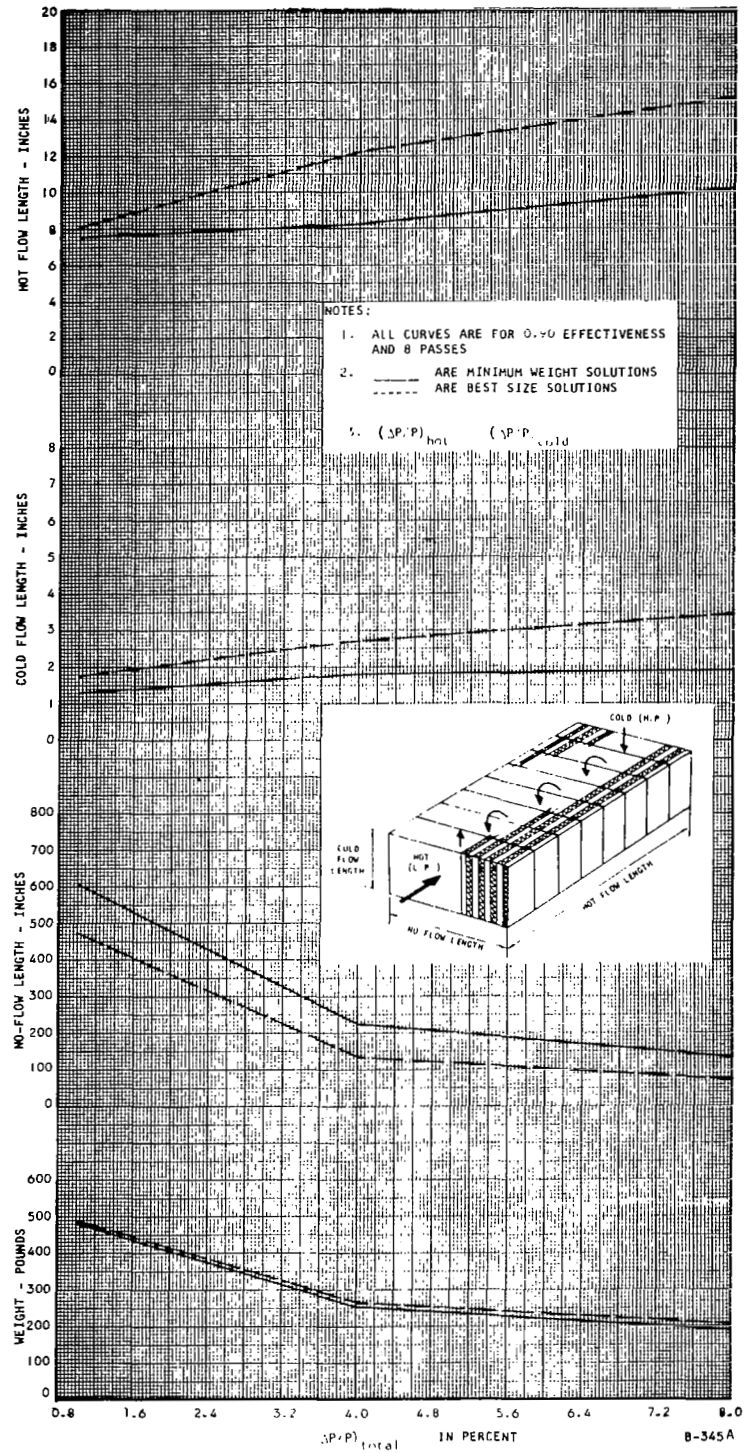
Figure 13. Plate-Fin Multipass Cross Counterflow Core Parameters Versus Percent Pressure Drop

HOT ARGON
OUT

79.0 IN.

COLD ARGON
IN

HOT ARGON
IN

COLD ARGON
OUT

EFFECTIVENESS = 0.80
(ΔP/P) OVERALL = 4.6 PERCENT
OVERALL WEIGHT = 129.1 LB
OVERALL INCLUDES MANIFOLDS
FOR BOTH WEIGHT AND PRESSURE
DROP

8.2 IN.   14.7 IN.
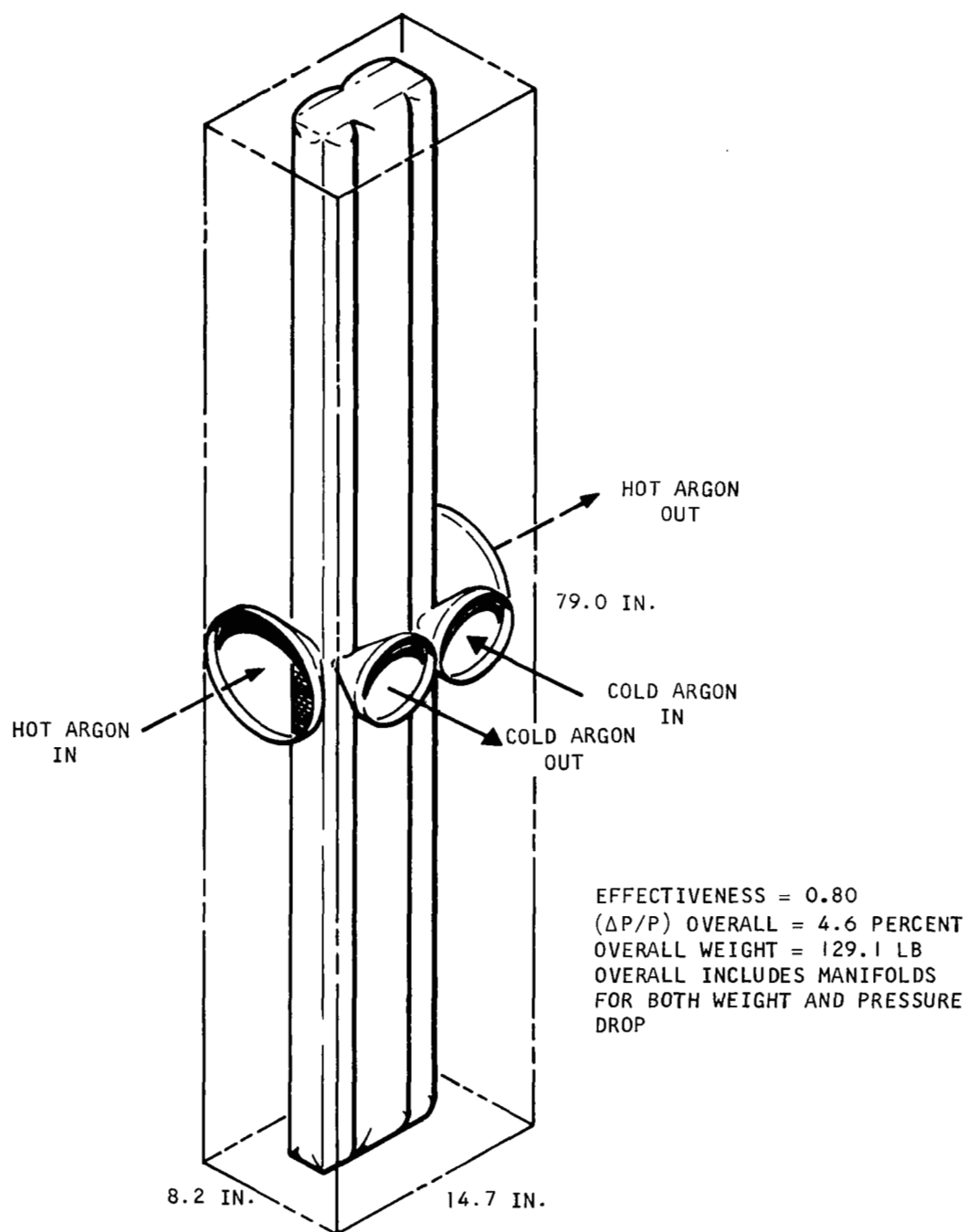
A-4364

Figure 14.   Simple Packaging of Plate-Fin
Cross Counterflow Heat Exchanger

21

HOT
ARGON
OUT

COLD
ARGON
OUT

14.8 IN.

COLD
ARGON
IN

31.9 IN.

11.5 IN.

HOT ARGON
IN

EFFECTIVENESS = 0.80
ΔP/P OVERALL = 6.9 PERCENT
OVERALL WEIGHT = 83.7 LB

B-474
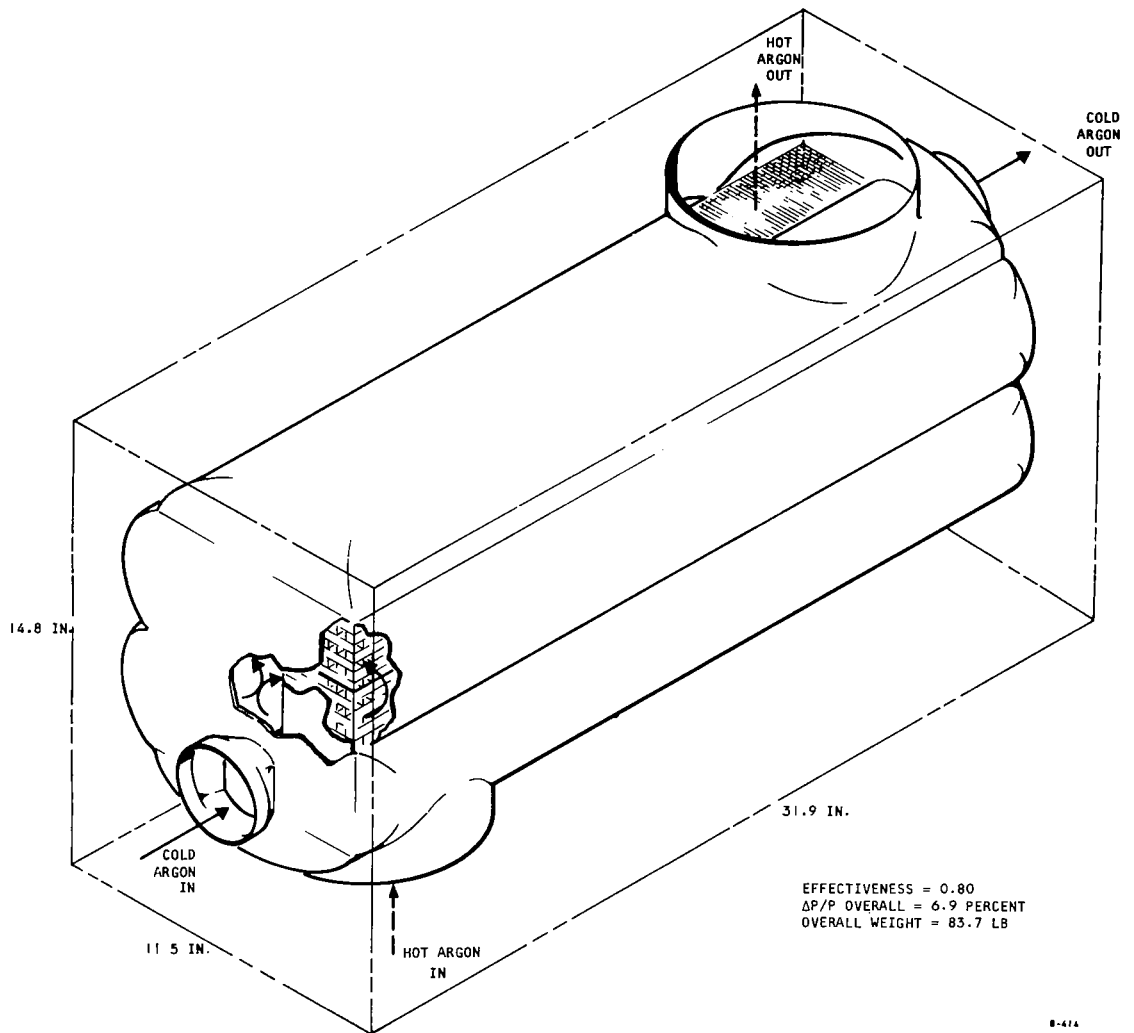
Figure 15. Typical Plate-Fin Cross-Counterflow Heat Exchanger

22

powered Brayton cycle recuperator, no plate fin matrix was found which resulted in a solution which gave both acceptable weight and simple packaging.

A comparison of Figures II, I2 and I3 with Figure IO plainly shows that over the entire range of operating conditions, not only are the plate and fin cores somewhat heavier than the wrapped-up tubular cores, but also the complexities of packaging the plate and fin cores would not yield as attractive packages as the tubular heat exchangers. There is, therefore, no point in the operating conditions of the solar Brayton cycle recuperator where a multipass plate and fin heat exchanger yields a optimum solution. Owing to this fact, no further packaging concepts were prepared and no curves showing overall dimensions and weight of fully packaged plate and fin heat exchangers are presented.

PURE COUNTERFLOW TUBULAR HEAT EXCHANGERS

When the contract to conduct this parametric survey was received from NASA, AiResearch did not have the computer program to design pure counterflow tubular heat exchangers. As part of this contract, a program was written and is described in Appendix C. The main limitation to the use of this program and to the design of this type of heat exchanger, is the lack of reliable heat transfer and friction factor data for flow outside and parallel to, tube bundles. This lack of data and the search conducted by AiResearch into the data that is available, is discussed in Appendix D.

In order to determine whether or not this type of matrix was suitable for any part of the range of operating conditions being studied, it was necessary to assume some predictable operating conditions for the flow outside the tubes. All preliminary investigations of this type of matrix, therefore, used the Colburn Modulus and Fanning friction factor data for flow inside plain round tubes. As with the cross-counterflow tubular heat exchanger designs, all stainless steel construction was used throughout and a wall thickness of 0.004 in.was maintained. By varying tube diameter and tube spacing, a large number of matrix geometries were examined for each problem condition. The results obtained from these preliminary computer runs are shown in Figures 16 and 17. In this particular type of heat transfer matrix, there are only two overall, package dimensions. These two dimensions are face area (or number of tubes) and tube length. There is no theoretical limitation in the way the face area is arranged and throughout the study all computer results were obtained as a rectangular tube bundle with the face aspect ratio of 1.0. The face dimension shown in Figures 16 and 17 is, therefore, one side of a square face. Also shown in Figures 16 and 17 are small tables showing both the assigned and actual pressure drop of each of the curves appearing on these figures. The assigned pressure drops shown represent the input conditions fed into the computer, while the actual pressure drops shown represent the core pressure drop utilized in the final design. The difference between the assigned and actual pressure drop results from the fact that only one side of these pure counterflow heat exchangers utilizes the full available pressure drop and the other side utilizes only a fraction of the given input. The program is so written that the side requiring the most pressure drop is always controlling and therefore, the core pressure drop for any design is always less than the assigned.
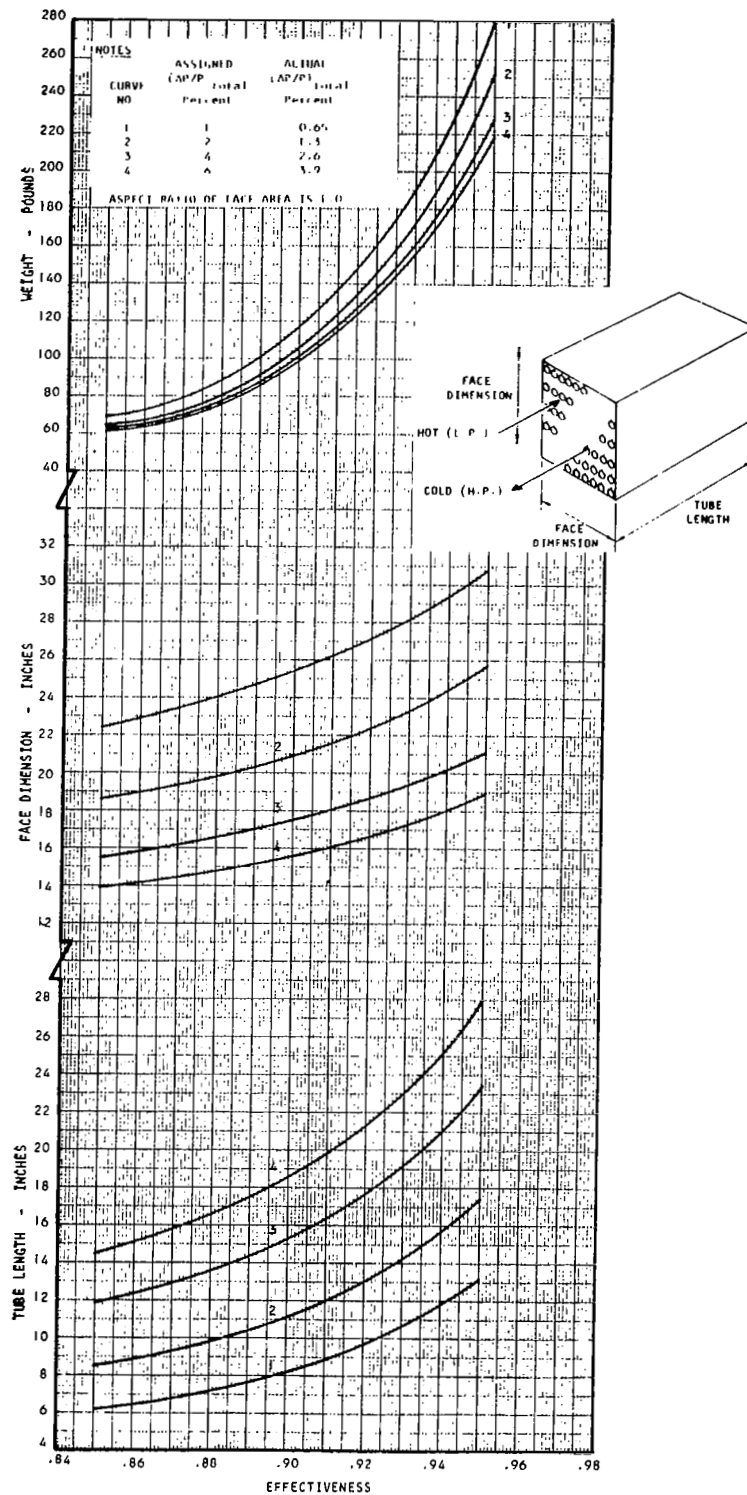
Figure 16. Tubular Pure Counterflow Minimum Weight Cores Versus Effectiveness
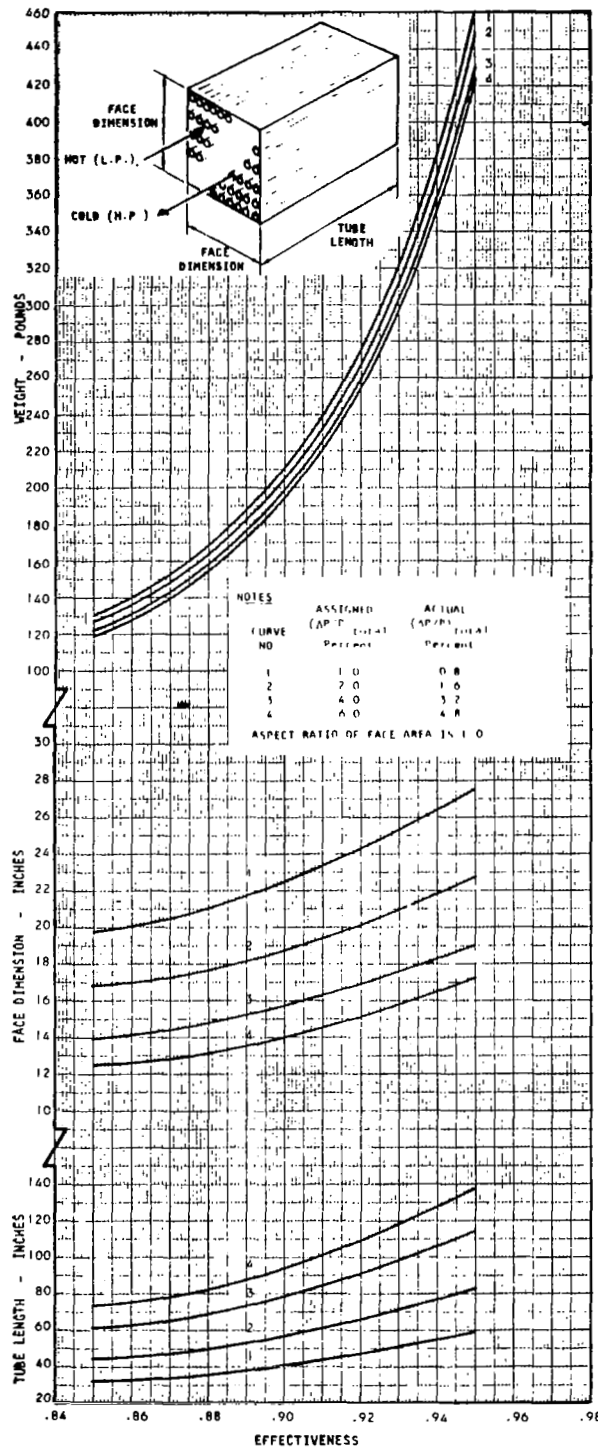
Figure 17. Tubular Pure Counterflow Minimum Face Area Cores Versus Effectiveness

Figure 16 presents a summary of the minimum weight solutions obtained for the range of operating conditions examined. The range of conditions examined for this type of heat exchanger, was limited to effectivenesses greater than 0.85 and assigned pressure drops of less than 6 percent. From the figure it can be seen that weight increases rapidly with increasing effectiveness while both face area and tube length increase at a somewhat slower rate. The influence of overall pressure drop on heat exchanger weight is not great, but its influence on package dimensions is pronounced. As pressure drop is decreased, face area increases and tube length decreases. In all the designs utilized to prepare Figure 16, no allowance is made to either dimensions or weight for manifolding and packaging. All designs of this figure do, however, consider the effect of axial conduction. The method of allowing for the effect of axial conduction in this type of heat exchanger, is described in Appendix A. It is of interest to note, that at the low end of the range considered (effectiveness 0.85, $(\Delta P/P) = 3.9$ percent) the effect of axial conduction increases heat exchanger size by approximately 3 percent. At the high end of the operating range (effectiveness 0.95, $(\Delta P/P) = 0.65$ percent) the effect of axial conduction on heat exchanger size increases to 53 percent.

In order to determine what effect variations in outside tube characteristics would have on heat exchanger performance some designs where prepared using hypothetical values for both heat transfer characteristics and friction factor. The changes selected in these characteristics were purely arbitrary but, were sufficiently large to ensure that appreciable changes in core size and weight would occur. The designs presented in Figures 16 and 17 utilized the Colburn modulus and Fanning friction factor for flow in plain round tubes. The arbitrary changes selected were to increase the friction factor by 25 percent with a corresponding increase in Colburn modulus of 10 percent and to decrease the friction factor by 25 percent with a decrease in Colburn modulus of 10 percent. The effect of these arbitrarily selected changes in outside the tube bundle characteristics on heat exchanger size is clearly shown in Figure 18. At all effectivenesses from 0.85 to 0.95, the effect on heat exchanger weight is very small while the effect on heat exchanger dimensions is somewhat greater. The curves shown in Figure 18 are all for a cold pressure drop (outside tubes) of 1 percent. If a higher nominal pressure drop core is considered the changes in heat exchanger weight and size are somewhat less while if a lower pressure drop design is considered the effects are slightly greater. The main purpose in preparing Figure 18 was to show, that although the data available for flow outside and parallel to tube bundles is very vague the use of flow inside plain round tubes does not invalidate a comparison of pure counterflow tubular heat exchangers with pure counterflow plate-fin heat exchangers. If, however, it is decided to fabricate a pure counterflow tubular heat exchanger more accurate data would be required in order to obtain an accurate determination of the dimensions required.

As with the cross-counterflow tubular solution, considerable attention must be devoted to the manifolding and packaging concepts in order to determine optimum heat exchanger configuration. As stated above, the computer program generates a tube bundle with a square face area. While this type of face area presents a very simple set of core dimensions, it is almost impossible to introduce the outside flow to the center of the bundle. In order to ensure
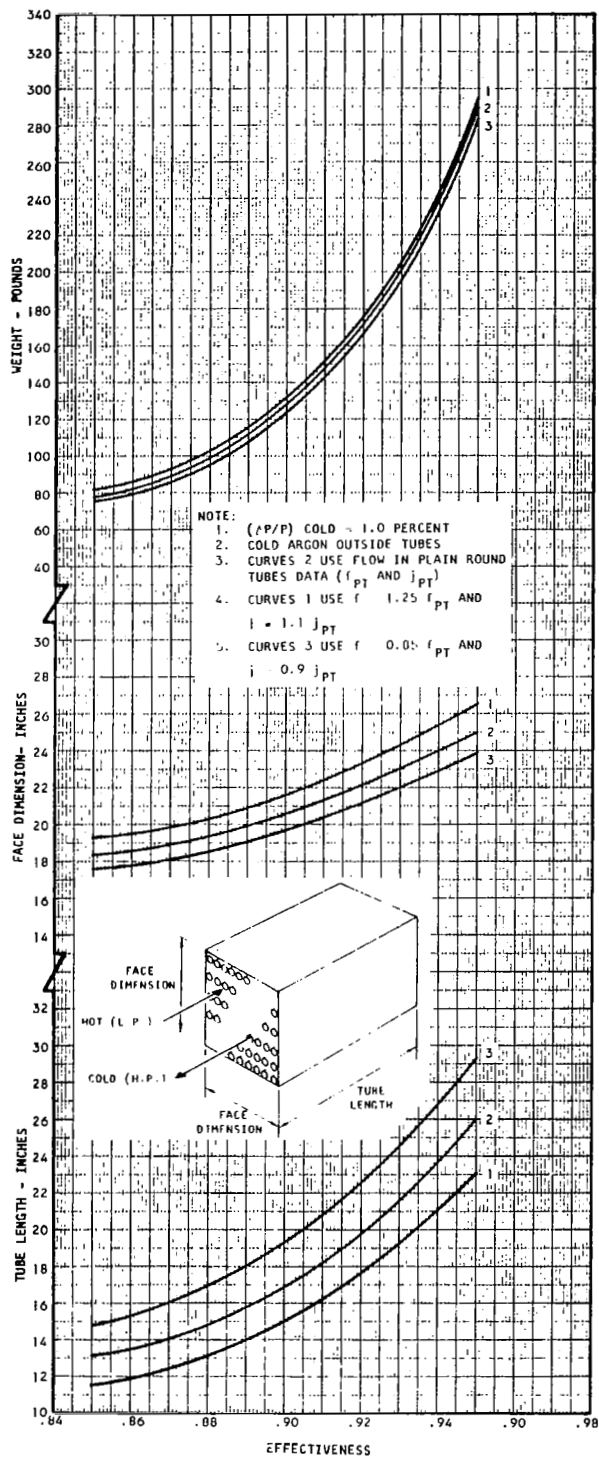
Figure 18. Effect of Outside Tube Performance
Characteristics on Pure Counterflow
Tubular Cores

satisfactory performance of cores of this type it is necessary to be sure that the flow on the outside of the tubes is actually parallel to the tubes rather than across them. It is, therefore, necessary to have one small dimension in the face area which minimizes the length across the tubes over which the flow must pass. By introducing this limitation the other dimension of the face area consequently becomes large and the same packaging problem exists as existed with the cross-counterflow tubular designs. Two different methods of packaging this type of heat exchanger core are illustrated in Figures 19 and 20. Figure 19 shows how the one long dimension of the face area may be divided into several shorter straight lengths. A means of introducing both the hot and cold fluids to this type of overall configuration is also illustrated in Figure 19. As a direct comparison to the heat exchanger shown in Figure 19, Figure 20 illustrates the identical core wrapped up in the same type of multi-concentric ring design as utilized for the cross-counterflow tubular heat exchangers. Again, Figure 20 illustrates how the fluid would be introduced to both inside and outside the tube bundle. The square design of Figure 19 has the limitation that it is not a good pressure vessel as it possesses a number of large flat faces. This design could be utilized by using honeycomb panels or some form of stiffening structure but is definitely less desirable than the concept shown in Figure 20. In addition to being a better pressure vessel, the multi-concentric ring design also has a slightly lighter weight.

Having selected the multi-concentric ring packaging concept as most suitable for this type of flow configuration, heat exchanger designs were generated covering the desired range of operating conditions. As the severity of the problem conditions being considered increases and the heat exchanger size increases more and more rings are required. In Figure 21, which illustrates the effect of pressure drop level and effectiveness on heat exchanger weight and size, the number of rings utilized varies from 3 to 6. As with the previous curves presented for heat exchanger core dimensions and weight, the small table on Figure 21 shows the nominal pressure drops which were used in the design, together with the actual overall total pressure drops.

PURE COUNTERFLOW PLATE FIN HEAT EXCHANGER

The matrices were assumed to be constructed of stainless steel and to utilize nickel fins 0.004 inches thick and plates 0.006 inches thick. The ratio of face area height to face area width is arbitrary for this type of heat exchanger and a ratio of 1.0 was utilized throughout the calculations.

As a preliminary step a series of designs was run off on AiResearch's IBM 7074 computer using the existing design program for this type of heat exchanger. This existing computer program did not include the effect of axial conduction but was used to establish the trends caused by changing effectiveness and pressure drop. The results of these runs are plotted in Figures 22, 23 and 24. Figure 23 shows the minimum core weight solutions, and the corresponding core dimensions, as a function of effectiveness for several total $\Delta P/P$ ratios. The assigned total $\Delta P/P$ ratios represent the total pressure drops that were given as input to the computer program. Each side of the heat exchanger was allotted one half of the given total $\Delta P/P$. However, since only one side of the heat exchanger used up its allotted pressure drop, the actual pressure drop for the designed core was less than the assigned pressure drop.

31.7 IN.

HOT
ARGON
IN

COLD
ARGON
OUT

HOT
ARGON
OUT

33.0 IN.

31.3 IN.

EFFECTIVENESS = 0.95
($\Delta P/P$) OVERALL = 1.64 PERCENT
OVERALL WEIGHT = 515.0 LB
OVERALL INCLUDES MINIFOLDS
FOR BOTH WEIGHT AND PRESSURE
DROP
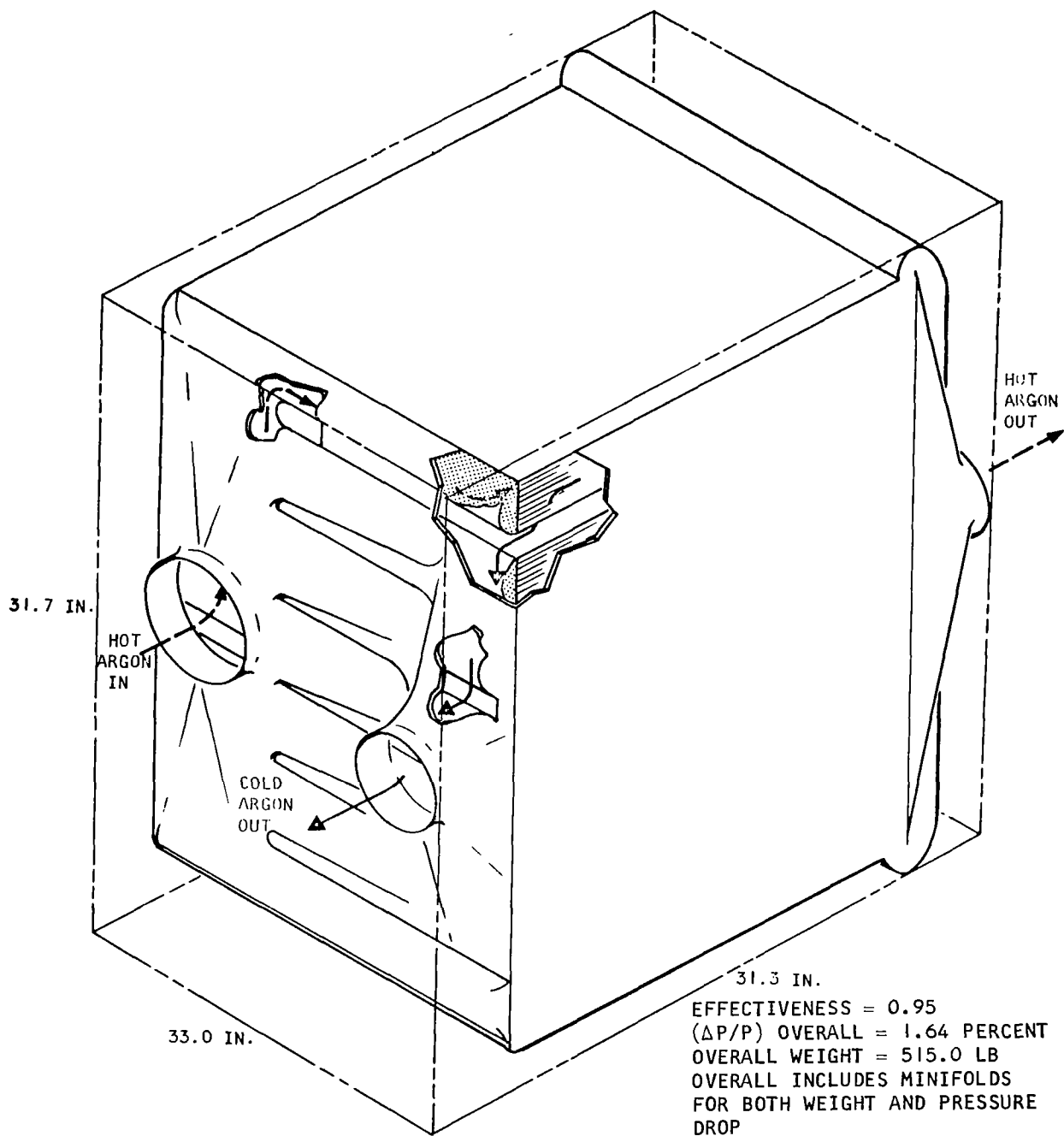
A-4368

Figure 19.   Rectangular Packaging of Tubular Pure Counterflow Heat Exchanger
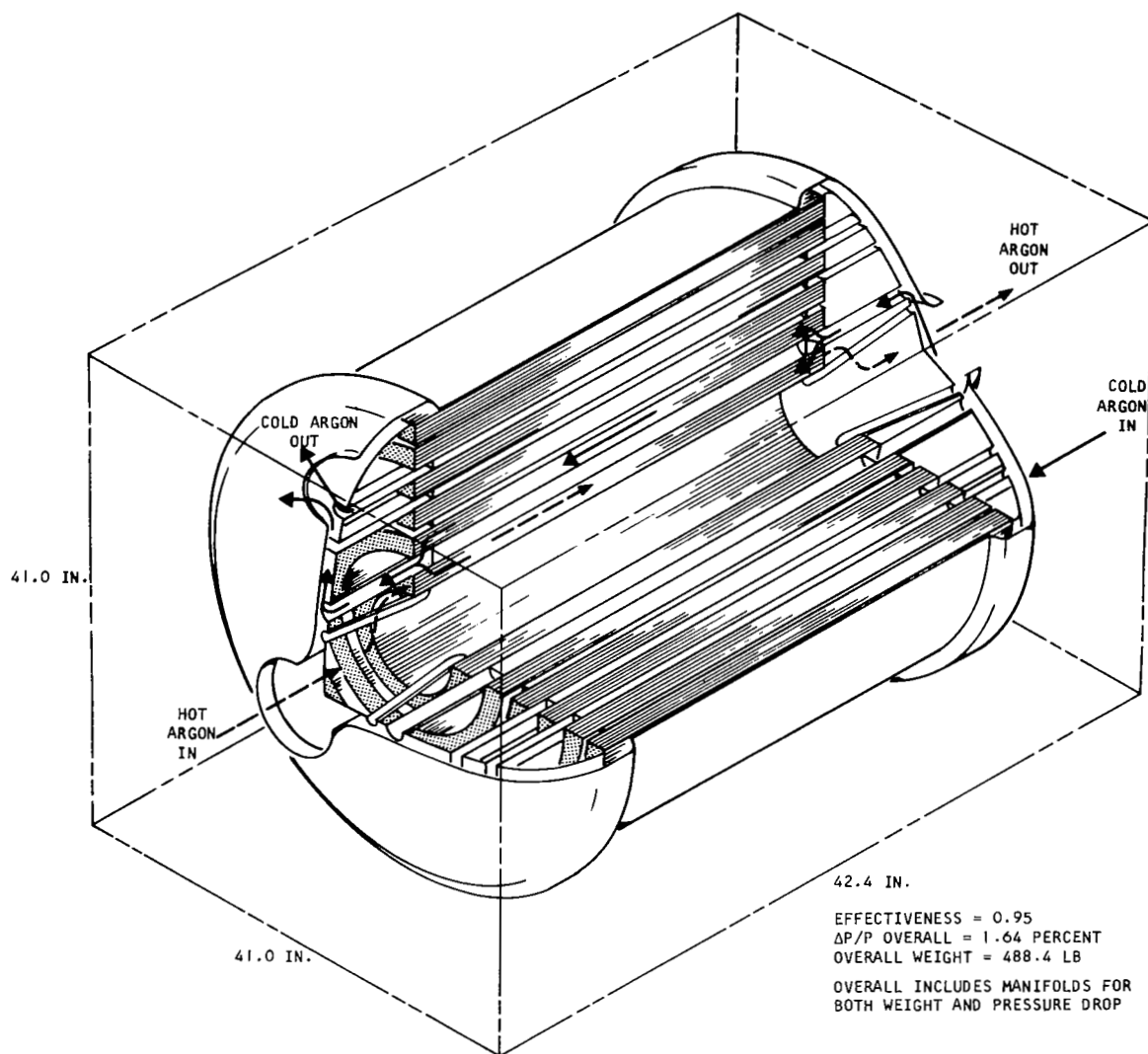
Figure 20. Multiconcentric Ring Packaging of Tubular Pure
Counterflow Heat Exchanger
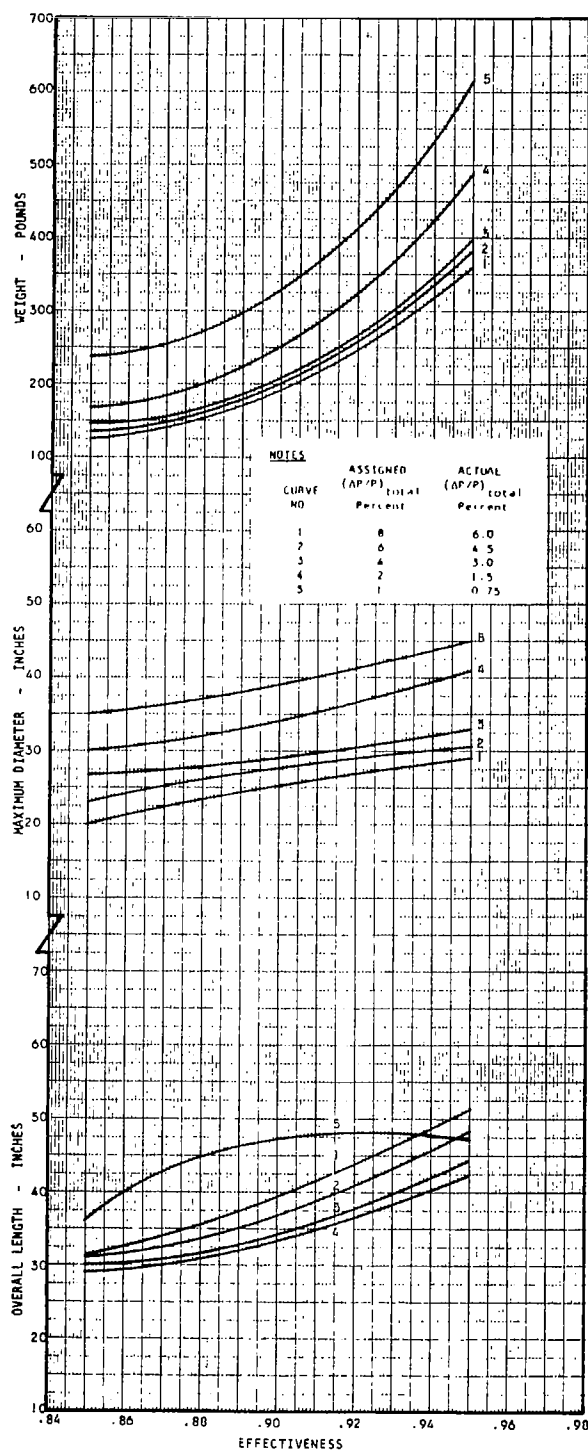
Figure 21.   Tubular Pure Counterflow Heat Exchanger
Parameters Versus Effectiveness

Figure 22. Plate-Fin Pure Counterflow Core Parameters
Versus Effectiveness
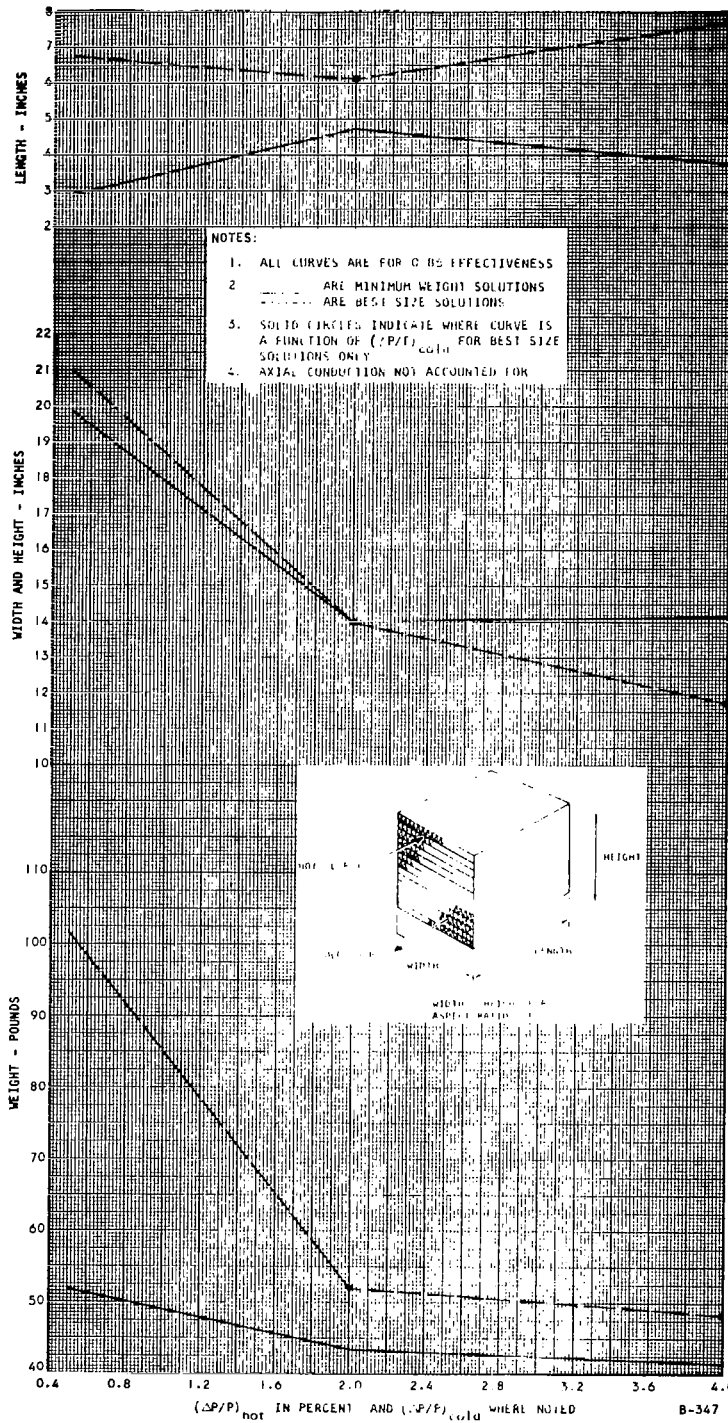
Figure 23. Plate-Fin Pure Counterflow Core Parameters
Versus Percent Pressure Drop
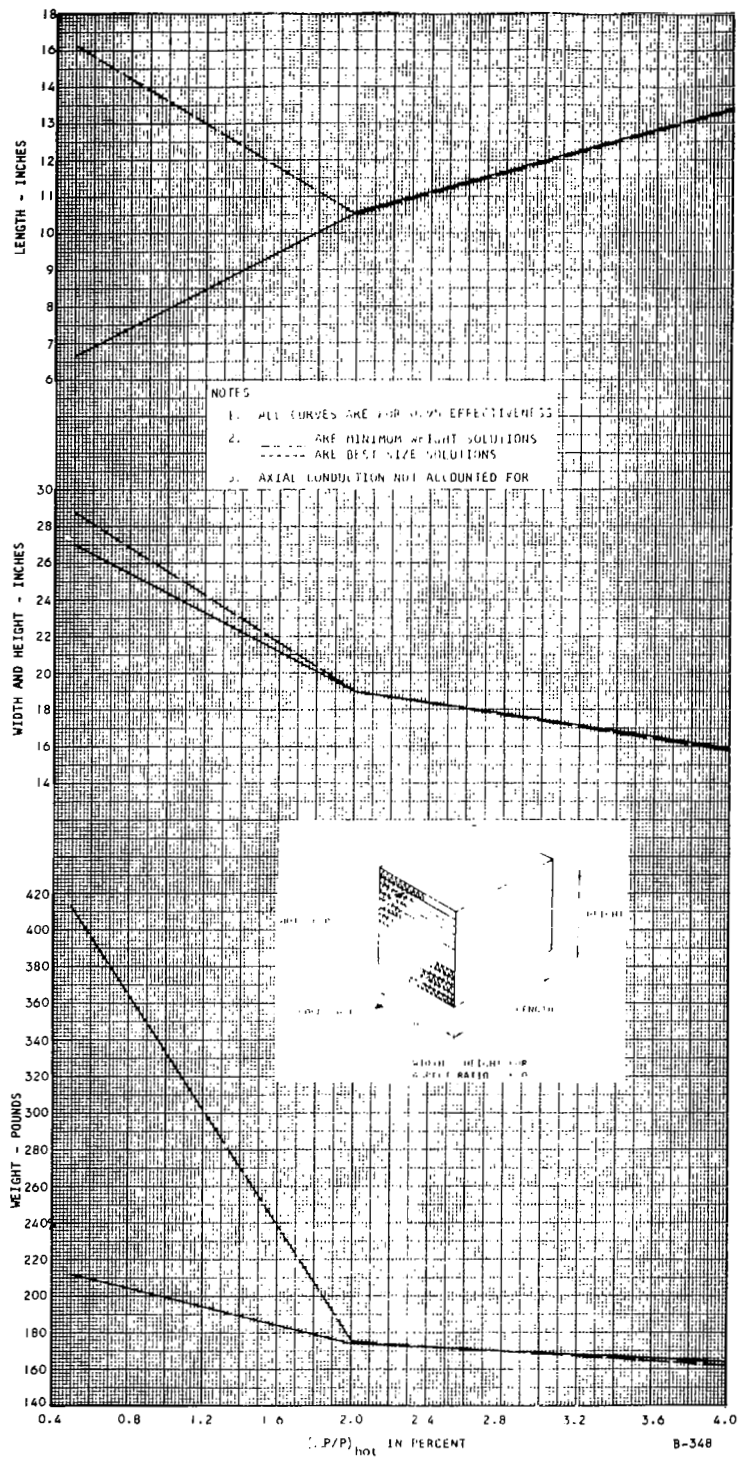
Figure 24. Plate-Fin Pure Counterflow Core Parameters
Versus Percent Pressure Drop

The curves show similar trends to the previous types of heat exchangers, that is, a large increase in both core weight and core face dimensions occurs at high effectiveness and low total $\Delta P/P$ ratios.

The effect of varying $\Delta P/P$ is shown in Figures 23 and 24. The heat exchanger parameters are plotted against percent pressure drop of the side which used up its alloted pressure drop, that is, one half of the assigned total pressure drop. From these figures it is seen that the core weight and core face dimensions are decreased with increasing $(\Delta P/P)_{hot}$ or $(\Delta P/P)_{cold}$ as the case may be. Generally, at low $(\Delta P/P)_{hot}$ ratios the flow lengths are small and the face areas are large. This is undesirable from the standpoint of axial heat conduction and also required manifold weights. As a result, before packaging and manifolding any of these designed cores, the heat exchanger design program was modified to include the effect of axial conduction and the above cores were recalculated. The effect of axial conduction was calculated according to the simplified equations presented in Appendix A.

Two types of manifolding and packaging concepts were developed for the plate-fin pure counterflow heat exchanger. These are shown in Figures 25 and 26. The principal difference between the two is the way the hot and cold fluids are introduced to and removed from the core. The transition sections in Figure 25 are formed by single triangular plate-fin sections while those of Figure 26 are formed from double triangular sections. The entrance and exit free flow areas on both sides of both concepts are identical, but weight savings are obtained in the double triangular concept as less area and mass is used in the transition. The reduction in surface area of the transition sections in the Figure 26 concept over the Figure 25 concept does not affect the heat exchanger performance as the slight additional heat transfer that occurs in these sections is not considered in the design. In both designs the inlet and outlet triangular transition sections are of a plate-fin construction with low density fins on the cold or high pressure side only. The weight of the packaged heat exchanger tends to be less when the fluids are introduced in the manner of Figure 26 as compared to Figure 25, but the double triangular concept of Figure 26 yields a longer overall length. Therefore, the computer designed cores for the rest of the problem statement range were all packaged and manifolded as shown in Figure 26. The weights and dimensions of these packaged cores are plotted in Figure 27 against effectiveness. Several curves are shown each for a different overall total $\Delta P/P$ ratio. These ratios are actual figures and include, besides core pressure drop, the pressure drop due to the inlet and outlet manifolds and transition sections. For these overall pressure drops the transition section losses are calculated from the computer program described in Appendix D while the allowance for the manifolds is the same 15 percent used for the other heat exchanger configurations.

COLD
ARGON
OUT

HOT
ARGON
OUT

HOT
ARGON
IN

COLD ARGON
IN

27.0 IN.
HEAT EXCHANGER
LENGTH

19.0 IN.
FACE DIMENSION

EFFECTIVENESS = 0.95
ΔP/P OVERALL = 4.1 PERCENT
OVERALL WEIGHT = 299.3 LB

OVERALL INCLUDES MANIFOLDS AND
TRANSITION SECTIONS FOR BOTH
WEIGHT AND PRESSURE DROP.
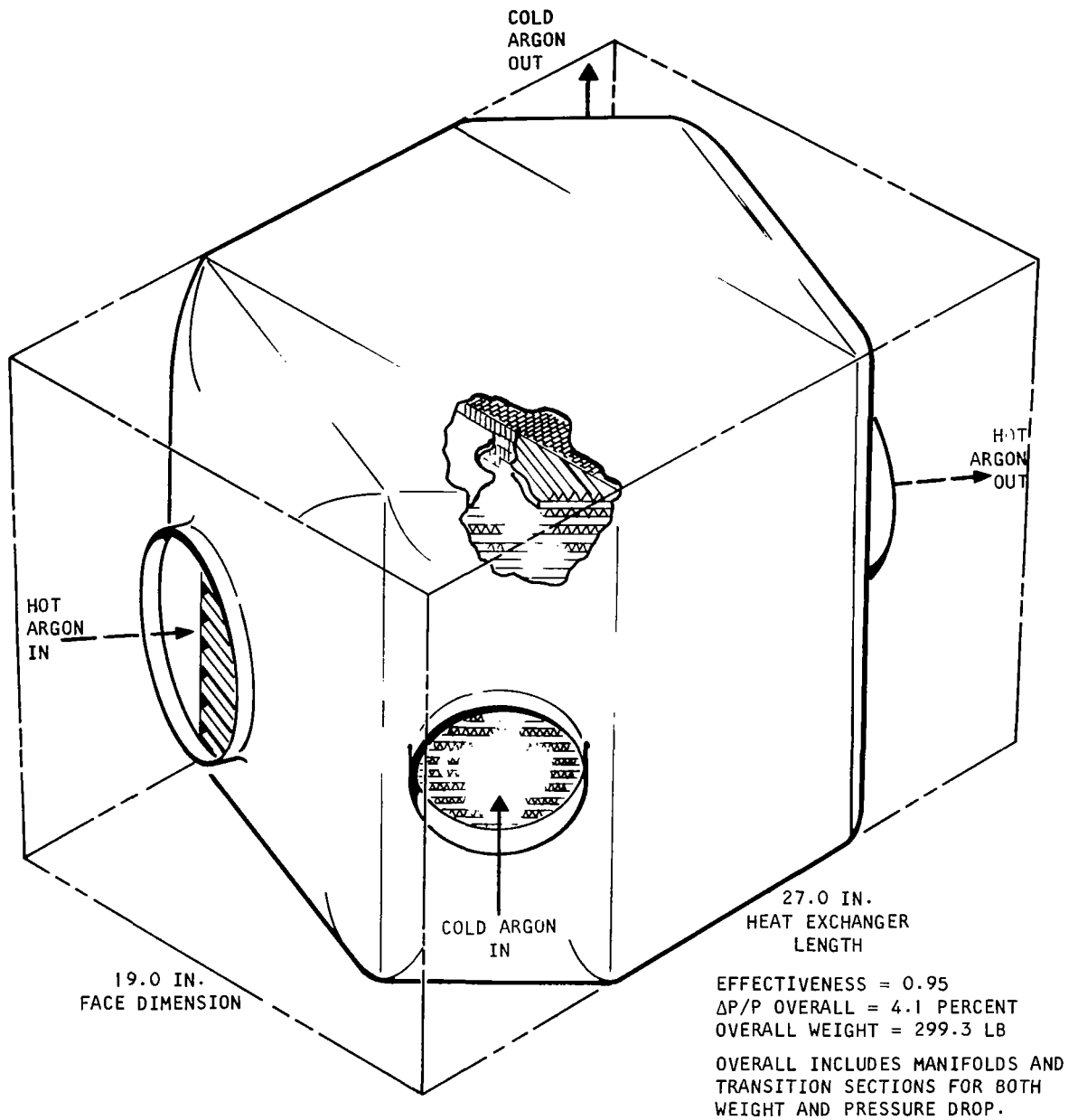
Figure 25.   Typical Plate Fin Pure Counterflow Heat Exchanger

36

HOT
ARGON
OUT

COLD
ARGON
IN

19.4 IN. COLD
ARGON
OUT

HOT
ARGON
IN

19.0 IN.
FACE DIMENSION

29.4 IN.
HEAT EXCHANGER
LENGTH

EFFECTIVENESS = 0.95
$\Delta P/P$ OVERALL $\approx$ 4.1 PERCENT
OVERALL WEIGHT = 274.1 LB

OVERALL INCLUDES MANIFOLDS AND
TRANSITION SECTIONS FOR BOTH
WEIGHT AND PRESSURE DROP.
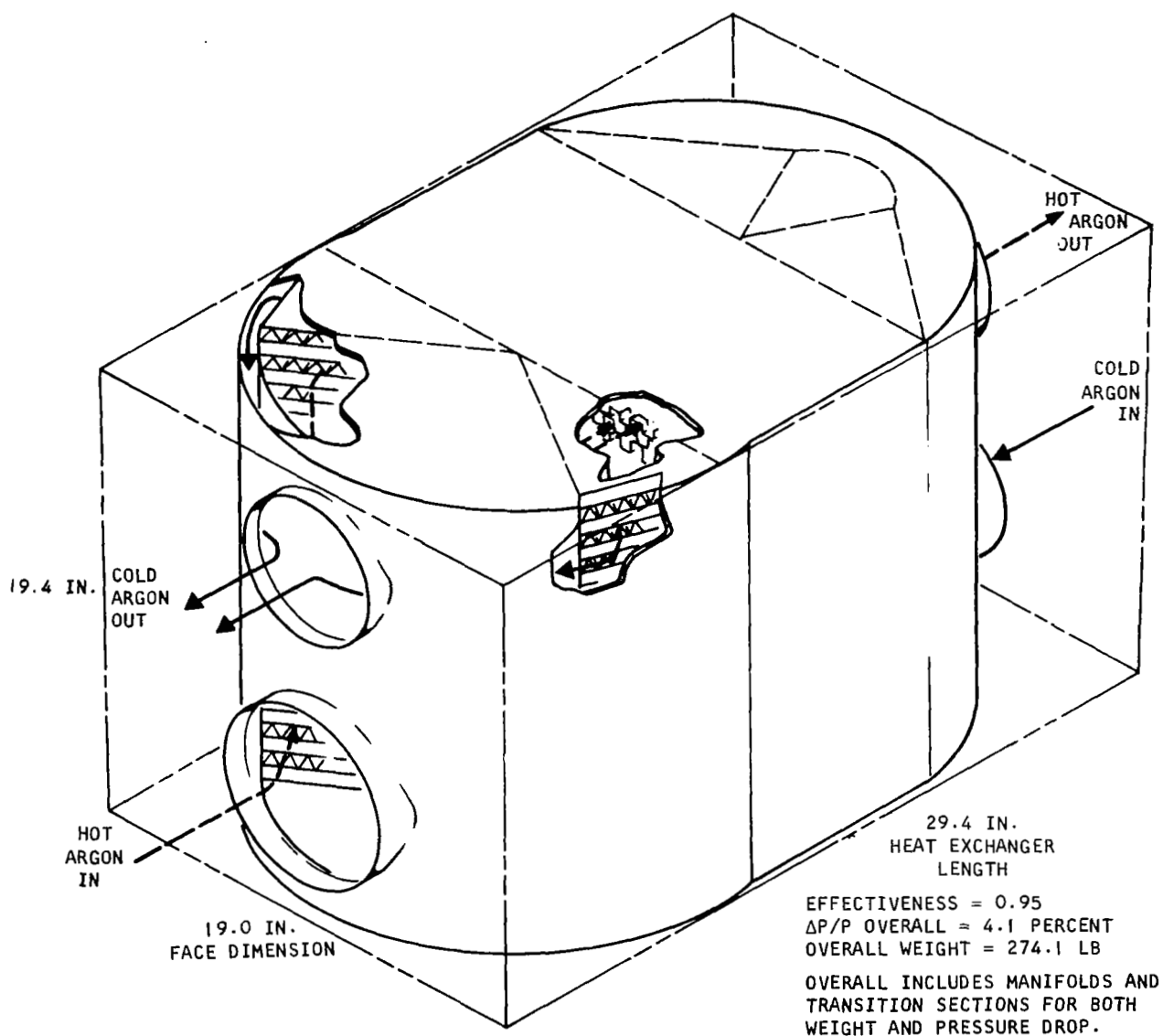
Figure 26.   Alternate Packaging of Plate-Fin Pure Counterflow
Heat Exchanger

37

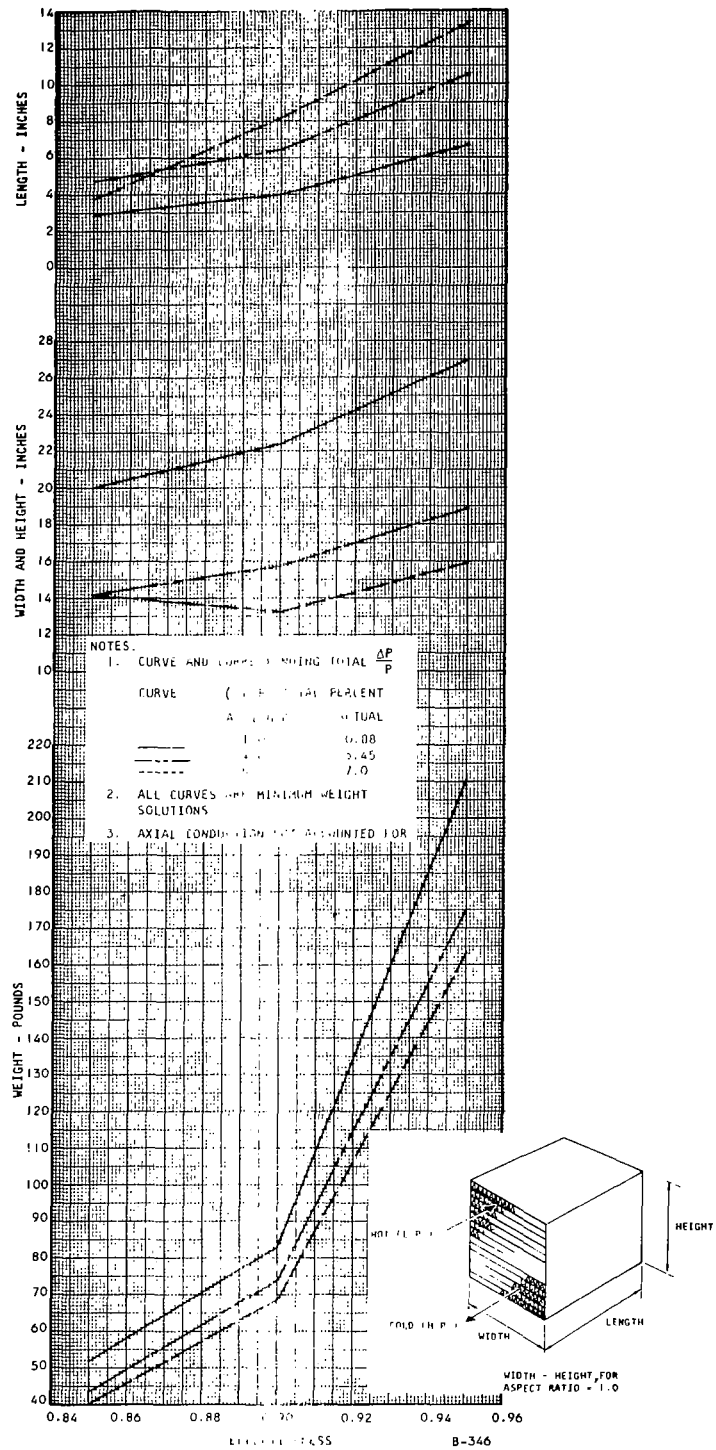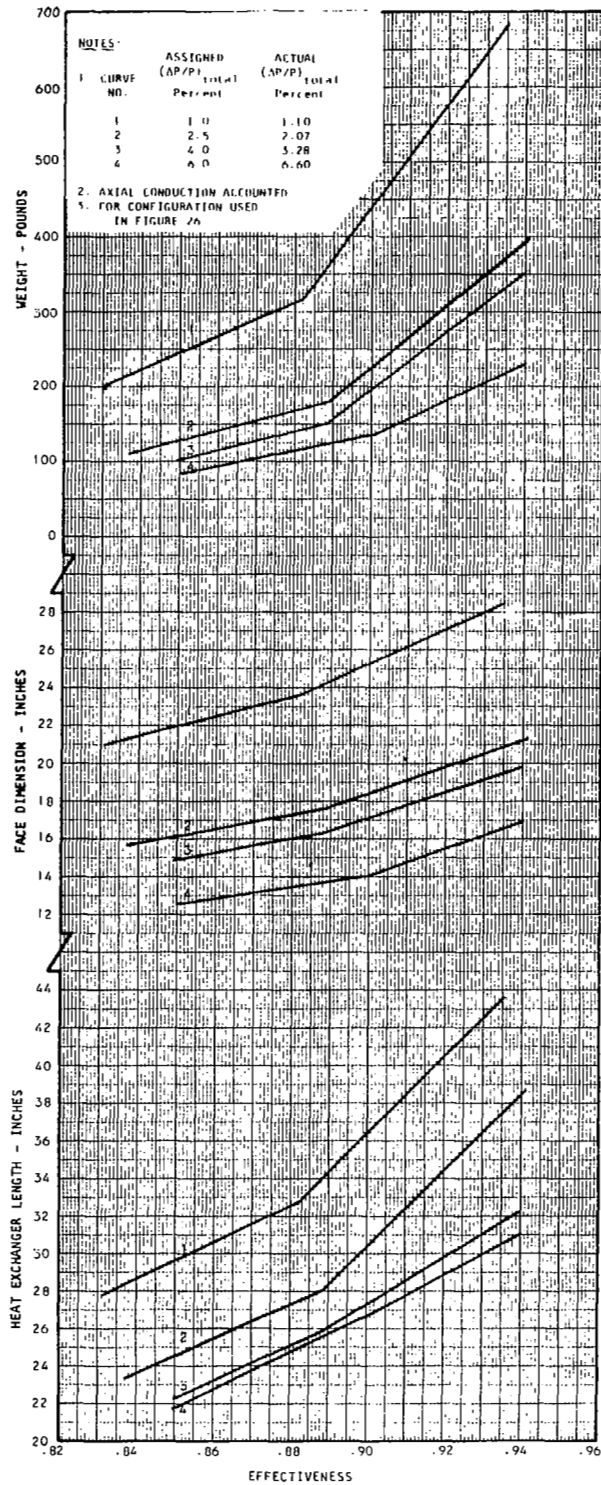Figure 27. Plate-Fin Pure Counterflow Heat Exchanger Parameters Versus Effectiveness

SECTION 3

OPERATING CONDITION AND HEAT EXCHANGER TYPE SELECTION

COMPARISON OF HEAT EXCHANGER TYPES

The previous section outlined the complete investigations conducted on the four types of heat transfer matrices which were considered. Several important conclusions were drawn regarding each of the types considered. For each point of all the curves used in Section 2 a large number of designs using different surface geometries were formulated to determine the "most suitable design". "Most suitable design" may be defined as that design which yielded minimum weight or close to minimum weight heat exchanger package coupled with reasonable dimensions. An examination of the heat transfer cores originally designed by the computer programs eliminated the multi-pass cross-counterflow plate fin heat exchanger from further consideration. This elimination was possible on the grounds that not only was this type of core much heavier than the other types considered, at all operating conditions, but it was also the most complex to package. Having eliminated this particular type, careful consideration was given to packaging concepts for each of the other three types. In the case of both the pure counterflow and the cross counterflow tubular matrices multiple concentric ring packaging was selected as optimum. This type of packaging is illustrated in Figures 8, 9, and 20. With the pure counterflow plate and fin heat exchangers the choice of manifolding and packaging was more limited and the double triangular transition sections illustrated in Figure 26 were selected as optimum.

In order to obtain the isometric diagrams, heat exchanger weights and dimensions used throughout this report at least one layout drawing was made of each of the concepts considered for each type of heat exchanger. As stated previously, there is no simple, unique heat exchanger concept or type which is most satisfactory at all conditions. For the range of problem conditions examined, that is, effectiveness from 0.75 to 0.95 and pressure drop ratio $(\Delta P/P)_{OVERALL}$ from 1 percent to 8 percent a very rough guide in the selection of the optimum cores may be made as follows. At the highest effectiveness and lowest pressure drop conditions pure counterflow tubular heat exchangers present the lightest weight solutions. If minimum projected area is more valuable than minimum weight, pure counterflow plate-fin cores may be used, but at a considerable weight penalty. In the intermediate range pure counterflow plate-fin solutions yield both minimum weight and minimum projected area. In the low effectiveness and high pressure drop section of the range, cross-counterflow tubular units have the lightest weights, but projected areas may be reduced by the selection of pure counterflow plate-fin units.

Figures 28 and 29 were prepared to compare in detail the three types of heat exchangers which are being considered for use in the Brayton cycle system. These two figures were prepared by carefully considering the information presented in Figures 10, 21 and 27. As the exact pressure drop values used in each of these figures do not coincide a slight amount of interpolation was required. The interpolations were based on the very large mass of data obtained by AiResearch while formulating these designs. In Figure 31 the heat exchangers are compared on the basis of weights and smallest projected area that the heat exchanger presents from any particular side. The three sets of curves are for three different total percent pressure drops. From these curves another set of curves, Figure 29, was prepared which presented the selected minimum weight and minimum projected area designs for the given problem statement range.

Figures 28 and 29 present a summary of the recommended recuperator designs which should be considered when making a selection for the Brayton cycle system. In order to obtain solutions over the entire effectiveness and pressure drop range examined interpolations of the curves in Figures 28 and 29 may be required. Interpolation of these curves does not yield exact solutions and therefore, when NASA finally selected the operating conditions and heat exchanger type a re-evaluation was necessary to determine the final design details.

PRELIMINARY DESIGN SELECTION

On July 15, 1964 official confirmation of the NASA selection of a pure counterflow plate fin heat exchanger as the unit to meet their specification was received. The final operating conditions selected for this unit were as follows:

	Hot Inlet	Cold Inlet
Temperature, $^{\circ}$R	1560	801
Pressure, psia	6.73	13.8
Argon flow rate, lb per min	36.69	36.69
Effectiveness	0.9	0.9

Total pressure drop ($\Delta P/P$ for both sides), percent = 2.0

With the decision to use this type of matrix at these conditions, a very careful survey of the results obtained during the parametric study was made to ensure that the optimum core was selected. This study of the heat exchanger designs formulated led to the selection of a heat exchanger matrix with a flow length of 7.28 in., a stack-up height of 25.46 in., a flow width of 25.19 in. This core consisted of 74 sandwiches of 12 rectangular

Figure 28. Heat Exchanger Weights and Projected Areas for Three Matrix Types
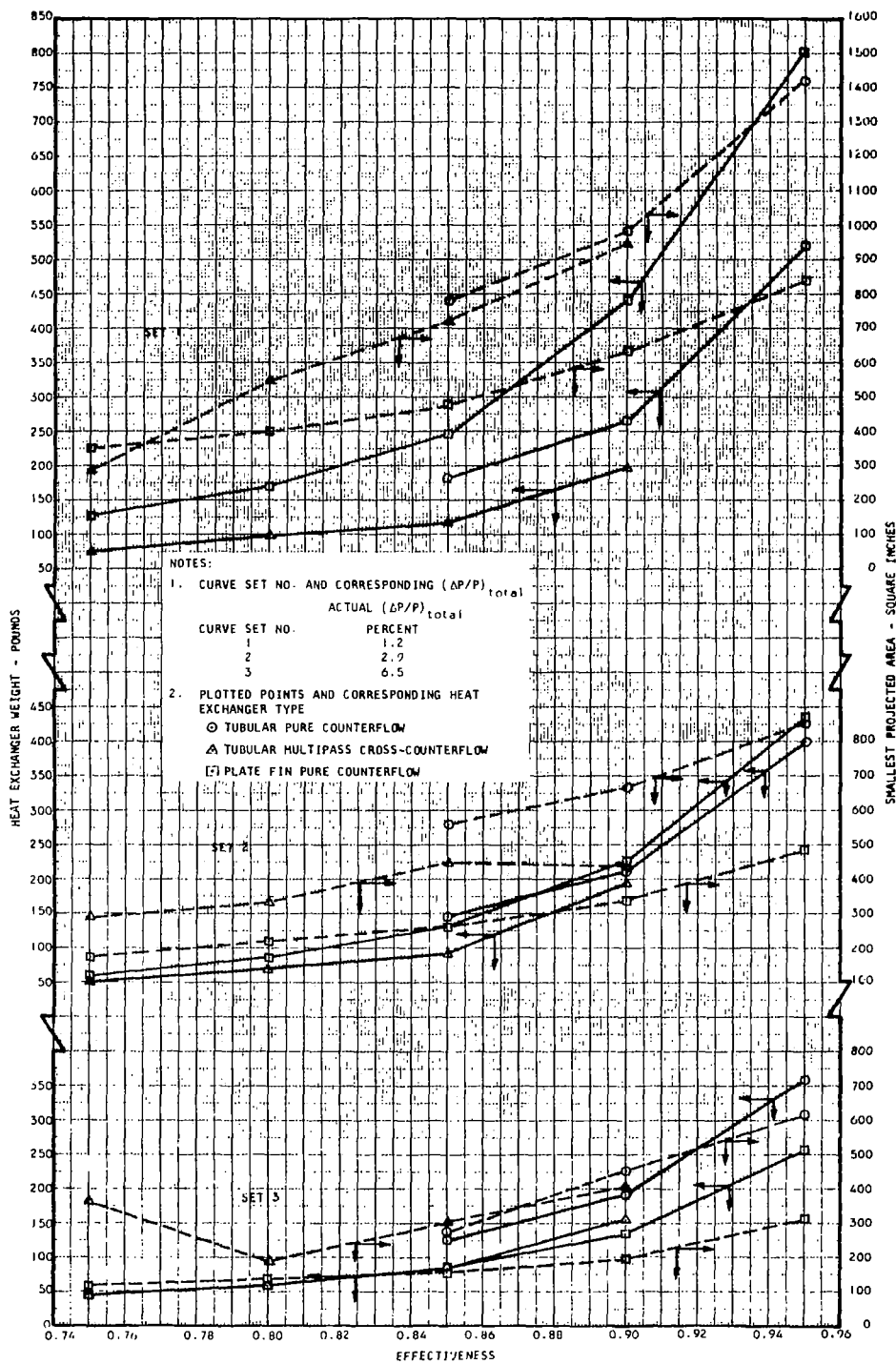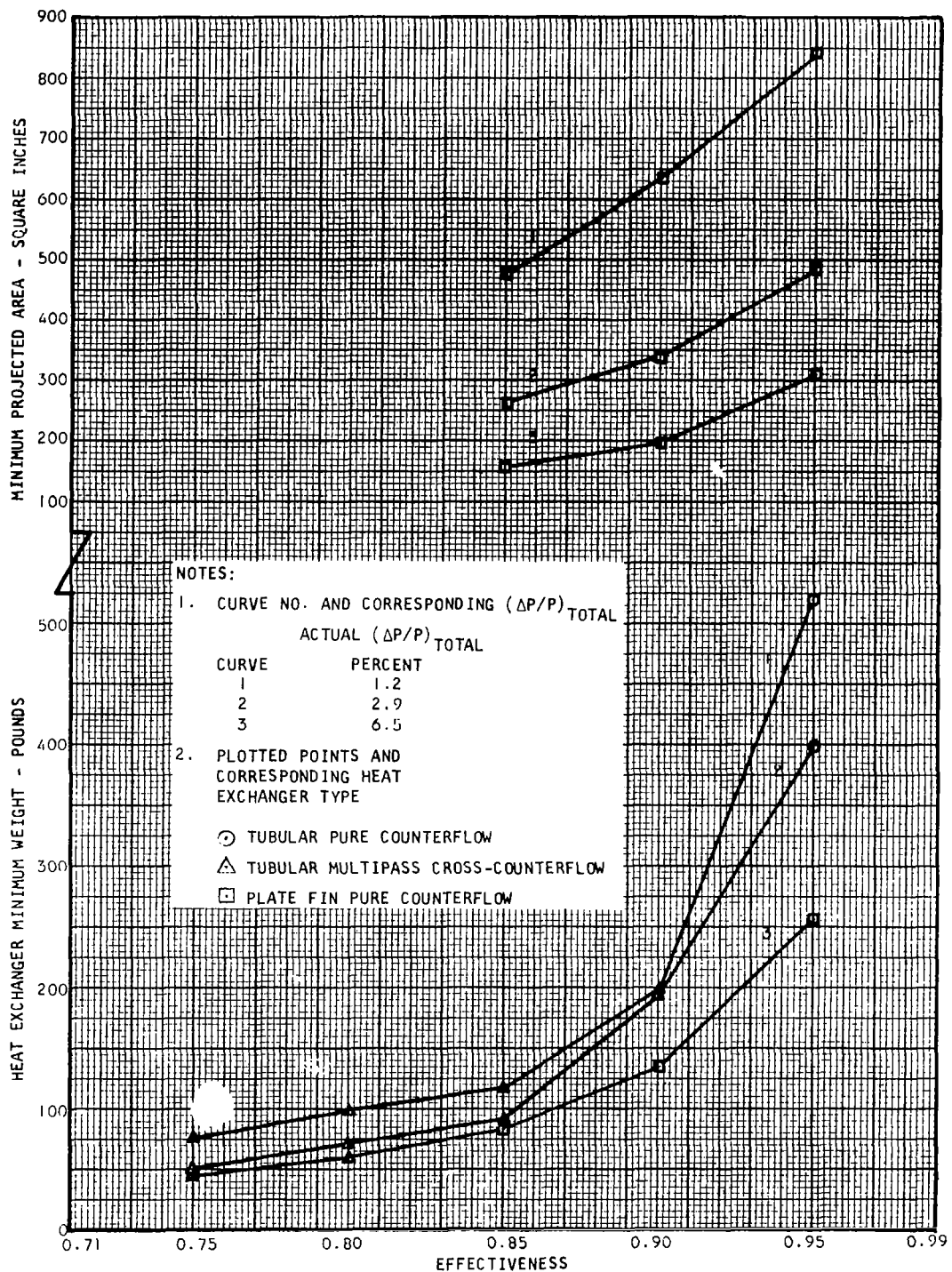
Figure 29. Heat Exchanger Minimum Weights and Minimum
Projected Areas for Brayton Cycle Application

offset fins per in., 0.178 in. high on the low pressure side and 74
sandwiches of 16 rectangular offset fins per in., 0.153 in. high on the
high pressure side. This unit has a core effectiveness of 0.90 with a
total pressure drop (ΔP/P) of 0.71 percent. The estimated expansion and
contraction losses for entering and leaving the 6 in. dia. high pressure
ducts and the 8 in. dia. low pressure ducts totals 0.63 percent (ΔP/P).
This left a total of 0.66 percent available for the triangular end sections
required for the introduction and removal of the flow from the heat ex-
changer. The preliminary end section designs which were prepared to uti-
lize this available pressure drop resulted in an overall heat exchanger
weight of 330 lb. The physical characteristics of the heat exchanger which
resulted in this weight are given below.

1. Hastelloy C tube plates, 0.005 in. thick

2. Hollow stainless steel header bars

3. Stainless steel side plates and manifolds

4. Nickel fins, 0.004 in. thick

5. Plain rectangular fins in both the high pressure and low pres-
   sure triangular and sections, 5 fins per in, 0.004 in. thick

DETAILED PARAMETRIC SURVEY

The heat exchanger design discussed above resulted from making the best
interpolation possible from the parametric study curves. In order to ensure
that the correct interpolation of these curves had been made NASA requested
some additional parametric studies in a narrow range band. The range of
interest was thermal effectiveness from 88 to 91 percent and a total pres-
sure drop from 1.5 to 3 percent.

In conducting this detailed parametric survey, the physical geometry
of the above described heat exchanger was maintained. Figure 33 shows the
results of this detailed parametric study on overall recuperator weight,
face area, and length. All the solutions generated are pure counterflow
plate fin matrices using the above described fins and using single triangular
end sections for the introduction and removal of the flows from the main coun-
terflow core. The length dimension shown in Figure 30 is the counterflow core
length plus the height of the triangular sections, while the face area
shown is the core width times the stack-up height of the recuperator. In
the preparation of all these cores the aspect ratio of the counterflow core
face was maintained at essentially 1.0. Therefore, as the face of the core
is essentially square the width or stack-up height of the core is essentially
the square root of the area shown. The abcissa parameter used for Figure 33
is overall pressure drop (ΔP/P). This overall pressure drop is the sum of
the ΔP/P for all manifolds, both triangular end sections and the pure coun-
terflow core for both the hot and cold sides.
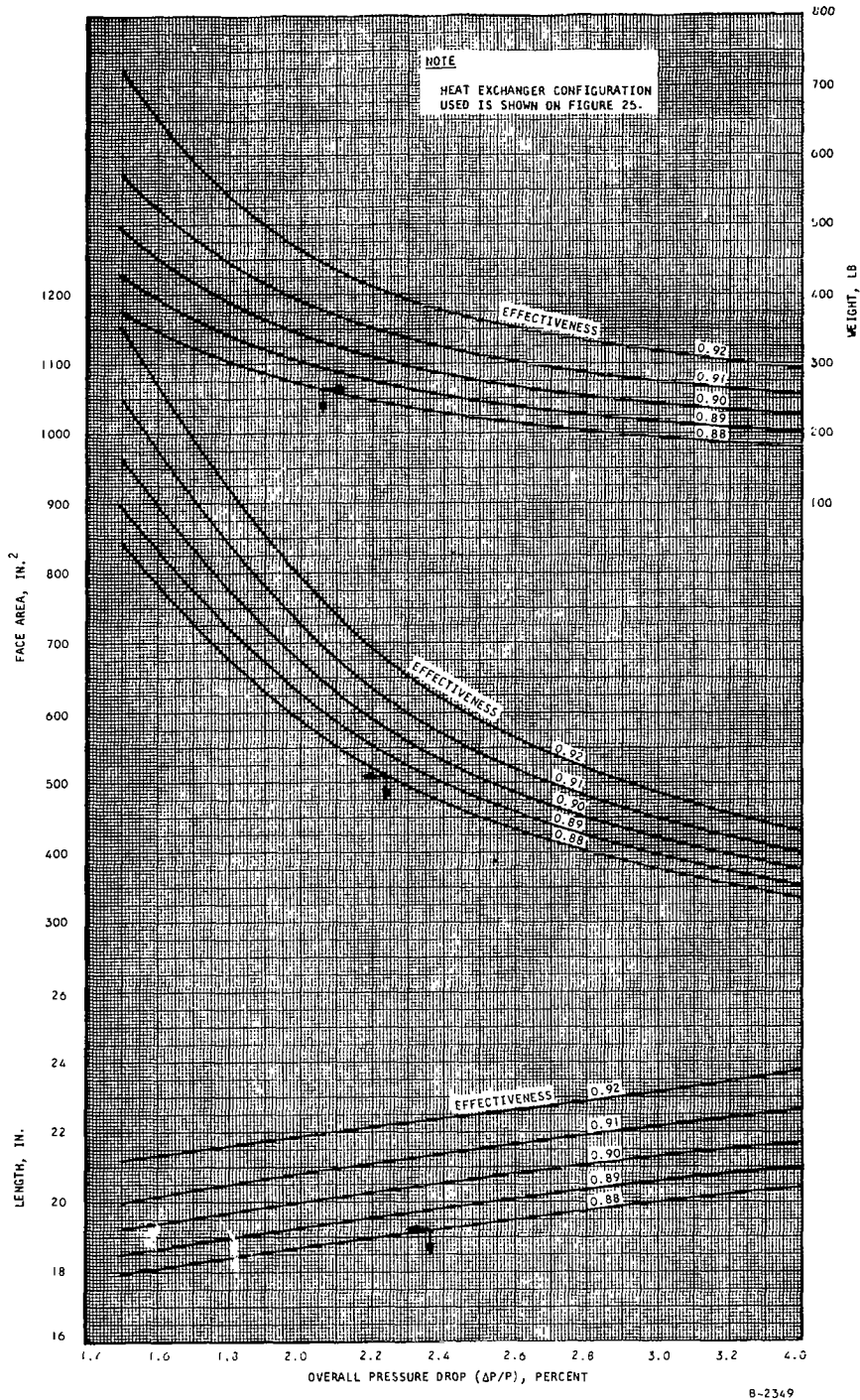
Figure 30. Effect of Total Pressure Drop and Effectiveness
on Heat Exchanger Dimensions

In preparing the curves for Figure 30 the analysis utilized minimum $(\Delta P/P)_{overall}$ rather than minimizing the pressure drop on either the hot or cold side. In order to present the ratio between core pressure losses and the overall recuperator losses the curves of Figure 31 were prepared. In all cases it was found that the pressure drop ratios are almost independent of effectiveness. The curves of Figure 31 are accurate to within four percent over the range of effectiveness and pressure drop covered in the detailed parametric study. Detailed information on the pressure drop for any of the recuperator solutions shown in Figure 30 may be obtained by consulting Figure 31. This detailed pressure drop information includes:

1. Total hot side pressure drop

2. Total core pressure drops

3. Hot and cold side core pressure drops

4. Hot, cold, and total manifold losses

By means of simple arithmetic, the hot and cold pressure drops in each of the three main recuperator areas (core, triangular ends, and manifolds) may be determined. Figure 31 clearly indicates that where minimum $(\Delta P/P)_{total}$ is maintained the ratio of the core to the overall pressure drop varies considerably with the actual overall pressure drop used.

The above described parametric study provided the preliminary selection of the final design. In preparing the parametric curves of Figures 30 and 31 designs of triangular end sections were formulated. In the above referenced weight of 330 lb the triangular sections used were 7 in. high, giving a total heat exchanger length of approximately 21 in. Using this preliminary configuration as the starting point, investigations were conducted into some of the detailed design effects. These detailed design effects included; manufacturing and structural considerations, detailed analysis of axial conduction and the detailed analysis of the effect of nonuniform flow distribution throughout entire recuperator. Each of these areas of investigation are discussed in considerable detail in the following sections of this report. The discussion of these areas of investigation also serves to present the chronological development from this preliminary configuration to the final configuration which was fabricated.

1. $\left(\dfrac{\Delta P}{P}\right)_{HOT\ CORE}$ = PERCENTAGE PRESSURE DROP ON HOT SIDE OF CORE ONLY

2. $\left(\dfrac{\Delta P}{P}\right)_{TOTAL\ CORE} = \left(\dfrac{\Delta P}{P}\right)_{HOT\ CORE} + \left(\dfrac{\Delta P}{P}\right)_{COLD\ CORE}$

   PERCENTAGE PRESSURE DROP ON HOT SIDE OF CORE PLUS COLD SIDE OF CORE

3. $\left(\dfrac{\Delta P}{P}\right)_{TOTAL\ HOT}$ = PERCENTAGE PRESSURE DROP ON HOT SIDE INCLUDING MANIFOLDS, TRIANGULAR SECTIONS, AND CORE

4. $\left(\dfrac{\Delta P}{P}\right)_{OVERALL} = \left(\dfrac{\Delta P}{P}\right)_{TOTAL\ HOT} + \left(\dfrac{\Delta P}{P}\right)_{TOTAL\ COLD}$

   PERCENTAGE PRESSURE DROP ON HOT SIDE PLUS PERCENTAGE PRESSURE DROP ON COLD SIDE

5. $\dfrac{\left(\dfrac{\Delta P}{P}\right)_{HOT\ CORE}}{\left(\dfrac{\Delta P}{P}\right)_{TOTAL\ CORE}}$ = 0.71

6. $\left(\dfrac{\Delta P}{P}\right)_{HOT\ MANIFOLD\ (8\ INCH)}$ = 0.40

7. $\left(\dfrac{\Delta P}{P}\right)_{COLD\ MANIFOLD\ (6\ INCH)}$ = 0.36

8. $\left(\dfrac{\Delta P}{P}\right)_{TOTAL\ MANIFOLDS\ (6,8\ INCH)}$ = 0.76
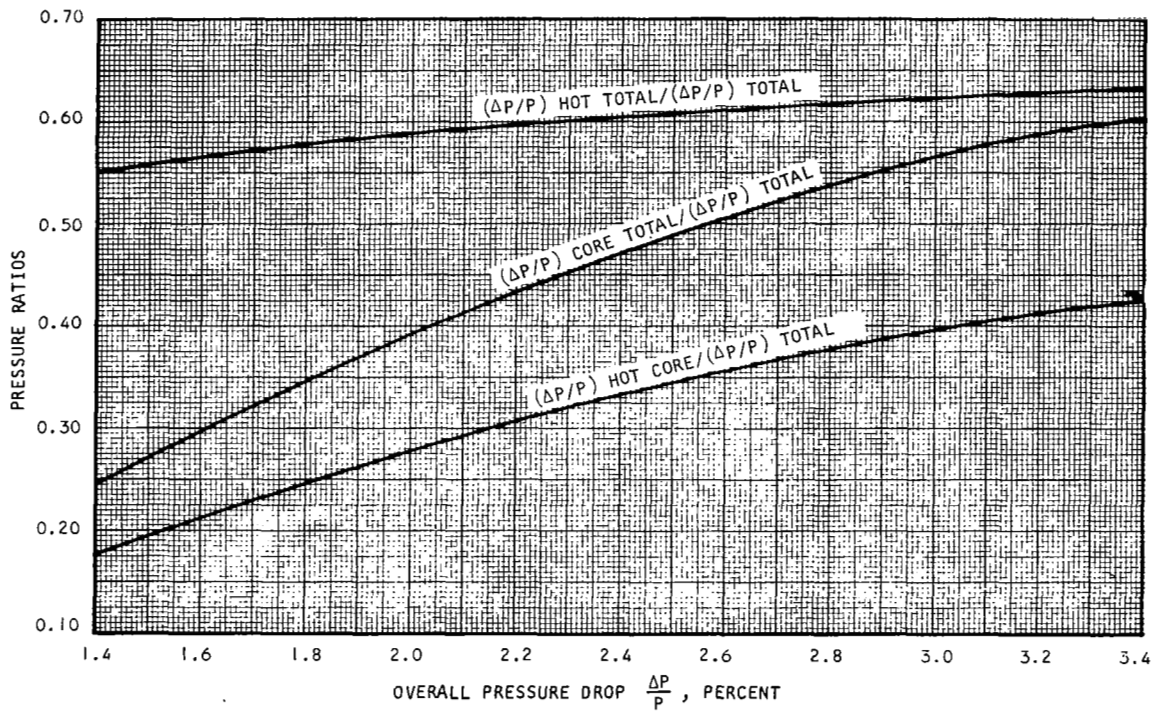
Figure 31. Recuperator Pressure Drops

B-2348

SECTION 4

TRIANGULAR END SECTION DESIGN

With the selection of a pure counterflow plate fin heat exchanger for
this recuperator application, particular attention must be paid to the methods
of introducing and removing both fluid streams from the heat exchanger core.
The design constraint in a pure counterflow configuration is that both fluids
must enter and leave the same face of the heat exchanger and consequently
some means of dividing this face between the two fluids must be employed.
The simplest and most direct method is obtained with the addition of either
rectangular or triangular end sections. Both these end section configurations
together with their appropriate flow paths are illustrated in Figure 32.
Where the available pressure drop os low, particularly if it is low on both
sides, triangular end sections are perferred. Should the operating con-
ditions required result in a high available pressure drop on one side and a
low available pressure drop on the other side then the rectangular configura-
tion is preferred. For both design concepts, the ends are fabricated as an
integral part of the heat transfer matrix. The plates used throughout the
heat exchanger cover the entire flow passage areas, but the fins used in the
end sections need not have the same configuration as the fins in the counter-
flow core. Only the fin height must be maintained throughout.

In most cases where pure counterflow heat exchangers are utilized the
effectiveness is high and consequently the temperature differences between
the fluid streams in the end sections are small. Where this is the case,
only a very small amount of heat transfer will be added to the overall heat
exchanger by the addition of the end sections. However, the end sections
will contribute parasitic pressure losses to the overall design. In order
to determine an optimum heat exchanger which utilizes end sections, trade-
offs must be conducted between additional heat exchanger weight and these
parasitic pressure losses. As there are a number of variables which in-
fluence both the weight and pressure losses of the end sections (including
end section height, number of fins per in. and the ratio of one fluid face
area to the other) many solutions must be determined to achieve the optimum
design. In order to facilitate this optimization procedure AiResearch
wrote a computer program to determine end section pressure losses. This
computer program is described in Appendix D.

TRIANGULAR END SECTION SELECTION

First use was made of the computer program described in Appendix D to
determine the most suitable triangular end dimensions for use with the pre-
liminary selected heat exchanger core discussed in Section 3. The fins used
in the triangular ends are required only to match the height of the appro-
priate passage. The fewer the fins used, the higher the hydraulic radius and
the lower the pressure drop. In the preliminary investigations for end
sections for this core, the range in fins investigated was from 0 to 10 fins
per in. The results of this preliminary investigation are shown in Figure 33.

a. Triangular Ends
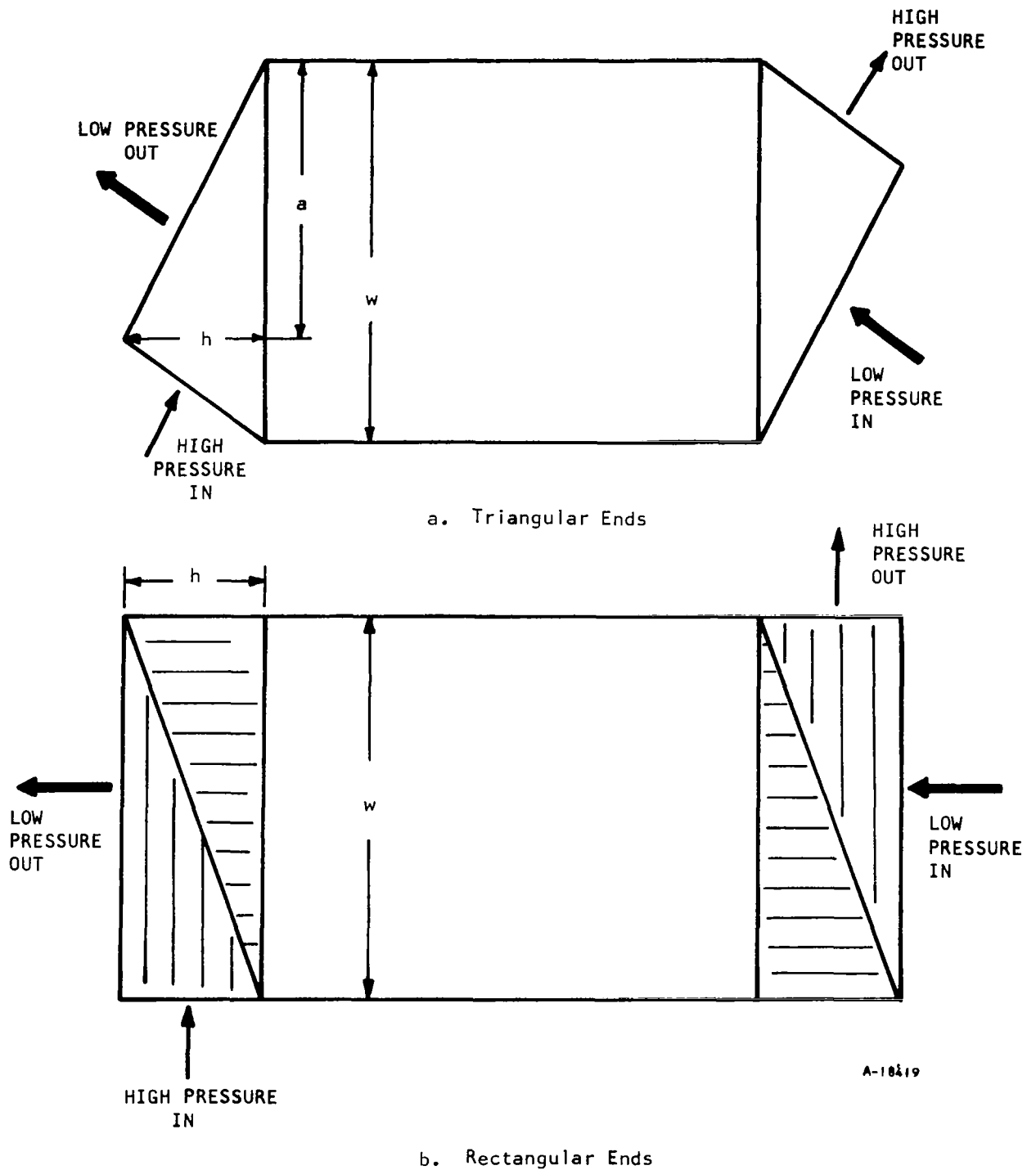
b. Rectangular Ends

Figure 32. Counterflow Design Concepts

A-18419
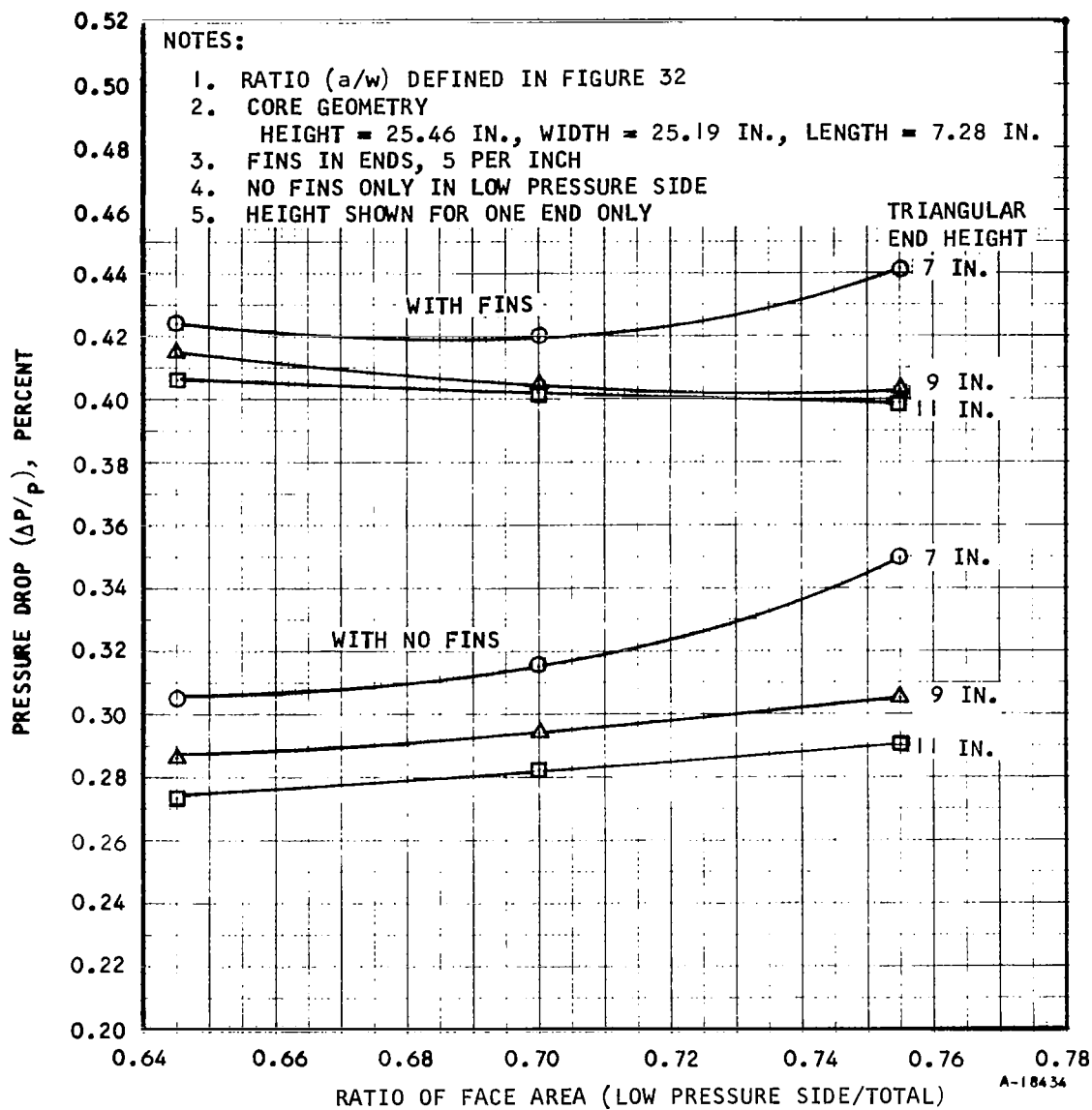
Figure 33. Pressure Drop In Triangular End Sections

This figure shows the effect of reducing the number of fins per in. from 5 to 0 and also illustrates the effect of varying triangular end height and varying face area ratio on the pressure drop. From this investigation the selection for the triangular ends on the preliminary core was 7 in. height with a face area ratio of approximately 65 to 35 percent (low pressure to high pressure) with 5 fins per in. in the high pressure side end sections and no fins at all in the low pressure side end sections. This selection was made to have the minimum pressure losses compatible with the apparent structural requirements. As with the preliminary selection pure counterflow heat exchanger core, this selection was subject to review with continuing detailed design investigations. Particular attention had to be given to the manufacturing and structural problems involved in the use of the very low fin densities.

Continuing studies into the manufacturing, structural and axial conduction problems in the main counterflow section of the heat exchanger resulted in a change in core configuration. Due to these various considerations the overall width of the core increased to 26.1 in. while the length increased to 7.89 in. and the number of fin passages on each side increased to 76. The plate material also changed from Hastelloy "C" to stainless steel and the thickness of the plates increased from 0.005 to 0.008 in. In addition to these changes in counterflow core configuration, manufacturing studies conducted in another program indicated that the minimum acceptable number of fins in the triangular end sections was 10. A further advantage derived from this parallel study program was that fin dies were produced which were suitable for the fabrication of plain rectangular fins 10 per in. in both the 0.178 in. high and 0.153 in. high fins used for the Brayton cycle recuperator.

On the basis of 10 fins per in. in the triangular end sections and a more precise definition of the counterflow core configuration a reevaluation of the end section pressure drops was conducted to determine the optimum split between high and low pressure side face areas, and also to determine end designs that would result in the best flow distribution. Optimum split between high and low pressure side face areas may be defined as that split which results in the lowest total pressure penalty to the recuperator. In order to determine this optimum, a large number of end section designs were prepared and their pressure losses evaluated. The results of this study are shown in Figure 34 where the sum of the end pressure losses is plotted against the ratio of low pressure side face area to total available face area. This figure clearly indicates that the minimum pressure loss occurs at the ratio of 0.75. This ratio was, therefore, adopted for the design of the flow distribution test unit.

Up to this point, all the preliminary designs that were considered utilized identical end sections. It was realized that while all flow paths followed by the fluids in these identical end sections, were of equal length they did not result in equal pressure drops because of density differences at the inlet and outlet, this is illustrated in Figure 35. These nonuniform pressure drops give a nonuniform flow through the counterflow core, that has an adverse affect on heat exchanger performance. To minimize this adverse effect on heat exchanger performance it is desirable to balance the pressure losses in the inlet end with the pressure drop in the outlet end thus balancing flow length with density difference. By varying the end section height this
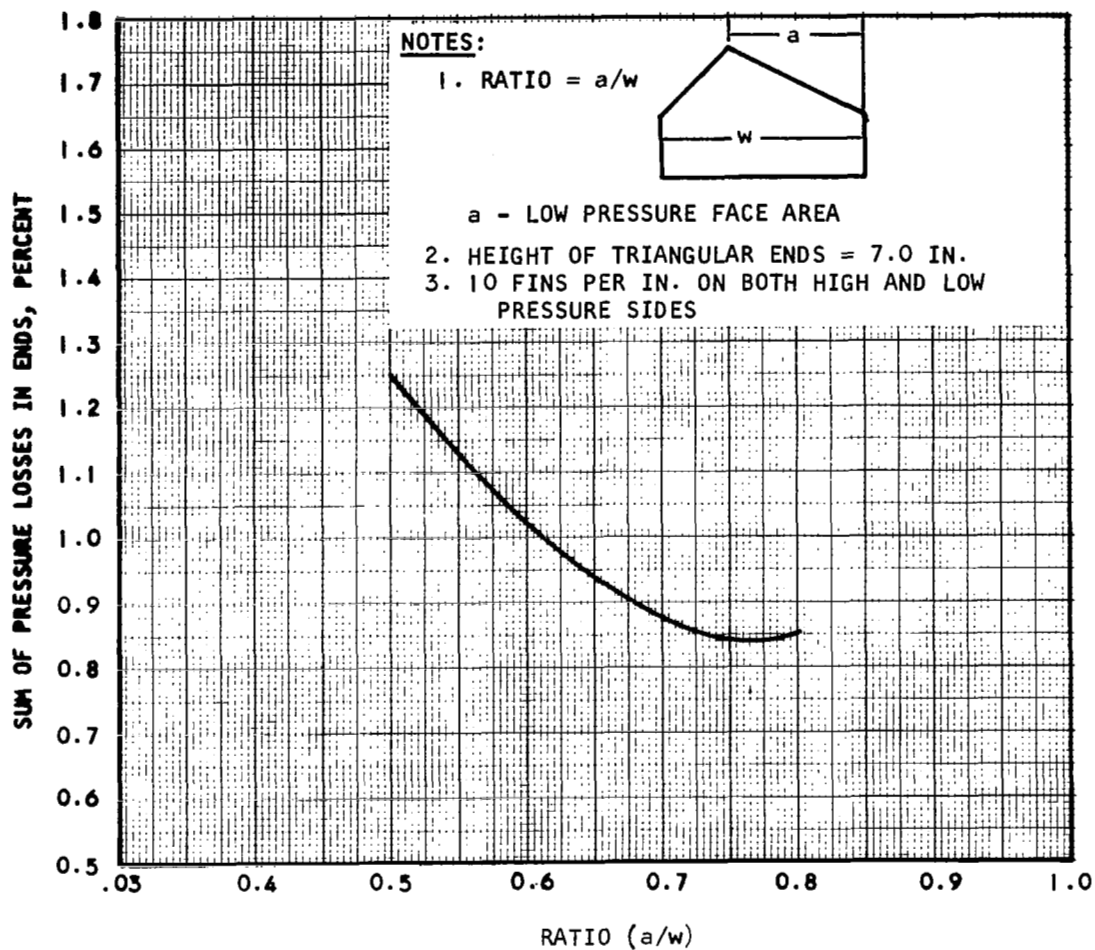
Figure 34. Effects of Split Between High and Low Pressure
Face Areas on End Pressure Losses

A-13674
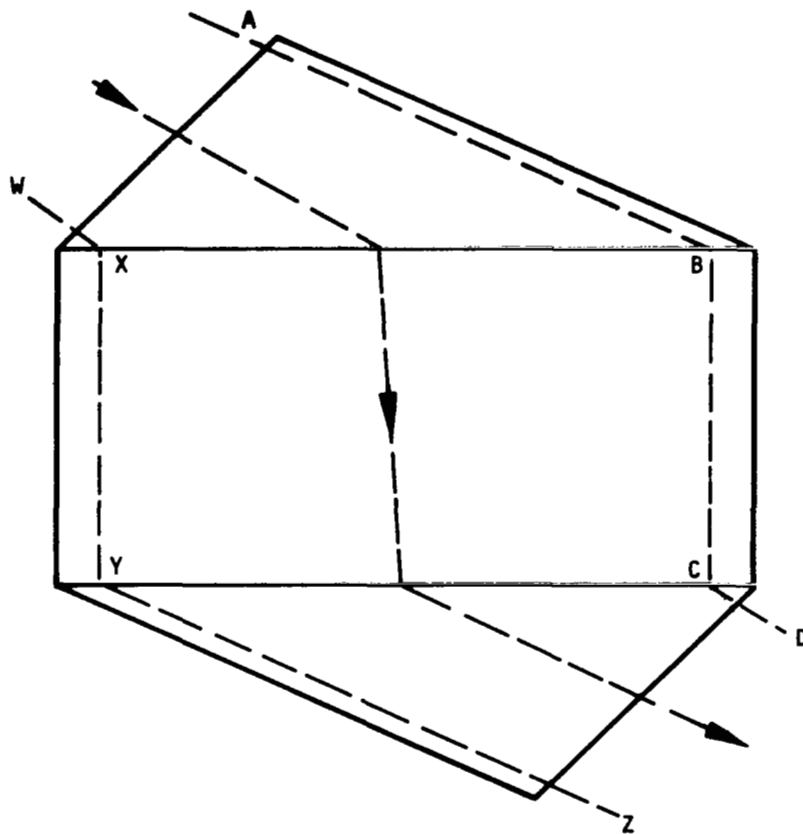
PATH A TO D EQUAL IN LENGTH TO PATH W TO Z. OWING TO TEMPERATURE
CHANGE OF GAS DENSITY AT INLET END IS NOT EQUAL TO DENSITY AT
OUTLET END. THEREFORE, ALTHOUGH LENGTH AB = LENGTH YZ

$$\Delta P_{AB} \neq \Delta P_{YZ}$$

FOR UNIFORM FLOW: $\Delta P_{AB} = \Delta P_{YZ}$

THIS REQUIRES NON-IDENTICAL ENDS.

Figure 35.   Effect on Flow Distribution of Identical
             Triangular End Sections
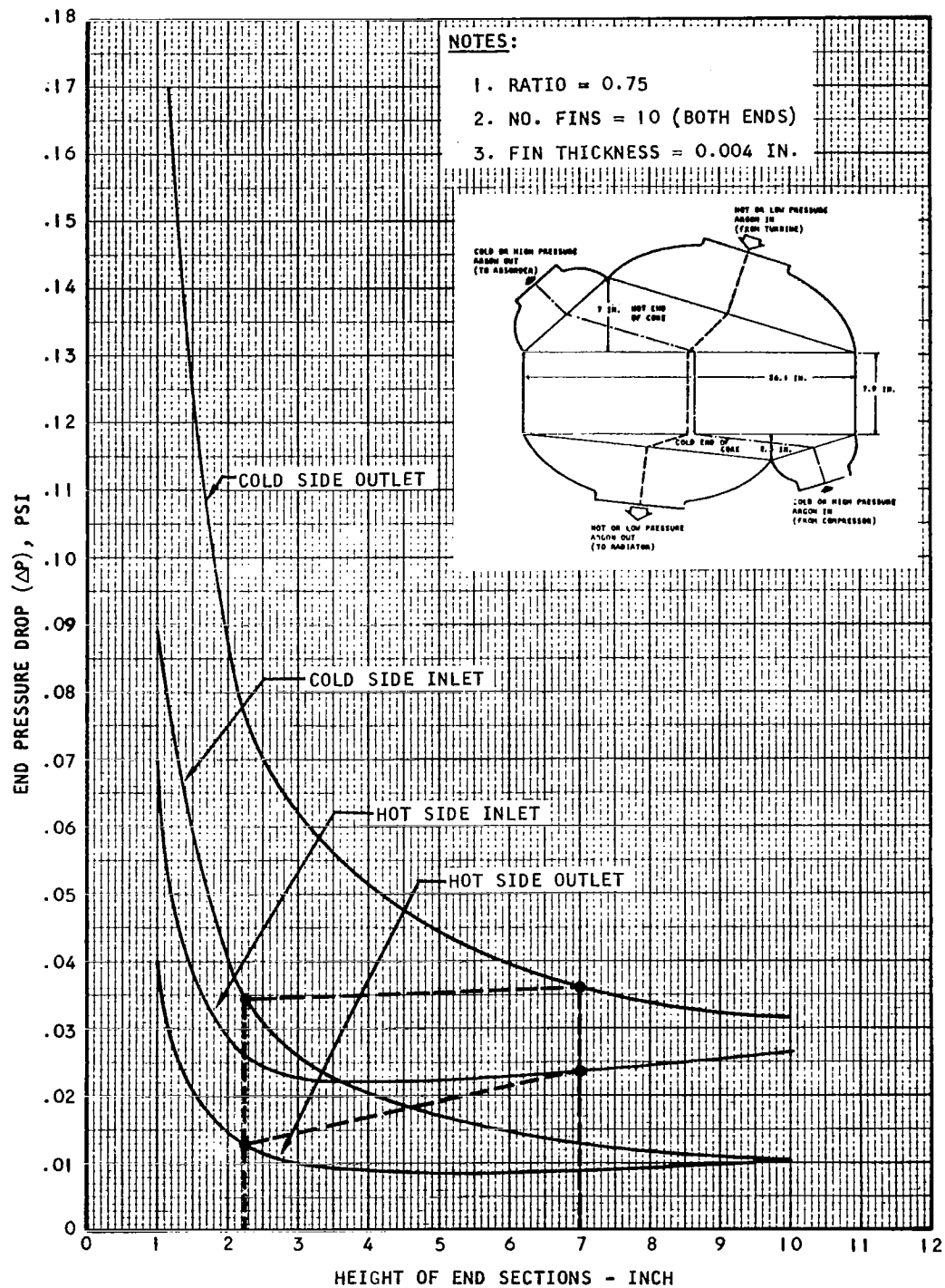
Figure 36.   Effect of End Section Height on End Pressure Losses

balance may be achieved. The end section computer program was, therefore, used to investigate a large number of end section designs to determine the most suitable height. Results of this investigation are shown in Figure 36 where the four individual pressure losses are plotted against triangular end height. Based on this study, a height of 7 in. was selected for the hot end of the heat exchanger and a height of 2.25 in. was selected for the cold end. A perfect balance of both sides is not possible but the heights selected provide the most reasonable compromise. With the selection of these end section heights an increase in pressure drop occurred. The hot end height of 7 in. is identical to that used in the preliminary selection end design. In order to provide the required pressure drop balance, it was, however, necessary to considerably reduce the height of the cold end triangle. This resulted in a considerable pressure drop increase in this end. Thus the overall heat exchanger pressure drop increased from 2.0 percent to 2.59 percent.

Figure 36 shows that the selection of the 7 in. and 2.25 in. height does not result in the best possible pressure drop balance. The best possible pressure drop balance occurs at heights of 4.0 in. and 2.0 in. However, this results in an overall pressure drop of approximately 2.84 percent. The selected 7.0 and 2.25 in. heights gave good pressure drop balance on the cold side and approximately 30 percent imbalance on the low pressure side. It was believed that this low amount of imbalance in pressure drop would not seriously compromise the heat transfer performance of the recuperator and, therefore, this was selected as the solution that best satisfies both the heat transfer and pressure drop requirements.

The above discussed recuperator design was used to fabricate the flow distribution test unit. The results of this flow distribution testing are discussed in Section 6 while the effects of this testing on overall heat exchanger configuration are discussed in Section 8.

TRIANGULAR END SECTION, HEAT TRANSFER ANALYSIS

Throughout the preliminary design analysis of the recuperator no allowance was made for the heat transfer that occurs in the triangular end sections. Although the flow in these areas is cross flow and is, therefore, less efficient than the main body of the heat exchanger some heat transfer will occur in these sections. It was assumed that this heat transfer would compensate for any loss in performance due to nonuniform flow distribution.

An analysis was conducted to determine this heat transfer, which also gave the temperature distribution of both exiting fluid streams. The results of this analysis indicate the overall heat transfer conductance (UA) of the complete heat exchanger is approximately 15 percent greater than that of the pure counterflow section alone. Figure 37 shows the gas outlet temperature distribution obtained from this analysis. The increase in heat transfer performance and the gas outlet temperature distribution shown in Figure 37 were obtained assuming that the flow throughout the heat exchanger is uniform.
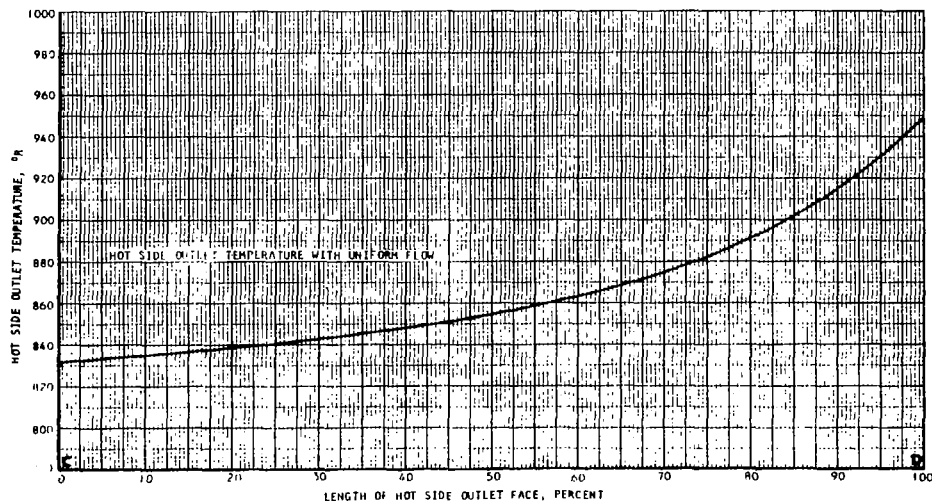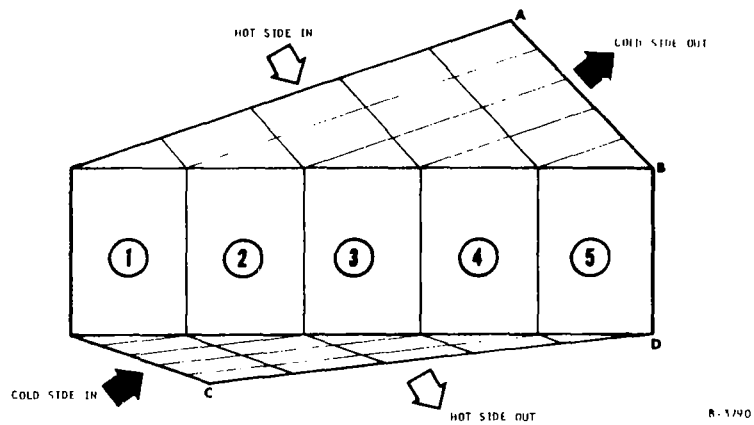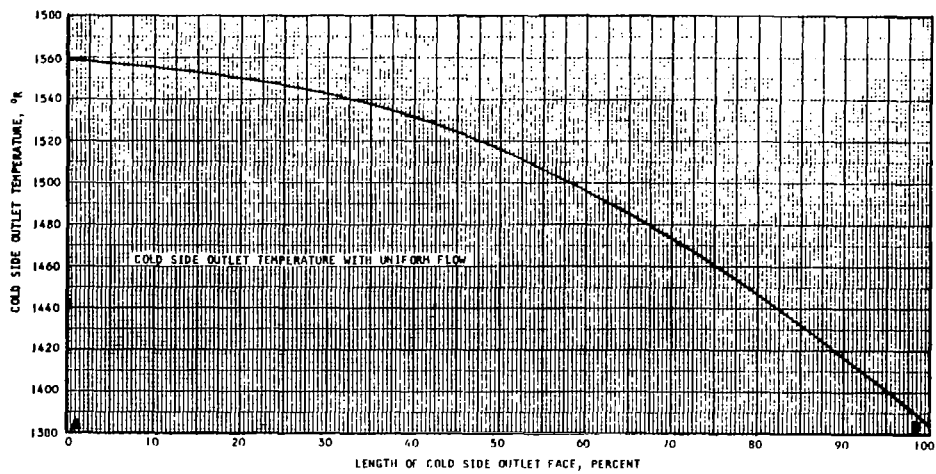
Figure 37. Gas outlet Temperature Distribution

The method of analysis used to determine these outlet temperature distributions was to divide the heat exchanger into five flow width sections as illustrated in Figure 37. Consideration is first given to flow section 1 where the deviation from the pure counterflow performance is only affected by a single small triangular section at either end. The effect of the small triangular end section is determined by an iterative procedure and the outlet temperatures from these small triangular sections then provide input for the first increment in the flow section 2 flow path. The same iterative procedure is then utilized for flow path 2 until all temperatures throughout this path are determined. This procedure is then followed successively through flow sections 3, 4, and 5 until the complete temperature distribution has been calculated. Throughout these calculations each of the small triangular sections shown in Figure 37 are treated as small individual crossflow heat exchangers.

SECTION 8

AXIAL CONDUCTION TESTING

IMPORTANCE OF AXIAL CONDUCTION

In any high effectiveness pure counterflow heat exchanger, the effect of axial conduction can result in appreciable weight penalties. In order to appreciate this effect, consideration should be given to relationship between effectiveness and overall heat transfer conductance. A convenient method of evaluating this relationship is shown in Figure 38, which shows a curve, effectiveness versus NTU, for counterflow and capacity rate ratio of 1.0. The definition of NTU is given on Figure 38; and it is important to realize that this parameter is a thermodynamic measure of heat exchanger size. From Figure 38, it can be seen that as effectiveness increases above 0.8, the increase in NTU is rapid. Therefore, if axial conduction results in even a relatively small change in effectiveness, the change on heat exchanger size is much greater.

Appendix A of this report presents an analytical method of allowing for the effect of axial conduction in pure counterflow heat exchangers. In order to further illustrate the importance of this axial conduction effect Table I was prepared. This table shows how heat exchanger effectiveness is influenced by the total axial conduction parameter λ,

where $\quad \lambda = \dfrac{KA}{C_{min} L}$

The values shown in Table I apply to conductance and heat capacity ratios of I only and an infinite metal to fluid capacity ratio. Conductance ratio is the ratio of the hot side and cold side η_o hA's (fin effectiveness x heat transfer coefficient, x heat transfer area) while capacitance ratio is the ratio of the hot and cold WCp (mass flow x specific heat). For the recuperator the capacitance ratio is I and the conductance ratio is very close to I. Typically for a value of 0.02 at a heat exchanger effectiveness of 90 percent (not considering axial conduction) the conduction effect ($\Delta E/E$) is 1.68. This reduces the effectiveness from 0.9 to 0.885 and from Figure 38, the corresponding reduction in NTU is from 9 to 7.7. This in turn would increase the heat exchanger size by approximately 14.4 percent.

From this example it is apparent that consideration must be given to the effect of axial conduction and that every endeavor must be made to reduce the effect. With the selection of a pure counterflow plate fin heat exchanger for this application the main problem to be resolved in the area of axial conduction is a realistic value for the axial conduction parameter, λ.

The basic problem associated with estimating this axial conduction parameter is obtaining the proper value of KA (where K is the thermal conductivity of the overall matrix and A is the true conductivity cross
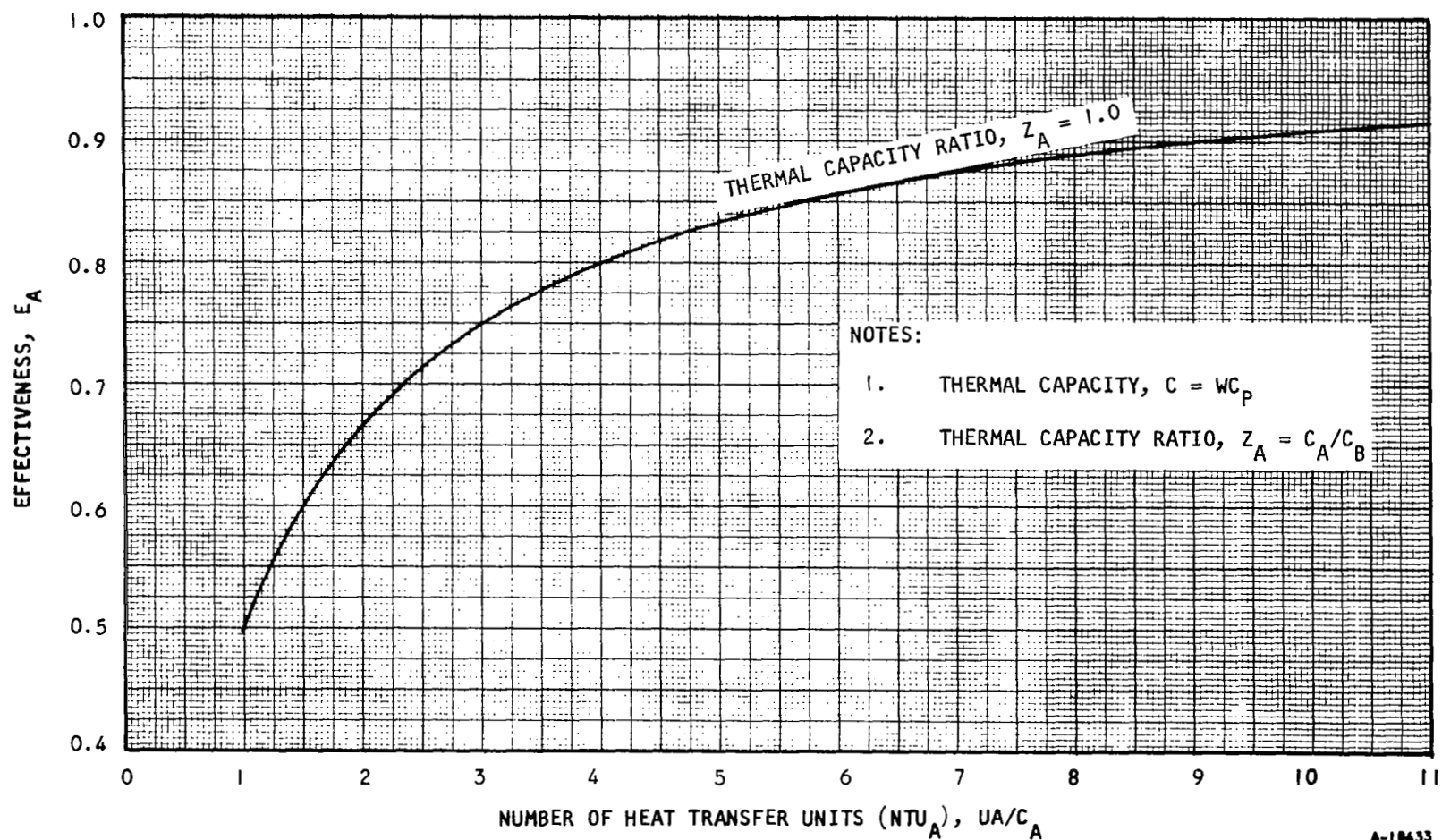
Figure 38. Number Heat Transfer Units, Counter Flow Heat Exchanger

TABLE I

EFFECT OF AXIAL CONDUCTION ON PERFORMANCE

AXIAL CONDUCTION PARAMETER (λ)	0.0	0.01	0.02	0.04	0.18	0.16	0.32
NTU	EFFECTIVENESS (E) (NO AXIAL CONDUCTION) PERCENT	CONDUCTION EFFECT ($\Delta E/E$), PERCENT					
1.0	50.00	.45	.86	1.56	2.78	4.56	6.79
2.0	66.67	.62	1.19	2.23	4.15	6.94	10.92
3.0	75.00	.70	1.36	2.57	4.72	8.18	13.07
4.0	80.00	.75	1.46	2.78	5.12	8.94	14.37
5.0	83.33	.79	1.53	2.92	5.40	9.46	15.24
6.0	85.71	.81	1.58	3.03	5.40	9.83	15.85
7.0	87.50	.83	1.62	3.11	5.76	10.10	16.31
8.0	88.89	.85	1.65	3.17	5.48	10.32	16.67
9.0	90.00	.86	1.68	3.22	5.97	10.50	16.95
10.0	90.91	.87	1.70	3.26	6.15	10.64	17.19
12.0	92.31	.89	1.73	3.32	6.18	10.87	17.55
14.0	93.33	.90	1.76	3.37	6.27	11.03	17.81
16.0	94.12	.91	1.77	3.41	6.34	11.16	18.01
18.0	94.74	.91	1.79	3.44	6.40	11.26	18.17
20.0	95.24	.92	1.80	3.46	6.44	11.34	18.30
40.0	97.56	.95	1.86	3.58	6.46	11.72	18.89
60.0	98.36	.96	1.88	3.62	6.74	11.85	19.09
80.0	98.77	.96	1.89	3.64	6.78	11.92	19.20
100.0	99.01	.97	1.90	3.65	6.80	11.96	19.26
200.0	99.50	.97	1.91	3.68	6.85	12.04	19.39

EXAMPLE: AT NTU = 9.0 AND NO AXIAL CONDUCTION EFFECTIVENESS (E = 90.0)

FOR AN AXIAL CONDUCTION PARAMETER (λ) = 0.02, $\Delta E/E$ = 1.68

$E_{AXIAL\ CONDUCTION}$ = 90.0 - (1.68 × 90/100) = 88.49

A-18468

sectional area). This parameter is difficult to obtain for a plate fin matrix as, where offset fins are used the true metal conduction area is not easy to define; and also as the fin-plate-braze material cross section area is unknown. A further factor influencing the determination of this thermal conductivity parameter is the effect on the basic materials of the brazing operation. Changes in thermal conductivity may be caused by the diffusion of the braze alloy into the parent materials. Therefore, the type and thickness of the braze alloy used, and the time and temperature of the braze cycle may influence the KA parameter.

In order to determine a realistic evaluation of the effect of axial conduction on the selected heat exchanger design, a test program was conducted to determine this KA parameter. Details of this test program are given below.

TEST PROGRAM

The intention of this program was to determine the KA product from electrical resistance measurements. Experiments have demonstrated that electrical and thermal conductivities are related by the following empirical equation:

$$K = \ell\sigma T + B \tag{1}$$

The work of Smith and Palmer (Reference 2) was done with copper alloys, ranging from pure copper to little over 50 percent copper. The K - σT plot was linear to σT values of approximately 9×10^{-7} °K/ohm cm and all experimental values fell within 10 percent of the line shown in Figure 39. Subsequent to the work of Smith and Palmer, the constants ℓ and B have been determined for aluminum beryllium, iron, magnesium, nickel, and titanium base alloys (References 3 through 10 respectively). A compilation of these constants is included in Reference 10.

Since the basic problem is to determine the KA parameter of the plate fin matrix, three specimens were made from materials considered for the program. Figure 40 shows an isometric sketch of the test specimen, a schematic of the test setup for measuring the specimen electrical resistance, and an isometric of rectangular offset fins.

Table 2 lists the equations for estimating thermal conductivity for nickel and iron base alloys.

Equation (6) shows that the calculated KA value should be multiplied by the ratio of calculated to the experimental resistances. Again it is pointed out that the expression is an approximation only.

In order to calculate the KA parameter, the cross sectional area of the plate and braze alloy, the conductance path for flow down the fins, and the thermal conductivities of the materials must be obtained. Conduction through header bars and side plate must also be evaluated. Each KA value is calculated, the total KA parameter for the heat exchanger is the sum.

60
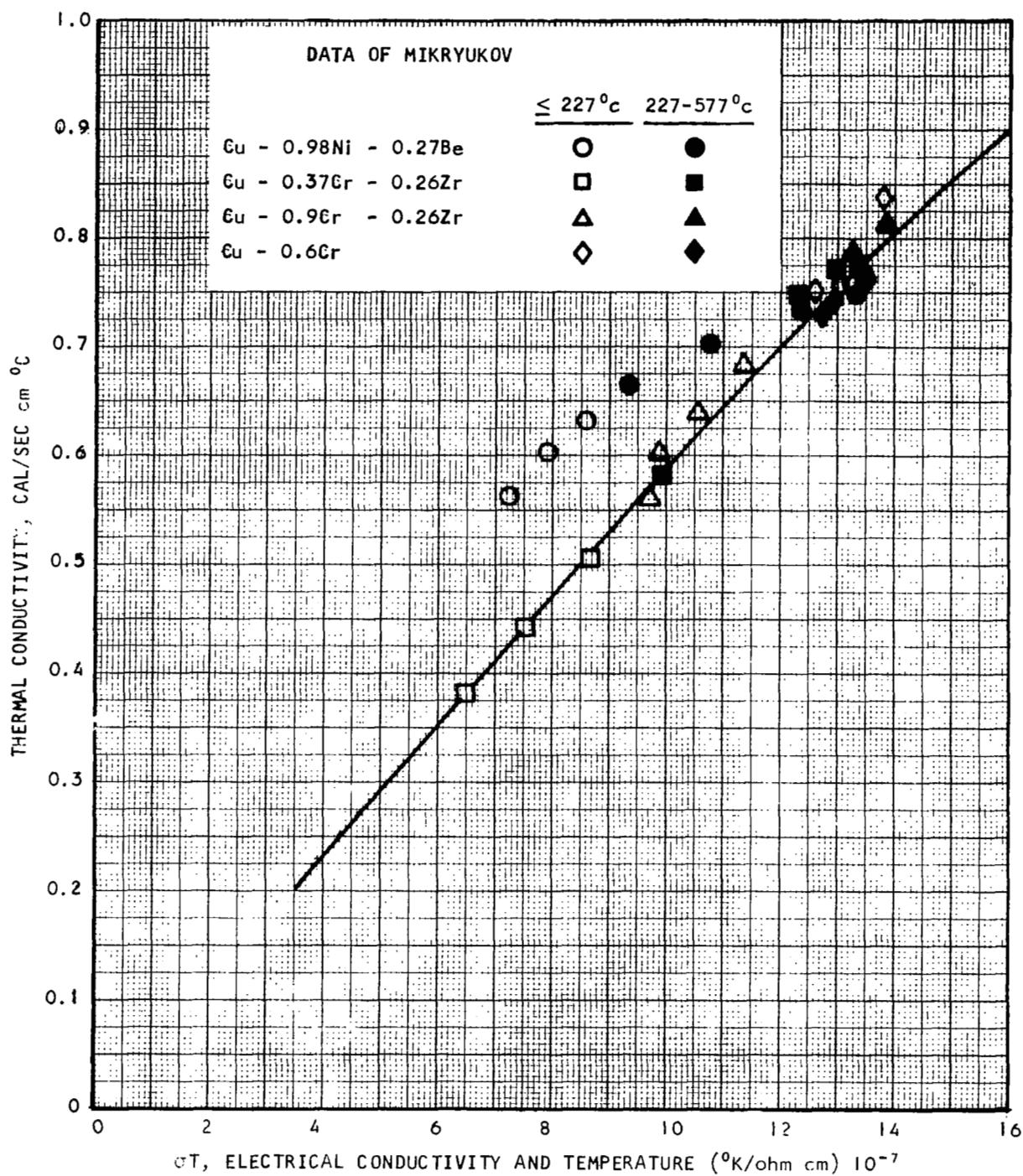
Figure 39. Electrical-Thermal Conductivity Data

A-8339

0.005 IN. THICK
HASTELLOY C
TUBE SHEETS

HIGH PRESSURE FINS

LOW PRESSURE FINS

AXIAL CONDUCTION
TEST SPECIMEN

FIN
HEIGHT

NUMBER OF FINS
PER INCH

OFFSET
LENGTH

OFFSET HEAT TRANSFER FINS

DC POWER
SUPPLY

A

L

R

V

CORE SPECIMEN

A-7422
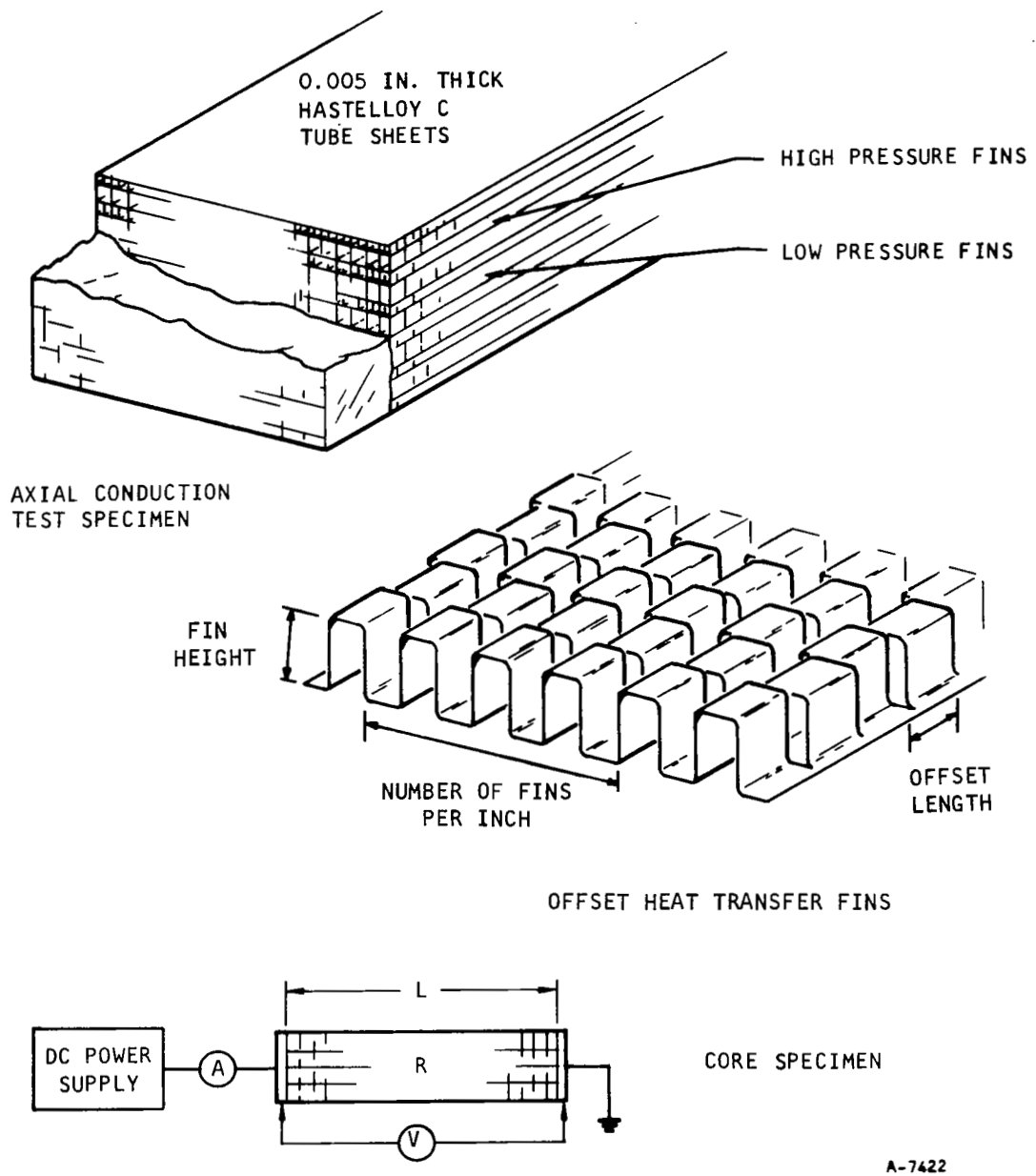
Figure 40. Test Specimen for Axial Conduction Test

TABLE 2

EQUATIONS FOR ESTIMATING THERMAL CONDUCTIVITY FOR NICKEL AND IRON BASE ALLOYS

Equations for conversion of electrical to thermal conductivity

Alloy System	Thermal Conductivity
Iron (347 stainless steel)	$K = 27 \times 10^{-8} \, T\sigma + 2.84$
Nickel (Hastelloy C)	$K = 33 \times 10^{-8} \, T\sigma + 1.25$

Electrical resistance and conductivity are related by Equation (2):

$$R = \frac{L}{\sigma A} \tag{2}$$

By substituting Equation (2) into Equation (1), the relationship between electrical resistance and thermal conductivity results:

$$K = \frac{\ell L T}{RA} + B \tag{3}$$

The lattice conduction constant (B) in Equation (3) is approximately 20 to 30 percent of the thermal conductivity. As a first order approximation this term may be neglected resulting in the following expression:

$$K \sim \frac{1}{RA} \tag{4}$$

or

$$KA \sim \frac{1}{R} \tag{5}$$

By calculating and measuring electrical resistance, the following expression may be written equating experimental and calculated resistances and KA parameters:

$$KA_{experimental} = \frac{R_{calculated}}{R_{experimental}} \, KA_{calculated} \tag{6}$$

Tube Plate KA Parameter:

(No. of Plates)(thickness)(width)(thermal conductivity) = KA_p

Braze Alloy KA Parameter:

(No. of Plates-1) 2 (Alloy thickness)(width)(thermal conductivity) = KA_b

Fin KA Parameter:

2 (No. of fin passages)(fin thickness/4)(passage width)
(thermal conductivity) = KA_f

KA Value of header bar and side plates = KA_{sh}

Total KA = Σ KA's

Discussion

Three plate-fin samples were prepared for axial conduction analysis. (Samples 2, 4 and 5). The results from samples prepared for another program have also been included. Samples were between 13 and 17 in. long, 1.5 in. wide and approximately 1 in. high. Table 3 is a description of the samples while Figure 41 shows a photograph of one sample.

Listed in Table 4 are the measured resistance values of the samples, the resistance per foot, the calculated sample resistance per foot and the ratio of experimental to calculated values.

Calculated resistance values were based on electrical measurements made on stainless steel and Hastelloy C samples.

Based on the experience AiResearch has gained in brazing stainless steel heat exchanger cores, 0.006 in. thick stainless steel tube sheets are the minimum thickness that will provide a highly reliable leak tight braze joint. Because Hastelloy C is somewhat more resistive to braze alloy penetration, a thickness of only 0.005 in. provides the same reliability. To show the effects of braze penetration and obtain resistivities of the value of the metals, some 1-in. wide strips of 0.005 in. Hastelloy C sheet and 0.006 in. type 347 stainless steel sheet were brazed and photomicrographs were made.

The metal strips were roller coated on both sides with Coast Metals No. 53 nickel base brazing alloy (AMS 4778). The approximate thickness of the braze alloy coating was 0.001 in. The coated and uncoated strips were heated in vacuum to $1965^\circ F$, held 20 minutes at temperature, and furnace cooled. This cycle is typical for average heat exchanger brazing.

TABLE 3

SAMPLE DESCRIPTION

Sample No.		Width in.	Length in.
	No of fins/in.↘ Rectangular↘ Fin Height↘ Offset Length↗ Fin Thickness↘		
1	6 Al fins: 12R - 0.178 - 0.178(0) - 0.006 7 Al plates: 0.006 Dipped brazed	1.5	17 5/8
2	6 Nickel fins: 16R - 0.153 - 1/7(0) - 0.004 7 347 SS plates: 0.006 thick Brazed with nicrobraze	1.5	17 11/16
3	11 Hastelloy C plates: 0.005 5 Hastelloy C splitters: 0.002 10 Ni fins: 40R - 0.025 - 0.050(0) - 0.001 5 Ni fins: 20R - 0.050 - 0.050(0) - 0.002	1	11 3/8
4	3 Nickel fins: 12R - 0.178 - 0.178(0) - 0.004 3 Nickel fins: 16R - 0.153 - 1/7(0) - 0.004 7 Hastelloy C plates: 0.005 thick Brazed with nicrobraze	1.5	12 3/16
5	3 Nickel fins: 12R - 0.178 - 0.178(0) - 0.004 3 Nickel fins: 16R - 0.153 - 1/7(0) - 0.004 7 347 SS plates: 0.006 thick Brazed with nicrobraze	1.5	16 7/8

TABLE 4

MEASURED RESISTANCE VALUES

Sample No.	Measured Resistance ohms	Measured Resistance ohms/ft	Calculated Resistance ohms/ft	Ratio (measured to calculated)	
1	0.00019956	0.000136			nicrobraze
2 (SS)	0.0012732	0.000865	0.00146	0.592	nicrobraze
3	0.001866	0.00197	0.00313	0.629	electroless nickel
4 (HC)	0.00101968	0.000928	0.00161	0.576	nicrobraze
5 (SS)	0.00120652	0.000859	0.00146	0.589	nicrobraze
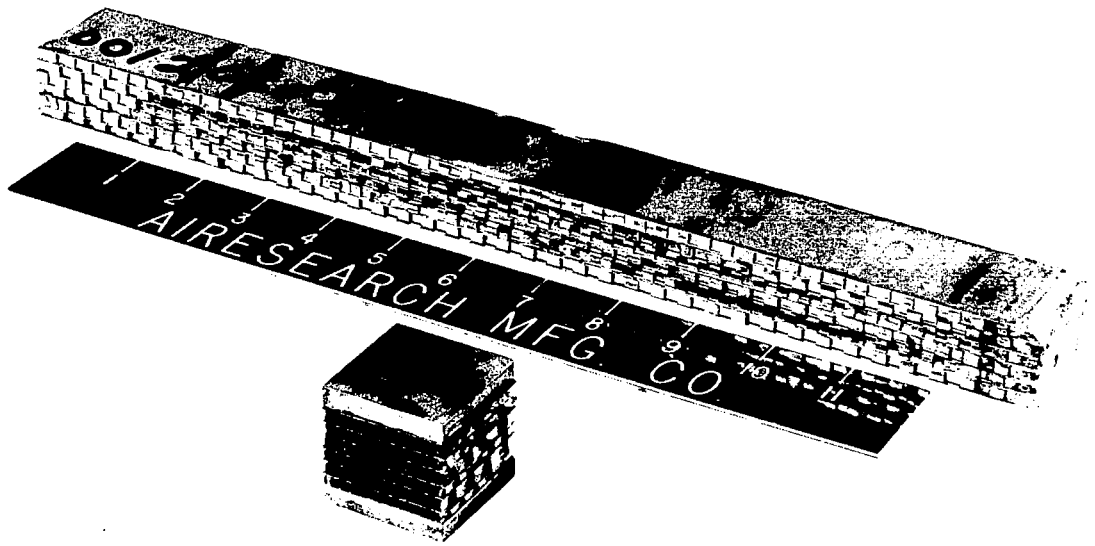
Figure 41.   Axial Conduction Test Sample

52256

Sections from the coated and uncoated strips were examined microscopically. Typical microstructures are shown on the photomicrographs on Figures 42 and 43. Braze alloy penetration of the 0.005 in. Hastelloy C sheets was about 29 percent through the sheet (see Figure 42). Figure 43 shows complete alloying of the braze alloy and the 0.006 in. stainless steel for about 10 percent of the sheet with a further braze penetration for an additional 26 percent of the sheet. Consequently, the total braze alloy penetration is more severe on the stainless steel sheets.

If both sheets were 0.005 in. thick, then the total braze alloy penetration from both sides would be 58 percent through the Hastelloy C sheets and 82 percent through the type 347 stainless steel sheets. Comparative bend tests were performed on the braze alloy coated specimens and no substantial difference between the materials was observed.

Table 5 lists the resistance values and physical dimensions of the above discussed braze coated strips.

TABLE 5

RESISTANCE VALUES AND PHYSICAL DIMENSIONS OF BRAZE COATED STRIPS

Strip Number	Resistance ohms	Length in.	Thickness in.	Width in.	Electrical Resistivity ohms in.
1 (SS)	0.05425	14 3/32	0.0085	1	32.8×10^{-6}
2 (HC)	0.07206	14 1/32	0.0077	1	39.5×10^{-6}
3 (SS)	0.06474	14 7/32	0.0063	1	28.6×10^{-6}
4 (HC)	0.12083	14 3/32	0.0055	1	47.1×10^{-6}
5 (SS)	0.06329	14 1/32	0.0063	1	28.4×10^{-6}
6 (HC)	0.09750	15	0.005	1.5	48.8×10^{-6}

Sample Description

1. 347 stainless steel coated with 0.0011 in. nicrobraze on each side.
2. Hastelloy C coated with 0.0011 in. nicrobraze on each side.
3. 347 SS not coated, heated in braze furnace.
4. Hastelloy C not coated, heated in braze furnace.
5. 347 SS not coated, not heated.
6. Hastelloy C not coated, not heated.
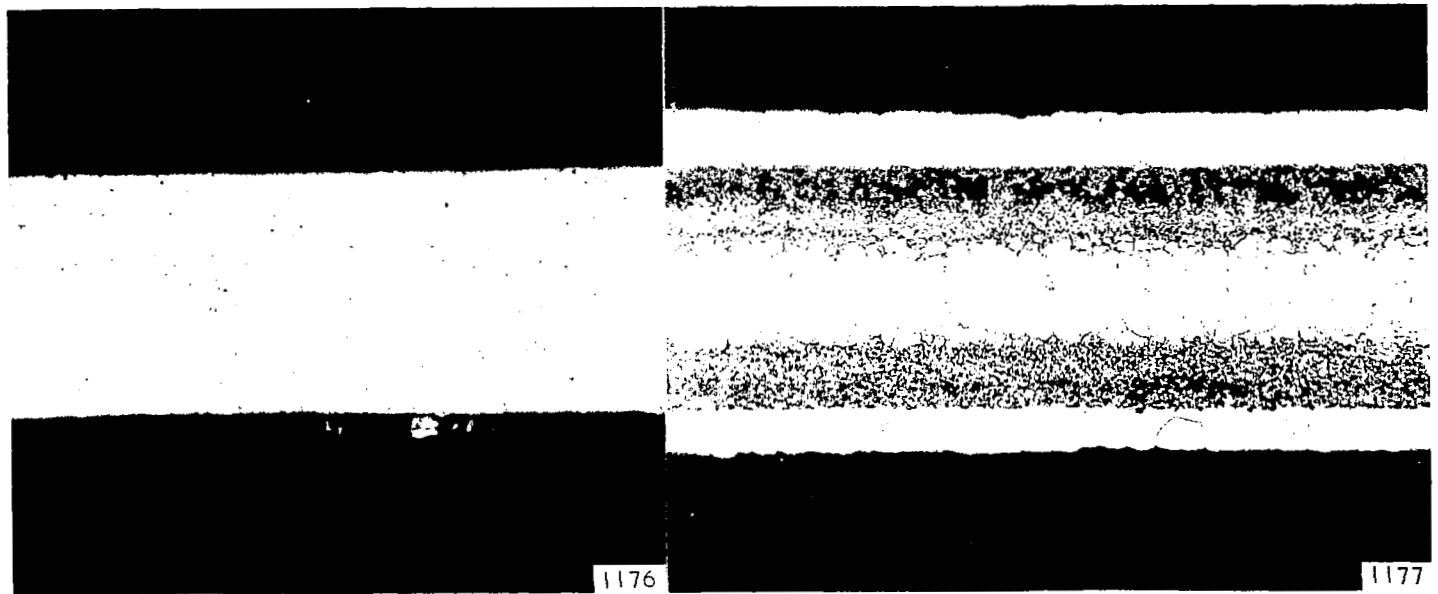
250X Hastelloy 'C', Uncoated   250X Hastelloy 'C', Braze Alloy Coated

F-1519

Figure 42.   Braze Penetration of Hastelloy "C"
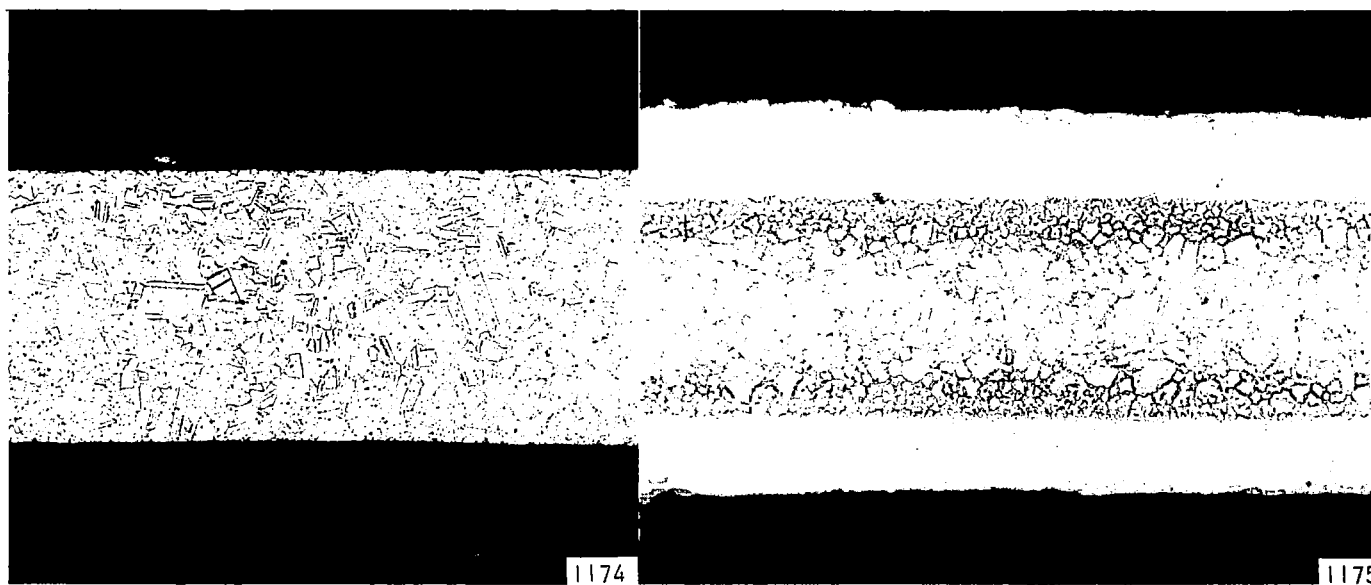
250X Type 347 Stainless Steel, Uncoated   250X Type 347 Stainless Steel, Braze Alloy Coated   F-1520

Figure 43. Braze Penetration of Type 347 Stainless Steel

By comparing samples 1 and 3, the effective resistivity (or resistance) increases by about 15 percent with the alloying. This shows that when stainless is brazed its thermal conductivity is reduced somewhat by the alloying. Comparing samples 2 and 4, a different trend appears to exist with Hastelloy C. By adding alloy to the Hastelloy samples the effective resistivity decreased indicating that the alloying of Hastelloy C results in an increased thermal conductivity. Hastelloy C is a better material for use for minimizing axial conduction but the difference between Hastelloy and 347 Stainless Steel is not large as previously concluded.

Calculated resistance values listed in Table 4 were based on the measured resistivity values listed above. A resistivity value of 13 was used for the alloyed nickel fin brazed to the tube plate material. The assumed fin area for conduction was that directly brazed to the tube plates. This was a first order assumption. After considerable effort was applied to the subject problem of axial conduction, this assumption of fin area was questioned. An improper selection of fin area may be responsible for the difference in calculated and measured electrical resistances.

INFLUENCE OF AXIAL CONDUCTION ON HEAT EXCHANGER DESIGN

During the parametric study (Section 2) the plate-fin heat exchangers used stainless steel plates and nickel fins. However, during the final selection studies (Section 3) the plates considered were Hastelloy C and the fins remained nickel. The increased strength of the Hastelloy C permitted the use of thinner gauge material. This, coupled with its lower conductivity reduces axial conduction and, therefore, the Hastelloy C is preferred for this application. A comparison of the thermal conductivity of Hastelloy C and stainless steel is shown in Figure 44. The influence of this change in thermal conductivities on the overall heat transfer conductance of the recuperator is shown in Figure 45a. This figure indicates that the overall conductance of the recuperator core must be increased by approximately 5.8 percent with a 90 percent effectiveness unit to accommodate a change from Hastelloy to steel. A comparison of heat exchanger core volumes as a function of effectiveness for stainless steel and Hastelloy C units is shown in Figure 45b. This second curve reflects the 10 percent change in the physical size of the recuperator core due to the change from Hastelloy to steel.

In addition to the change in thermal conductivities a further factor, which resulted in this 10 percent core volume change, is increased thickness of the stainless steel plates. Based on AiResearch's experience in brazing stainless steel heat exchanger cores, 0.006 in. thick stainless steel tube sheets are the minimum thickness that will provide a highly reliable leak type braze joint. As Hastelloy C is somewhat more resistive to braze alloy penetration a thickness of 0.005 in. could probably be used.

The curves shown in Figure 45 were prepared for the preliminary selected recuperator design discussed in Section 3. The estimated heat exchanger weight for this preliminary design of utilizing 0.005 in. thick Hastelloy plates, 0.004 in. nickel fins, hollow stainless steel header bars and no fins in either triangular end section was 303 lb. With a change to 0.006 in. thick stainless steel plates and maintaining the same 0.90 effectiveness the heat exchanger weight increased to 353 lb. This increase in weight was based on the original estimated values of the KA factor. As a result of the above

70
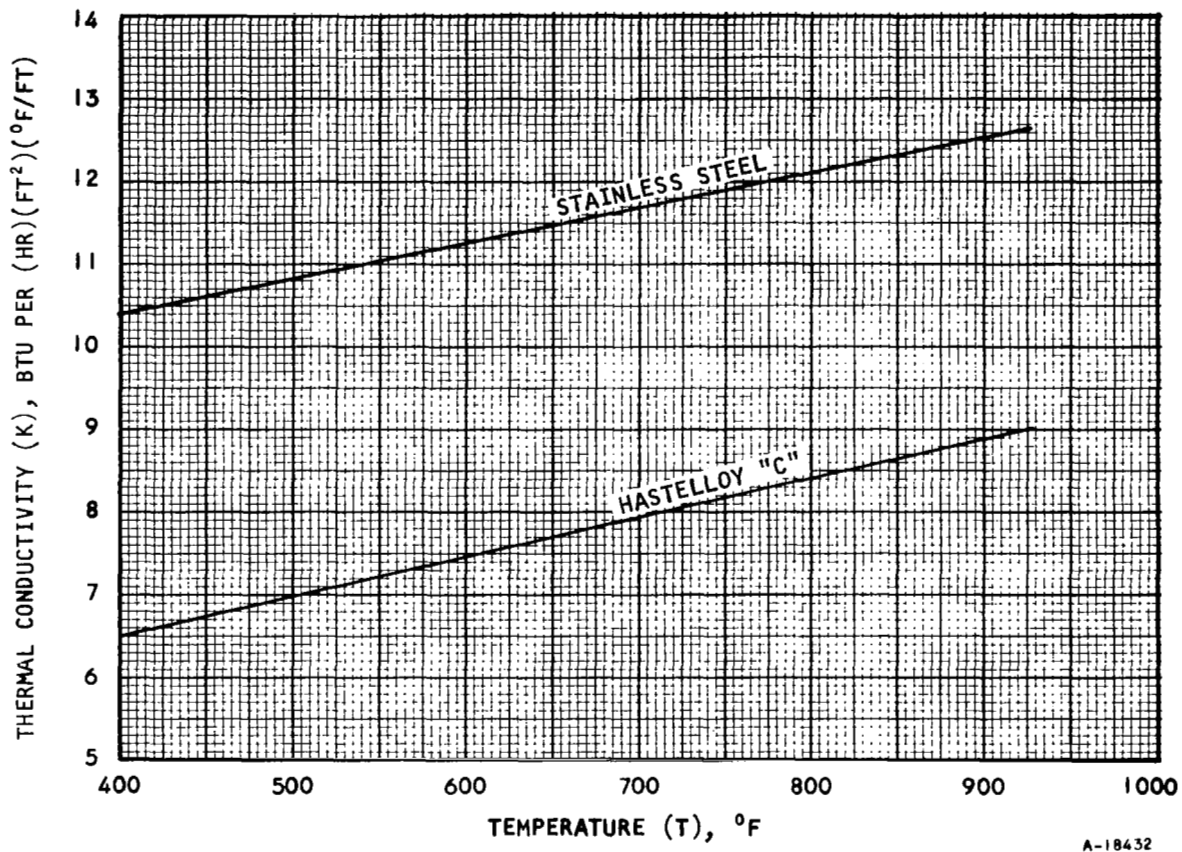
Figure 44. Thermal Conductivity of Stainless
Steel and Hastelloy "C"
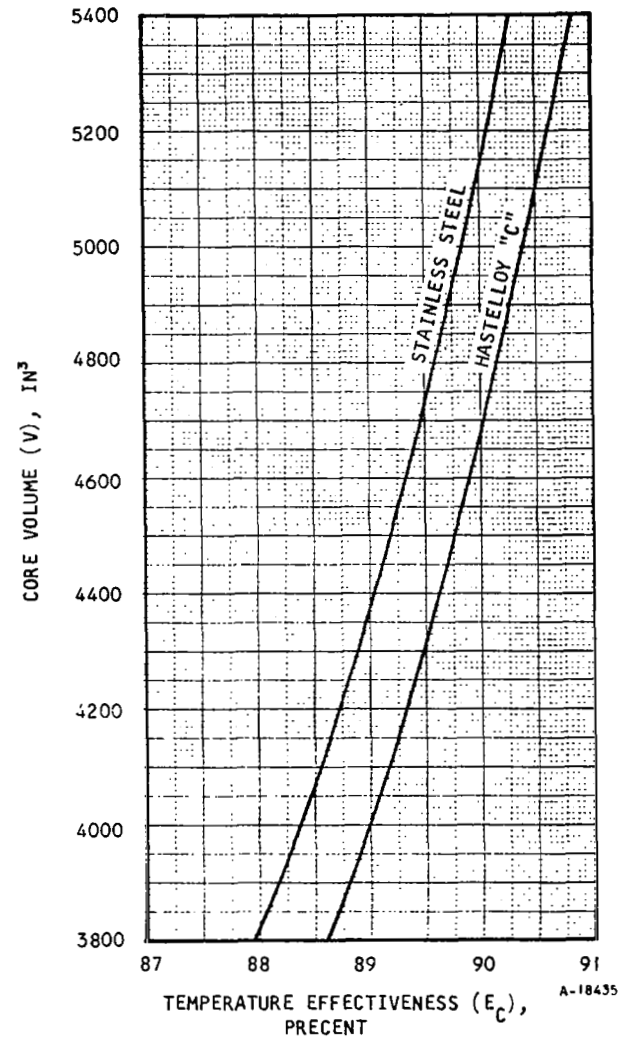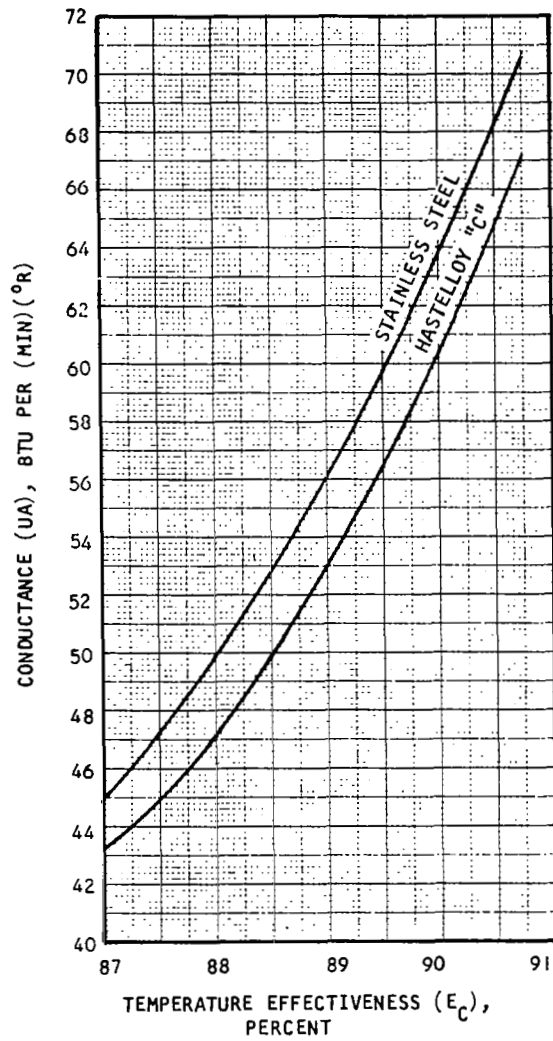
A-18432

Figure 45. Comparison of Stainless Steel and Hastelloy "C" Plates
in the Recuperator Design

described test program, this KA factor was increased. This resulted in a weight for the Hastelloy C unit of 341 lb while the weight of the stainless steel unit increased to 413 lb.

With this weight increase NASA requested that an investigation be made to determine if the overall weight could be reduced by increasing the overall pressure loss of the recuperator. The changes in the recuperator weight resulting from changing the total pressure drop are shown in Table 6. All numbers shown in this table are for an effectiveness of 0.9. This table shows that only small savings in weight are obtainable even with fairly substantial increases in total pressure drop. This is an agreement with Figure 22, 23, and 24 which indicated the tradeoff between weight, effectiveness and pressure drop for pure counterflow plate fin heat exchangers. Also shown in Table 7 is the reduction in effectiveness which results from the increased KA factor if the original designs are maintained.

TABLE 6

EFFECT OF PRESSURE DROP ON RECUPERATOR WEIGHT

$\Delta P/P$	Stainless Steel		Hastelloy C	
Percent	Decrease in Weight, percent	Total Weight, lb	Decrease in Weight, percent	Total Weight, lb
2.0	0	413	0	341
2.4	2	405	2	334
2.8	5	392	5	324
3.2	7	384	7	317

With the increased effect of the KA factor from the test program, either the heat exchanger size must increase or effectiveness must decrease. Both alternatives are illustrated below.

Recuperator Type	Recuperator Weight, pounds	Effectiveness percent
Hastelloy C	341	90
	303	88.9
Stainless Steel	415	90
	353	88.6

As a further means of attempting to reduce the overall recuperator weight while allowing for the increased effect of axial conduction, consideration was given to the fin material. Throughout the study, to this date, nickel was used as the fin material. Nickel was selected for this application owing to its higher thermal conductivity than steel thus increasing fin effectiveness. Increasing fin effectiveness results in decreasing core size but at the same time increases the effect of axial conduction which may increase core size. In order to determine whether any weight savings would result from changing from nickel to steel fins, a series of heat exchangers were designed having exactly the same performance and all utilizing identical core matrix geometry. The only variable in this series of core was fin conductivity. The results of this evaluation are shown in Figure 46 which shows that as fin conductivity is reduced through the range of 30 to 10 Btu per hr ft ^{0}F, the overall weight and size of the recuperator is reduced. This indicates that the effect of axial conduction overrides the increase in fin effectiveness. As a result of this analysis the fin material in the selected recuperator design was changed from nickel to stainless steel.
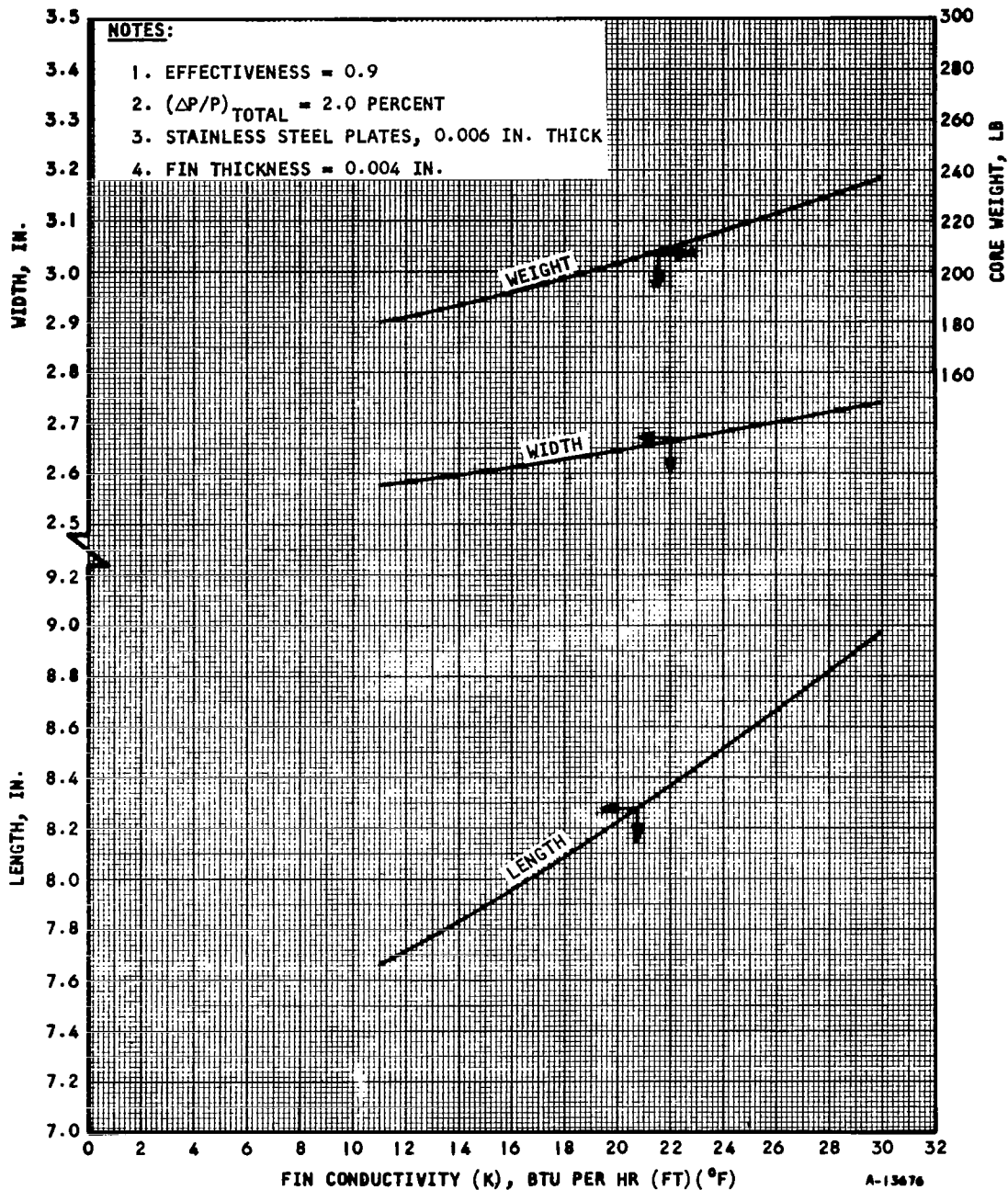
Figure 46.   Effect of Changing Fin Conductivity
on Recuperator Design

NOMENCLATURE

K	Thermal conductivity
A	Area
L	Length
C_{min}	$(WC_p)_{min}$
W	Fluid flow rate
C_p	Heat capacity
ϵ, E	Effectiveness
ΔE	Change in effectiveness
λ	Total axial conduction parameter
ℓ	Lorenz constant
T	Absolute temperature
B	Lattice conduction constant
σ	Electrical conductivity
R	Electrical resistance
ρ	Electrical resistivity $= 1/\sigma$

76

SECTION 6

FLOW DISTRIBUTION

In any heat transfer device the problem of flow distribution must be considered. Any nonuniformities in flow distribution will reduce the heat transfer performance and increase the pressure drop. If the degree of non-uniformity in flow distribution is known, it is possible to make a realistic estimate of its influence on heat exchanger performance. However, the problem of defining the degree of nonuniformity is considerably greater. In the initial stages of the final design program a brief analysis was made to determine the effect of an arbitrary selected nonuniformity on the preliminary selected design configuration. The flow distribution assumed for this analysis is shown in Figure 47. The results of the analysis are also shown in Figure 47. Although this arbitrary assumed nonuniformity in flow reduced the effectiveness by only 1.7 percent this in turn reduced the unit heat transfer units (NTU) by 22.5 percent. In terms of heat exchanger weight this would result in the heat exchanger weight increasing by approximately 70 lb to account for this amount of nonuniformity.

In the design of the heat transfer matrix every attempt was made to provide uniform flow distribution. The specific approach utilized in the design of the triangular end sections which provide the entrance and egress of the fluids was discussed fully in Section 4. Considerable design attention was also directed towards the inlet and outlet manifolds for both the fluid streams. Inefficient design of these manifolds would result in nonuniformities of flow distribution through the heat transfer matrix. The results of the manifold flow distribution analysis and test program are discussed below.

In addition to the manifold flow distribution testing, flow distribution testing was also conducted on the heat transfer matrix. The flow distribution test core design resulted from the work conducted during the parametric survey and also during the triangular end section analysis and axial conduction testing. While this test program was entitled "Flow Distribution Test" the objective was mainly to obtain the performance capabilities of the heat transfer matrix. Although instrumentation was included on the test unit to obtain flow distribution information directly, the main emphasis placed on the test results on this unit were on its heat transfer performance and pressure drop. As the analysis leading to the selection of the flow distribution test unit has been discussed completely in Sections 7 and 8 only the results of the actual testing are discussed in this section.

58.3 PERCENT W

41.6 PERCENT W

↑ ↑ ↑ ↑

HOT FLOW

COLD FLOW

↓ ↓ ↓ ↓

33.3 PERCENT W

66.7 PERCENT W
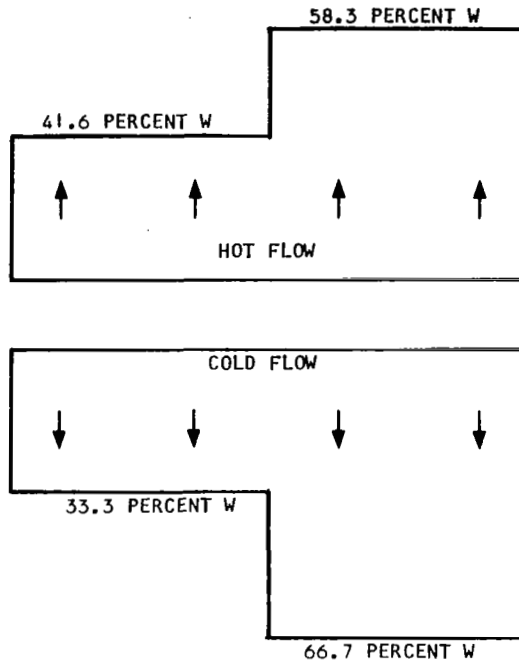
ASSUMED FLOW NONUNIFORMITY WITH W = 36.7 LB PER MIN

	Uniform Flow	Nonuniform
Effectiveness (E, percent)	90.0	88.3
Heat transfer units (NTU = $\frac{UA}{WC}$ min	9.00	7.35
Hot temperature out (T, $^{\circ}$R)	877	892
Cold temperature out (T, $^{\circ}$R)	1484	1473

The results above are based on the following design conditions:

Cold inlet temperature, $^{\circ}$R	801
Cold inlet pressure, psig	13.80
Hot inlet temperature, $^{\circ}$R	1560
Hot inlet pressure, psig	6.73
Argon flow rate, lb per min	36.7 (each side)
Design point effectiveness, percent	90
Overall pressure drop, percent	2
Estimated weight, lb	300

A-18451

Figure 47. Effect of Nonuniform Flow on Recuperator Performance

78

MANIFOLD FLOW DISTRIBUTION

In order to ensure that satisfactory flow distribution would be obtained through the heat transfer matrix a complete analysis was performed to determine the best shape and any required internal arrangement for the inlet and outlet manifolds to provide uniform flow.

Manifold Analysis

The initial analysis of the anticipated manifolds for the Brayton cycle recuperator indicated that in order to provide uniform flow over the entire inlet face of the recuperator, vanes would be required in the manifold. While these vanes provided uniform flow they had the disadvantage that they increased pressure drop. Consequently, the continuing analysis of the manifolds concentrated on providing uniform flow without the addition of vanes. These continuing studies were conducted using the recuperator layout shown on AiResearch Drawing 198005 which describes the relative position and flow directions of the entrance and exit ducts. Throughout the analysis low pressure side duct diameter was maintained at the NASA specified 8-in. diameter while the high pressure side diameter considered was 6-in. The analysis considered box-type inlet and exit headers, as shown in Figure 48, for both the high pressure and low pressure sides. A two-dimensional analysis was conducted to determine the static pressure distribution in the header regions and to determine the effect of header design on flow distribution. When conducting this two-dimensional analysis, use was made of the data of M. Perlmutter and A. L. London (References 11 and 12). The estimated static pressure distributions in the inlet and exit headers for both high and low pressure sides of the recuperator are shown in Figure 49. The estimated flow distribution resulting from these pressure distributions is shown in Figure 50. Since box-type headers are used, the static pressure distributions follow the square law; that is, the static pressure is proportional to X^2 where X is the distance along the surface of the core as shown in Figure 48.

Because the flow exits from the center of the exit header with the direction perpendicular to the inlet direction, the exit region may be considered to consist of two identical but opposite parts. The flow model is, therefore, a composite one if parallel flow plus counterflow, as illustrated by the typical streamlines shown in Figure 48, the static pressure distribution in the exit region is therefore, also a composite curve of two parabolic shapes symmetric to the axis of the exit duct as shown in Figure 49.

The header pressure distributions and flow distribution resulting from this preliminary analysis were unacceptable and consequently the analysis was continued to improve the manifold configuration from the original assumed box type. The main cause of the estimated nonuniformities in flow distribution is attributable to the combination of the centrally located exit duct
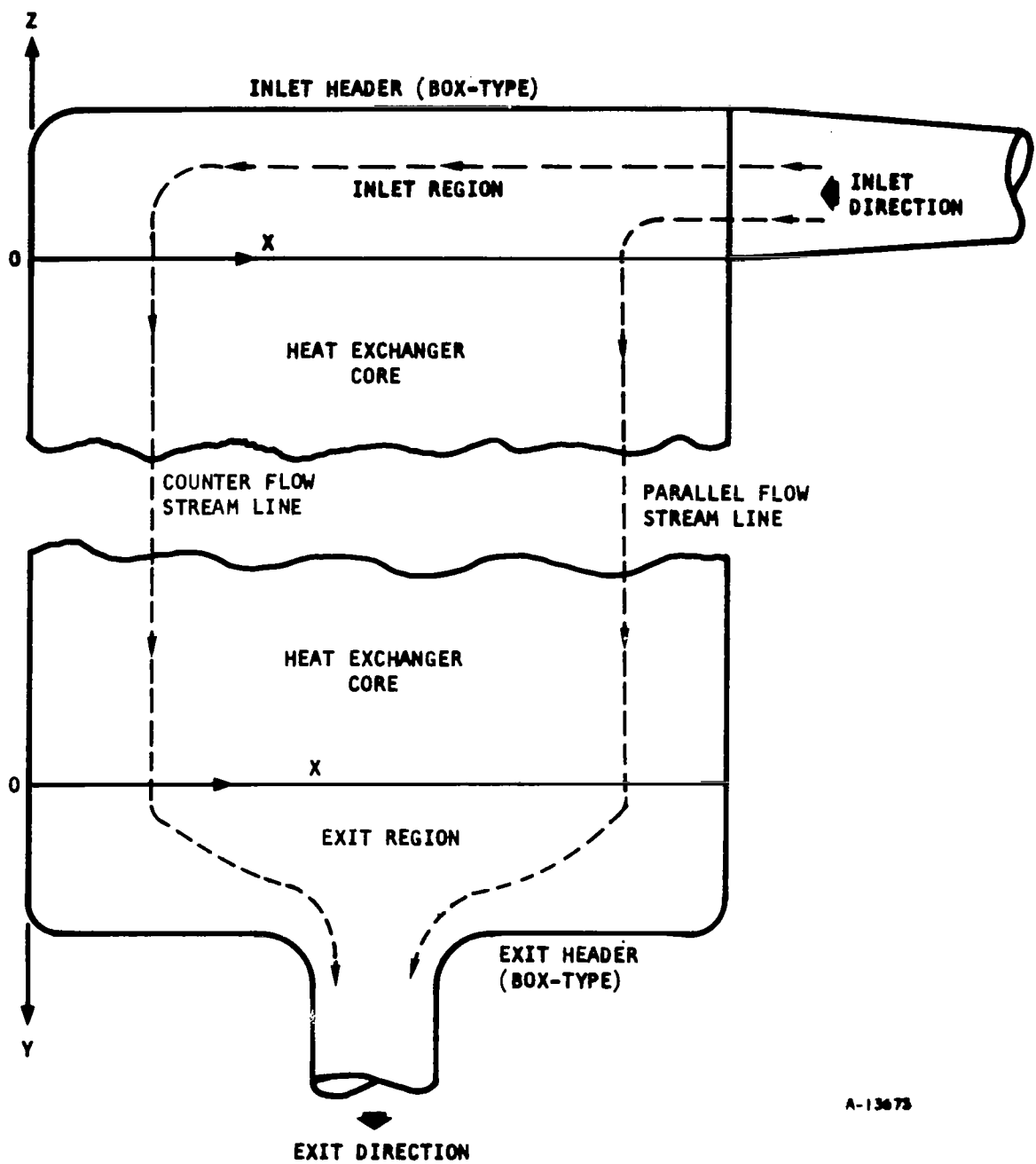
Figure 48.   Schematic Diagram of Inlet and
Exit Headers
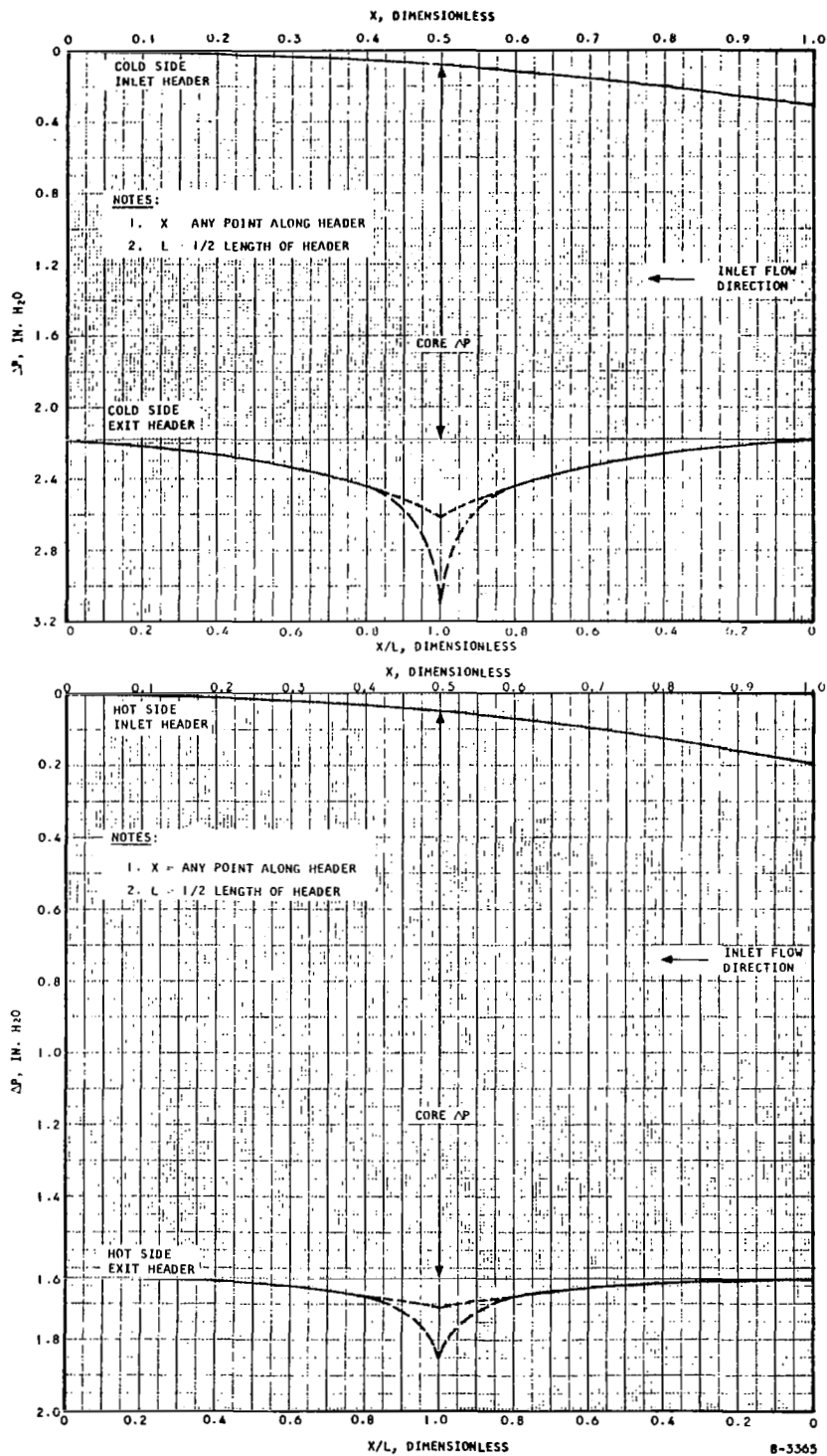
Figure 49. Recuperator Pressure Distribution in Inlet and
Exit Headers for Design Point Condition and
Geometry of Drawing LI98005

81
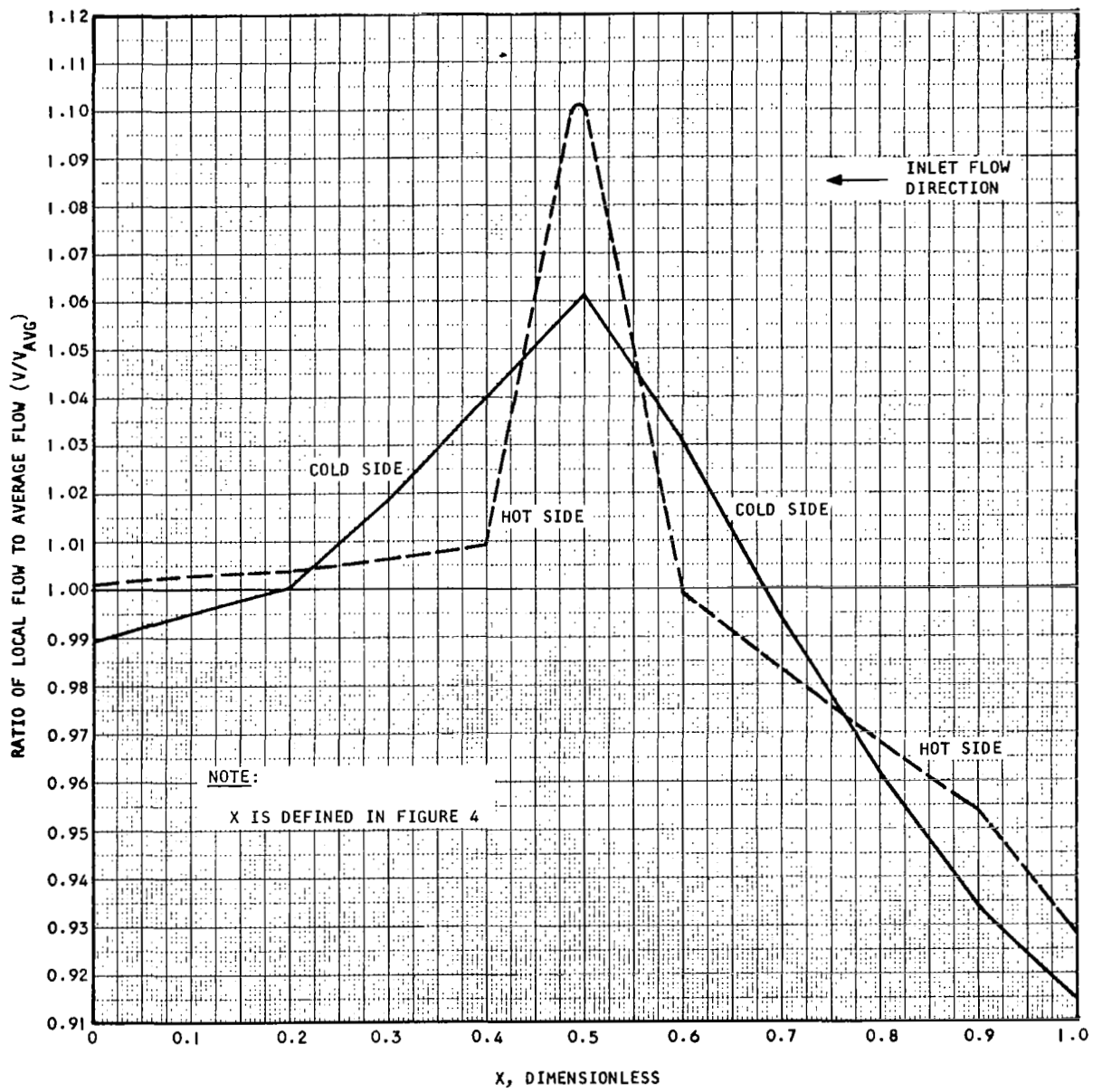
Figure 50. Flow Distribution in Vertical Direction

in the constant cross-section of the box-type inlet headers. As the exit duct location is fixed, improvement in flow distribution should, therefore, be obtained by redesigning the inlet header shape. This, in fact, is the approach utilized by both Perlmutter and London in the above references. Using the analytical techniques of these references new inlet manifold headers were designed. These new header designs are illustrated in Figure 51. The header cross-sectional area decreases linearly to approximately half of the core height, from which point the area is constant to the end of the core. The exit header configuration maintains the original box-type configuration except that a plate divider is being incorporated to reduce mixing losses. The larger manifold curvature was used to increase the exit area and the junction of the exit header and exit duct.

Characteristically, the pressure in the inlet header decreases first, then increases according to the square law. The pressure distribution profile of each pair of inlet and outlet headers are now matched more effectively, as shown in Figures 52 and 53, for the low pressure and high pressure sides respectively. The flow distribution curves resulting from this pressure distribution for both high and low pressure sides are shown in Figure 54. Minimum nonuniformity in each case is within a 2 percent tolerance.

Manifold Flow Distribution Tests

In order to verify the above analysis, full scale manifold distribution tests were run. The actual manifolds constructed for the flow distribution tests are shown in Figure 55. All manifolds were full size. As no full size heat exchanger was available for these tests it was necessary to find a method of simulating heat exchanger pressure losses. The method selected for doing this was to utilize several layers of fine mesh screen with the same pressure drop as the heat exchanger matrix at the same flow rates. Photographs of the screen matrices simulating both the high and low pressure sides of the core are shown in Figure 56. The test setup used for the low pressure side manifold tests is illustrated in Figure 57. The high pressure side test setup was essentially the same and the same amount of instrumentation was used for the tests.

The test manifolds and associated test hardware used for the high and low pressure side tests are shown schematically in Figure 58. The test manifolds are identical to the design configuration, including structural shapes and reinforcement. As stated above, flow resistance similarity was obtained with screen matrices and the test fluid was ambient air, at flow rates which gave the Reynolds numbers close to the design condition. Pressure probe grids were placed upstream and downstream of the simulated core. On the low pressure side, ten traversing probes were used to record the pressure over the full matrix area. Pressure was measured at lateral (no flow direction) intervals of 2.5 in. and longitudinal (flow direction) increments of 2 in. Three permanently located pressure probes were placed in the inlet group to assure identical test conditions at the start of each recording sequence. Inlet static pressure and static pressure drop
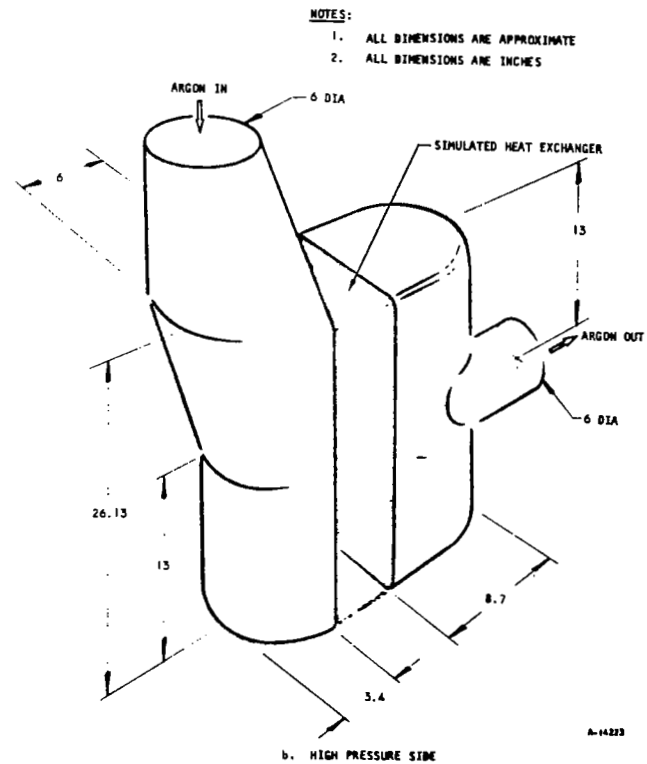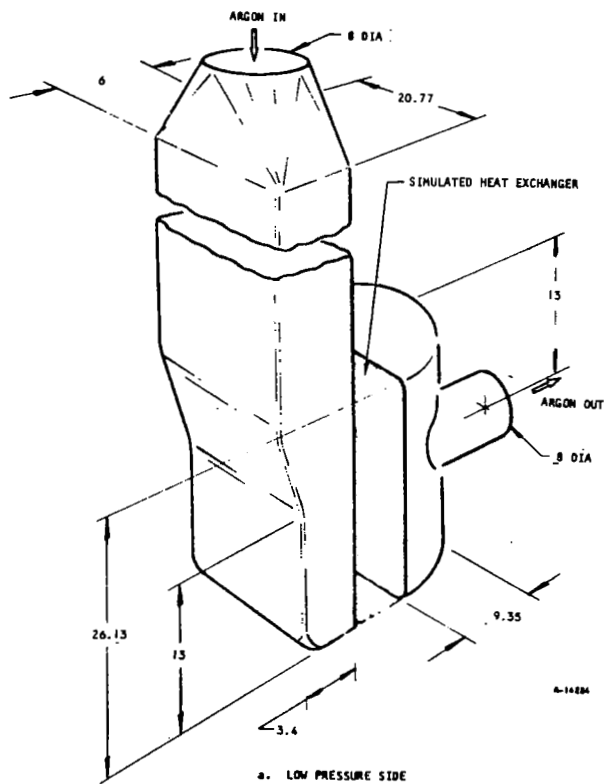
Figure 51. Schematic of Full Scale Manifolds
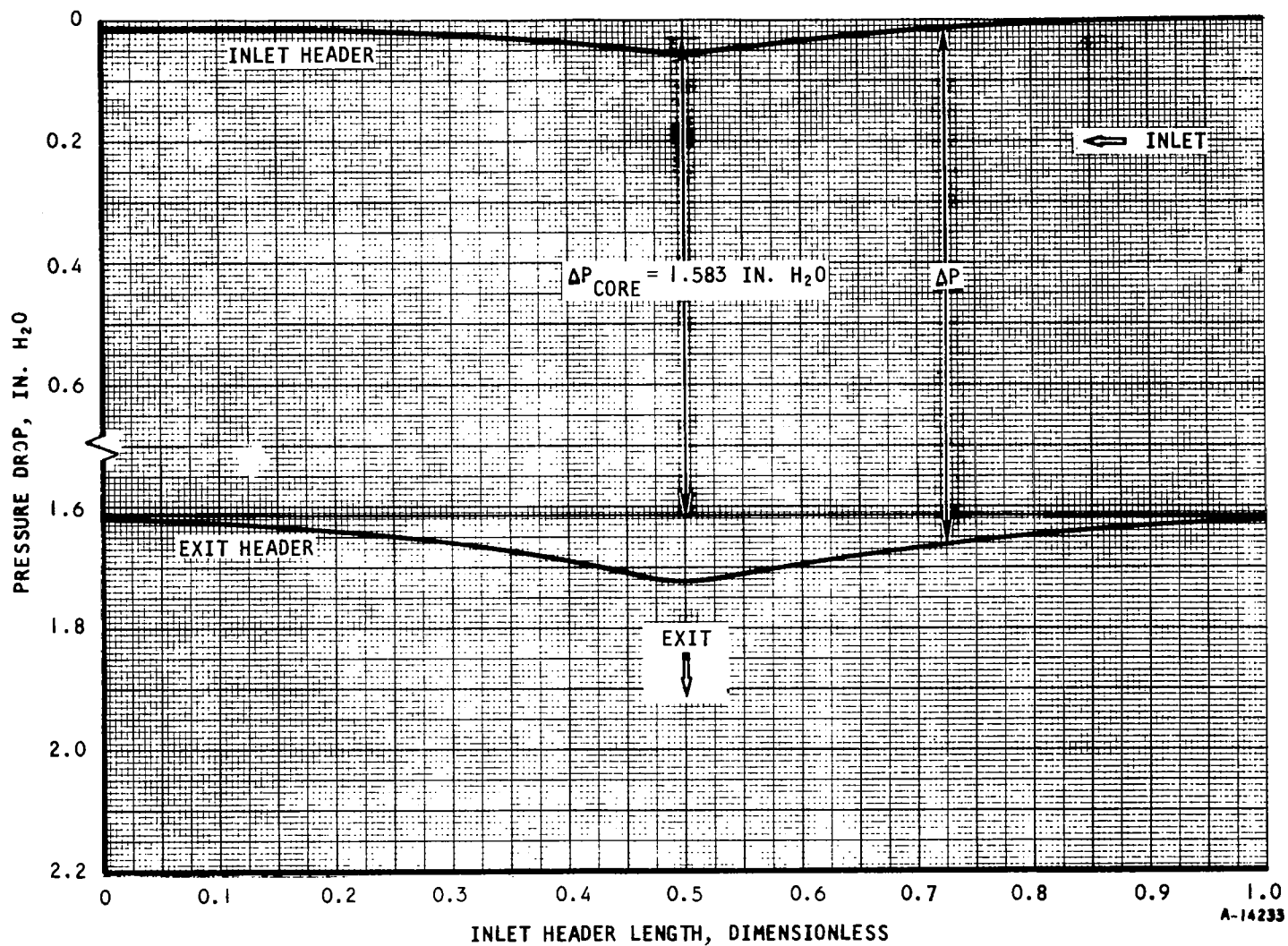
Figure 52. Low Pressure Side Pressure Distribution in Inlet and Exit Headers for Design Point Condition and Manifold Geometry shown in Figure 51a

A-14233
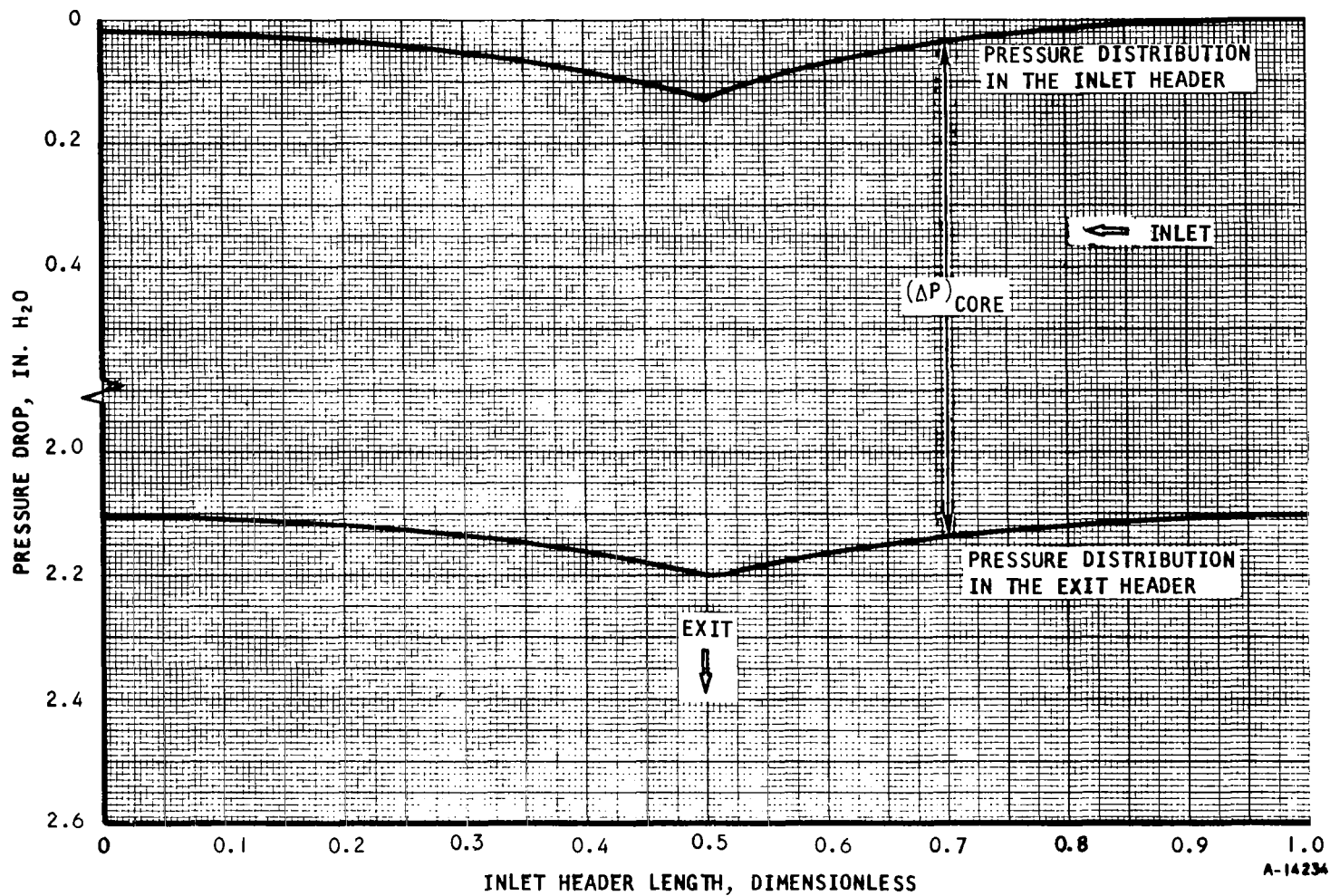
Figure 53. High Pressure Side Pressure Distribution in Inlet
and Exit Headers for Design Point Condition and
Manifold Geometry of Figure 51b
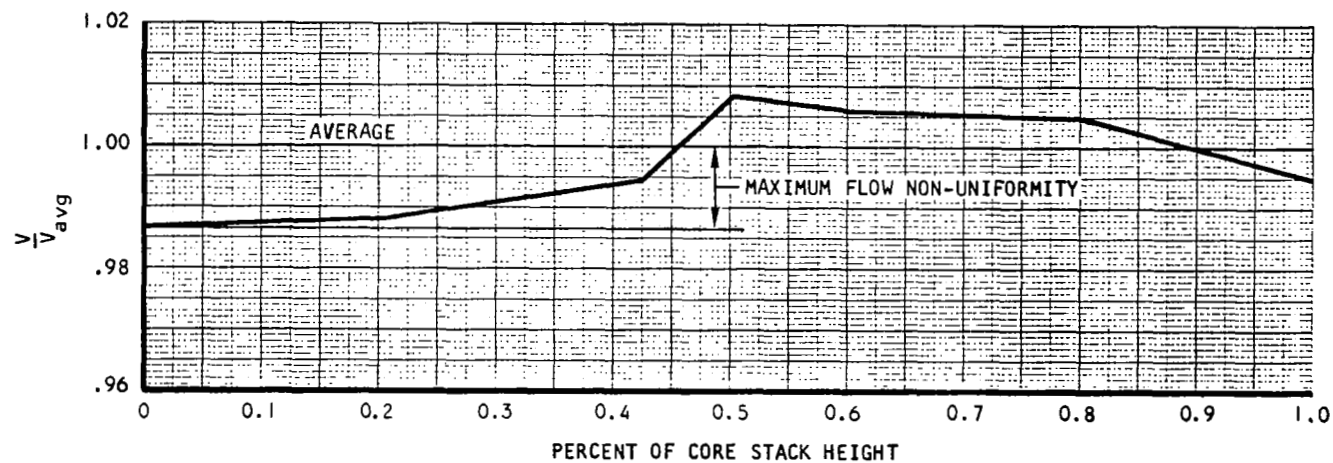
a. High Pressure Side

High Pressure
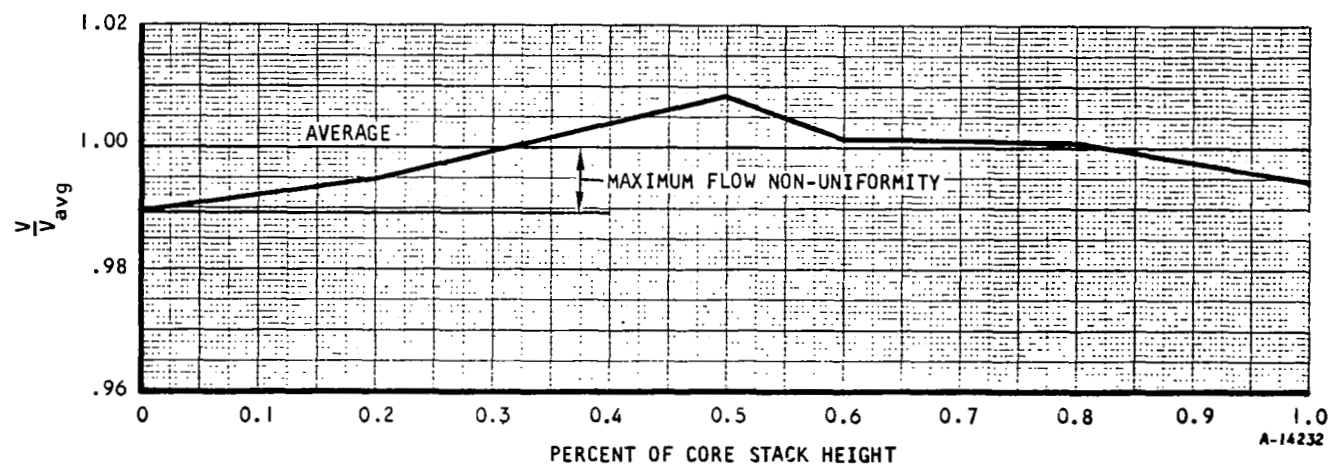
b. Low Pressure Side

Figure 54. Flow Distribution in Recuperator Core Based on Pressure Distributions of Figures 52 and 53

A-14232

87
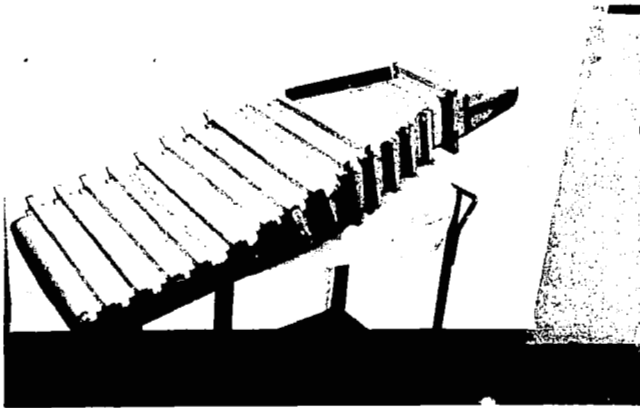
LOW PRESSURE INLET MANIFOLD
(STRUCTURALLY REINFORCED)
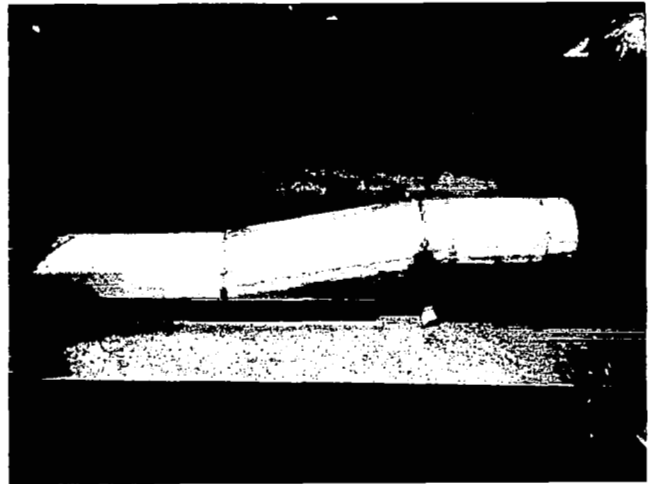
HIGH PRESSURE INLET MANIFOLD

LOW PRESSURE OUTLET MANIFOLD

F-2729

Figure 55.   Recuperator Manifold Construction
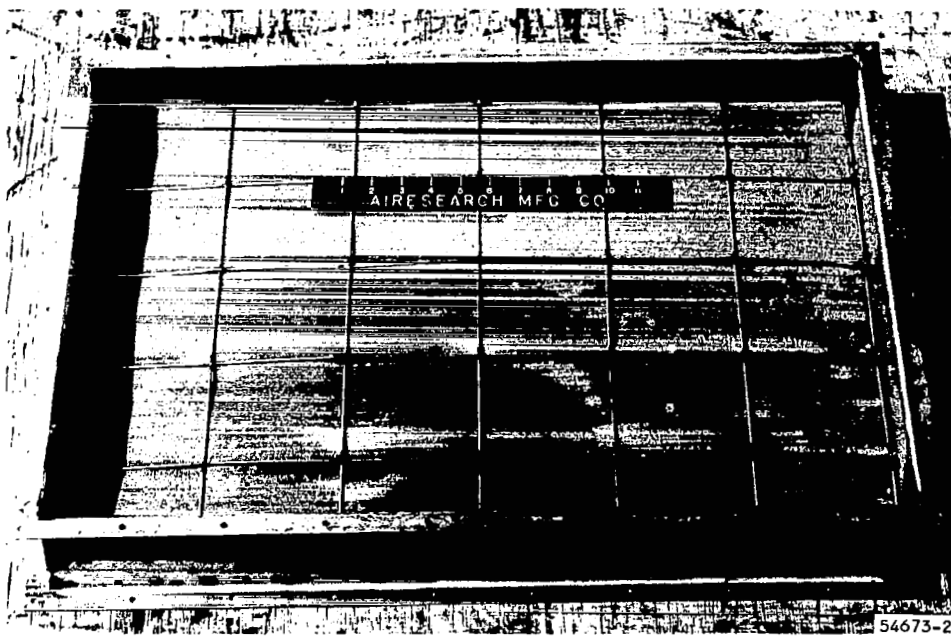
LOW PRESSURE SIDE OF CORE
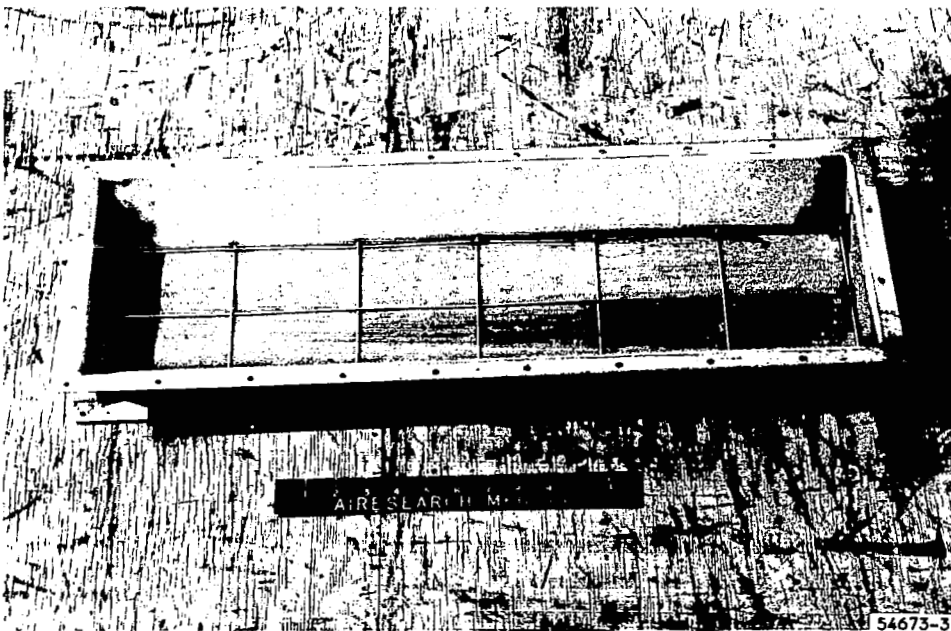
HIGH PRESSURE SIDE OF CORE

F-3664

Figure 56.   Screen Matrices Simulating Recuperator Core

89
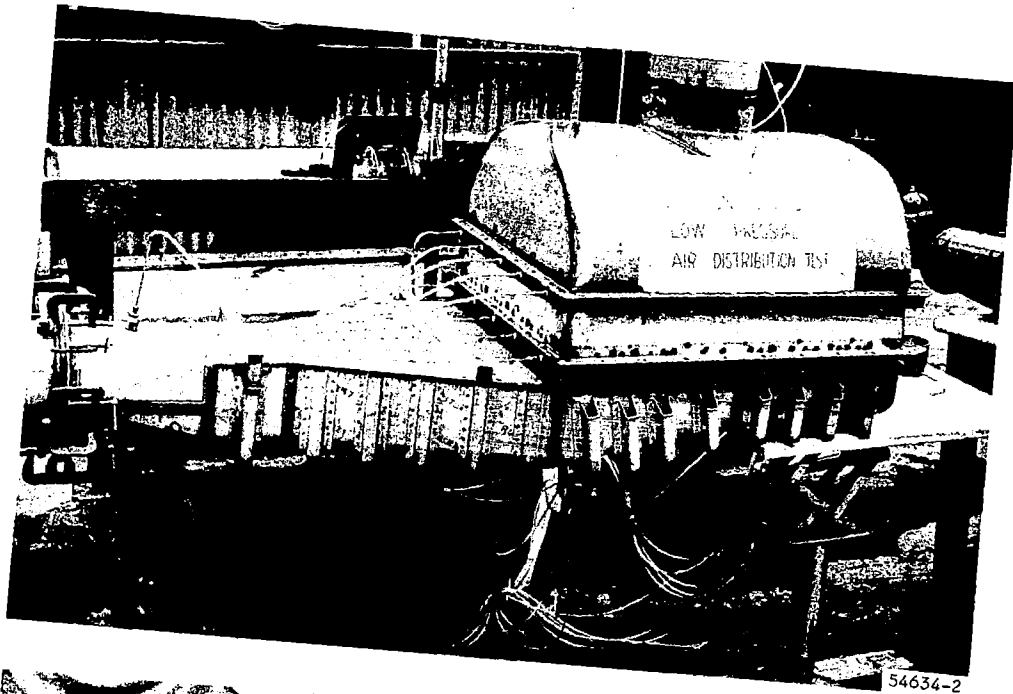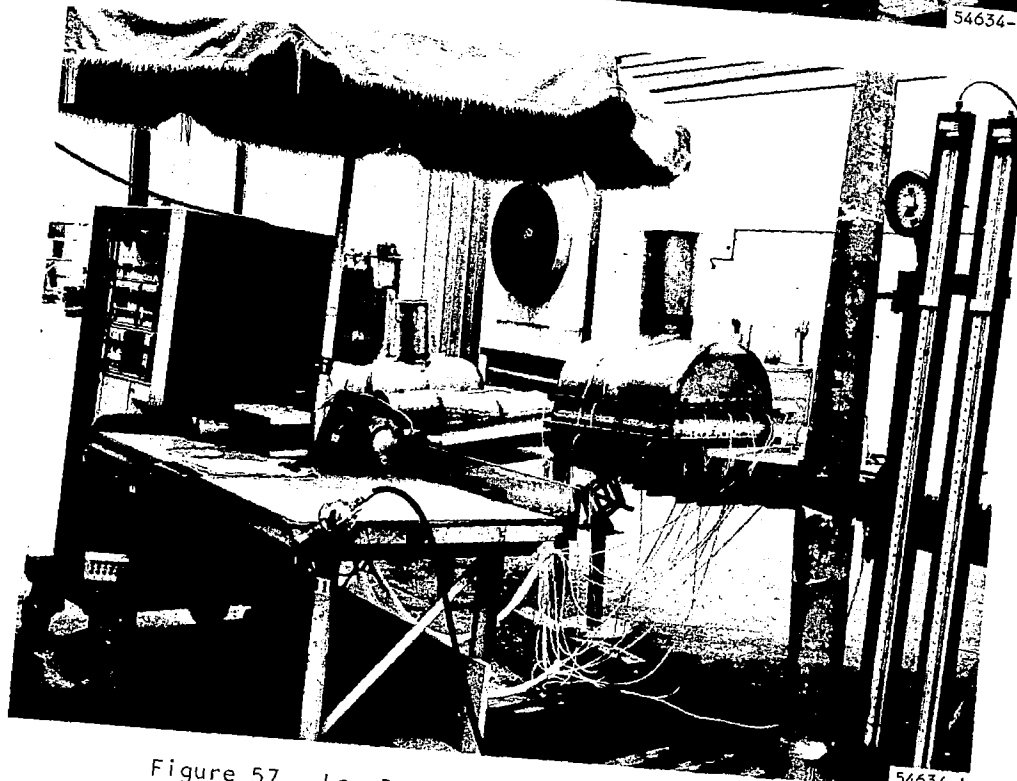
Figure 57. Low Pressure Manifold Test Setup

54634-2

54634-1

F-3662

90

INLET PAN
ASSEMBLY

AIR
IN

INSTRUMENTATION FLANGE

SCREEN MATRIX SIMULATING
CORE

INSTRUMENTATION
FLANGE

OUTLET PAN ASSEMBLY

A-14760

AIR OUT

High Pressure Manifold

INLET MANIFOLD ASSEMBLY

AIR
IN

INSTRUMENTATION FLANGE

SCREEN MATRIX SIMULATING CORE

INSTRUMENTATION FLANGE

OUTLET MANIFOLD ASSEMBLY

A-14779

AIR OUT
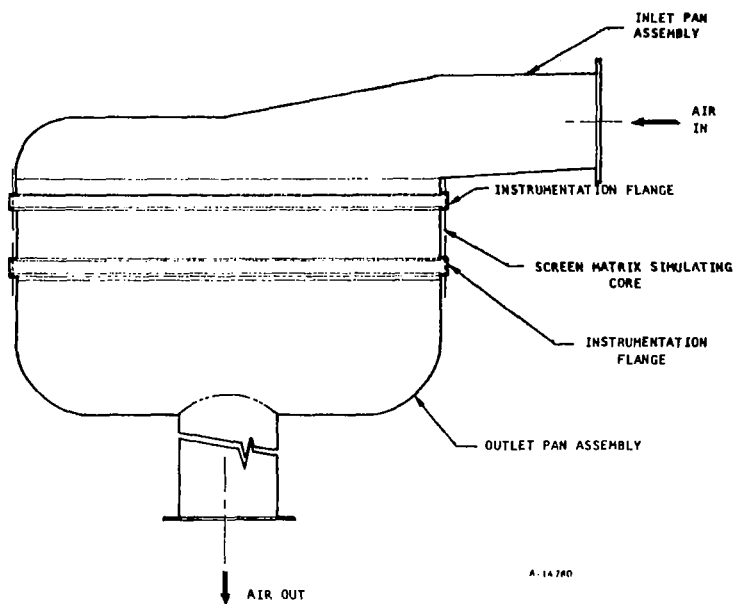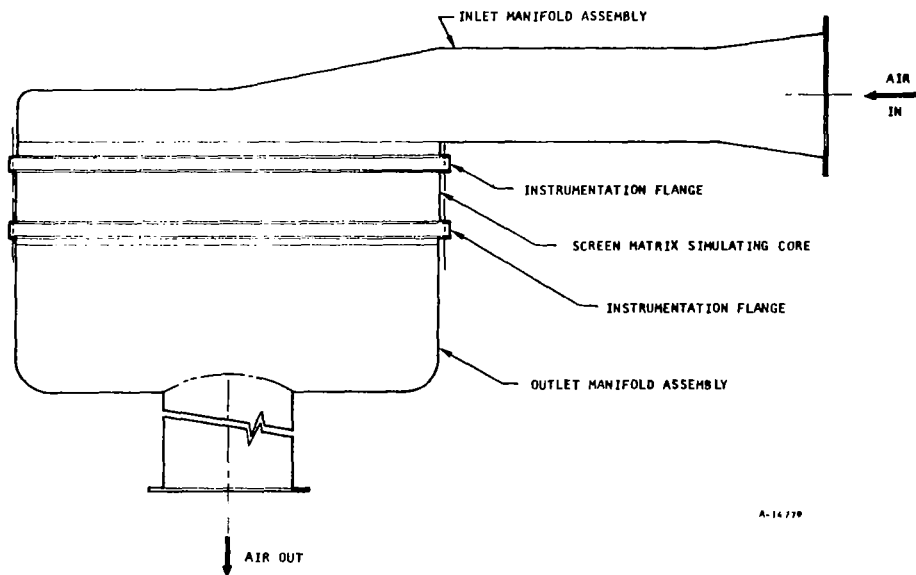
Low Pressure Manifold

Figure 58. Manifold Test Schematic

were recorded at each of the 60 points. The high pressure system was arranged similarly to the low pressure system except that fewer probes (6 traversing) were used, since the frontal area is appreciably smaller. The average low pressure frontal area is approximately 21 in. by 26 in.; the high pressure frontal area is 9.5 in. by 26 in.

Test Results

On the high pressure side preliminary results indicate that the tapered inlet pan in combination with the center outlet pan produces fairly good flow distribution, however, the 2 percent (max) nonuniformity target was exceeded.

A slight manifold modification could effect the improvements necessary to achieve the desired uniformity. Improved uniformity could also be obtained by modifying the duct slightly with an insert.

Preliminary results on the low pressure side indicate that tapering the inlet pan was effective, however, the 2 percent (max) nonuniformity target was again exceeded. The results indicate that slightly more acute taper on this manifold is required to give the necessary flow distribution. Further improvements in flow distribution would also be achieved on this side of the unit by the addition of the gas to liquid heat exchanger.

At the conclusion of the above described manifold testing consideration was given to running further tests. These tests would have included the fabrication of the modified manifolds and the closer simulation of the heat exchanger core impedance. However, at this time the final design configuration was not fully defined and as it was known that the modifications required to the ducts and manifolds were minor it was decided that these additional tests were unnecessary. This decision not to run further tests was later substantiated as the finally selected design configuration required overall geometry changes to the manifolds. With the pressure drop reduction investigations, described in Section 8, with the aspect ratio of inlet and outlet face of the counterflow core changed from 1.0 to 2.25. This, of course, increases any flow length within the manifolds and reduces the cross-section area. From the methods of analysis used to predict the pressure and flow distribution in the manifolds and from the test data obtained from the above described program it is believed that satisfactory manifold designs can be made without further testing.

HEAT EXCHANGER FLOW DISTRIBUTION

The analytical studies discussed in Sections 3, 4, and 5 of this report led to the design of the flow distribution test heat exchanger. As a result of the manufacturing and axial conduction investigations the size of the basic counterflow core increased slightly from the preliminary selected configuration. The triangular end section analysis and design discussed in Section 4 gave the final configuration for the triangular ends.

The intent of the flow distribution test was to evaluate the performance capabilities of this final selected design. The test unit used was full size in all but one dimension. In order to reduce cost and to ensure satisfactory test operation the no flow dimension (or stack height) of the test core was limited to 2 in. In the full size heat exchanger this dimension is approximately 26.2 in. From the results of the axial conduction analysis and test program the entire flow distribution test unit was fabricated from stainless steel. The low pressure side fins used in the counterflow core are the originally selected 12 rectangular fins per in 0.178 in. high and the fins used in the high pressure side are the originally selected 16 rectangular fins per inch 0.153 in. high. Both fins are fabricated from 0.004 in. thick stainless steel. The tube sheets throughout the test core are 0.008 in. thick stainless steel and the overall width of the counterflow core is 26.2 in. and the flow length of the counterflow core is 7.85 in. From the triangular end investigations the hot end triangle height is 7.0 in. and the cold end triangle height is 2.25 in. There are 10 plain rectangular fins per in., 0.004 in. thick in both the high and low pressure triangular end sections. The ratio of the low pressure side inlet face area to total available face area is 0.75. Definition of hot and cold end together with definition of high and low pressure side flows is shown in Figure 59.

Special manifolds were designed for this test core to ensure that the nonuniformities in flow distribution occurring in the tests were the result of the heat exchanger matrix and not of the manifolds or ducts. These heat exchanger manifolds are shown in Figure 58. Also shown in Figure 60 is the complete flow distribution test heat exchanger with manifolds installed.

Initially two complete series of tests were conducted on this unit. Figure 61 shows the unit installed in the test setup and clearly indicates the different inlet and outlet flows. In the first series of tests a hot side inlet temperature of approximately 400°F was used while in the second series of tests the hot side inlet temperature was increased to approximately 600°F. In both series of tests the cold side inlet temperature was room ambient and the flow range covered by the test was from 1 to 4 lb per min. This range of flow rate covers both the equivalent mass flow and the equivalent Reynolds numbers to the design point operating conditions.

Difficulties were encountered with the data obtained from these first two runs. In both series of tests conducted, inlet and outlet temperatures of both fluids to the heat exchanger were measured in mixing boxes which were some distance from the unit. As all ducting, mixing boxes, and the heat exchanger itself were well insulated it was originally believed that the heat leak from this setup should be negligible. However, during a number of the runs additional temperatures were taken by a traversing thermocouple across the inlet and outlet faces of the heat exchanger and the results of these temperature traverses differed considerably from the values read in the mixing boxes. In order to eliminate this type of uncertainty from the test results a calibration of the heat leak between ducting and mixing boxes was conducted.

HOT OR LOW PRESSURE
ARGON IN
(FROM TURBINE)

COLD OR HIGH PRESSURE
ARGON OUT
(TO ABSORBER)

7 IN.   HOT END
OF CORE

26.1 IN.

7.9 IN.

COLD END OF
CORE   2.3 IN.

HOT OR LOW PRESSURE
ARGON OUT
(TO RADIATOR)

COLD OR HIGH PRESSURE
ARGON IN
(FROM COMPRESSOR)
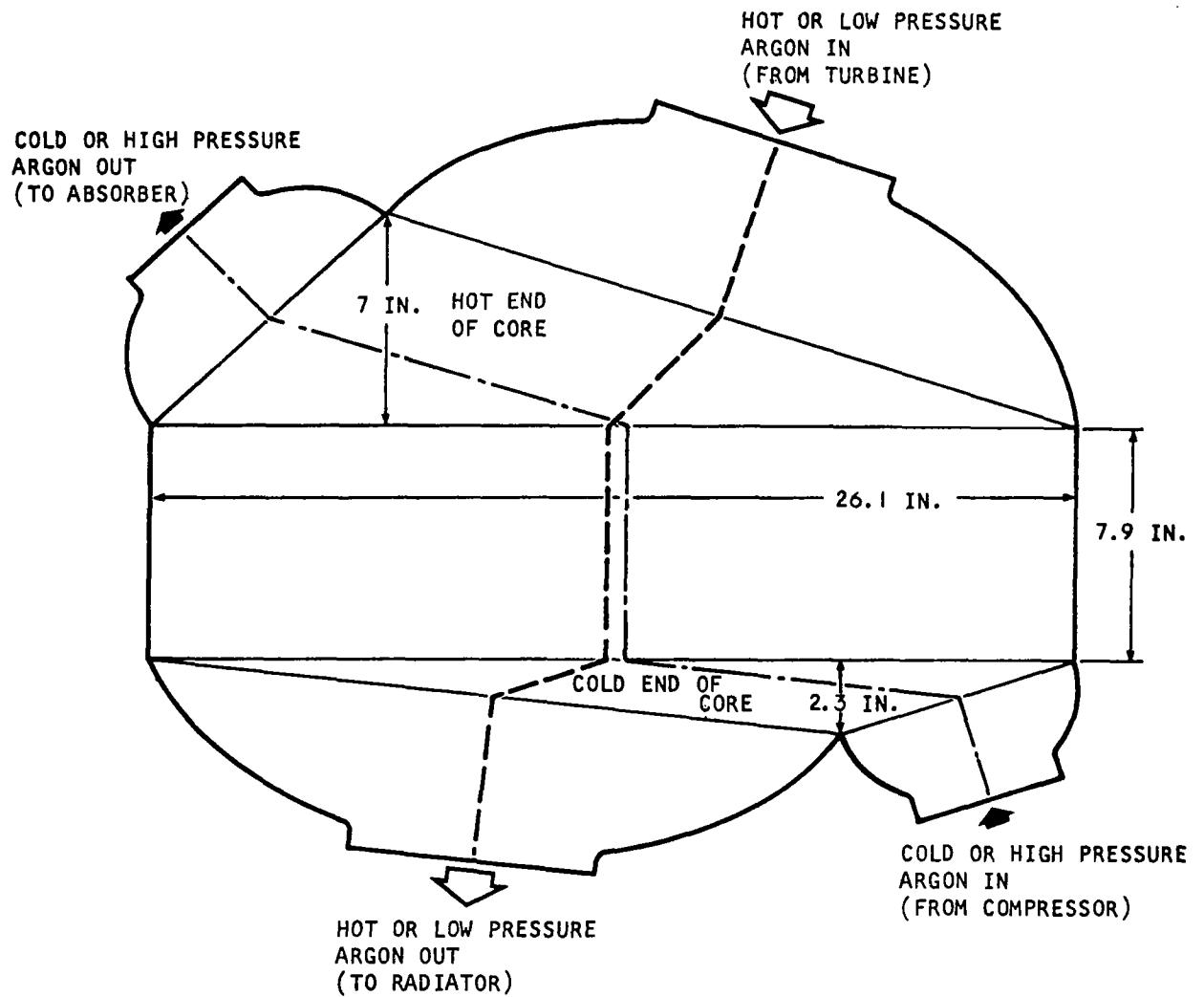
A-14756

Figure 59.   Recuperator Flow Schematic
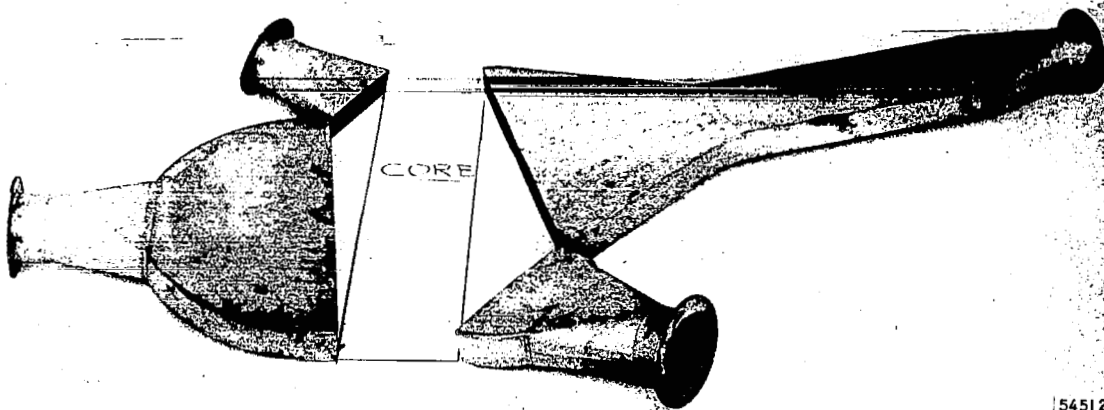
TEST CORE MANIFOLDS

54512
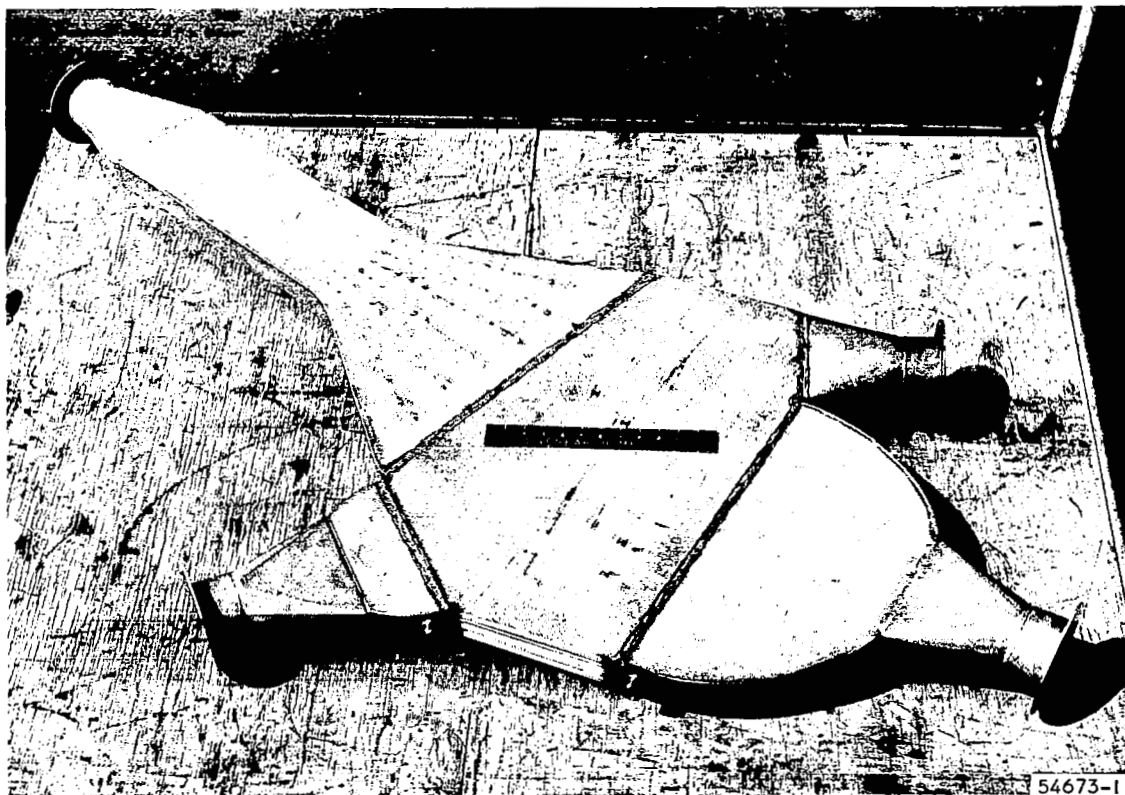
TEST CORE WITH MANIFOLDS

54673-1

F-3663

Figure 60.   Flow Distribution Test Unit

95
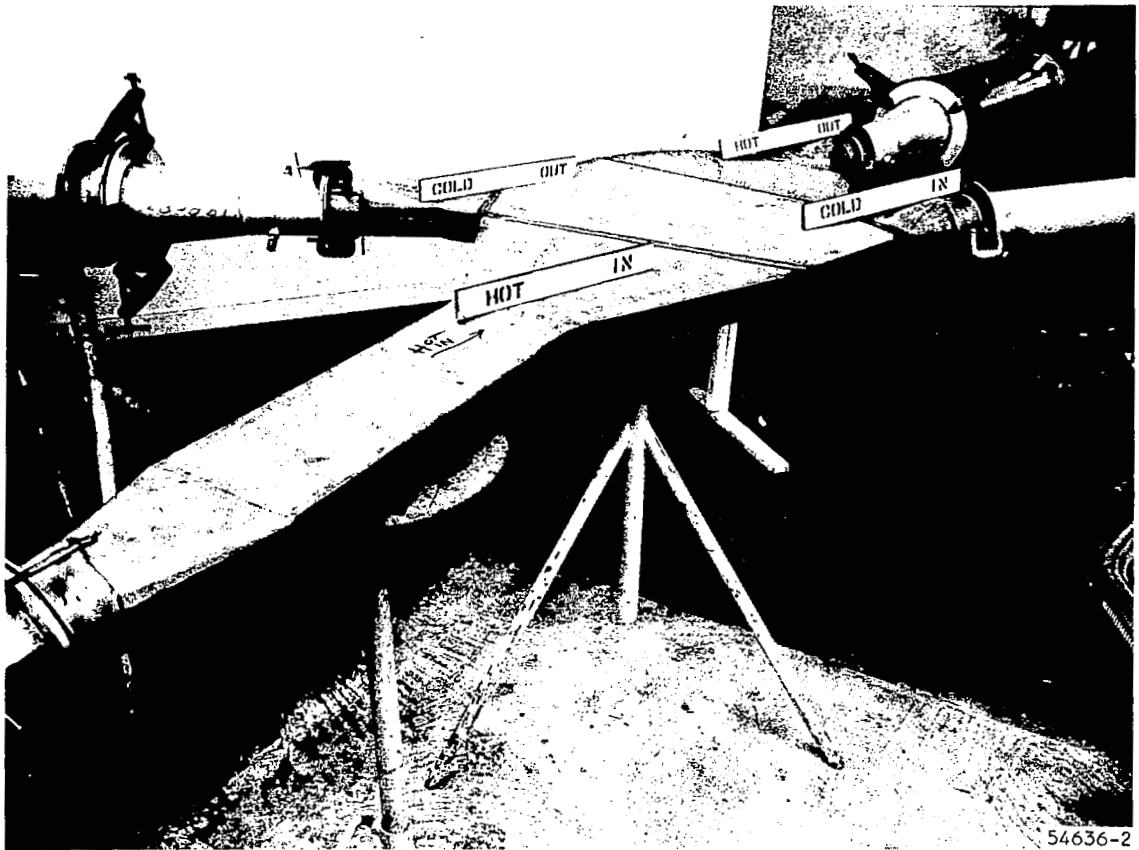
Figure 61.   Installed Flow Distribution Test Unit

The two areas where duct and mixing box heat leak have a substantial effect on the data obtained are the hot inlet and the cold outlet. At the other two locations, that is, the hot outlet and the cold inlet, the gas temperatures are close to ambient and, therefore, the heat leak is very small. In order to evaluate the heat leak from the hot inlet duct and the cold outlet duct, thermocouples were installed at the hot inlet and cold outlet faces of the heat exchanger as well as in the normal locations in the mixing boxes. The unit was then insulated, as it was throughout all heat transfer tests, and hot gas passed through the heat exchanger on one side only. With a hot gas inlet temperature of $600^\circ F$ flowing through the hot side of the heat exchanger it was established that, with a flow rate of 1.8 lb per min the temperature loss between mixing box and heat exchanger was approximately $12.5^\circ F$. This data then established the amount of heat flowing away from the hot inlet duct while operating at a temperature of $600^\circ F$. This test was isothermal and as readings were taken for over an hour after stability had been achieved it is believed that this is a very accurate evaluation of the heat leak from this duct. A similar test was conducted to determine the heat leak from the cold outlet duct, only during this test a gas temperature of $520^\circ F$ was used. In this case, with a flow rate of 1.8 lb per min through the system the temperature loss was approximately $46^\circ F$. The much greater heat leak on the cold side ducting was apparently due to the use of less insulation around this section and also to the final method of mounting the unit within the test setup. There is no support structure between the hot inlet mixing box and the inlet face of the heat exchanger. However, there is a metal support stand located between the cold outlet face of the heat exchanger and the mixing box. This stand supports the ducting directly and is not separated from it by any insulation. While the tests were being run it was observed that the metal of this test stand was too hot to touch, thus indicating a substantial heat leak from this area.

With this heat leak evaluated further heat transfer tests were conducted on the two inch stack-height heat exchanger core. After the conclusion of the heat leak evaluations four different flow rates were run through the heat exchanger to establish its heat transfer performance. The hot inlet temperature was maintained at approximately $600^\circ F$ while the cold inlet temperature was room ambient. In examining the data obtained directly from the mixing boxes the heat balances ranged from approximately 5 percent to approximately 15 percent. However, when the duct temperature loss corrections were applied to this data all heat balances were below 2 percent. Further confirmation of the accuracy of the heat loss calibration was obtained by comparing this data with the data obtained from the first set of tests where the fluid temperatures were measured by a traversing probe at the outlet faces of the heat exchanger. Both the data obtained from the duct loss calibrations and the data obtained from the temperature probe traverses is shown in Figure 62. Also, shown in this figure is an estimated effectiveness curve for the actual test conditions. In all cases the test data indicates slightly higher effectiveness than predicted.
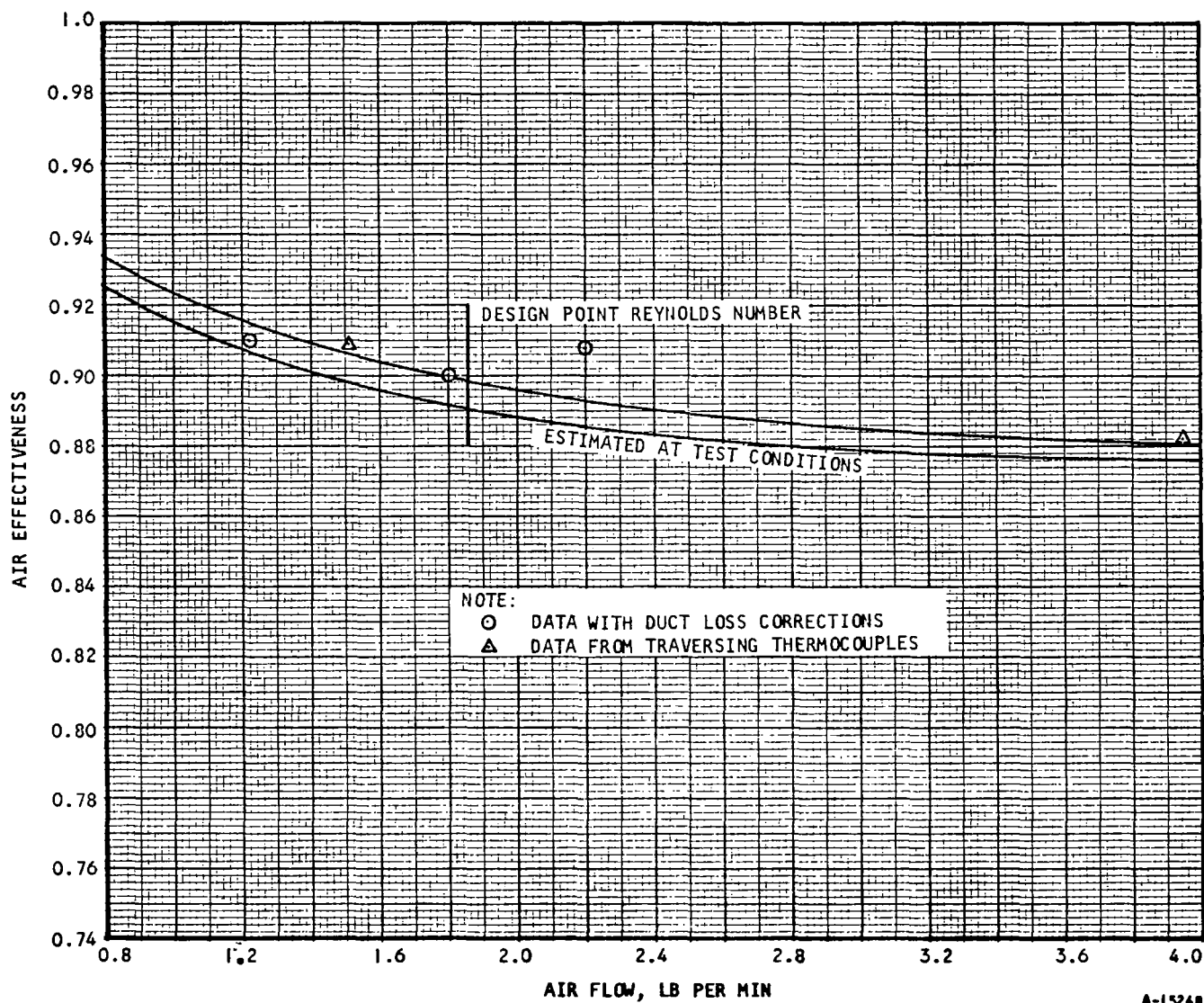
A-15248

Figure 62. Estimated and Test Performance of
2 in. High Test Core

As it is not possible to test the two inch high core at actual design conditions it is believed that the data shown in Figure 62 provides the most reliable means of determining heat exchanger performance. The method of analysis used to obtain the predicted curve of Figure 62 is exactly the same as that used to design the full sized unit. Therefore, a comparison between this curve and the test data obtained provides adequate confirmation of overall heat transfer performance of the full size unit.

From the temperature probe traverses, run during the initial series of tests on this unit, it is possible to obtain the outlet temperature distribution. Owing to the small amount of heat transfer occurring in the triangular shaped ends this outlet temperature distribution is not uniform. This is a result of the fact that the heat transfer in the triangular ends is the cross-flow type which imposes a definite temperature profile. A comparison of the actual outlet temperature distribution obtained with the theoretical outlet temperature distribution gives a fair indication of the nonuniformity in flow which exists within the heat transfer matrix. Figure 63 illustrates the cold side outlet temperature distribution as a deviation from the mixed mean outlet temperature. Both the test distribution data and the theoretical distribution data are shown on this figure. The theoretical distribution is taken from analysis described in Section 7. Where the test temperature is higher than the predicted, less flow than average has passed through this section of the heat exchanger, where the test temperature is lower than is estimated more flow has passed through that section of the heat exchanger. The difference between the test and estimated temperature distributions indicates that the flow through the center section of the heat exchanger is less than at either side.

In addition to the extended heat transfer tests further tests were performed on the 2-in. heat exchanger core to obtain a more accurate evaluation of flow distribution and pressure drop. The overall test setup used for these extended tests is shown in Figure 64. Much of this extended testing to examine the flow distribution in the exchanger was conducted at isothermal conditions. A very large number of static pressure taps were added to the heat exchanger core to obtain both overall flow distribution and flow distribution within the pure counterflow section. Figure 64 illustrates the large number of taps used. It is the flow distribution within the pure counterflow section that is of greatest interest and over a fairly wide series of flows it was determined that at isothermal conditions the ratio of maximum to minimum flow rate on the cold side of the heat exchanger was approximately 1.25. The ratio of the maximum to minimum flow rate on the hot side was approximately 1.45. At all of the isothermal conditions examined a prediction was made of the overall heat exchanger pressure drop and this value was compared with test data. The deviation between test and predicted values varies slightly with flow rate but at the equivalent flow rate to the design conditions (equal Reynolds numbers) the test pressure drop on the cold side of the heat exchanger is 52 percent greater than the predicted value. The hot side variation from test is 63 percent greater than the predicted. This large difference between
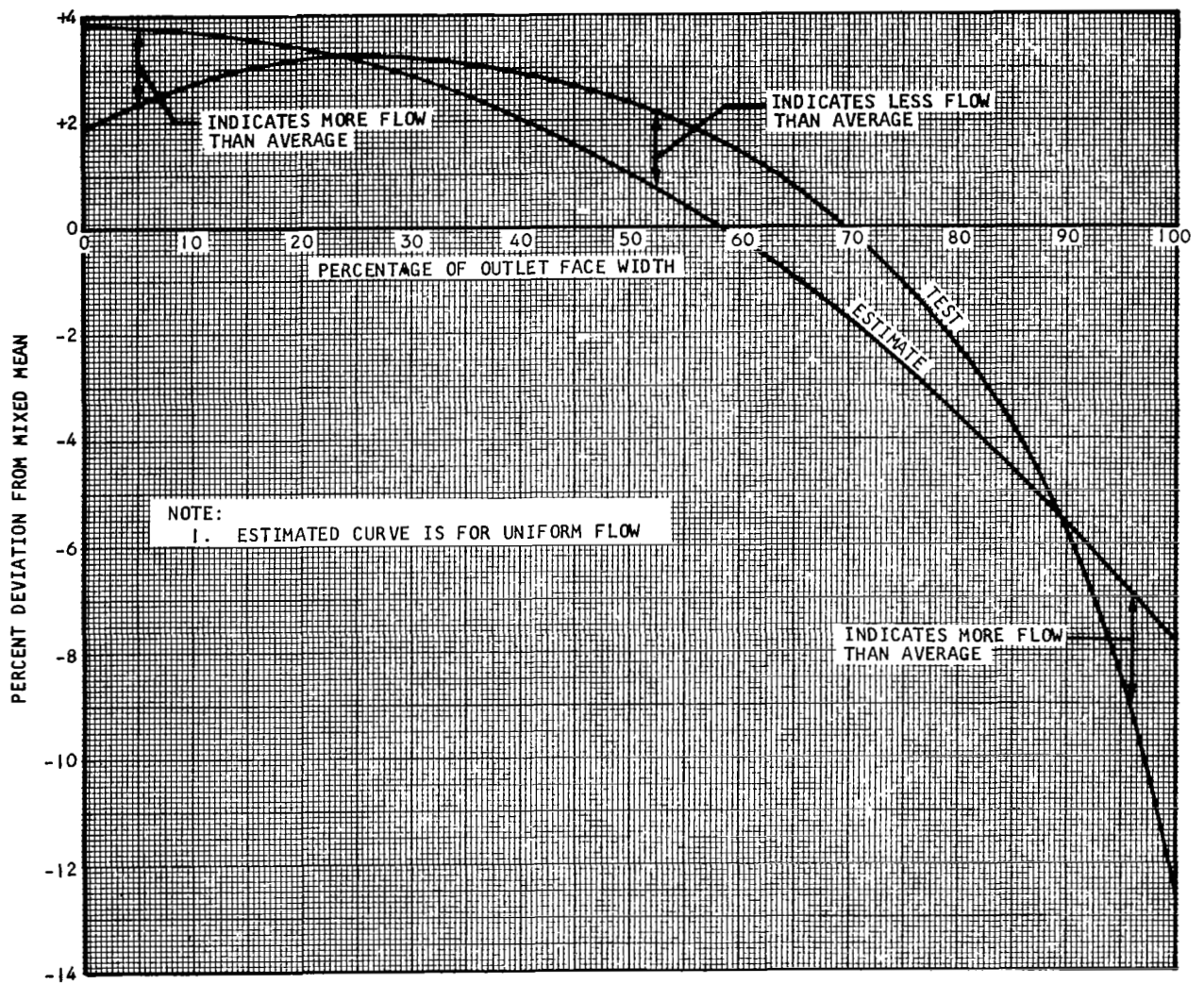
Figure 63. Cold Side Outlet Temperature Deviation From Mixed-Mean
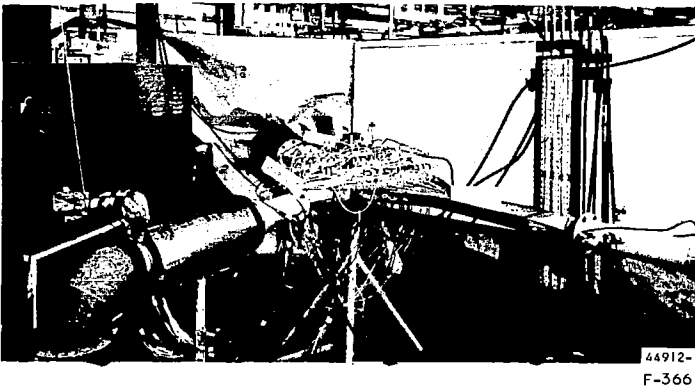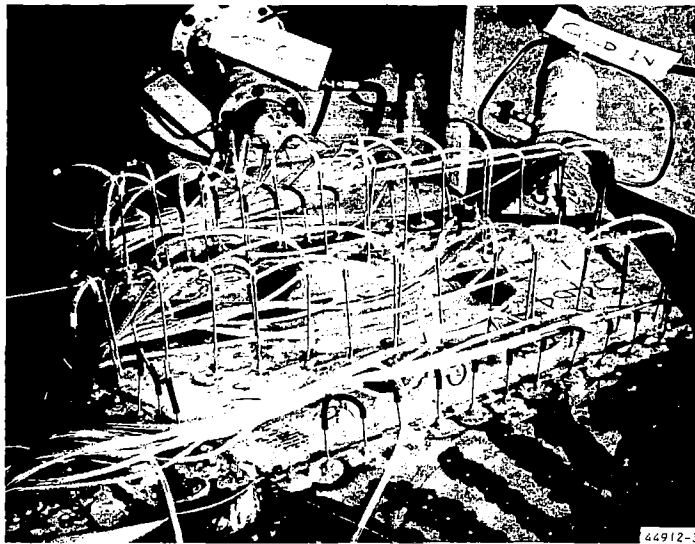
Figure 64. Heat Exchanger Flow Distribution
Test Setup

101

test and predicted values may be attributed almost entirely to non-uniform flow distribution. It is, therefore, necessary to evaluate the differences between the test and predicted values under heat transfer conditions to obtain any accurate evaluation of the design performance. As pointed out in previous reports the use of non-equal triangular shaped ends for this recuperator is desirable to obtain uniform flow distribution. The inequality in the ends compensates for the large density difference between the hot and the cold ends of the core and, therefore, when isothermal tests are run the unequal ends tend to increase the non-uniformity of flow rather than to decrease it. A careful examination was made of all pressure drop data obtained during heat transfer tests and it was determined that the deviation between predicted and test values was much lower under these conditions thus confirming the improved flow distribution. Throughout the heat transfer tests conducted the hot side inlet temperature was maintained at approximately 600°F while the cold side inlet temperature was maintained at approximately 80°F. Under these conditions the cold side pressure drop exceeded the predicted pressure drop by only 20 percent while the hot side test pressure drop exceeded the value by 35 percent. As the ratio of inlet to outlet densities during these tests is almost identical to the density ratio which occurs at the design conditions it may be anticipated that the predicted heat exchanger pressure drops will increase by these values. While every attempt was made in the design to balance the pressure drops in the triangular end sections to obtain uniform flow the practical limitations in the construction of the heat exchanger has not quite met the theoretical requirements and therefore some small amount of non-uniformity in flow distribution still exists, causing this increase in pressure loss.

SUMMARY OF FLOW DISTRIBUTION TESTS

The design of the unequal triangular ends achieved its main objective; obtainment of the required heat transfer. As stated in Section 7 the use of the unequal triangular ends resulted in a pressure loss increase from 2.0 percent to 2.6 percent. With the data obtained from the flow distribution tests the overall pressure drop for the flightweight recuperator at design conditions would be estimated to be 3.13 percent. This overall estimate of pressure loss, as with all previously discussed values includes a 0.63 percent loss for the manifolds. Owing to the careful aerodynamic design of the manifolds and from the test data obtained on the manifold tests it appears that this allowance for manifold losses is slightly generous. It is, therefore, concluded that if the flow distribution heat exchanger core configuration is extended to the flightweight recuperator design, overall pressure loss for this flightweight recuperator at flight conditions would be approximately 2.9 percent. The majority of the difference between the original design goal of 2.0 percent and this 2.9 percent is due to deliberate design changes and not to a failure of the test results meeting the predicted.

Since it was realized that this increase in pressure loss may be unacceptable to NASA further consideration was given to methods of reducing total pressure drop. These methods of reducing pressure drop together with the finally selected heat exchanger configuration are discussed further in Section 8.

SECTION 10

MECHANICAL DESIGN

CONFIGURATION CHANGES

Throughout the foregoing sections of this report various aspects of the heat exchanger mechanical design have been referred to in their relationship to the specific problem under discussion. The originally selected heat exchanger resulting from the parametric design study was a pure counterflow plate fin unit. At the time of this selection, the heat exchanger design incorporated 0.005 in. thick Hastelloy tube sheets, hollow stainless steel header bars, all nickel fins in the counterflow core and either five fins per in. or no fins at all in the triangular end sections. Through the detailed design investigations all of these parameters have changed. Detailed investigation of the axial conduction problem resulted in the replacement of the nickel fins with stainless steel. Manufacturing design investigations further revealed that the use of hollow stainless steel bars would both increase the cost of the recuperator considerably and also reduce its structural integrity. Therefore, solid bars have been used for the final design.

Perhaps the major mechanical design change between the originally selected core and the unit which to be fabricated is the change from 0.005 in. thick Hastelloy tube sheets to 0.008 in. thick stainless steel tube sheets. The original selection of Hastelloy "C" was discussed in some detail in Section 5. However, when NASA reviewed the effects of changing from Hastelloy to steel, they decided to accept the weight penalty in favor of the development cost reduction resulting from the use of the cheaper stainless steel material. As greater experience exists with the use of stainless steel, reliability is improved by the use of this material. At the time of this decision, the stainless steel plate thickness under consideration was 0.006 in. Information obtained from manufacturing studies in another program for the development of a pure counterflow plate fin heat exchanger indicated that difficulties are encountered in brazing a recuperator if thin tube sheets and low numbers of fins per in. are used in the triangular end sections. Structural and pressure considerations determine that at least 5 fins per in. should be used on both sides of the triangular end sections, but manufacturing considerations indicated that this was insufficient to produce a reliable leak tight unit. In the above referenced parallel development program, attempts were made to braze cores using 5 fins per in. in the end sections with 0.006 in. tube sheets. Where this combination was used the tube sheets were, in many cases, drawn into the spaces between the fins thus forming a wavy edge to the plate which did not result in the satisfactory braze joint between the tube sheet and the header bar in the adjacent passage. Continuing development indicated that the minimum combination to ensure satisfactory brazing was 0.008 in. thick tube sheets and no less than 10 fins per in. on both sides of the triangular end sections. This configuration was, therefore, adopted for the final unit design.

STRESS ANALYSIS OF RECUPERATOR STRUCTURE

In order to ensure that satisfactory structural integrity would be maintained in the final design unit attention was directed to two areas of

stress analysis. These two areas of analysis are pressure stresses, particularly in the manifolds, and thermal stresses.

Pressure Stresses

The first stage in the pressure stress analysis considered the original manifold designs to determine if the shapes selected for aerodynamic purposes were adequate structural designs. As a result of this stress analysis several changes were made to the original manifold configurations. Aerodynamically the outlet manifolds play little part in the determination of flow distribution. Therefore, the original box shape outlet manifolds were changed to incorporate semicircular rather than rectangular cross sections. The required aerodynamic configuration for the inlet manifolds coupled with their aspect ratios precluded the implementation of circular elements. Analysis showed that eliptical cross sections would require approximately the same external stiffening as a rectangular cross section; therefore, the optimum aerodynamic box shapes were retained. Figure 55 showed the full size actual manifolds, constructed for the flow distribution test. The outlet manifolds shown in this figure have the semicircular cross section described. The low pressure inlet manifold shown in this figure has the structural stiffening required for pressure containment while maintaining the aerodynamically ideal box configuration.

To complete the pressure stress analysis the plate fin structure was checked for stresses due to internal pressure at operating temperatures. These computed stresses were found to have a safety factor in excess of 5.0 based upon the 10,000 hr stress rupture properties of the heat exchanger material at maximum normal operating temperatures. The heat exchanger core structure was also checked for an external pressure condition of 14.7 psia at room temperature and with the appropriate design internal pressures and was found to be satisfactory.

Recuperator Thermal Stresses

The nonlinearity in temperature profile from the hot end to the cold end of the heat exchanger produces thermal stresses in the plate fin structure. In particular, each triangular section at the end of the pure counterflow core is at a nearly uniform temperature, whereas, the counterflow core is exposed to a linear temperature rise from cold to hot end. Any structure is free from thermal stresses only if the free thermal expansion of every point in the structure can be written as a linear first order function of its cartesian coordinates. Any disparity from this condition leads to a state of internal thermal stress.

Throughout the stress analysis conducted on this Brayton cycle recuperator certain assumptions were maintained and these assumptions are listed on the following page.

a. The temperature differences between fluids and metal do not cause significant stresses in the plates; or equivalently, there is no temperature variation in the stack height direction.

b. The fins do not have an appreciable effect on the plates as far as thermal stresses are concerned.

c. The counterflow core has linear temperature gradient along the flow length and no appreciable temperature gradient in the width.

The initial analysis of the two dimensional thermal stress problem involved the solution of a stress function that satisfied the bi-harmonic plate differential equation with free boundary conditions along the plate edges. This type of problem is frequently encountered by AiResearch in the manufacture of plate fin heat exchangers and consequently a computer program written in Fortran for a high speed digital computer was used to solve this problem.

Initially thermal stresses were calculated for the most extreme temperature condition of $926^{0}R$ at the cold end and $1685^{0}R$ at the hot end, which constitutes a temperature differential in the metal of $759^{0}R$. A limited amount of heat exchanger matrix restraint was also assumed. This is considerably more severe than the actual worst case. The resulting maximum equivalent stress of 34,800 psi occurs at the cold end of the unit. This stress slightly exceeds the local yield strength, which will produce a small amount of local yielding on the first cycle with no adverse effects on the fatigue life of the unit. This indicated thermal stress of 34,800 psi when compared to a yield strength of 30,000 psi will not jeopardize the cycle life expectancy of the heat exchanger. The recuperator thermal stress cycle with this peak stress valve is shown in Figure 65. With ductile materials such as stainless steel, a total stress range equal to the yield strength will produce yielding on the first cycle only. Upon returning the unit to uniform temperature a residual stress will remain in the local yielding region that will be equal to the difference between the indicated stress and the local yield strength. During subsequent cycles of usage, the residual stress will first be relieved, and the part will be exposed only to the yield stress without further plastic flow of metal, as illustrated in Figure 65. No physical damage will occur to the recuperator during the 0-1-2 portion of the first cycle or during any subsequent cycle. Brazed joints, though not as ductile, have a higher yield strength than the parent material. In all cases of destructive testing on stainless steel heat exchangers where good brazing has been obtained, failure occurs with the parent metal not at the brazed joint.

The stress analysis was continued with use of a more accurate metal temperature prediction. In this continued analysis an available AiResearch computer program "Matrix Metal Temperature" was used to determine the temperature distribution throughout the unit. This temperature distribution is shown in Figure 66. Assuming that constant fluid temperatures exist in the triangular end sections the metal temperatures of the recuperators change

DURING THE 1ST CYCLE, THE PATH FOLLOWED WILL BE 0 - 1 - 2. ON ALL
SUBSEQUENT CYCLES THE STRESS-STRAIN PATH WILL BE 2 - 3 - 2, AND THE
HEAT EXCHANGER WILL BE WELL WITHIN THE ENDURANCE STRENGTH OF THE
COMPONENT.

$(f + y)$ = YIELD STRESS

ϵ_1 = STRAIN THAT CORRESPONDS TO INDICATED THERMAL STRESS, σ_1

σ_2 = RESIDUAL STRESS = INDICATED STRESS - $(f + y)_2$
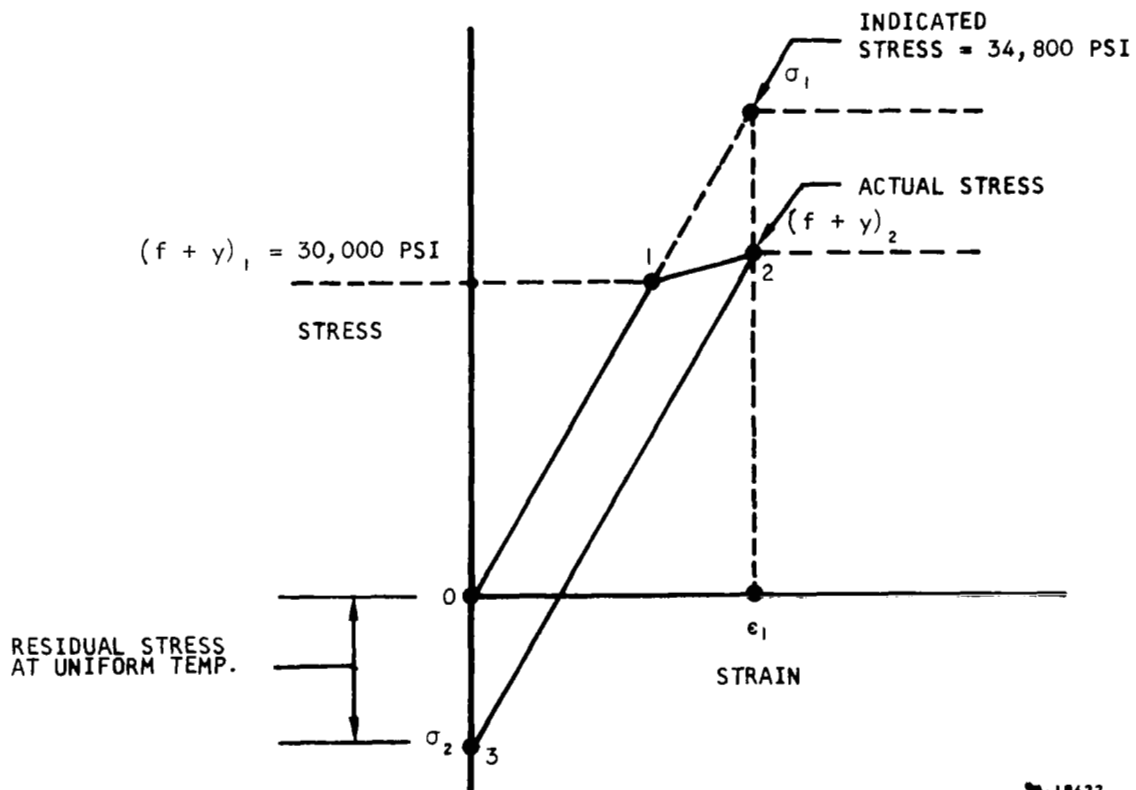
Figure 65. Recuperator Thermal Stress Cycle

NOTES:

		STRESSES LOCATION		MAXIMUM STRESS
I.	CASE I	POINT 22	σ_{MAX1}	+ 17308 PSI
	(NO CONSTRAINT)	POINT 21	σ_{MAX2}	– 16671 PSI
	CASE II	POINT 35	σ_{MAX1}	+ 84087 PSI
	(FIXED CONSTRAINT)	POINT 28	σ_{MAX2}	– 211820 PSI

2. ALL TEMPERATURES ARE °F

3. ALL DIMENSIONS ARE IN INCHES
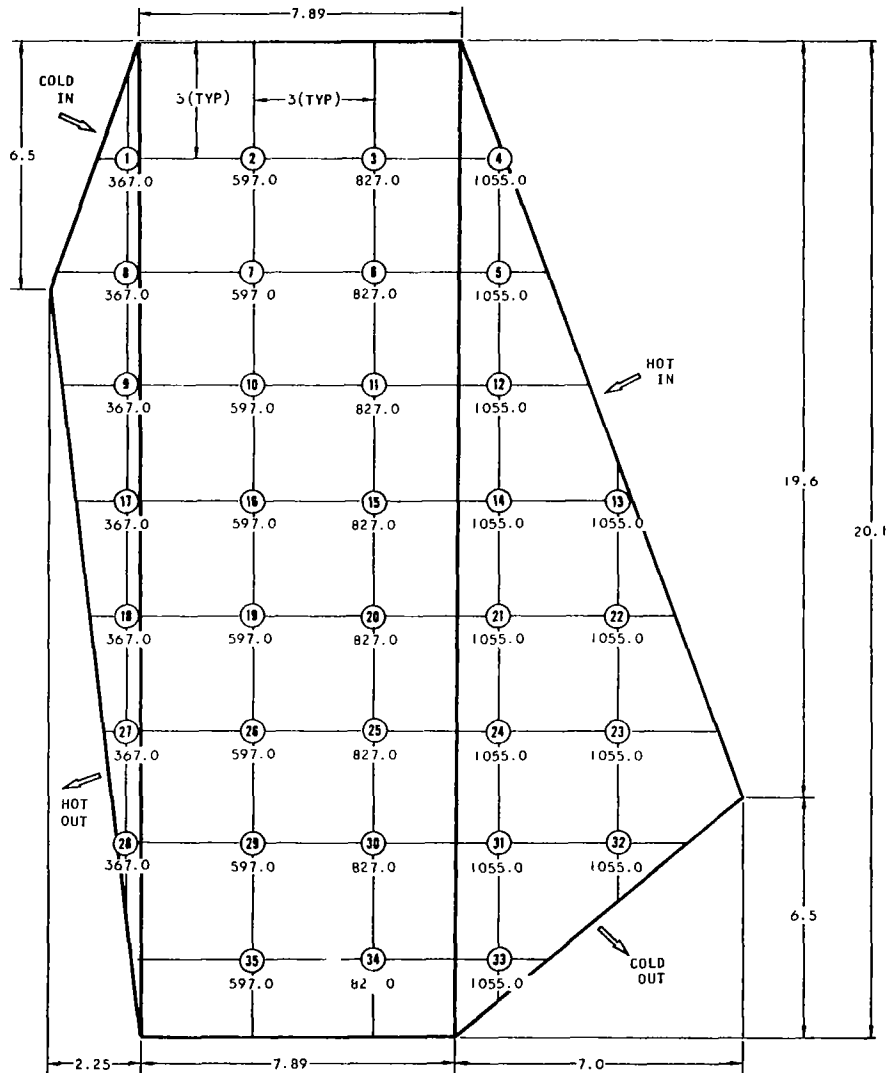
Figure 66.   Heat Exchanger Subdivisions and Resultant Temperatures

B-3552

from approximately 1055°F at the hot end to approximately 367°F at the cold end. The temperature gradients differ from point to point along the flow length. Depending upon the degree of recuperator restraint, the maximum thermal stresses resulting from this temperature distribution may be as low as 1/4 of the yield strength for no constraints or go beyond rupture point for completely fixed constraints.

From the above described temperature distribution, the two dimension thermal stress computer program was used to determine the stresses. The maximum stresses and their locations are illustrated in Figure 66 and are summarized below.

Hot End Temp, °F	Cold End Temp, °F	Yield Stress at Max Temp, psi	Rupture Stress at Max Temp, psi	Max Tensile Stress, psi		Max Compr. Stress	
				No Constraint	Fixed Constraint	No Constraint	Fixed Constraint
1055	367	46,000	60,000	+17,300	+84,000	-16,900	-211,000

As indicated by the above, where no constraints are encountered, the thermal stress is only 1/4 of the yield strength and, therefore, will cause no damage to the heat exchanger. This case is closely resembled by a heat exchanger with good expansion joints between the heat exchanger and the ducting. In the case of absolutely fixed constraints, the thermal stress is well above the rupture stress. While absolutely fixed constraint will not exist, in a heat exchanger with a large temperature gradient, plate buckling and splitting between fin and plate could occur if allowances are not made for thermal expansion. It is, therefore, recommended that no completely rigid method of mounting be used for this recuperator. Should a limited amount of restraint be used the stress will fall between the fixed and no constraint cases. This is illustrated by the values calculated in the above described preliminary stress analysis.

Summarizing the result of the stress analysis indicate that satisfactory structural integrity may be maintained throughout the recuperator providing that no fixed method of mounting is used.

SUPPORT BRACKET DESIGN AND ANALYSIS

This task required that the environmental loads specification be interpreted in relation to the method of mounting the recuperator, the location of the mount points and the loading interaction with other components through the interconnecting ducts. Hence, a careful review was made of the load specification to determine the load levels that should be used to design the brackets. The bracket locations were specified by NASA Lewis, and the first phase of the analysis was the determination of bracket reaction loads at the mount points. Next the sizing of the brackets was carried out, and this required matching the already existing recuperator structural design at the specified mount locations with respect to load intensity and load distribution. A final task that was carried out was the determination of allowable duct loads as applied to the recuperator by the interconnecting pipes.

Data was not provided regarding magnitudes and direction vectors of these externally applied forces and moments. This work was accomplished by computing the maximum permissible forces and moments that could be safely applied to the recuperator at the duct flange points without jeopardizing the ducts, support brackets or any critical part of the recuperator.

Environmental Input Loads

The environmental specification for the Solar Brayton Cycle Space Power System was used to determine applied loadings at the mount points of the recuperator. In reality the specified inputs related to a particular location in the launch vehicle, and these inputs will be greatly altered by transmission from the vehicle structure through the supporting truss structure and into the recuperator. The size, method of mounting and location of the other components in the power system will heavily influence the response characteristics of the entire power system as well as the recuperator. It will therefore be eventually necessary to conduct a similar analysis on the whole Solar Brayton Cycle Power System to determine the structural performance of the individual components and the system taken as a whole. The design and analysis approach that was employed on the recuperator bracketry has led to a realistic bracket design, and one in which the bracket strength is well matched to the overall structural strength of the recuperator. The systems work that must yet be carried out should lead to a supporting truss structure and possibly to a primary isolation mounting concept of the entire truss that will not amplify the vehicle applied loads.

On the various specified loads, the environmental conditions due to manufacture, storage and transportation do not influence the bracket design. The launch, lift-off and boost forces produce the major loads on the recuperator and therefore the brackets. A rigid load transmission from the vehicle structure to the recuperator mount points was assumed to be the most logical starting point in the design. The following text was taken directly from the Environmental Specification No. P0055-I (Revision A - June 19, 1964), which was supplied as part of Modification 5 to Contract No. NAS3-2793 (The paragraph numbers shown below are those written in the specification).

2.2 Launch, Lift-Off, Boost

The nonoperating system and components shall be capable of withstanding without performance impairment the following simultaneous launch loads applied at the system mounting points and in the directories and magnitudes specified:

2.2.I Shock

35 g shock along each of three mutually perpendicular axes within one of the following wave shape and pulse times -

Triangular pulse of IO milliseconds. Half sine pulse of 8 milliseconds. Rectangular pulse of 5 milliseconds.

2.2.2 Vibration

Sinusoidal input applied at the system mounting points along each of three mutually perpendicular axes

16 - 100 cps	at 6 g peak
100 - 180 cps	at 0.018 in double amplitude
180 - 2000 cps	at 19.0 g peak

2.2.3 Acceleration

The nonoperating system and/or each of its components shall be capable of withstanding each of the following combinations of longitudinal and lateral accelerations for five minutes duration each.

2.2.3.1 Max Q - 2 g's longitudinal and 0.25 g's lateral

2.2.3.2 Max boost acceleration - 4.6 g's longitudinal and no lateral acceleration. The longitudinal accelerations are positive along the vehicle lift off axis. No negative longitudinal acceleration will be experienced during the launching phase.

2.2.3.3   4.5 g - all directions in plane normal to lift off axis.

The effects of acoustic noise will not be consequential because the recuperator will be an interior component that will be isolated from the acoustic effects by the surrounding vehicle shell structure. The orbital operation will also produce shock, vibration and acceleration loads, but these are very small compared to launch, lift-off and boost effects, and they do not influence the structural design of the recuperator or its support brackets.

Environmental Applied Recuperator Loads

The possibility of hard mounting the recuperator to the supporting truss structure was considered first. The calculations of loads applied to the recuperator, and the structural analysis of the bracket mounts are shown in an appendix to this report entitled "Stress Analysis of Recuperator Mounting and System Integration of Solar Brayton Cycle Space Power System." Since amplification factors due to vibratory inputs are generally as high as 10 to 1 at resonance and frequently 20 to 1 or higher, the minimum reasonable design loading would be 10 x 6 g's = 6 g's (provided the fundamental resonant frequency does not exceed 100 cps. Adding to this the direct transmission of 35 g's shock and approximately 5 g's acceleration, the total g load on a hard mounted unit would be 100 g's. Then further assuming that only two of the support brackets would carry load under lateral loading (this requirement is a direct result of the need for providing for free thermal expansion of the

110

recuperator), the load applied to each bracket would exceed 25,000 lb. This would be combined with longitudinal loads in excess of 15,000 lb. These localized loads exceed the structural capability of the recuperator plate-fin structure in the region of the specified bracket locations. Even if the brackets were located in the most favorable mount positions, it would present a very serious design problem. In summary the design difficulty arises due to a combination of effects related to the structural limitations of this type of component and the extremely severe environmental loads.

It was concluded that an isolation mounting system would be mandatory to preserve the structural integrity of the recuperator, and that this could reduce loads at the recuperator brackets to tolerable values. Acutally the entire system will require soft mounting because other components in the system such as the turboalternator are much more sensitive to shock and vibration inputs than the recuperator. The soundest design concept would be to isolation mount the entire system rather than providing individual isolation mounting of system components. This would eliminate the potential problem of large relative displacements between components.

The isolation mounts will have to be designed to accommodate loads and displacements due to both shock and vibratory inputs. Isolation is obtained by designing the resonant frequency of the mounted system to fall in the low input portion of the frequency-load specification. For the purposes of vibration input, a natural frequency of 70 cps or less would be acceptable. The 70 cps is sufficiently well removed from the increased inputs above 100 cps to keep the maximum applied loads on the recuperator within the 6 g inputs specified for frequencies up to 100 cps. The shock load pulses called out in the specification will require mounting system frequencies less than 30 cps to obtain some degree of isolation from the shock loads. Progressively greater shock isolation is attained when the resonant frequency of the mounting is lowered, but this necessitates that provisions be made to accommoate the large relative displacements between the mounting structure and the system components. It was determined that a system mounting frequency of 10 cps would satisfy the various problem sources cited above, and that displacement requirements would not exceed 2 inches. It was assumed that the specification cut-off point of 16 cps was not entirely realistic, and that it would be more reasonable to consider the vibratory input level of 6 g's to apply to the 10 cps frequency. For the soft mounting concept to be effective, it must also provide adequate damping to prevent excessive amplification at the resonant frequency. A damping coefficient equal to 20 percent of critical damping was assumed which would limit the amplification factor at resonance to 2.5 to 1. The shock isolation factor was also determined to be 0.3 for the three different shock pulse wave forms delineated in the specification. Hence the total load factor for combined vibration, shock and acceleration is:

Vibration	6 g x 2.5 =	15 g
Shock	35 g x 0.3 =	10.5 g
	4.5 g x 1.0 =	4.5 g
		30 g

A 30 g load vector in the vehicle longitudinal axis will be combined with a 30 g load vector in the lateral direction to establish the maximum loading on each of the four support brackets.

Support Bracket Reactions

Loads due to unit 1 g vectors at the four brackets were computed for the longitudinal vehicle axis and for each of two orthogonal transverse axes. The nomenclature for these three axes as related to the recuperator orientation in the launch vehicle is shown below:

Recuperator width axis	x_1 (transverse)
Recuperator depth (no flow)	x_2 (transverse)
Flow axis (vehicle longitudinal)	x_3

The four bracket stations have been denoted as brackets S_1, S_2, S_3 and S_4. The recuperator duct locations, reference coordinate axes and the support bracket locations are depicted on Figure 67. The supports provide full restraint for applied loads and thermal freedom of expansion by utilizing the following design approach:

Bracket S_1	Slotted hole in the x_1 direction. This bracket provides support for longitudinal forces and for the x_2 traverse axis.
Bracket S_2	Full restraint in all directions. This becomes the reference point for all thermal expansions.
Bracket S_3	An oversize hole. The bracket supports vertical loads, but it provides full thermal growth freedom in the x_1 and x_2 axes.
Bracket S_4	Slotted hole in the x_2 direction. This bracket provides support for longitudinal vehicle forces and for loads in the x_1 transverse axis.

A tabulation of vector load diagrams on each of the four brackets due to combined longitudinal (x_3 axis) with each of the two transverse axes is shown in Table 7.

Bracket Stress Analysis

The detailed stress analysis and design approach is shown in Appendix E. The design problem was primarily one of determining bracket height, width and permissible overhang dimensions that would keep the load intensity on the recuperator plate fin structure within safe limits. The limiting loading on the fins was determined to be 250 psi compressive crushing force to

DUCT A - HIGH PRESSURE INLET (COLD)
DUCT B - LOW PRESSURE INLET (HOT)
DUCT C - LOW PRESSURE OUTLET (HOT)
DUCT D - HIGH PRESSURE OUTLET (COLD)
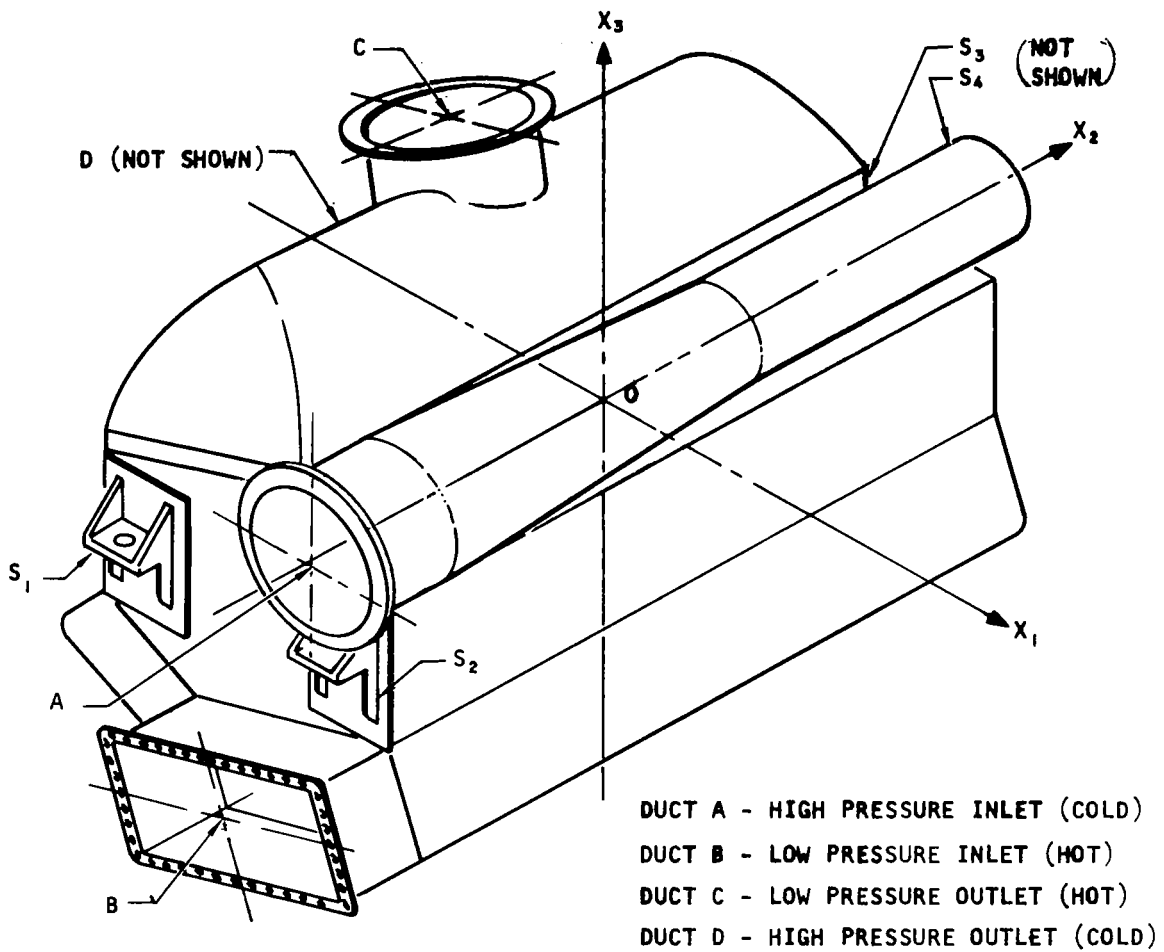
A-26374-A

Figure 67.   Duct and Support Locations on Recuperator

113

TABLE 7

LOAD RESULTANTS

Support Station	CASE 1 30g LONG. + 30g IN X_1 AXIS	CASE 2 30g LONG. + 30g IN X_2 AXIS
S_1	X_3 X_2 $F_3=6290$ LB $F_2=218$ LB $F_1=0$ X_1	X_3 X_2 $F_3=5710$ $F_2=9070$ $F_1=0$ X_1
S_2	X_3 X_2 $F_3=3430$ $F_2=218$ $F_1=9680$ X_1	X_3 X_2 $F_3=4530$ $F_2=8870$ $F_1=326$ X_1
S_3	X_3 X_2 $F_3=5510$ $F_2=0$ $F_1=0$ X_1	X_3 X_2 $F_3=4410$ $F_2=0$ $F_1=0$ X_1
S_4	X_3 X_2 $F_3=2690$ $F_2=0$ $F_1=8260$ X_1	X_3 X_2 $F_3=3270$ $F_2=0$ $F_1=326$ X_1

114

prevent fin buckling. A doubler plate of 0.100 in. thickness was determined
to be needed to reinforce the 0.040 in. thick side plates. A bracket base
plate size of 6 in x 8 in was required to attain the required design limita-
tion on fin crushing force. The analysis was based on a beam on an elastic
foundation calculation, and the details of these computations are provided
in the appendix. The bracket base plate thickness was established as 3/16 in.
to provide a rigid load foundation for transmission from the mount points to
the recuperator side plates. Side gusset plates of 3/16 in were used as well
as a reinforced mounting plate of 3/8 in. to provide structural continuity
and to obtain satisfactory stress levels.

Allowable Duct Loads

The ducting interconnections between the recuperator and the rest of the
system will be a source of loading at the duct flange points, and this will
in turn produce loads at the support brackets. The ducting will require
adequate flexibility to provide for thermal growth of the system components
and the ducting itself after system start-up. Since the system layout design
has not been firmly established to date, it is desirable to provide flange
load limitations based upon the structural strength of the recuperator. It
will then eventually be necessary to apply these loads as design constraints
on the interconnecting ducting design. The assumptions form the basis of
calculations of the limiting duct flange loads:

1. System start-up and operation does not coincide with launch and
    lift-off.

2. Pressure forces at the flange points will be due to a maximum
    pressure differential of 13 psi.

3. The interconnecting ducts will be self sufficient for launch and
    lift-off loads, i.e. long pipe lengths or heavy valves must not
    rely upon the flanges for their sole source of support.

4. Flexibility in the form of expansion joints or pipe expansion loops
    must be provided in the interconnecting ducts to control flange
    loads induced by thermal expansion.

5. The allowable loads determined are limitations that the recuperator
    can withstand. If these loads are reflected back into the system,
    they may exceed the capability of other system components. In this
    event the limitations will be established by these sensitive com-
    ponents, and they will be lower than recuperator capability.

Figure 67 showed the duct locations. The limiting stress of the ducts
was taken to be the 10,000 hour rupture stress for Type 347 stainless steel
at 1250°F with a safety factor of 2. Simultaneous bending and torsional
loads were assumed to occur at the flange points. This allowed calculation
of the permissible bending and torsional moments at each duct flange.

The limiting axial force at each duct was determined from the maximum pressure differential multiplied by the duct area. To make an allowance for the possibility of oversized bellows in each duct the pressure force was increased by 50 percent to arrive at air upper bound limitation. Since allowable shear stresses are generally 35 - 60 percent of the allowable direct stresses, the permissible shear load at each flange was taken to be equal to 60 percent of the direct load. Concurrent application of these loads at the duct flange points was used to determine the support bracket reactions. The support loads were found to be much lower than the launch and lift-off forces. The allowable loads and moments are shown in Table 8.

TABLE 8

ALLOWABLE DUCT FLANGE LOADS

Duct Location (See Fig. 71)	Effective Diameter, in.	Allowable Moments		Allowable Forces	
		Bending, lb-in.	Torsion, lb-in.	Direct, lb	Shear, lb
A	6	5100	5100	550	330
B	11.7	19,500	19,500	1400	840
C	8	9060	9060	650	390
D	6	5100	5100	550	330

RECUPERATOR 180636 FABRICATION

The overall configuration of the final recuperator is shown on AiResearch Drawing 180636 included with this report. The physical appearance of the manifolds and mounting brackets is clearly illustrated in Figure 68.

The final recuperator selected for the Solar Brayton Cycle System is a pure counterflow plate-fin heat exchanger. This type of unit is constructed of multiple-brazed sandwiches of plates and fins. The flow configuration chosen for this application results in a rectangular counterflow center section and two triangular end sections to permit entry and exit of the two gas streams from the same face. Although the fins in each section may be different each plate is shaped to cover bo ' :riangular ends and the center section. All stainless steel constructic ι. used for this unit and the plate thickness used is 0.008 in. while the fin thickness throughout is 0.004 in. The fins used for the hot argon flow in the counterflow core have 12 fins per inch with a height of 0.178 in. The cold argon fins in the counterflow core have 16 fins per in. with a height of 0.153 in. Both these fins are offset periodically in the flow direction for improved heat transfer. The fins used in the triangular end sections on both sides are plain rectangular and they have

1. All dimensions for installation purposes only.
   Tolerances to be ± .06; angles ±1°.
2. Shipping covers are provided for all openings.
   Remove only at time of installation.

6.01
5.99 dia   46°06'

High pressure
(cold) outlet

Heat sink heat exchanger
181168 (ref)

17.18

Low pressure
(hot) outlet

8.01
7.99
dia   8°17'

8.60

Low pressure
(hot) inlet

Low pressure
(hot) inlet

8.01
7.99 dia

High pressure
(cold) inlet

3.50

5.20

Starting dimension line
(edge of sideplate)

Nameplate (ref)

Starting dimension line
(corner of sideplate)

6.01
5.99
dia

5.66

18.07

3.93   29.43

40.46
High pressure
(cold) outlet   over sideplates

Low pressure
(hot) outlet

High pressure
(cold) inlet

20.23
(typ)

48.40

68.40

Recuperator outline, Brayton cycle 180636

117
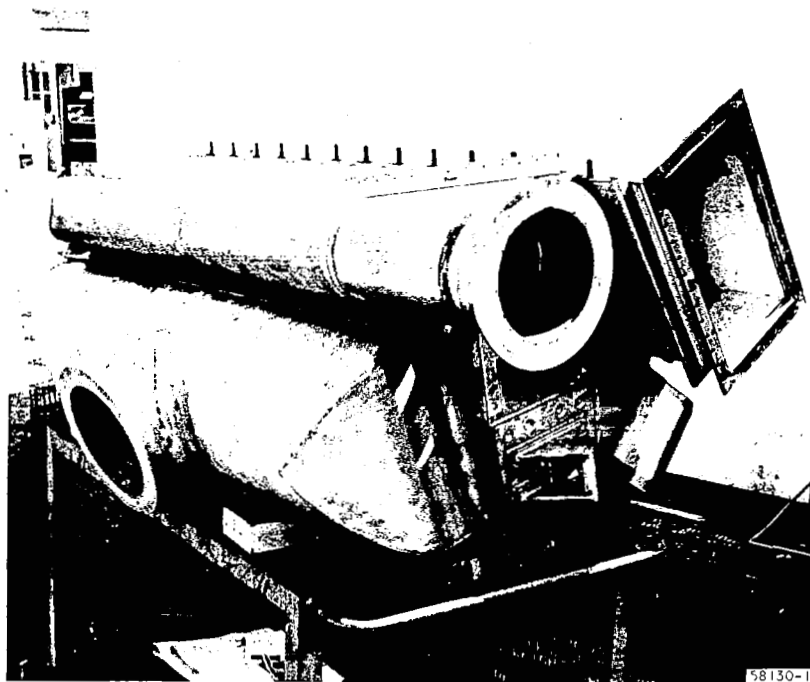
Figure 68.   Final Recuperator 180636

58130-1

F-6541

10 fins per inch. The tube plates and header bars (which provide closure of the sandwiches) are coated with a nickel base braze alloy prior to stacking. The individual plates, fins and bars are then stacked in a fixture which remains integral with the core through brazing. The core is pressure loaded through the fixture to maintain pressure in the stack height dimension during brazing.

The final configuration of the recuperator is a face aspect ratio of 2.25 which results in a width of 17.5 in. and a total stack height of approximately 39.7 in. The counterflow center section has a flow length of 7.89 in. while the overall length of the core is 14.94 in. (one 5 in. high triangular end and one 2.05 in. high end). With this large stack height the core is brazed in three separate modules as illustrated in Figure 69. This figure also shows the mounting bracket provisions which are brazed to the core sides.

Final assembly of the heat exchanger first welds the three cores together; then adds the four manifolds and the mounting brackets. The basic cylindrical configuration of three of four manifolds avoids the requirement of any additional support structure. The supporting ribs used on the rectangular shaped hot side (low pressure) inlet duct are shown in Figure 68.

START-UP RECOMMENDATIONS FOR THE RECUPERATOR

The recuperator proper (i.e., plates, fins, header bars and pans) is fabricated of material gauges which are compatible; thusly, severe temperature gradients which might result in excessive thermal stresses are inherently avoided.

The mounting brackets, however, which were designed to meet NASA specified launch and flight environmental loads, are fabricated of substantially heavier material. This disparity in metal thickness, though perfectly suitable for slow start-up machines such as this Brayton cycle system, requires that certain precautions be exercized during start-up in order to avoid thermal stress problems. Previous analyses on similar heat exchangers, combined with actual test and operational experience, indicate that safe operation of this recuperator is assured if the temperature difference between the recuperator and bracket extremities does not exceed 200°F.

An analysis was performed to determine the required start-up characteristics. Based on this analysis, it is recommended that during system start-up the gas temperature should be increased in 100°F increments and a minimum time of 25 min be allowed between step increases. The analysis which indicated the 25 min time period assumes that the argon design point flow will be passing through the unit throughout the start-up period. The analysis also assumes that only the mass of the brackets is being heated. If these brackets are attached to much a larger mass without thermal insulation, the time for temperature stability is increased. To ensure safe operation, regardless of mounting arrangement and temperature increase, it is suggested that thermocouples be attached to the core and brackets, and the temperature difference between the two kept below 200°F at all times.

58073-1
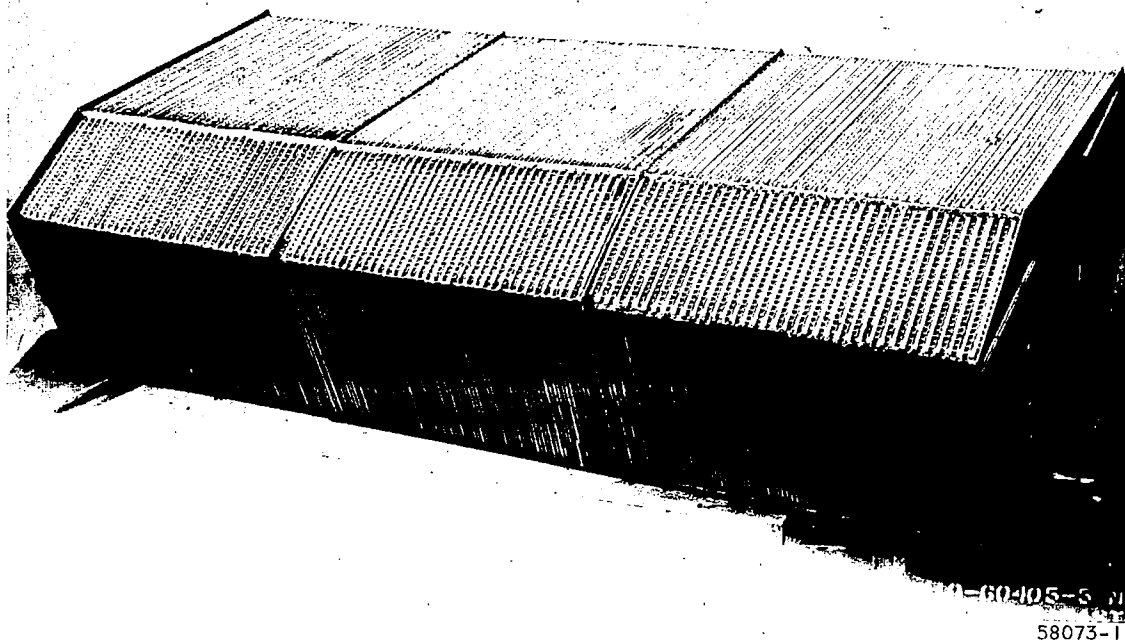
Figure 69. Three-Module Core

SECTION 8

PRESSURE DROP REDUCTION STUDIES
AND FINAL DESIGN SELECTION

The results of the flow distribution test described in Section 6 provided a complete evaluation of the preliminary selected heat exchanger design. The summary of the results of this test program is given in Figure 70. This summarizing figure shows that while satisfactory heat transfer performance was achieved the final design test pressure drop was considerably greater than the design goal of 2.0 percent. It must be emphasised that the majority of this difference is caused by design changes rather than by variance from the prediction. Owing to this considerably greater pressure drop than the design goal AiResearch conducted a brief study to determine methods of reducing this pressure drop.

PRESSURE DROP STUDIES

There are various methods available to reduce the overall pressure drop in this type of recuperator. The most obvious method of obtaining this reduction is to simply increase the size of the heat exchanger core to reduce the pure counterflow core losses. Associated with the increase in heat exchanger size is a definite weight penalty. Other methods which may be considered are to change the aspect ratio of the pure counterflow section face area. In this instance no pressure loss or weight changes are encountered in the pure counterflow section, however, substantial reductions in pressure loss can be achieved in the triangular end sections. Further extension of this reduction in triangular end section losses is the use of a split end design illustrated in Figure 71. Each of these possibilities was investigated and the results of the candidate designs are summarized in Table 9.

For each of the three different aspect ratio designs shown in this table, two solutions are presented. The difference between these two solutions is in the degree of pressure drop unbalance allowed between the hot and cold ends of the recuperator. As stated in Section 4 and Section 6 the recuperator design utilizing unequal size triangular end sections was derived to provide the most uniform flow distribution within the heat exchanger. However, to obtain this uniform flow distribution, penalties were paid in increasing the pressure losses in the cold end triangle. To avoid confusion in the definition of hot and cold ends Figure 72 is included. From the investigations conducted to provide uniform flow distribution it was decided that some degree of pressure drop unbalance would be acceptable to obtain lower pressure drops. This compromise in pressure drop unbalance for the reference design is illustrated in the table. If the best possible pressure drop balance is obtained between the hot and cold triangles the estimated overall pressure loss for the heat exchanger is 2.836 percent. In the actual reference design selected a unbalance

HEAT TRANSFER

Figure data includes:
- DESIGN POINT REYNOLDS NUMBER
- ESTIMATED AT TEST CONDITIONS

NOTE:
○ DATA WITH DUCT LOSS CORRECTIONS
▲ DATA FROM TRAVERSING THERMOCOUPLES

AIR FLOW, LB PER MIN

A-15248
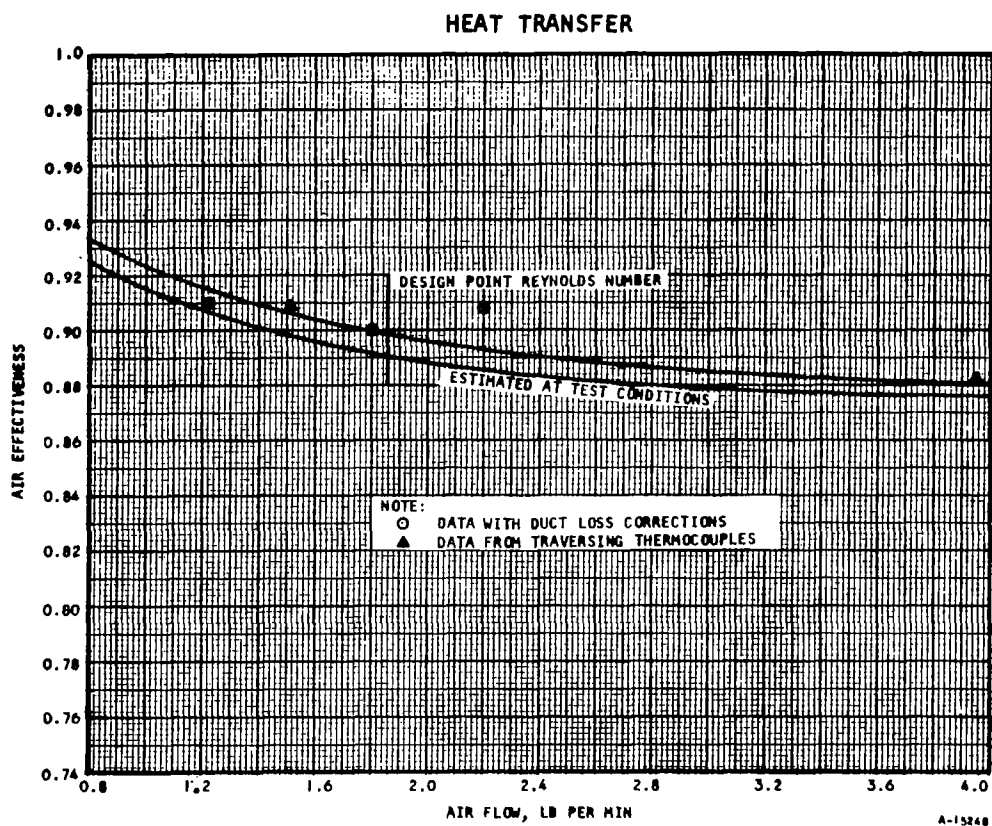
PRESSURE DROP

	PREDICTED %	TEST %
HOT SIDE (LOW PRESS)		
COUNTERFLOW CORE	0.5	
TRIANGULAR END SECTIONS	0.422	
OVERALL CORE	0.922	1.245
COLD SIDE (HIGH PRESS)		
COUNTERFLOW CORE	0.202	
TRIANGULAR END SECTIONS	0.839	
OVERALL CORE	1.041	1.25
MANIFOLDS	0.628	0.4
OVERALL ΔP	2.591	2.895

COLD SIDE OVERALL CORE LOSSES INCREASE BY 1.2
HOT SIDE OVERALL CORE LOSSES INCREASE BY 1.35

Figure 70. Comparison of Predicted and Test Performance

122
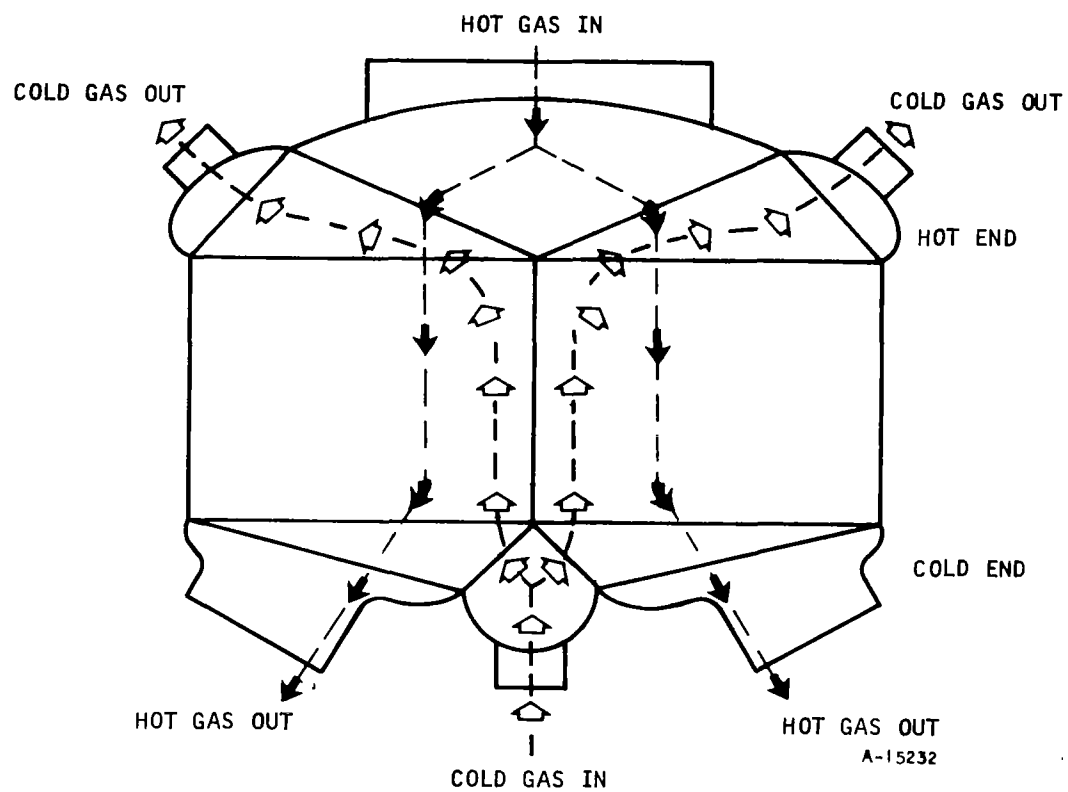
Figure 71. "Split End" Recuperator Configuration

TABLE 9

SUMMARY OF RECUPERATOR PRESSURE DROPS

Counter Flow Core Dimensions (Width x Stack Height x Flow Length) in.	Face Aspect Ratio	End Section Heights		Degree of Pressure Drop Unbalance *	Effectiveness	Pressure Drop		Weight lb
		Hot	Cold			Predicted	Test**	
		in.				Percent		
26.1 x 26.1 x 7.98	1.0	7.0	2.25	Approx 30%	0.9	2.591	2.865	392
26.1 x 26.1 x 7.98	1.0	4.0	2.0	Best	0.9(+)	2.836	3.214	359
17.6 x 39.6 x 7.98	2.25	5.0	2.05	Approx 30%	0.9	2.092	2.286	388
17.6 x 39.6 x 7.98	2.25	3.0	1.5	Best	0.9(+)	2.380	2.640	360
13.05 x 52.2 x 7.98	4.0	5.0	2.0	Approx 30%	0.9	1.863	1.994	381***
13.05 x 52.2 x 7.98	4.0	3.5	1.6	Best	0.9(+)	1.951	2.117	360***

NOTE:

1.   *For flow distribution, end section pressure losses (hot to cold) should be balanced. "Best," indicates the best balance which may be achieved. "Approx. 30%," indicates the degree of unbalance accepted to reduce pressure drop.

   **Based on results of both heat exchanger core and manifold tests.

   ***For split end configuration, would increase by approximately 10 lb for 4.0 aspect ratio face.

2.   All weights based on 0.008 in. plates, 0.004 in. fins and solid header strips.

3.   (+) after effectiveness, indicates that with the better flow distribution (pressure drop balance) slightly higher effectiveness may be achieved.

COLD OR HIGH PRESSURE
ARGON OUT
(TO ABSORBER)

HOT OR LOW PRESSURE
ARGON IN
(FROM TURBINE)

7 IN.   HOT END
OF CORE

26.1 IN.

7.9 IN.

COLD END OF
CORE   2.3 IN.

COLD OR HIGH PRESSURE
ARGON IN
(FROM COMPRESSOR)

HOT OR LOW PRESSURE
ARGON OUT
(TO RADIATOR)
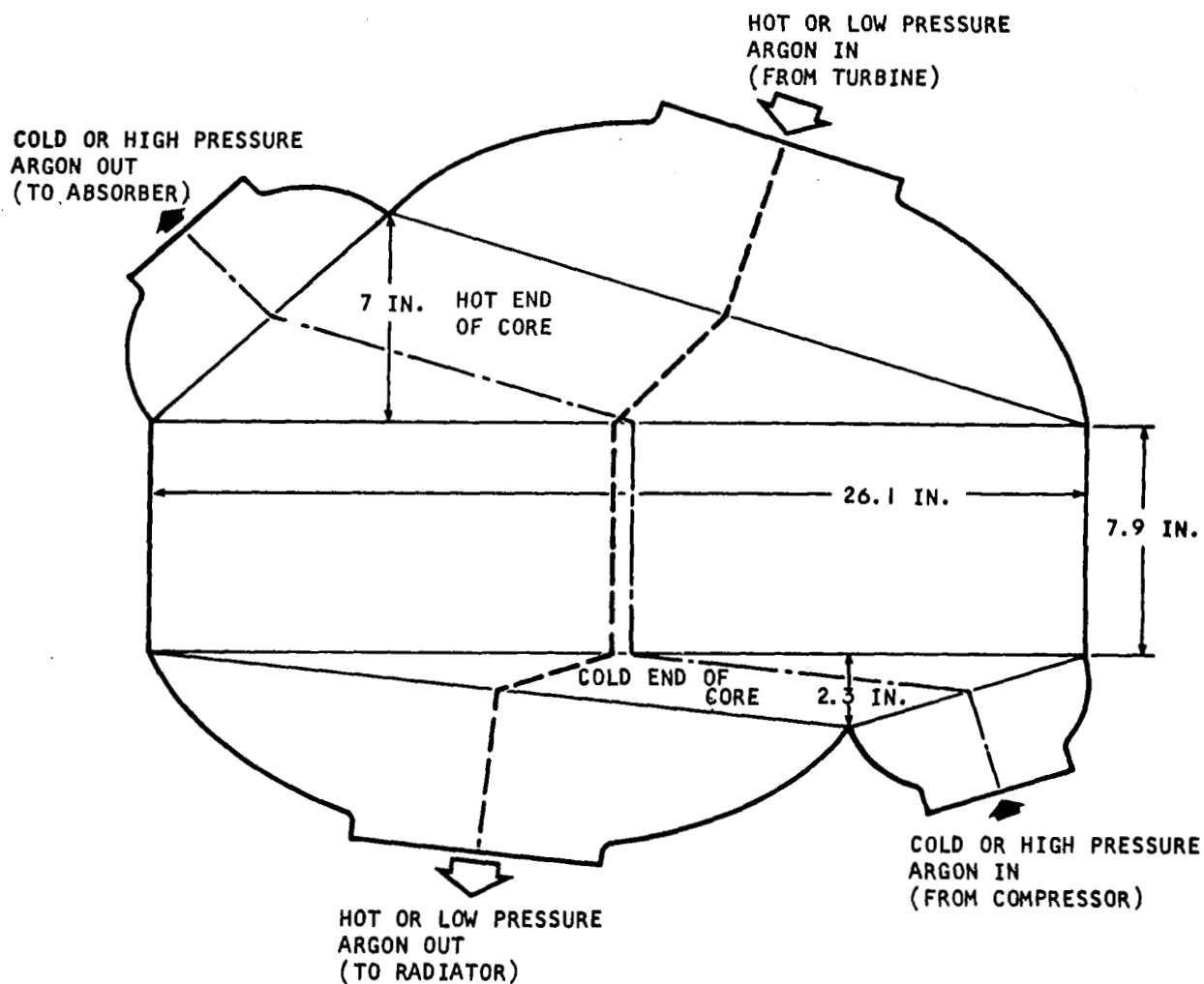
A-14756

Figure 72. Recuperator Flow Schematic

of approximately 30 percent was selected and this reduced the overall pressure losses to 2.591 percent. This compromise was obtained by increasing the heights of both triangular ends, as shown in the table. A slight weight penalty was also accepted to achieve this lower pressure drop.

As clearly indicated by the test results this degree of pressure drop unbalance in the reference design still permitted the achievement of the required 0.9 effectiveness. Consequently, as the heat exchanger configurations were varied, solutions were determined for both the best possible pressure drop balance and for the same degree of unbalance used in the reference design.

In addition to the candidate designs shown in Table 9 consideration was also given to decreasing the pressure losses in the pure counterflow section of the core. Core designs were prepared which reduce the pressure losses in the counterflow core from the present value of 0.71 percent to 0.42 percent and to 0.28 percent. It was determined that to reduce the overall pressure losses to 2.0 percent by simply allowing the counterflow core to increase in size, the counterflow core pressure drop should be approximately 0.35 percent. This approach should not be considered as a realistic method of obtaining the required reduction in pressure drop as a very substantial weight penalty is associated with this change. From the designs prepared it is estimated that the weight penalty involved in this type of change would be from 100 to 150 lbs.

An examination of the information presented in Table 9 clearly indicates that in order to reduce the overall pressure drop to 2.0 percent the aspect ratio of the pure counterflow core face must change from 1.0 (square face) to a value of approximately 4.0 (approximately 13 by 52 in.). A second means of obtaining this reduced pressure drop is the use of the split end design, which is essentially the same as the 4.0 aspect ratio with two halves of the core placed side by side. The 4.0 aspect ratio introduces manifold flow distribution problems and would also result in a less convenient packaging configuration. Attention is, therefore, drawn to the solution with the aspect ratio of 2.25 percent (counterflow face dimensions of 17.6 by 39.6 in.). Utilizing the data available from the test program the overall pressure loss of this configuration is estimated to be approximately 2.3 percent. There is no weight penalty involved in this design, in fact, a small weight reduction is achieved and the face dimensions of this core should not increase the manifold flow distribution problems appreciably.

FINAL DESIGN SELECTION

At the conclusion of the above described pressure drop studies, Table 9 was presented to NASA and it was recommended that final selection be the third solution on this table. This is a heat exchanger core with a face aspect ratio of 2.25 and with an overall pressure loss, based on the results of the test program, of 2.286 percent. The estimated weight of this unit is 388 lb and it has the same degree of pressure drop unbalance used in the flow distribution test unit. A breakdown of the predicted and test pressure losses for this finally selected configuration are given on Table 10.

TABLE 10

PRESSURE LOSSES FOR FINAL RECUPERATOR CONFIGURATION

	Predicted %		Test* %
Hot Side (Low Pressure)			
Counterflow core	0.5		
Triangular end sections	0.348		
Overall core	0.848	0.848	1.144
Cold Side (High Pressure)			
Counterflow core	0.198		
Triangular end sections	0.419		
Overall core	0.617	0.617	0.742
Manifolds	0.628	0.628	0.4
Overall Heat Exchanger		2.093	2.286

*Change in pressure losses from predicted to test based on data from flow distribution test program described in Section 6.

This was, in fact, the unit selected by NASA. AiResearch Drawing 180636 shows the overall dimensions of this finally selected heat exchanger. This outline drawing is included with this report.

SECTION 9

RECUPERATOR ACCEPTANCE TEST

The final task, as required contractually, was the performance of a limited acceptance test on the final configuration recuperator. The overall configuration of the final recuperator was discussed in Section 8. The purpose of the acceptance test was to obtain information on the overall heat transfer performance capabilities of the recuperator and to determine the overall pressure losses at equivalent design pressure and gas flow rate and at 1/2 and 2 times the design point.

TEST SETUP

The test setup for the heat transfer performance test is shown schematically in Figure 73 and photographically in Figure 74.

The test setup on the hot side included a hot air source, a flow regulating valve, laboratory inlet and outlet ducts, a mixing box and a back pressure valve. The test setup on the cold side included an ambient temperature air source, a flow regulating valve, inlet and outlet laboratory ducts, a mixing box and a back pressure valve.

The air flows were measured by calibrated orifice measuring sections, upstream of the heat exchanger. Pressures were measured by manometers and pressure drops by inclined manometers. Temperatures were measured by thermocouples, connected to a direct reading potentiometer. Four thermocouples were placed at the hot side inlet and four at the outlet and two thermocouples were placed at the cold side inlet and two at the outlet. The unit outlet temperature was calculated by adding the mixing box temperature loss to the mixing box outlet temperature. Mixing boxes were necessary to use in this testing since the unit outlet temperature is not uniform, inherent to the triangular end section design, and even a number of thermocouple readings would not be sufficiently accurate to obtain the mixed mean outlet temperature of the unit.

The pressure taps and the thermocouples were located two inches upstream and four inches downstream of the unit inlet and outlet flanges, respectively.

The test unit was insulated with Refrasil insulation as shown on Figure 74.

The test setup for the isothermal pressure drop tests was identical with that of the performance tests except only one side of the test unit was in operation at a time. The pressure drops for the isothermal pressure drop tests were measured by micromanometers.

TEST PROCEDURE

The recuperator was placed in the test setup and was subjected to the performance tests. The test conditions at representative test points are shown on Table II.
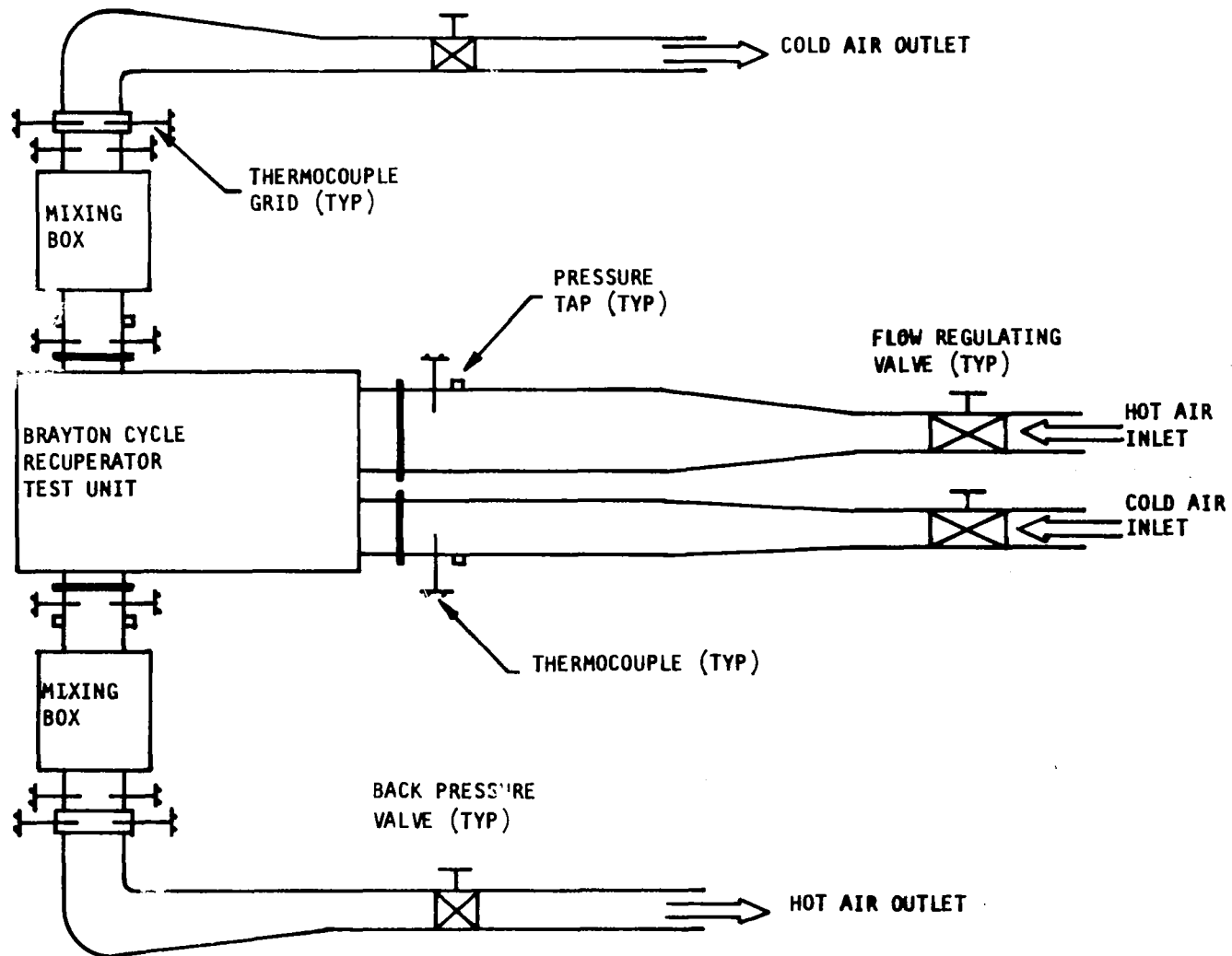
Figure 73.   Schematic Diagram, Heat Transfer Performance Test Setup
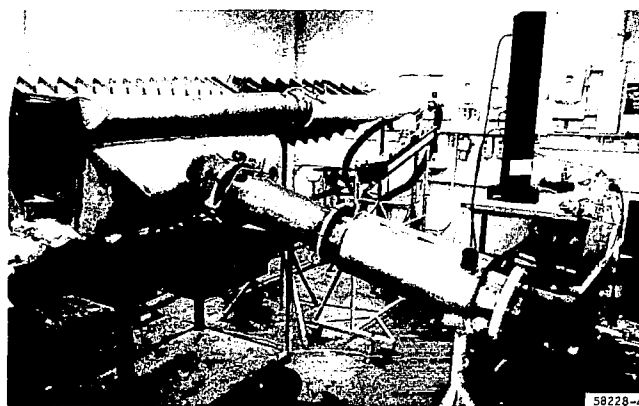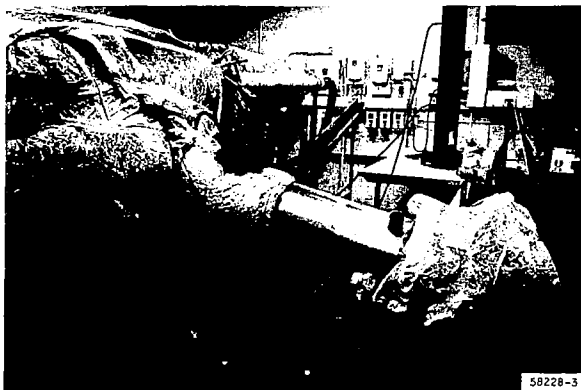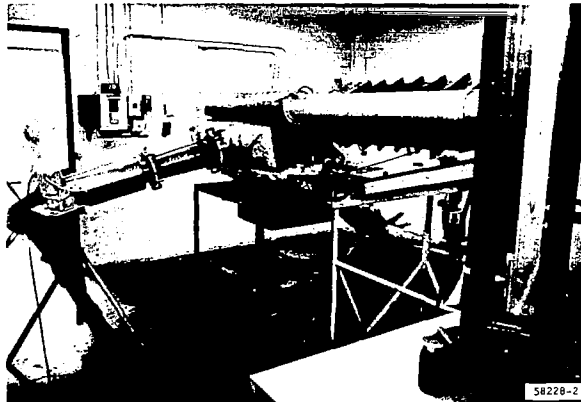
Figure 74.   Performance Test Setup

F-6435

130

TABLE 11

SAMPLE TEST CONDITIONS

		Run Number		
	207	404	405	408
Hot Flow, lb per min	23.7	11.1	46.5	22.9
Cold Flow, lb per min	22.5	12.0	45.5	23.4
Hot Inlet Temperature, $^\circ$F	644	629	653	811
Cold Inlet Temperature, $^\circ$F	93	75	76	75
Hot Inlet Pressure, in. HgA	43.5	36.8	57.4	43.5
Cold Inlet Pressure, in. HgA	59.3	44.5	86.2	57.6

TABLE 12

TYPICAL TEST DATA

	Unit Data				Orifice Data				
	Inlet Temp. $^\circ$F	Inlet Static Press. in. HgA	ΔP in. H_2O	Mixing Box Outlet Temp. $^\circ$F	Inlet Static Press. in. HgA	ΔP in. H_2O	Inlet Temp. $^\circ$F	Duct Dia. in.	Orifice Dia. in.
	1	2	3	4	5	6	7	8	9
Low Temp. (Cold)	92.5	59.3	0.88	590	60.3	6.75	92.5	6.07	2.5
High Temp. (Hot)	643.8	43.6	0.79	153.0	88.5	8.8	718	4.0	2.5

At each test point condition at least three sets of data was taken after establishing steady-state condition.

The isothermal pressure drop tests were run with ambient temperature air on both sides of the recuperator.

TEST RESULTS

As indicated above, the purpose of the acceptance tests was to verify the heat transfer and pressure drop characteristics of the final design recuperator. The performance test was carried out using air as the heat transfer fluid. The temperature and pressure levels of the tests were compatible with the values available from standard AiResearch testing sources. The test conditions, therefore, do not simulate the actual design point requirements during the operation of the recuperator within the Brayton cycle. In order to verify the performance of the recuperator at the actual design point, the following procedure is adopted.

Randomly select several operating conditions for which test data is available, and from this data, determine the overall heat transfer conductance of the recuperator. A typical set of data taken from the final design recuperator test data together with a sample calculation is shown in Table 12. Note that actual data reduction was made by an AiResearch data reduction computer program.

Readings of room temperature and barometric pressure are also taken. In many cases, the information shown on the above table is the average of several readings taken at the same location.

Barometric Pressure = 29.69 in. HgA, Room Temperature = $80^{\circ}F$

For Low Temperature Flow Rate

Using Orifice Data (Columns 5, 6 and 7)

P_o = 60.3 in. HgA

T_o = 92.5 + 460 = $552.5^{\circ}R$

$\sigma\Delta P_o = 17.35 \left(\dfrac{60.3}{552.5} \right) 6.75 = 12.8$ in. H_2O

From standard ASME orifice curves for a 2.5 in. dia. orifce in a 6.07 in. dia. duct

Flow Rate = 22.53 lb per min

This calculation is repeated using high temperature data and the High Temperature Flow Rate = 23.72 lb per min.

132

Now From Unit Test Data

Cold outlet temperatue = Mixing box outlet temperature + Mixing box

$$\Delta T = 590 + 9 = 599^\circ F$$

Cold $\Delta T = 599 - 92.5 = 506.5^\circ F$

Hot outlet temperature = Mixing box outlet temp. + Mixing box

$$\Delta T = 153 + 1.2 = 154.2$$

Hot $\Delta T = 643.8 - 154.2 = 489.6^\circ F$

Overall $\Delta T = 643.8 - 92.5 = 551.3^\circ F$

Heat rejection (Cold) = $WC_p \Delta T = 22.53 \times 0.244 \times 506.5$

$$= 2787 \text{ Btu per min}$$

Heat rejection (Hot) = $23.73 \times 0.245 \times 489.6 = 2845$ Btu per min

C_p is evaluated at the average temperature.

As the two heat transfer values are within 5 percent, this is an acceptable data point.

Thermal Effectiveness (Cold) $= \dfrac{506.5}{551.3} = 0.92$

Thermal Effectiveness (Hot) $= \dfrac{489.6}{551.3} = 0.89$

From conventional log mean temperature relationships for counterflow units

Log Mean $\Delta T = .095 \times 551.3 = 52.4^\circ F$

Overall Heat Transfer Conductance $(UA)_{cold} = \dfrac{2787}{52.4} = 53.3$ Btu per min $^\circ F$

$UA_{hot} = 54.4$ Btu per min $^\circ F$

The next step is to predict the performance of the recuperator at this set of test conditions by the same technique that was used to design the unit.

Cold Side

Recuperator geometry is determined.

Total Heat Transfer Surface Area (A_T)

Free Flow Area (Ac)

Hydraulic Radius (r_h)

Effective Fin Length (L_e)

Ratio of Extended Surface to Total Surface (A_F/A_T)

$$\text{Mass Velocity (G)} = \frac{\text{Flow Rate}}{\text{Free Flow Area}} \left(\frac{W}{Ac}\right)$$

$$\text{Reynolds Number} = \frac{\text{Hydraulic Diameter } (4x \ r_h) \times G}{\text{Viscosity (at average temperature)}}$$

Colburn Modulus (j) and Friction Factor (f) are then read from standard AiResearch data curves for the appropriate heat transfer surface at the Reynolds number calculated.

$$\text{Heat Transfer Coefficient (h)} = \frac{j \ G \ C_p}{P_r^{2/3}}$$

where C_p (specific heat) and P_r (Prandtl No.) are determined at the average temperature in the heat exchanger.

Fin effectiveness is then determined.

$$m = \sqrt{\frac{2 \ h}{K \ \delta}} \quad \text{where K = metal conductivity}$$

$$\delta = \text{fin thickness}$$

$$\text{Fin Effectiveness } (\eta_f) = \frac{\text{Tanh} (m \ L_e)}{(m \ L_e)}$$

Overall Effectiveness $(\eta_o) = 1 - A_F/A_T \ (1 - \eta_f)$

Heat Transfer Conductance $= \eta_o \ h \ A_T$

134

This is repeated for the hot side of the unit and the Overall Heat Transfer $\left(UA_{calc}\right)$ is determined.

$$\frac{1}{UA_{calc}} = \frac{1}{\eta_o \, h \, A_{cold}} + \frac{1}{\eta_o \, h \, A_{hot}}$$

This value of UA_{calc} must now be modified to allow for the effect of Axial Conduction. This is done by following the procedure laid out in Appendix A of this report.

For the representative test conditions shown above, the prediction technique resulted in a $UA_{predict} = 53.0$ Btu per min ^{o}F. The unit, therefore, performed approximately 1.6 percent better than predicted at this condition.

The prediction of the overall pressure drop of the unit is as follows. For the pure counterflow section of the core, the frictional pressure drop is calculated using the Fanning friction factor (f) previously obtained. The triangular end section pressure drops are estimated by an AiResearch computer program, H1400. The duct and manifold pressure losses are estimated as shown in Section 6 of this report. The pressure losses are then added to obtain the overall predicted pressure loss on one side of the recuperator.

Discussion of Heat Transfer Results

The above sample calculation illustrates and validates the method of predicting the performance of the recuperator at the design operating conditions, by predicting test data obtained at off-design conditions. To provide a complete comparison of test to predicted data for the final design configuration at the conditions tested, Figure 75 was prepared. The solid curve shown on Figure 75 represents the predicted performance for the recuperator over the range of airflow rates shown. This curve is essentially the same as that shown in Figure 70 for the estimated performance of the 2-in. high test core. The performance of the 2-in. high test core and the final design configuration are identical at equivalent mass velocities. Each of the actual data points taken during the performance test are also shown in Figure 75. The majority of the data was obtained at an airflow rate which resulted in the same Reynolds number within the heat exchanger core as exists at the actual design point operating conditions. The airflow during this condition is approximately 23 lb/min and the Reynolds number is approximately 80. Data was also obtained at half of this flow rate and twice of this flow rate and this data is also shown on Figure 75.

At the actual operating conditions of the recuperator, the flow rates on both sides of the recuperator are identical and as the effectiveness of the unit is high and the actual operating fluid is argon the specific heats of the fluids on both sides are also identical. As a result, the effectiveness on both sides of the unit is the same. During the acceptance test, the flow

135
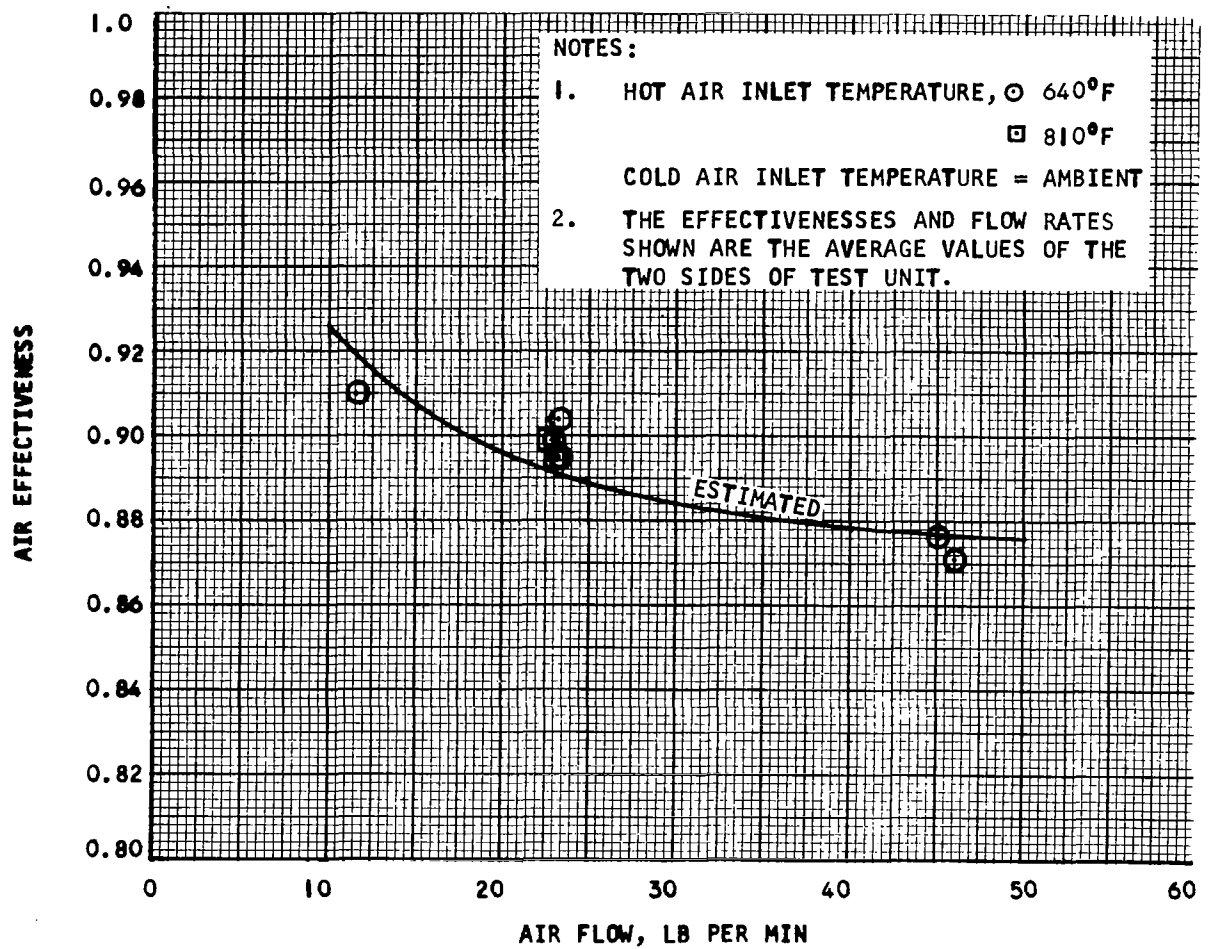
Figure 75. Estimated and Test Performance
Recuperator 180636

136

rates of air on both sides of the recuperator were set to give equal Reynolds numbers to those existing in the actual design point operation. As a result, throughout the testing, the flow rates on both sides of the recuperator were not identical. This resulted in slightly different effectiveness on each side. The values shown on Figure 75 represent the average of the two flow rates and the average of the two effectivenesses. This is not a completely accurate evaluation of the data. However, it does serve to illustrate the basic comparison between predicted and tested data. To obtain a true evaluation of this comparison, the overall heat transfer conductance (predicted vs test) must be examined. The inaccuracy of the average effectiveness is emphasized at the lowest flow rates of approximately 11 lb/min. At this reduced flow rate the deviations between the two sides of the heat exchanger in flow rate and effectiveness are greatest and consequently the reliability of the average effectiveness and of the average overall heat transfer conductance obtained is most suspect to error. Figure 75 indicates that the average effectiveness is below the predicted value, while, when the comparison is made on the basis of average overall heat transfer conductance, the test performance is in excess of the predicted value.

The comparison between the overall conductances predicted to those obtained during the test was made for all test data points shown. The test data ranged from approximately 8 percent above the predicted value to approximately 5 percent below the predicted value. At the condition which most closely simulated the design point, that is, an airflow rate of approximately 23 lb/min and a hot side inlet temperature of 640^0F the overall heat transfer conductance test value was approximately 2 to 4 percent greater than the predicted value. At the same inlet temperature but at the reduced flow rate of approximately 11 lb/min the test heat transfer conductance was approximately 8 percent greater than the predicted value. At the flow rate of approximately 46 lb/min the test value of overall heat transfer conductance is approximately 5 percent below the predicted value. The overall characteristics of the heat exchanger are therefore, slightly different from the predicted values. This is almost entirely the result of flow distribution throughout the unit. The triangular end sections of the final recuperator configuration were designed to impose the best possible flow distribution at the design point operating conditions. During the tests at conditions other than the design point either improved or much worse flow distribution may be obtained. It is estimated that at the reduced flow rate of 11 lb/sec the nonuniformity in flow distribution is essentially zero, and consequently better performance is obtained.

At the higher flow rate condition, 36 lb/min, the flow distribution is considerably worse than at the design point. The unequal triangular ends were sized to match the pressure drops with the density differences that existed between the hot and cold ends. At an airflow rate of approximately 23 lb/min with the hot air entering the unit at 640^0F the density differences between the two ends are essentially the same as those that exist at the design point operating condition. Therefore, at this test condition, essentially the same performance should be achieved. As the flow rate is increased, the pressure drops in the end increase by approximately the square of the flow rates while the density difference remains essentially the same. Consequently the balancing between pressure loss and density difference achieved for the design condition by the use of the unequal size triangular ends is negated during the high flow test condition and the flow distribution is much less uniform.

137

This same effect is reflected in the comparison of the test data to predicted values obtained at the flow rate of 23 lb/min and a hot side inlet temperature of 810°F. In this case the increase in hot side inlet temperature alters the density ratio between hot and cold inlet ends while the pressure drops remain essentially the same. Again the balance is negated and slightly nonuniform distribution occurs. The influence of this slightly nonuniform flow distribution on performance is shown in Figure 75 as the test data points obtained at this condition on the average are lower than those obtained with the 640°F inlet temperature.

The results of the heat transfer testing on the final design recuperator were completely satisfactory. Although some scatter exists in the test data and although the heat balances obtained are approximately 3 percent, which is slightly greater than desired, the test data clearly indicates that the recuperator satisfies its required performance. The majority of the scatter in the test data point can be explained by the variation in flow distribution resulting in the different operating conditions tested.

Discussion of Pressure Loss Results

The same procedure is employed to determine the pressure drop characteristics of the recuperator at the design point as used for the heat transfer data. That is, a direct comparison between test and predicted values of pressure drop is made at the test data conditions and providing this comparison is in close agreement, then the predicted performance at the design point will be achieved. Exactly the same method of prediction is used at the design point and at the test data conditions.

For all the test data points obtained, this comparison between test and predicted values of pressure drop was made for both sides of the recuperator.

Reference is made to Table 9, where it is noted that the pressure drop measured for the two inch test core is 2.865%. This number corresponds to an aspect ratio of 1 (square face, 26 in. x 26 in.) as discussed in the section entitled "Pressure Drop Studies". A change in the aspect ratio was clearly indicated in order to reduce the pressure drop. The unit selected, finally, by NASA and which was fabricated and tested has an aspect ratio of 2.25 to 1 (face dimensions of 17.6 in. x 39.6 in.). It was anticipated that the pressure drop would be lower, down to 2.28%, as shown in Table 9.

The pressure drop data resulting from tests on the 2 in. test core were considered highly accurate and reliable, since an extensive multiplicity of instrumentation was used to obtain this data (see Figure 64).

In all cases the test values, obtained during the limited performance test on the full scale unit were considerably in excess of the predicted. As the test values were in some cases approximately 2.5 times the predicted values and as this is in complete contradiction with the test data obtained from the 2-in. test core, it is assumed that the test data from the performance test was highly unreliable. A possible explanation is discussed below.

The data was obtained from two static taps located at both the inlet and outlet of the unit. The pair at the inlet and the pair at the outlet were connected in parallel and the pressure drop measured was the difference between these two pairs. Since the predicted test ΔP is in the order of 1 in. H_2O, any unusual local pressure from conditions which might exist at the static tap location or if either of the static lines is even very slightly plugged, the inaccuracy in pressure drop recorded could be substantial. Figure 76 shows the actual pressure drop points recorded during the heat transfer tests on the hot (or low pressure) side of the unit. Also shown on Figure 76 is the predicted pressure drop at heat transfer conditions. This predicted curve is based on the data obtained from the 2-in. test core and consequently reflects the anticipated flow distribution characteristics. The third line shown on Figure 76 is the isothermal pressure drop data obtained from the final design configuration during the performance tests. This isothermal test data was obtained after the heat transfer tests had been completed. The instrumentation used to record pressure drop for these isothermal tests was changed, from manometers to a much more accurate water micromanometer which will record pressures to within 0.001 in. H_2O. A comparison of this isothermal data with the predicted heat transfer pressure drop characteristics shows the anticipated affect.

The recuperator was designed to provide uniform flow distribution during operating conditions with high density differences between the hot and cold ends, therefore, uniform flow distribution cannot be achieved at isothermal conditions. This effect is reflected in the comparison of the estimated pressure drop with the isothermal, as nonuniform flow will result in substantially higher pressure drop. It could, therefore, be assumed that the isothermal pressure drop data obtained is valid and represents the true characteristics of the recuperator. However, the difference between this isothermal data and the data obtained during the heat transfer testing is very large and could not be entirely accounted for by the improved accuracy of the instrumentation and it is, therefore, submitted that the pressure drop data obtained during the performance tests is not representative of the recuperator performance at all. The data obtained from the 2-in. high test core was of a much more meaningful nature as a great many more pressure taps were available on the unit and much greater attention was directed to obtaining highly accurate data.

The data for the cold (or high pressure) side of the recuperator exhibit the same differences between isothermal and heat transfer data obtained with the hot side and again both values are greater than predicted. This data is shown on Figure 77. At a flow rate of 23 lb per min, where the majority of the test data was obtained the ratio of test to predicted pressure loss is approximately 1.44. At this same flow rate the maximum scatter in the test
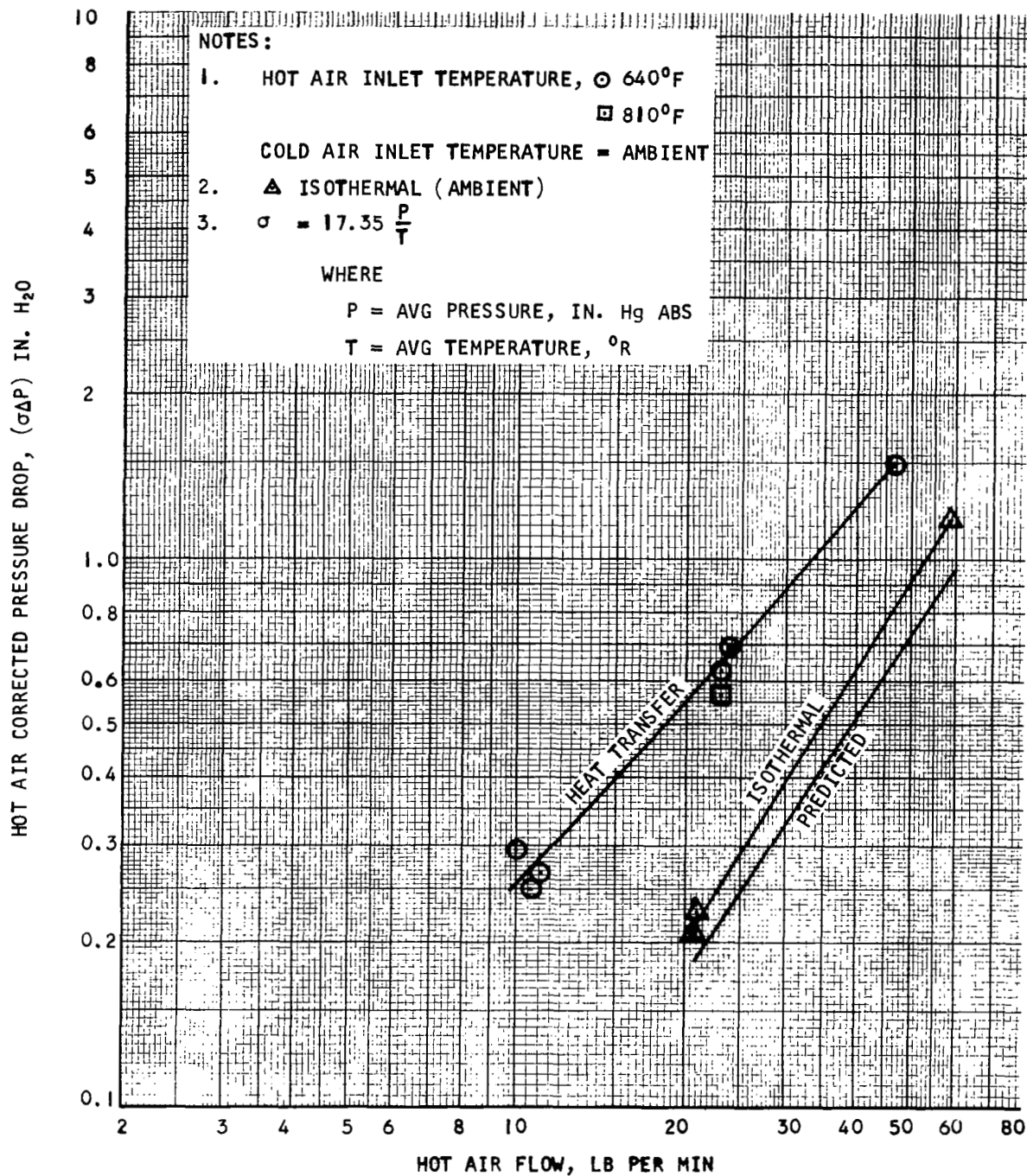
Figure 76. Predicted and Test Pressure Loss
(Hot or Low Pressure) of Recuperator
180636
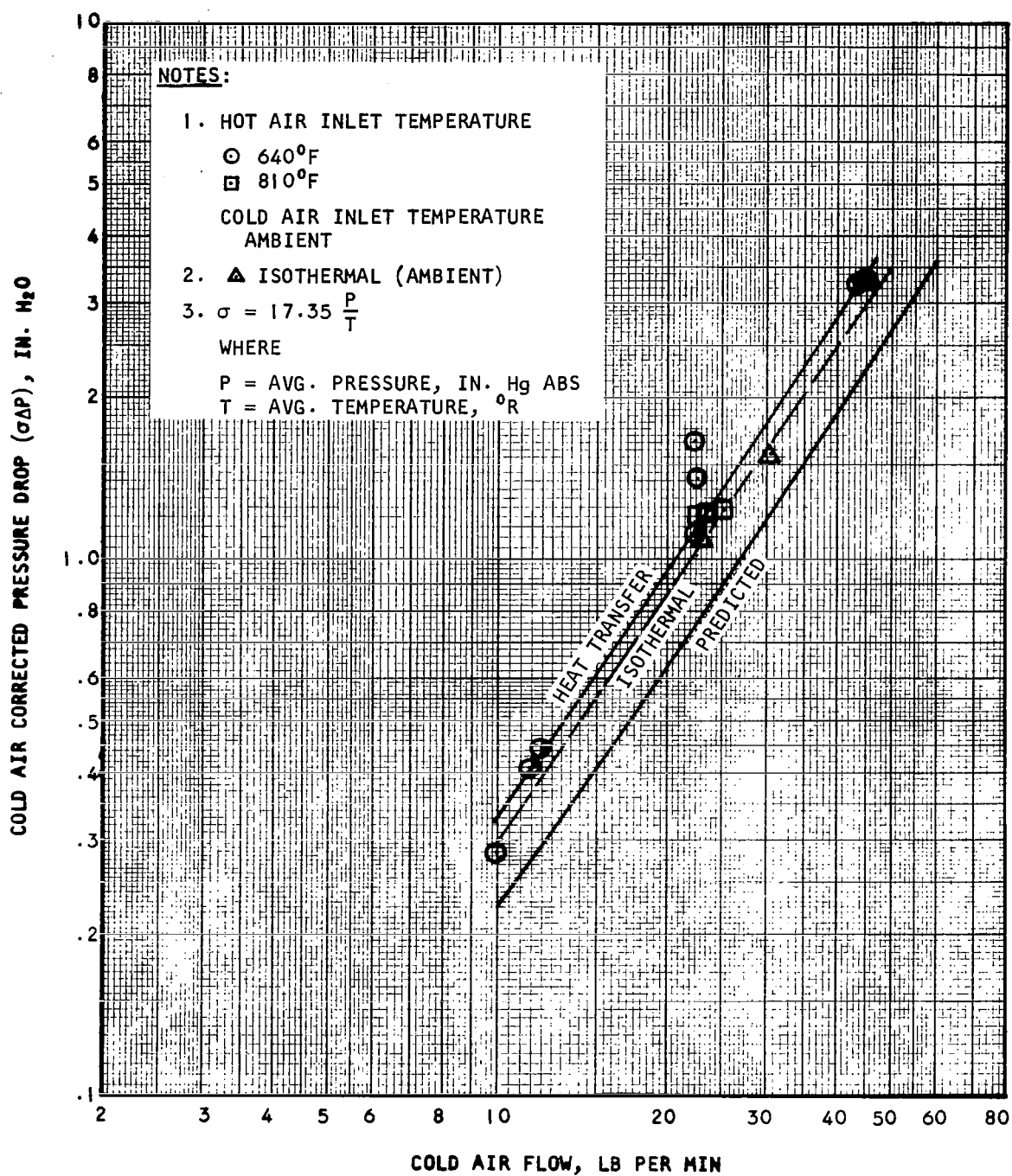
Figure 77. Predicted and Test Pressure Loss (Cold or High Pressure) of Recuperator 180636

data is 1.55. Consequently, as the data scatter is greater than the difference between test and predicted values little confidence can be placed in the data. Also as indicated for the hot side, the heat transfer pressure drop on the cold side is greater than the isothermal pressure drop which is in direct contradiction with the design characteristics of the recuperator. The instrumentation and methods of connection to the test unit were again not sufficiently accurate to establish reliable pressure loss information and consequently the 2 in. high test core data must be believed.

Three different values of pressure loss for the recuperator have been evolved during the course of the program. A purely analytical value was first calculated, and then this was amended by the data from the 2 in. high test core (described in Section 6). It was anticipated that the final recuperator performance test would confirm the 2 in. core data, however, due to the reasons discussed above this confirmation was not achieved and a third value of pressure loss was evolved. Although this latter value from the performance test is completely discounted the three values are summarized below.

| | Predicted | 2 in. Test Core | Final Recuperator | | Believed Value |
			Isothermal	Heat Transfer	
Overall Heat Exchanger Pressure Drop, Percent	2.093	2.286	2.83	5.45	2.286

The two values shown under Final Recuperator indicate clearly that the difference between the test isothermal and heat transfer data is very large. If the isothermal data is corrected for the anticipated improvement in flow distribution at the operating condition the overall pressure loss is 2.35 percent which is very close to the believed value.

NASA Schedule requirements precluded reduction of the data prior to shipment of the recuperator and therefore a rerun of the pressure drop tests at AiResearch was not possible.

It is anticipated that test data will be obtained at some future time at NASA Lewis facilities during component testing.

For any future testing, it is recommended that a greater number of static taps be used to preclude or minimize the possibility of grossly erroneous readings due to some unusual local condition, at any single tap. Also it is probably advisable to use several traversing probes in order to obtain a good pressure average.

To assist NASA in evaluating the pressure loss characteristics of the recuperator throughout their component and system testing AiResearch prepared pressure drop curves for both air and argon. The air pressure drops are shown on Figure 78 and the values correspond to the predicted curves of Figures 76 and 77. Figure 79 shows the estimated pressure losses for the recuperator with argon as the working fluid. These curves correspond to the design point overall pressure loss of 2.286 percent.
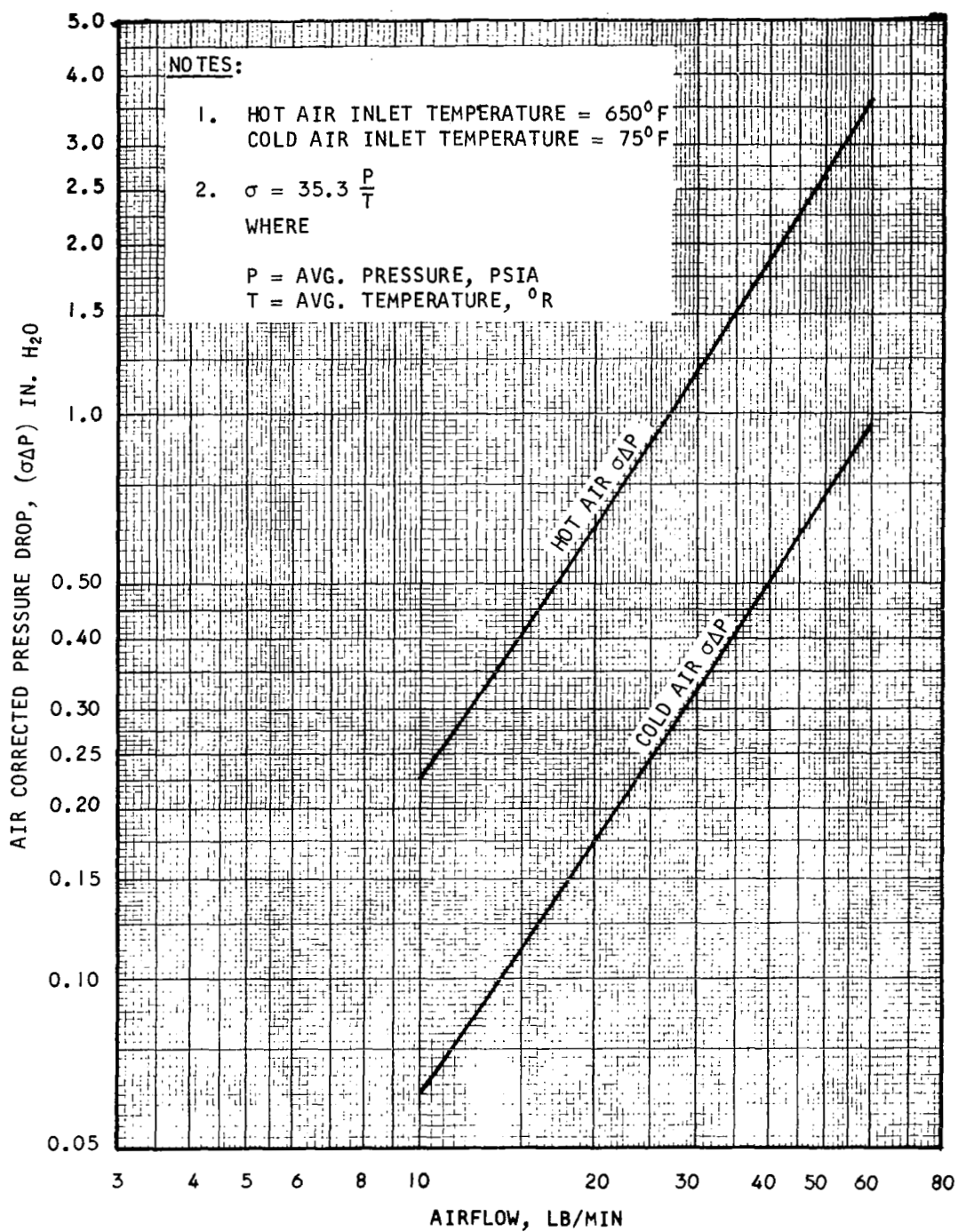
Figure 78.   Estimated Performance with Air of Recuperator 180636
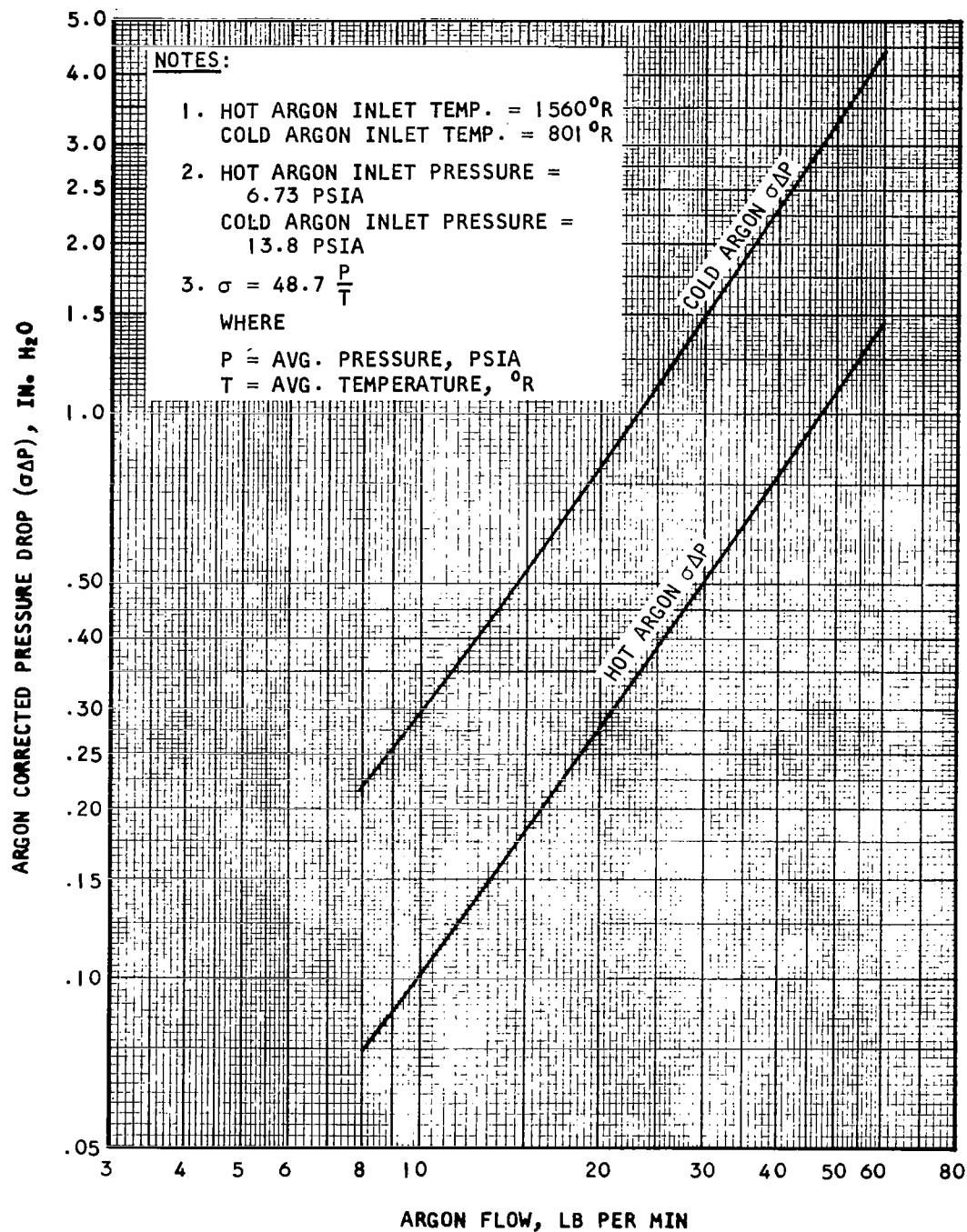
Figure 79. Estimated Performance With Argon of
Recuperator 180636

REFERENCES

1. AiResearch Report L-3895, Vol. I, Rev. I, "Recuperator Development Program, for a Solar Brayton Cycle System," August 19, 1963. (NASA RFP: APGO-1527)

2. Smith, C. S., and Palmer, E. W., "Thermal and Electrical Conductivities of Copper Alloys," Trans. AIME, 117, (1935).

3. Kempf, L. W., Smith, C. S., and Taylor, C. S., "Thermal and Electrical Conductivities of Aluminum Alloys," Trans. AIME 124, 287-299 (1937).

4. Powell, R. W., "The Thermal and Electrical Conductivities of Beryllium," Philosophical Magazine, Series 7, Vol. 44, No. 153, 645-663 (June, 1953).

5. Powell, R. W., and Hickman, M. J. Second Report of the Alloy Steels Research Committee, Iron and Steel Institute, Special Report No. 24, 242-251 (1939).

6. Powell, R. W., "The Thermal and Electrical Conductivities of Some Magnesium Alloys," Philosophical Magazine, 27, 677-686 (1939.

7. Fine, M. E., "Correlation Between Electrical and Thermal Conductivity in Nickel and Nickel Alloys," Trans. AIME, 188, 951-952 (1950).

8. Deem, H. W., Wood, W. D., and Lucks, C. F., "The Relationship Between Electrical and Thermal Conductivities of Titanium Alloys," Titanium Metallurgical Laboratory Memorandum, Battelle Memorial Institute (July 18, 1957).

9. Mikryukov, V. E., "Thermal and Electrical Properties of Copper Alloys," Vestnik Moskov. Univ., Sar. Mat., Mekh., Astron., Fiz. i Khim., Vol. II, pp. 53-70 (USSR).

10. Hume-Rothery, W., The Metallic State (1931) Oxford.

11. Perlmutter, M., "Inlet and Exit-Header Shapes for Uniform Flow Through A Resistance Parallel to the Main Stream," Journal of Basic Engineering, ASME, September, 1961.

12. London, A.L., "Flow Losses for Heat Exchangers with Oblique Flow Headers," Supplement to TR No. 60, Mechanical Engineering Dept., Stanford University, Stanford, California.

APPENDIX A

AXIAL CONDUCTION EFFECT

In all heat transfer devices, temperature gradients exist in the structure of the device. In any material where such a temperature gradient exists, there is a flow of heat from the high temperature portion of the structure towards the low temperature section. In many heat transfer devices, this leakage of heat through the heat exchanger material is very small and is generally ignored in the design of heat exchangers. In heat exchangers where high effectiveness is required, it is generally necessary to use some form of pure counterflow device, the temperature gradient that exists in the material structure is at a maximum value, as the hot end of the heat exchanger is essentially at maximum fluid temperature and the low end is at minimum fluid temperature. The flow of heat through the metal in this type of situation results in a loss of heat from the hot end and addition of heat to the cold end, both of which have adverse effects on heat exchanger performance. In order to compensate for the reduced temperature difference at both ends of the heat exchanger, the heat exchanger size must be increased.

In order to determine exactly how much it is necessary to increase the heat exchanger size to account for the effects of axial conduction, it is necessary to conduct an energy balance over the entire heat exchanger and a rigorous mathematical analysis is required to permit the accurate evaluation of these effects. During the period when the parametric design study was being conducted, only limited information was available on this phenomenon. Papers by H. W. Hahnemann (Reference 1) and by G. D. Bahnke and C. P. Howard (Reference 2) presented two methods of analyzing this effect. Both these papers were sufficiently general to permit their adaption to the specific problem of axial conduction in a pure counterflow plate-fin heat exchanger. In addition to considering the information presented in these references, AiResearch also conducted an analysis to obtain a simple closed-form solution to the problem. This analysis is presented below.
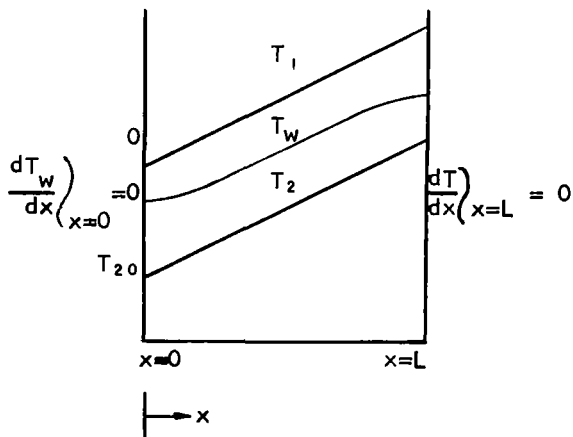
T_1, T_2	temperature of hot, cold fluid
T_W	wall temperature of surface separating hot and cold fluids
C_{p1}, C_{p2}	specific heat of hot, cold fluid
h_1, h_2	film heat transfer coefficient on hot, cold side
W_1, W_2	flow rate of hot, cold fluid

L   heat exchanger length

A_m metal cross-sectional area available for heat conduction
                     (in direction of flow)

$(hA)_1$ $(hA)_2$ heat transfer conductance on hot, cold side

k   metal thermal conductivity

The conditions of steady state, constant specific heats and constant film heat transfer coefficients were assumed. Also, the thermal resistance of the metal surface separating the hot and cold fluids was assumed to be negligible compared to that of the fluid films. In other words $\partial T_w/\partial y = 0$. The problem thus becomes one-dimensional.

For a differential length Δx of the heat exchanger, energy balance equations may be written for the hot and cold fluids and for the surface separating them. By allowing $\Delta x \to 0$ one obtains the differential equations of temperature distributions,

$$A(T_1 - T_w) = \frac{dT_1}{dx}$$

$$B(T_w - T_2) = \frac{dT_2}{dx}$$

$$D(T_w - T_2) - C(T_1 - T_w) = \frac{d^2 T_w}{dx^2}$$

where $A = \dfrac{(hA)_1}{W_1 C_{p1} L}$

$B = \dfrac{(hA)_2}{W_2 C_{p2} L}$

$C = \dfrac{(hA)_1}{k A_m L}$

$D = \dfrac{(hA)_2}{k A_m L}$

By introducing $dT_w/dx = u$ the above equations are changed into four first order differential equations. That is, in matrix notation

$$\{T'\} = [M]\,\{T\}$$

$$\{T\} = \begin{Bmatrix} u \\ T_1 \\ T_2 \\ T_w \end{Bmatrix}$$

and $[M] = \begin{bmatrix} 0 & -C & -D & (D + C) \\ 0 & A & 0 & -A \\ 0 & 0 & -B & B \\ 1 & 0 & 0 & 0 \end{bmatrix}$

Seeking solutions of the form

$$\{T\} = \{K\}\, e^{\mu x}$$

leads to the characteristic equation

$$\mu\,[\mu^3 - (A - B)\,\mu^2 - (AB + D + C)\,\mu + AD - BC] = 0$$

If μ_2, μ_3 and μ_4 are the nonzero, real and distinct roots of the expression in brackets above, then the solution of the differential equations is

$$\{T\} = \{K_1\} + \{K_2\}\, e^{\mu_2 x} + \{K_3\}\, e^{\mu_3 x} + \{K_4\}\, e^{\mu_4 x}$$

where $\{K_i\} = \lambda_i \begin{Bmatrix} \mu_i \\ \dfrac{A}{A - \mu_i} \\ \dfrac{B}{B + \mu_i} \\ 1 \end{Bmatrix}$

The coefficients λ_i are determined from the equations which result from the substitution of the boundary conditions into the solution above. Hahnemann (Reference 2) carried this through and then proceeded to find an explicit expression for the heat exchanger temperature effectiveness. His results are rather lengthy and therefore, will not be repeated here. However, it must be pointed out that when the characteristic equation has multiple roots the solution above must be modified according to well established rules. Multiple roots occur for instance when $A/B = C/D$ or when $A = B$ and $C = D$.

The heat exchanger temperature effectiveness was found for the case when $A = B$ and $C = D$, that is, when $W_1 C_{p1} = W_2 C_{p2} = WC_p$ and $(hA)_1 = (hA)_2$. It is

$$E = 1 - \frac{(NC_m + 1)}{(1 + N - \psi)}$$

where $C_m = \dfrac{kA_m}{L W C_p}$

$N = NTU = \dfrac{(UA)}{WC_p}$

$\psi = \dfrac{1}{2p} \left[\dfrac{\phi + 1}{1 - p} + \dfrac{\phi - 1}{1 + p} \right]$

$p = \sqrt{1 + \dfrac{1}{NC_m}}$

$\phi = \dfrac{\cosh 2Np - 1}{\sinh 2Np}$

If thermal conductivity is negligible, the above equation for effectiveness reduces to the familiar equation

$$E = 1 - \frac{1}{1 + N}$$

When $C_m \to \infty$, the effectiveness equation becomes

$$\lim_{C_m \to \infty} E = 1 - \frac{1}{\dfrac{\cosh 2N - 1}{\sinh 2N} + 1}$$

and when $N \to \infty$, the effectiveness equation is in the limit

$$\lim_{N \to \infty} E = 1 - \frac{C_m}{2 C_m + 1}$$

If in the above equations $N \to \infty$ and $C_m \to \infty$, $E \to 1/2$ as expected.

The effectiveness equation discussed above was verified by comparison with results obtained by G. D. Bahnke and C. P. Howard (Reference 2). Bahnke and Howard used a numerical finite-difference method to calculate the effectiveness of a periodic flow (rotary) type heat exchanger when heat conduction in the direction of flow is allowed for. Their case of "infinite rotor speed" is equivalent to a direct transfer type counterflow heat exchanger. The verified effectiveness equation was used in the design of all pure counterflow heat exchangers determined during the parametric design study. Both the

plate-fin and tubular-type of pure counterflow heat exchanger were designed by use of high-speed digital computer techniques. The tubular heat exchanger design program was written as part of this program and incorporated the above effectiveness equation to allow for axial conduction. The previously-existing plate-fin pure counterflow heat exchanger program was also adapted to utilize the above expression for the determination of axial conduction.

REFERENCES

1. Hahnemann, H. W., "Approximate Calculation of Thermal Ratios in Heat Exchangers Including Heat Conduction in Direction of Flow," National Gas Turbine Establishment Memo No. M36, 1948 also available from the Defense Documentation Center as ATI 74031.

2. Bahnke, G. D., and Howard, C. P., "The Effect of Longitudinal Heat Conduction on Periodic - Flow Heat Exchanger Performance," Paper No. 63-AHGT-16, ASME 1963.

APPENDIX B

BASIC DATA FOR AXIAL FLOW OUTSIDE TUBE BUNDLES

A literature search was conducted to obtain either analytical or empirical data on the fluid friction and heat transfer characteristics of gas flow parallel to, and outside of, plain tube bundles. Most of the pertinent papers that were found dealt with the problem of cooling fuel rod bundles in nuclear reactors. As a consequence the test models that were used in gathering the experimental data presented in these papers had relatively low tube spacing to diameter ratios and also low length to diameter ratios. All of the available experimental data falls in the turbulent flow region. Only a theoretical friction factor expression has been obtained for flows in the laminar region.

Figure B-1 gives a summary of these data. Cruves (1) are from Kays and London (Reference 1) and they are for gases flowing inside of plain round tubes when the wall temperature is constant. Except for curves (1), all other curves and data points are for flows outside of tube bundles. The data points located within the triangles and circles were obtained from tests conducted at AiResearch. The test conditions were discussed in detail in AiResearch Report L-3895 (Reference 2). It will suffice to mention here that the tubes were arranged in a triangular bundle utilizing an equilateral tube spacing. Curve (2) was calculated from Sparrow's (Reference 3) analytically derived curves and it seems to be in fairly good agreement with the plotted AiResearch data near the transition region.

Curves (3) are Palmer's (Reference 4) data for very closely spaced smooth tubes. The test fluid was air. The test lattice consisted of seven rods spaced in an equilateral cluster within a hexagonel chamber with circumferential segments of tubing attached to the chamber walls to simulate the adjacent rods of a large array. In Reference 5, test data has been correlated for water flowing parallel to a bundle of tubes arranged equilaterally with a center spacing to diameter ratio of 1.4. This test core also included tube sections at the outer limits of the tube bundle to simulate a large array. The recommended correlation is

$$j = 0.0205 \ Re^{-0.16} \ Pr^{-0.209}$$

for Reynolds numbers from 10^4 to 1.2×10^5. The equation is plotted as curve (7). The aforementioned provision of tube sections to simulate large arrays was not made in any of the other tests discussed here.

Curves (4) are Kattchee's (Reference 6) data for a symmetrical and circular cluster of 19 tubes. Equal spacing between all tubes and the channel walls was maintained by means of helically applied spacer wires. The heat transfer data was obtained with air, the friction data with water. Curve (5) is Mackewicz's (Reference 7) data for a symmetrical circular cluster of 19 tubes. The tubes were equally spaced, but without mechanical spacers. The test fluid was water. Finally, curve (6) is Le Tourneau's (Reference 8) data. The test core consisted of 19 rods equilaterally spaced to form a hexagonal cluster. A special test section with a hexagonal interior cross section was constructed to accommodate the core. Water was used as the test fluid.

Figure B-I. Data for Axial Flow Outside Tube Bundle

NOTES:

1. ⊙ HEAT TRANSFER POINTS
   △ ISOTHERMAL POINTS
   TUBE DIAMETER = 0.15 IN.
   TUBE SPACING - EQUILATERAL TRIANGLE
   0.225 IN. BETWEEN CENTERS

2.

CURVE NO.	TUBE SPACING TO DIAMETER RATIO
2	1.50
3	1.015
4	1.145
5	1.137
6	1.12
7	1.40

3. SEE TEXT FOR FURTHER DETAILS

$f = \dfrac{\Delta P}{\rho} \dfrac{r_h}{L} \dfrac{2g}{V^2}$

$j - St\ Pr^{2/3}$

REYNOLDS NUMBER x 10^{-3}

A-10430
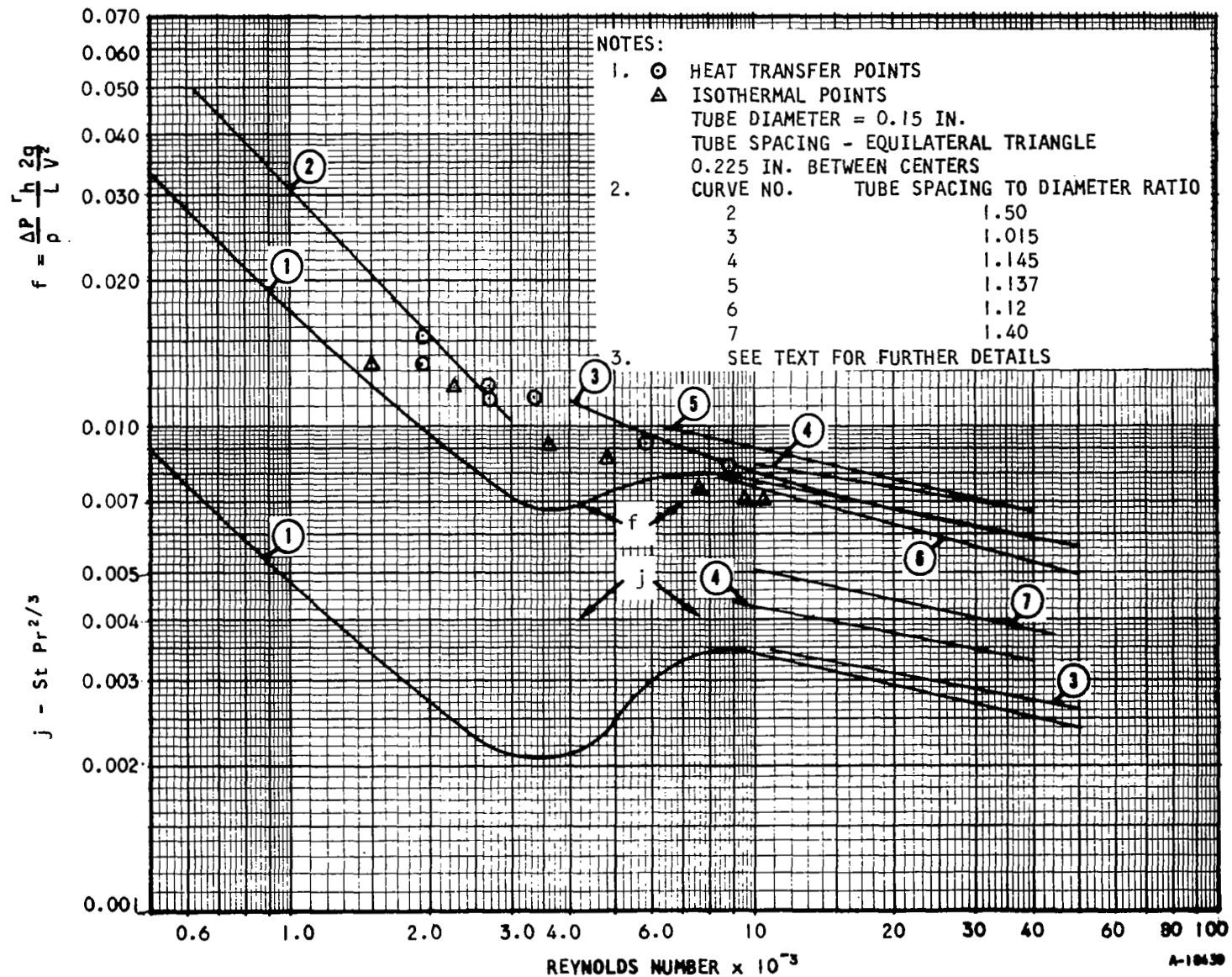
In summary, a considerable amount of data is available in the turbulent flow region (Re > 5000) and no satisfactory data has been obtained for the fully developed laminar flow region (Re < 2000). However, at high effectiveness and low pressure drop conditions the pure counterflow tubular heat exchanger is certainly an attractive possibility.

During the parametric study of pure counterflow tubular heat exchangers the data used for outside the tube bundles was that of flows inside a plain round tube (Curve I of Figure B-I). This was adequate for the comparison of problem conditions and heat exchanger types but it was recommended that if further consideration was given to pure counterflow tubular units a test program to establish reliable data should be conducted. With the selection of the plate-fin type for the final design this test program was unnecessary and no further work in this area was conducted.

REFERENCES

1. Kays, W. M., and London, A. L., Compact Heat Exchangers, McGraw-Hill, 1958.

2. AiResearch Report L-3895, Vol. I, Rev. I, "Recuperator Development Program, for a Solar Brayton Cycle System," August 19, 1963. (NASA RFP: APGO-1527)

3. Sparrow, E. M., and Loeffler, A. L., "Longitudinal Laminar Flow Between Cylinders Arranged in Regular Array," A. I. Ch. E. Journal, Vol. 5, September 1959, pp. 325-330.

4. Palmer, L. D., and Swanson, L. L., "Measurement of Heat-Transfer Coefficients, Friction Factors, and Velocity Profiles for Air Flowing Parallel to Closely Spaced Rods," International Developments in Heat Transfer, ASME 1961.

5. "Heat Transfer During Longitudinal Flow of Water Around Bundle of Rods, With Relative Pitch of s/d = 1.4." Inzhenerno - Fizicheskii Zhurnal (Russian), v. 4, n. 3, March 1961, p. 3-9.

6. Katchee, N., and Mackewicz, "Heat-Transfer and Fluid Friction Characteristics of Tube Clusters with Boundary-Layer Turbulence Promoters," Paper No. 63-HT-I, ASME, 1963.

7. Mackewicz, M. V., "Experimental Investigation of Fluid Flow Characteristics of Pin-Type Fuel Elements," (paper presented at the American Nuclear Society Meeting, San Francisco, December 1960).

8. LeTournead, B. W., et al., "Pressure Drop Through Parallel Rod Subassemblies Having a 1.12 Equilateral Triangular Pitch," Report No. WAPD-TH-118, Westinghouse, 1955.

APPENDIX C

COUNTERFLOW TUBULAR HEAT EXCHANGER DESIGN PROGRAM

Throughout the parametric analysis four types of heat transfer matrix have been considered, pure counterflow and cross-counterflow plate and fin heat exchangers and pure counterflow and cross-counterflow tubular heat exchangers. At the time of the proposal AiResearch was able to analyze and design heat exchangers of three of those types rapidly and accurately, utilizing IBM digital computer programs. No computer program was available at this time to analyze pure counterflow tubular heat exchangers in sufficient detail to permit their accurate design. A program was therefore written for the IBM 7074 Digital Computer which would permit the rapid and accurate evaluation of pure counterflow tubular heat exchangers. This computer program is described briefly below.

Pure counterflow, two fluid heat exchangers are designed by an iteration procedure. Any fluid combination of liquids and gases can be utilized. Five fluid properties for the fluids on both sides are available in the form of Lagrangian tables. These five fluid properties are specific heat, viscosity, Prandtl number, compressibility and density. If the fluid being considered is a liquid, density is estimated from the table and no use is made of the compressibility table. If the fluid is a gas then compressibility may be read from the table and utilized in an equation to calculate gas density. In this case no use is made of the density table. The Lagrangian tables utilized are curves of the particular fluid property vs temperature stored in the computer in the form of pairs of points. When utilizing these tables the computer interpolates between the stored values to determine the fluid properties at the actual temperatures required. In addition to being able to consider bundles of plain round tubes the computer program is capable of analyzing surfaces with longitudinal fins on the outside of the tubes and turbulators inside the tubes. Heat transfer and friction factor data for both inside and outside the tube bundle is fed into the machine in the form of Lagrangian tables of Reynolds number vs Colburn modulus and Reynolds number vs Fanning friction factor. In all designs formulated by this computer program the effect of axial conduction on heat exchanger performance is calculated. An option is available in the input to this program as to whether or not it is desired to resize the heat exchanger where the effect of axial conduction is appreciable.

Problem condition input parameters required include flow rate, inlet temperature, inlet pressure and pressure drop available on both sides of the heat exchanger. It is also necessary to specify either effectiveness on one side of the heat exchanger or total heat rejection required. Pressure drops may be specified either in psi or as a percentage of the inlet pressures. The fluid properties are evaluated at bulk average temperatures and gas densities are calculated on the basis of the perfect gas law, but as mentioned above compressibility factors (Z) can also be utilized. Bulk average temperature was selected as in all designs formulated for solar Brayton cycle applications as the flow regime within the heat exchanger is laminar. The program designs only the actual heat transfer matrix and the computer does not

formulate manifolding or packaging concepts. Allowances are, however, made for shock losses at the entrance, and exit of the tube bundle and momentum pressure losses on both sides of the heat exchanger are calculated.

In addition to supplying the heat transfer and pressure drop characteristics of any surface being analyzed in the form of Lagrangian tables, other surface property parameters are required. The surface input information required includes tube diameter, tube spacing, number of fins and fin height (where fins are utilized) and all material thicknesses. Material densities and thermal conductivities are also supplied in order to determine the weight, fin effectiveness and axial conduction parameters for the heat exchanger design. Options are available as to the type of overall heat exchanger configuration required. Basically the program merely sizes the heat exchanger in terms of the number of tubes required and the length of tubes required. It is, of course, possible to arrange this tube bundle into almost any shape and still have a heat exchanger with the same performance capability. Heat exchanger face area may, therefore, be expressed either in terms of aspect ratio or in terms of one controlling dimension.

Output data from this computer program is available in two forms. Both of these forms clearly specify the problem conditions being examined, that is, flow rates, temperatures and pressures. In the short form output all the information that is specified, is the surface geometry being considered and the actual solution obtained with this geometry. This type of output form is shown in Figure C-1. The second or long form of output that is available is shown in Figure C-2. This long form output shows the same information as the short form output but has a number of additional quantities also shown. These additional quantities include mass velocity, Reynolds number and heat transfer conductance on both sides of the heat exchanger. In the examples illustrated in Figures C-1 and C-2 there are two answers given for each surface considered. The first of these answers is the solution obtained by the program for a heat exchanger without allowing for axial conduction. The second solution is the resized heat exchanger which allows for axial conduction.

The design technique utilized by the computer program is very straight forward. For any given problem condition and specified matrix surface the program determines a minimum number of tubes and tube length required to meet the heat transfer requirements within the allowable pressure drop limits. The program first applies what is known as the impossibility equation to determine the free-flow area for inside the tubes. This so-called impossibility equation is a parameter which links the neat transfer and pressure drop requirements of one side of a heat exchanger into a single parameter. The name impossibility equation stems from its most common use which is to determine whether or not it is possible to build a heat exchanger to the given conditions within a specified envelope. Having determined a free-flow area inside the tubes on the tube side of the heat exchanger, the program then calculates the length of tubes corresponding to this free-flow area. With this now established tube bundle, the program next checks whether or not the available pressure drop on the outside of the tube bundle is exceeded. If this allowable pressure drop is exceeded the program then sizes a new tube bundle based on the outside the tubes conditions. Having now determined a tube bundle which does not exceed

156

COUNTERFLCW HEAT EXCHANGER   BRAYTON CYCLE RECUPERATOR

LEG=   3   LP=   1

FLOW(LB/SEC).	INSIDE WI	OUTSIDE WO
	0.61150	0.61150

INLET TEMPERATURE(DEG R)	TI1	TO1
	801.00000	1560.00000

OUTLET TEMPERATURE(DEG R)	TI2	TO2
	1522.05000	838.94990

INLET PRESSURE(PSIA)	PI1	PO1
	13.80000	6.73000

PRESSURE DROP	DPI	DPO
	3.00000	3.00000

EFFECTIVENESS	EI	EO
	0.95000	0.95000

HEAT REJECTION(BTU/SEC)	QX	
	54.7184	

SUMMARY CF SCLUTICNS
FACE ASPECT RATIC=   1.00000

TUBE DIA (IN.)	SPACING		NC.OF FINS	FIN HEIGHT (IN.)	SURFACE IN	OUT	NO. OF TUBES	TUBE LENGTH (IN.)	FACE DIMENSION (IN.)	WEIGHT (LB)	EFF. AXIAL	PRESSURE DROP INSIDE	OUTSIDE
0.2100	1.500	1.500	0.0	0.000	PL TB	PL TB	2874.	274.4	16.887	579.0	0.9494	0.4140	0.1176
0.2100	1.500	1.500	0.0	0.000	PL TB	PL TB	2874.	274.4	16.887	579.0	0.9494	0.4140	0.1176
0.2100	1.250	1.250	0.0	0.000	PL TB	PL TB	4810.	119.4	18.205	421.6	0.9493	0.1064	0.2019
0.2100	1.250	1.250	0.0	0.000	PL TB	PL TB	4810.	119.4	18.205	421.6	0.9493	0.1064	0.2019
0.2100	1.100	1.100	0.0	0.000	PL TB	PL TB	10781.	42.3	23.985	334.5	0.9475	0.0175	0.2019
0.2100	1.100	1.100	0.0	0.000	PL TB	PL TB	11184.	43.9	24.429	359.9	0.9509	0.0175	0.2019
0.1500	1.500	1.500	0.0	0.000	PL TB	PL TB	5861.	138.8	17.225	423.1	0.9493	0.4140	0.1106
0.1500	1.500	1.500	0.0	0.000	PL TB	PL TB	5861.	138.9	17.225	423.1	0.9493	0.4140	0.1106
0.1500	1.250	1.250	0.0	0.000	PL TB	PL TB	9521.	61.5	18.295	304.6	0.9488	0.1131	0.2019
0.1500	1.250	1.250	0.0	0.000	PL TB	PL TB	9676.	62.5	18.444	314.6	0.9503	0.1131	0.2019
0.1500	1.100	1.100	0.0	0.000	PL TB	PL TB	21293.	21.6	24.077	239.7	0.9445	0.0186	0.2019
0.1500	1.100	1.100	0.0	0.000	PL TB	PL TB	22818.	23.2	24.924	275.2	0.9506	0.0186	0.2019
0.1250	1.500	1.500	0.0	0.000	PL TB	PL TB	8676.	95.0	17.465	355.5	0.9491	0.4140	0.1058
0.1250	1.500	1.500	0.0	0.000	PL TB	PL TB	8676.	95.0	17.465	355.5	0.9491	0.4140	0.1058
0.1250	1.250	1.250	0.0	0.000	PL TB	PL TB	13898.	42.0	18.420	251.5	0.9482	0.1183	0.2019
0.1250	1.250	1.250	0.0	0.000	PL TB	PL TB	14297.	43.2	18.683	266.2	0.9508	0.1182	0.2019
0.1250	1.100	1.100	0.0	0.000	PL TB	PL TB	30762.	15.0	24.116	199.6	0.9411	0.0195	0.2019
0.1250	1.100	1.100	0.0	0.000	PL TB	PL TB	34218.	16.7	25.435	247.0	0.9502	0.0194	0.2019
0.1000	1.500	1.500	0.0	0.000	PL TB	PL TB	14122.	59.2	17.825	286.0	0.9487	0.4140	0.0989
0.1000	1.500	1.500	0.0	0.000	PL TB	PL TB	14354.	60.2	17.971	295.6	0.9502	0.4140	0.0990
0.1000	1.250	1.250	0.0	0.000	PL TB	PL TB	21848.	26.9	18.476	201.3	0.9470	0.1267	0.2019
0.1000	1.250	1.250	0.0	0.000	PL TB	PL TB	22797.	28.1	18.873	219.2	0.9508	0.1266	0.2019
0.1000	1.100	1.100	0.0	0.000	PL TB	PL TB	48223.	9.6	24.156	159.1	0.9337	0.0209	0.2019
0.1000	1.100	1.100	0.0	0.000	PL TB	PL TB	59632.	11.9	26.862	243.4	0.9499	0.0207	0.2019

Figure C-1.   Typical Short Form Output from IBM Digital Computer Program
for Designing Pure Counterflow Tubular Heat Exchangers

158

INSIDE SURFACE IS PL TB OUTSICE SURFACE IS PL TB

TUBE DIA	XT	XL	WALL T	TURB. T	FIN T	FIN HT	NO. OF
(IN)			(IN)	(IN)	(IN)	(IN)	FINS
0.21000	1.5CCC0	1.50C00	C.C0400	0.00000	C.00000	0.00000	0.00000

NO. TUBES	TUBE L	FACE HT	FACE W	ASPECT	WEIGHT	VOLUME	PRESSURE DROP	
	(IN)	(IN)	(IN)		(LB)	(CU. FT.)	INSIDE	OUTSIDE PERCENT
2874.000	274.44848	16.88706	16.88706	1.00000	578.99741	45.29236	3.00000	1.74783

PRES DROP,PSI		UAM	CPM	DPSUM	SHOKI	SHOKO	AFACE	ETAI	ETAO
INSIDE	OUTSIDE		0.0	(PERCENT)			(SQ FT)		
0.4140	C.1176	3.7625	41.7391	4.7478	1.5000	1.5000	1.9804	1.0000	1.0000

NTHI,	NATC	UA	REI	REO	GI	GO	RHO	
BTU/SEC R	BTU/SEC R	BTU/SEC R			LB/SEC SQ FT	LB/SEC SQ FT	(FT)	EAX
4.23607	2.31810	1.51395	585.59352	548.55687	C.95638	0.47437	0.00816	0.94943

INSIDE SURFACE IS PL TB OUTSICE SURFACE IS PL TB

TUBE DIA	XT	XL	WALL T	TURB. T	FIN T	FIN HT	NO. OF
(IN)			(IN)	(IN)	(IN)	(IN)	FINS
0.21C00	1.5CC00	1.50C00	C.C0400	0.C0C00	C.00000	0.00000	0.00000

NO. TUBES	TUBE L	FACE HT	FACE W	ASPECT	WEIGHT	VOLUME	PRESSURE DROP	
	(IN)	(IN)	(IN)		(LB)	(CU. FT.)	INSIDE	OUTSIDE PERCENT
2874.C00	274.44848	16.88706	16.88706	1.00000	578.99741	45.29236	3.00000	1.74783

PRES DROP,PSI		UAM	DPM	DPSUM	SHOKI	SHCKO	AFACE	ETAI	ETAO
INSIDE	OUTSIDE		0.0	(PERCENT)			(SQ FT)		
0.4140	C.1176	3.7625	41.7391	4.7478	1.5000	1.5000	1.9804	1.0000	1.0000

NTHI,	NATC	UA	REI	REO	GI	GO	RHO	
BTU/SEC R	BTU/SEC R	BTU/SEC R			LB/SEC SQ FT	LB/SEC SQ FT	(FT)	EAX
4.23607	2.31810	1.51395	585.59352	548.55687	C.95638	0.47437	0.00816	0.94943

Figure C-2. Typical Long Form Output for First Two Cases of Figure 2

the allowable pressure drop on either side and which utilizes all the available pressure drop on one side, the program then calculates the heat transfer capabilities of this tube bundle. If this estimated value of the heat transfer capabilities is not sufficient to meet the required problem conditions an adjustment is made to the free-flow area on the controlling side of the heat exchanger and the pressure drop and heat transfer calculations repeated. This process is repeated until a satisfactory solution is found which meets both the heat transfer and pressure drop requirements. The effect of axial conduction on this heat exchanger design is then calculated. The method utilized to determine the effect of axial conduction on this heat exchanger is that determined by AiResearch and described in some detail in Appendix A. At the present time the method utilized by the program is the limited case solution, that is, the case that requires the capacity rates and heat transfer conductances to be the same on both sides of the heat exchanger. As the capacity rate ratio for the recuperator for the solar powered Brayton cycle system is one, this is a valid approximation for calculating the effect of axial conduction in this particular application.

Having determined the effectiveness of the heat exchanger design with the allowance for axial conduction, the program then compares this effectiveness with the effectiveness required. If the two values of effectiveness, that is, the required effectiveness and the calculated effectiveness, do not fall within one tenth of one percent of each other the program then designs a second heat exchanger. As in the previous design iteration, a factor is applied to the controlling side free-flow area, a new tube bundle size is determined and its effectiveness allowing for axial conduction again compared with the required effectiveness. The process is again repeated until a satisfactory solution is determined. All loops (iteration processes) are counted and if no convergence is found within the specified number of iterations the attempt to find a solution for that particular problem is abandoned. When this occurs a message informing the program's user of this failure to converge is printed out together with a solution available in the machine at that time. The program then moves on to the next problem condition. With the finally accepted solution for any problem conduction, heat exchanger weight, actual dimensions, and performance margins (always present due to tolerances or convergence) are estimated and the solutions made available as output data sheets in either the short or long form described above.

The above described computer program was written for the IBM 7074 Digital Computer (an AiResearch in-house facility). Utilizing this program on this machine, it is possible to obtain solutions for approximately 25 different matrix surfaces in one minute of operating time. This program can, therefore, be utilized to determine solutions for a large number of surfaces and a large number of problem conditions with minimum usage of either engineering or machine time.

END SECTION PRESSURE LOSS COMPUTER PROGRAM

There are two types of end section design, triangular and rectangular, which may be considered. The program will calculate the pressure losses in the four individual ends of either type of design. The approach taken to determining the pressure losses in the two types of design is slightly different, and they are described separately below. The approach used in this computer program is theoretical only, but it is believed that the theory used will accurately determine the true pressure losses. However, the overall pressure losses determined by use of this program were treated as approximations during this program and final definition of the pressure drop was not made until the completion of the flow distribution tests. While the paragraphs below describe both the approach used for triangular and rectangular end shape designs, throughout this program only triangular end sections were considered. This is due to the very low available pressure losses in the Brayton cycle application.

TRIANGULAR END SHAPE DESIGNS

It is first necessary to define the geometry of the ends. Some of this is obtained directly from the design of the counterflow matrix. Information used from the core design includes core widths, stack-up height, number of passages on both sides and plate spacing on both sides. In addition, the height (h) of the ends must be defined, together with the number of fins and the fin thickness to be used on both sides of the ends. One further parameter is required to define end geometry, and the one chosen is the ratio a/w defined in Figure D-1. With the end geometry defined, the effective flow width and length in the ends for both the high pressure and low pressure fluids is calculated. These effective dimensions are also defined in Figure D-1. With both flow rates and all terminal pressure and temperature conditions of the heat exchanger known, the pressure losses are computed by the following steps. Mass velocity on one side of one end is computed using the appropriate flow and based on the effective flow width. Reynolds number is computed from viscosity (read curve) and from hydraulic diameter of the fin spacing selected (calculated within the program). Friction factor is also obtained from an appropriate stored curve (Reynolds number versus friction factor for surface to be considered is part of the program input). An entrance shock loss coefficient is determined from the area ratio (end section free flow area to frontal area) from a stored curve. Other curves used by the computer program are the laminar expansion and construction coefficients and the turbulent expansion and contraction coeefficients taken from "Compact Heat Exchangers" by W. Kays and A. L. London (Reference 1). If the end section Reynolds number is lower than 2000, the laminar curves are used. For Reynolds numbers above this value the turbulent curves are used. A second expansion or contraction loss is allowed for between the end section and the straight counterflow core based on the area ratio between the end section free flow area and the counterflow core free flow area. At this junction, there is also a turning loss based on the angle θ defined in Figure D-1. The coefficient for this turning loss is taken from the SAE Aeronautical Information Report No. 23 (Reference 2).
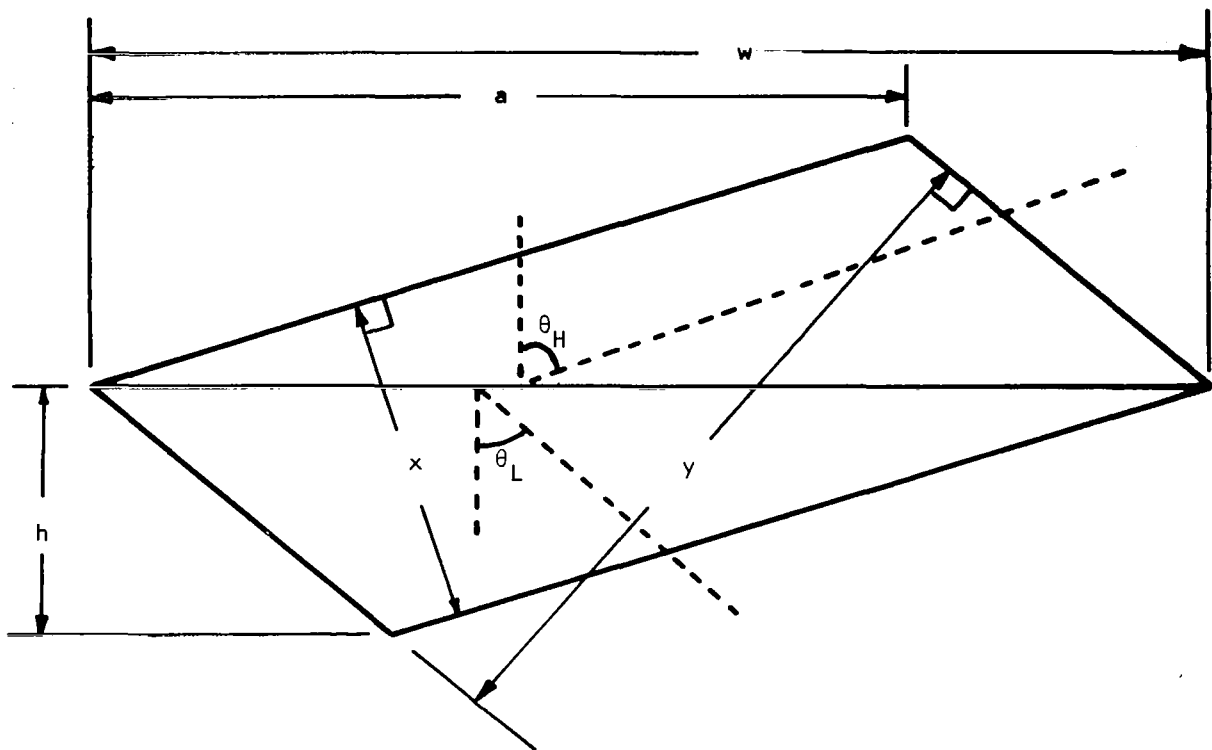
EFFECTIVE FLOW WIDTH (LP) = y

EFFECTIVE FLOW WIDTH (HP) = x

EFFECTIVE FLOW LENGTH (LP) PER END = x/2

EFFECTIVE FLOW LENGTH (HP) PER END = y/2

TURNING ANGLE (LP) = θ_L $\Big\}$ SIN θ IS USED IN PROGRAM
TURNING ANGLE (HP) = θ_H

NOTE: SKETCH SHOWS TWO ENDS OF TRIANGULAR DESIGN TOGETHER, WITH CORE REMOVED

A-18420

Figure D-1. Triangular End Geometry

The overall pressure loss is then computed from the sum of the friction term, the inlet face shock loss, the velocity head change and turning loss at the junction of the ends with the core. Each of the four ends, low pressure inlet and outlet and high pressure inlet and outlet, are computed separately at the appropriate fluid properties and with the appropriate type of shock loss (expansion or contraction). The two ends of the heat exchanger are identical in the calculations, but if non-similar ends are required, the results obtained from different solutions may be combined.

RECTANGULAR END SHAPE DESIGN

With this type of design and with the core geometry specified, only the height (h) and the fin characteristics of the end need be defined. In the straight through (low pressure) side of the unit, the pressure loss in the ends is computed from a friction term and from a single shock loss based on the free flow to frontal area ratio. In the high pressure side where the flow enters at right angles to its flow path in the core, the pressure losses are more complicated. Two velocity heads are computed, one based on entrance and exit areas "that is, based on h), and one based on the second set of fins in the end (uses core width, w). Using the velocity head based on h, a friction term is calculated for the first set of fins, a shock loss for the entrance or exit, and a shock loss (expansion or contraction) from these fins into the second set. A turning loss coefficient, also based on the "h" velocity head, is added to the pressure loss. This coefficient is an input quantity and should normally be based on a 90° turn (1.6 from SAE 23). The turning coefficient was left as an input quantity so that it may be varied at the users discretion. This approach is of particular advantage if test data is obtained, as the coefficient may be varied until agreement with the test data is achieved. The velocity head and the second set of fins is used only to compute a friction drop through that section.

INPUT REQUIREMENTS

The above described computer program was written in Fortran for use in a high speed digital computer. The complete listing of the input parameters required for this program is shown in Table I. This table defines the name of the parameter as used in the program together with its physical meaning. In addition to the parameters defined in Table I, further information is available in the program in the form of the Lagrangian tables. This method of providing input information permits the computer to interpolate accurately, information normally in a curve form. There are a total of nine tables of information given in the computer program and these are listed below.

Table 1. Temperature ($^\circ$R) vs Viscosity (lb per sec ft) for pressure side fluid.

Table 2. Temperature ($^\circ$R) vs Viscosity (lb per sec ft) for high pressure side fluid.

Table 3. Reynolds number vs friction factor for low pressure side fins.

TABLE D-I

END SECTION
COMPUTER PROGRAM INPUT

CARD I   Title of Job to be Run

    Insert Tables at this point

CARD 2.   Control Card for Other Variables (3I5)

JI	No. of sets of cards 3 and 4 (5 max)
J2	No. of sets of cards 5 and 6 (I2 max)
J3	No. of sets of cards 7 (50 max)

CARD 3.

WIDTH	Heat exchanger core width - In.
ANPL	Total No. of passages on low pressure side of heat exchanger
ANPH	Total No. of passages on high pressure side of heat exchanger
ALN	Stack-up height of heat exchanger, In.
HPL	Plate spacing, low pressure side, In.
HPH	Plate spacing, high pressure side, In.
TEST I =	0.0 if triangular ends = I.0 if rectangular ends
BWL	Ac/bw for fins in counterflow core, low pressure side.

CARD 4.

BWH	Ac/bw for fins in counterflow core, high pressure side
WTF	Weight factor, Weight of ends = WTF X Volume
AK	Turning loss coefficient for rectangular ends
	(Normally = I.6 rectangular 0.0 triangular)

CARD 5.

WL	Flow rate, low pressure side, lb per sec
WH	Flow rate, high pressure side, lb per sec
TINL	Inlet temperature, L.P. side, °R
TINH	Inlet temperature, H.P. side, °R
TOUTL	Outlet temperature, L.P. side, °R
TOUTH	Outlet temperature, H.P. side, °R
PINL	Inlet pressure, L.P. side, psia
PINH	Inlet pressure, H.P. side, psia

CARD 6.

POUTL	Outlet pressure, L.P. side, psia
POUTH	Outlet pressure, H.P. side, psia
ROEL	Density factor, L.P. side $\rho = \text{ROEL} \frac{P, \text{ psia}}{T, {}^{\circ}R}$
ROEH	Density factor, H.P. side

CARD 7.

HEIGHT	Height of triangle or rectangle, defined in Figure 36.
RATIO	a/w as defined in Figure 36 if greater than 0.5 wider face will be low pressure side, if less than 0.5 wider face will be high pressure side.
ANFL*	No. of fins per inch, in low pressure ends.
ANFH	No. of fins per inch, in high pressure ends.
TFL	Fin thickness of fins in low pressure ends, In.
TFH	Fin thickness of fins in high pressure ends, In.

*If desired to look at zero fins on either side ANF = 0.0 and also TF = 0.0. Care should be taken in this case to be sure that friction factor is for flow between flat plates.

Table 4.   Reynolds number vs friction factor for high pressure side fins.

Table 5.   Area Ratio vs Laminar Expansion Coefficients.

Table 6.   Area Ratio vs Laminar Contraction Coefficients.

Table 7.   Area Ratio vs Turbulent Expansion Coefficient.

Table 8.   Area Ratio vs Turbulent Contraction Coefficients.

Table 9.   Turning Angle vs Turning Coefficient.

The data used in these tables may be stored up to 30 pairs of points and interpolation of tables is performed by the computer by drawing a second order curve through the nearest three points to the table entrance value.

OUTPUT INFORMATION

A typical output sheet from this computer program is shown in Figure The first line of data shows the flow, temperature, pressure data being determined. The second line defines the end geometry being evaluated while the third line identifies the counterflow core. The fourth line of computer output presents the solutions for all four end pressure drops. Here, pressure drops are shown in both psia and as a percentage of the inlet pressure on the appropriate side. The fifth and last line of the output presents some additional information which may be of benefit to the user. This information includes the volume of one end, the length of the two sides of the triangular end and also the appropriate hydraulic radii and the Reynolds number in all four end sections.

REFERENCES

1.   Kays, W. M., and London, A. L., _Compact Heat Exchangers_, McGraw-Hill, 1958

2.   SAE Aeronautical Information Report, No. 23, Fluid Dynamics, October 15, 1951.

R 1 0.15600E 04
R 21 0.14860E 04

	LOW PRESSURE SIDE					HIGH PRESSURE SIDE			
FLOW LB/SEC	INLET TEMP R	OUTLET TEMP R	PRESS IN PSIA	PRES OUT PSIA	FLOW LB/SEC	INLET TEMP R	OUTLET TEMP R	PRESS IN PSIA	PRES OUT PSIA
0.6120	1560.000	875.000	6.730	6.960	0.6120	801.000	1486.000	13.800	13.730

HEIGHT,IN	RATIO	TEST1	RECT.TURN CON	NO.FIN(LP)	NO.FIN(HP)	FIN THICK(LP),IN	FIN THICK(HP),IN
9.000	0.5000	0.0	0.000	0.00	5.00	0.0000	0.0040

WIDTH,IN=23.2600   NO.FLOW,IN= 23.290   PASSAGE HT.(LP)=.178   PASSAGE HT.(HP)=.153

	LOW PRESSURE SIDE,PRESSURE DROPS				HIGH PRESSURE SIDE,PRESSURE DROPS		
INLET,PSIA	OUTLET,PSIA	INLET,PERCENT	OUTLET,PERCENT	INLET,PSIA	OUTLET,PSIA	INLET,PERCENT	OUTLET,PERCENT
0.0067	0.0028	0.0996	0.0414	0.0081	0.0225	0.0586	0.1631

VOLUME,CU.IN	WEIGHT,LB	DIMENSIONS,IN		L.P. RH,FT	H.P. RH,FT	IN RE (LP)	OUT RE (LP)	IN RE (HP)	OUT RE (HP)
2437.7643	2437.7643	14.706	14.706	0.007417	0.003527	351.47	522.20	646.71	422.50

. . . .

R 1 0.15600E 04
R 21 0.14860E 04

	LOW PRESSURE SIDE					HIGH PRESSURE SIDE			
FLOW LB/SEC	INLET TEMP R	OUTLET TEMP R	PRESS IN PSIA	PRES OUT PSIA	FLOW LB/SEC	INLET TEMP R	OUTLET TEMP R	PRESS IN PSIA	PRES OUT PSIA
0.6120	1560.000	875.000	6.730	6.960	0.6120	801.000	1486.000	13.800	13.730

HEIGHT,IN	RATIO	TEST1	RECT.TURN CON	NO.FIN(LP)	NO.FIN(HP)	FIN THICK(LP),IN	FIN THICK(HP),IN
9.000	0.6500	0.0	0.000	0.00	5.00	0.0000	0.0040

WIDTH,IN=23.2600   NO.FLOW,IN= 23.290   PASSAGE HT.(LP)=.178   PASSAGE HT.(HP)=.153

	LOW PRESSURE SIDE,PRESSURE DROPS				HIGH PRESSURE SIDE,PRESSURE DROPS		
INLET,PSIA	OUTLET,PSIA	INLET,PERCENT	OUTLET,PERCENT	INLET,PSIA	OUTLET,PSIA	INLET,PERCENT	OUTLET,PERCENT
0.0047	0.0020	0.0702	0.0290	0.0118	0.0321	0.0855	0.2327

VOLUME,CU.IN	WEIGHT,LB	DIMENSIONS,IN		L.P. RH,FT	H.P. RH,FT	IN RE (LP)	OUT RE (LP)	IN RE (HP)	OUT RE (HP)
2437.7643	2437.7643	17.595	12.136	0.007417	0.003527	290.05	430.94	773.78	505.51

. . . .

R 1 0.15600E 04
R 21 0.14860E 04

	LOW PRESSURE SIDE					HIGH PRESSURE SIDE			
FLOW LB/SEC	INLET TEMP R	OUTLET TEMP R	PRESS IN PSIA	PRES OUT PSIA	FLOW LB/SEC	INLET TEMP R	OUTLET TEMP R	PRESS IN PSIA	PRES OUT PSIA
0.6120	1560.000	875.000	6.730	6.960	0.6120	801.000	1486.000	13.800	13.730

HEIGHT,IN	RATIO	TEST1	RECT.TURN CON	NO.FIN(LP)	NO.FIN(HP)	FIN THICK(LP),IN	FIN THICK(HP),IN
9.000	0.7500	0.0	0.000	0.00	5.00	0.0000	0.0040

Figure D-2. Typical Output

A-10421

STRESS ANALYSIS OF RECUPERATOR MOUNTING
AND SYSTEM INTEGRATION

ASSUMPTIONS

1. Consider the whole unit, including the pipes connected to the pans, as a rigid body.

2. The positions of the centers of mass are picked up by estimates based on the NASA Drawing dated July 20, 1966.

3. The whole unit is supported at S_i ($i = 1$, through $i = 4$) as shown in Figure E-1.

4. Attach a set of mutually perpendicular unit vectors $\underline{n}_i$ ($i = 1, 2, 3$) to the unit and let OX_i ($i = 1, 2, 3$) be the associated axes.

LOADS FORMULATION

Inertia Forces

Suppose there are n rigid bodies B_i ($i = 1, n$) of mass m_i, and B_i^* the corresponding mass center. Let $\underline{a}$ be the acceleration vector of the system, E_i the inertia forces exerted at B_i^* due to $\underline{a}$, then

$$\underline{F}_i = -m_i\underline{a} \tag{1}$$

$$i = 1, .., n$$

where

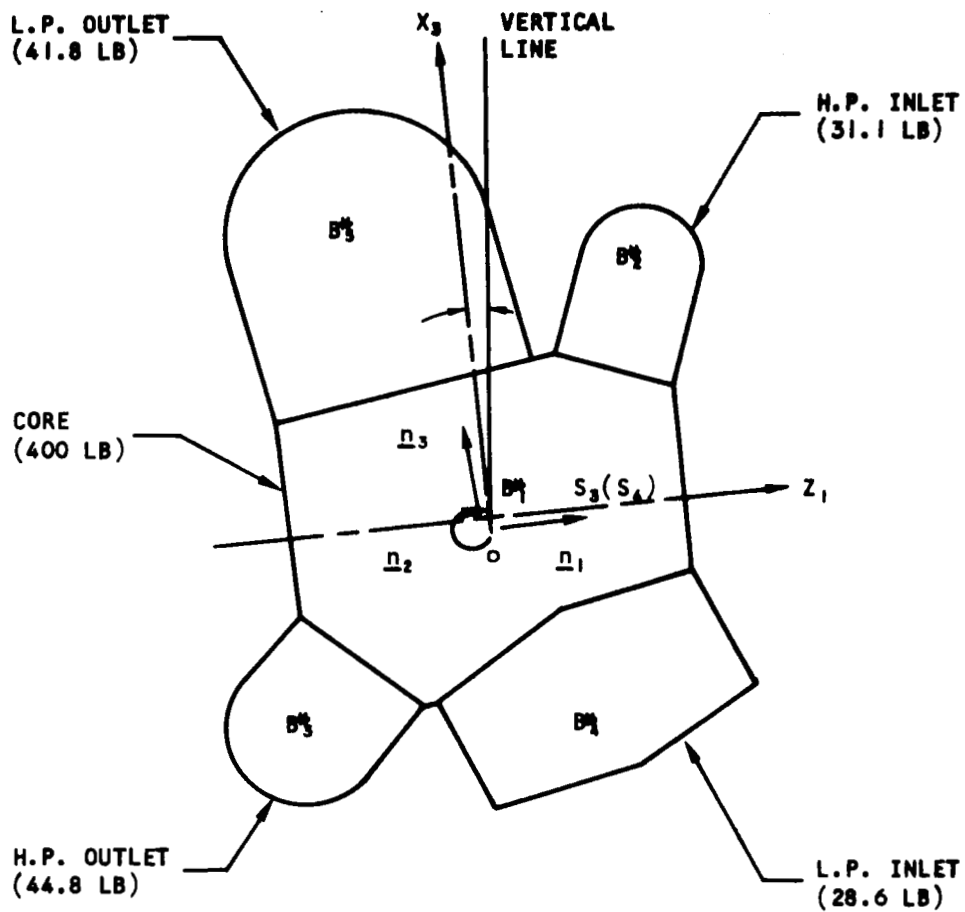$$\underline{a} = \sum_{j=1}^{3} a_j\underline{n}_j \tag{2}$$

$$i = 1, .., n$$

write

$$\underline{F}_i = \sum_{j=1}^{3} F_{ij}\underline{n}_j \tag{3}$$

$$i = 1, .., n$$

where

$$F_{ij} = -m_i\underline{a}_j \tag{4}$$

$$i = 1, .., n: \quad j = 1, 2, 3$$

Figure E-I. Loads Formulation

NOTE:

    H.P. - HIGH PRESSURE
    L.P. - LOW PRESSURE

Let $\underline{r}_i$ $(i = 1, .., n)$ be the position vectors of B_i^* relative to 0. The "equivalence" of this set of inertia forces relative to 0 can be represented by a single force $\underline{F}$ and a torque $\underline{T}$,

$$\underline{F} = \sum_{i=1}^{n} \underline{F}_i = \sum_{i=1}^{n} \sum_{j=1}^{3} F_{ij} \underline{n}_j = \sum_{j=1}^{3} \left[\sum_{i=1}^{n} F_{ij} \right] \underline{n}_j$$

$$= \sum_{j=1}^{3} F_j \underline{n}_j \tag{5}$$

where

$$F_j = \sum_{i=1}^{n} F_{ij} \tag{6}$$

and

$$\underline{T} = \sum_{i=1}^{n} \underline{r}_i \times \underline{F}_i \tag{7}$$

$\underline{r}_i$ can be resolved into three components parallel to $\underline{n}_i$ $(i=1, 2, 3)$, i.e.,

$$\underline{r}_i = \sum_{j=1}^{3} r_{ij} \underline{n}_j \tag{7a}$$

substitution Equations (3) and (7a) into (7) yields

$$\underline{T} = \sum_{j=1}^{3} T_j \underline{n}_j \tag{8}$$

where

$$T_1 = \sum_{i=1}^{n} [r_{i2} F_{i3} - r_{i3} F_{i2}]$$

$$T_2 = \sum_{i=1}^{n} [r_{i3} F_{i1} - r_{i1} F_{i3}] \tag{9}$$

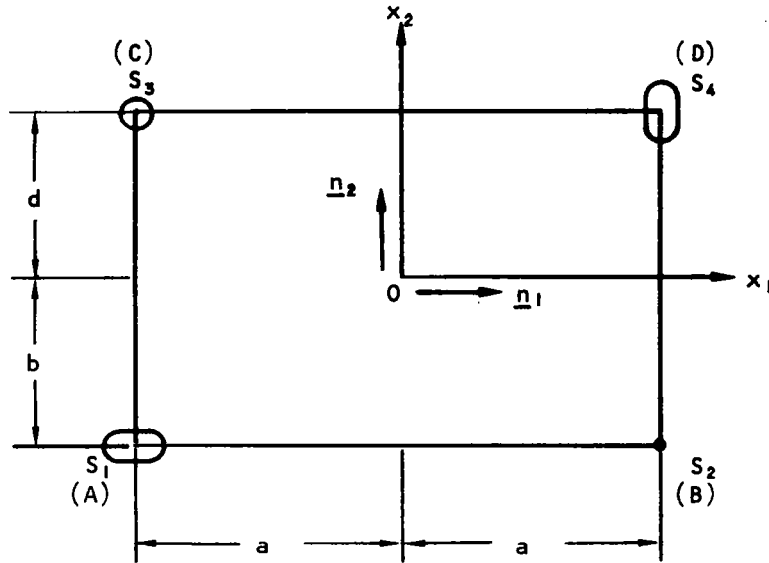$$T_3 = \sum_{i=1}^{n} [r_{i1} F_{i2} - r_{i2} F_{i1}]$$

168

Figure E-2

In order to allow the expansion due to thermal growth, we make two slots at S_1 and S_4 with their longer axes parallel to OX_1 and OX_2 axes respectively, an oversized hole at S_3 and a fixed hinge at S_2 as shown in Figure E-2. Consequently, the $\underline{P}_i$'s and $\underline{P}_i^*$'s are under certain restrictions, i.e.,

S_1 Can <u>not</u> resist the forces in $\pm\underline{n}_1$ direction

S_2 Can resist force of <u>any</u> direction

S_3 Can <u>only</u> resist the forces in $\pm\underline{n}_3$ direction

S_4 Can <u>not</u> resist the forces in $\pm\underline{n}_2$ direction

Based on the above assumptions, we may write the reaction forces Q_i ($i = 1, .., 4$) as

$$\underline{Q}_1 = Q_{12}\,\underline{n}_2 + Q_{13}\,\underline{n}_3$$
$$\underline{Q}_2 = Q_{21}\,\underline{n}_1 + Q_{22}\,\underline{n}_2 + Q_{23}\,\underline{n}_3$$
$$\underline{Q}_3 = Q_{33}\,\underline{n}_3$$
$$\underline{Q}_4 = Q_{41}\,\underline{n}_1 + Q_{43}\,\underline{n}_3$$

(10)

Let S_i ($i = 1$, through 4) be the supports and $\underline{P}_i$ be the reaction forces due to $\underline{F}$ alone, and they can be resolved into three components parallel $\underline{n}_1$, $\underline{n}_2$, $\underline{n}_3$, i.e.,

$$\underline{P}_i = \sum_{j=1}^{3} P_{ij} \underline{n}_j$$

$$i = 1, .., 4 \tag{11}$$

from equilibrium, we obtain

$$\sum_{i=1}^{4} \underline{P}_i = \underline{F} \tag{12}$$

Furthermore, let $\underline{\eta}_i$ be the position vectors of S_i relative to 0, then

$$\underline{\eta}_i = \sum_{j=1}^{3} \eta_{ij} \underline{n}_j \tag{13}$$

$$\sum_{i=1}^{4} \underline{\eta}_i \times \underline{P}_i^* = \underline{T} \tag{14}$$

where $\underline{P}_i^*$ are the reaction forces at S_i due to $\underline{T}$ alone.

1. Due to $\underline{F}$

$$\underline{P}_1 = P_{12} \underline{n}_2 + P_{13} \underline{n}_3$$

$$\underline{P}_2 = P_{21} \underline{n}_1 + P_{22} \underline{n}_2 + P_{23} \underline{n}_3$$

$$\underline{P}_3 = P_{33} \underline{n}_3 \tag{15}$$

$$\underline{P}_4 = P_{41} \underline{n}_1 + P_{43} \underline{n}_3$$

$$P_{21} + P_{41} = -F_1$$

$$P_{12} + P_{22} = -F_2 \tag{16}$$

$$P_{13} + P_{23} + P_{33} + P_{43} = -F_3$$

Since

$$P_{21} = P_{41}$$

$$P_{12} = P_{22} \tag{17}$$

$$P_{13} = P_{23} = P_{33} = P_{43}$$

Then

$$P_{21} = P_{41} = -\frac{1}{2}F_1$$

$$P_{12} = P_{22} = -\frac{1}{2}F_2 \tag{18}$$

$$P_{13} = P_{23} = P_{33} = P_{43} = -\frac{1}{4}F_3$$

2. **Due to $\underline{T}$**

$$\underline{P}_1{}^* = P_{12}{}^*\,\underline{n}_2 + P_{13}{}^*\,\underline{n}_3$$

$$\underline{P}_2{}^* = P_{21}{}^*\,n_1 + P_{22}{}^*\,\underline{n}_2 + P_{23}{}^*\,\underline{n}_3$$

$$\underline{P}_3 = P_{33}{}^*\,\underline{n}_3 \tag{19}$$

$$\underline{P}_4 = P_{41}{}^*\,\underline{n}_1 + P_{43}{}^*\,\underline{n}_3$$

3. **Due to T_I (T_1)**

$$\underline{T} = T_I\,\underline{n}_1 + T_{II}\,\underline{n}_2 + T_{III}\,\underline{n}_3 = \sum_{i=1}^{3} T_i\underline{n}_i$$

$$P_{13}^I = P_{23}^I = -P_{33}^I = P_{43}^I \tag{20}$$

$$[(2\,P_{13}^I)(2b)] = T_1$$

$$4bP_{13}^I = T_1$$

$$P_{13}^I = \frac{T_1}{4b} \tag{21}$$

4. **Due to T_{II} (T_2)**

$$P_{23}^{II} = P_{43}^{II} = -P_{13}^{II} = -P_{33}^{II} \tag{22}$$
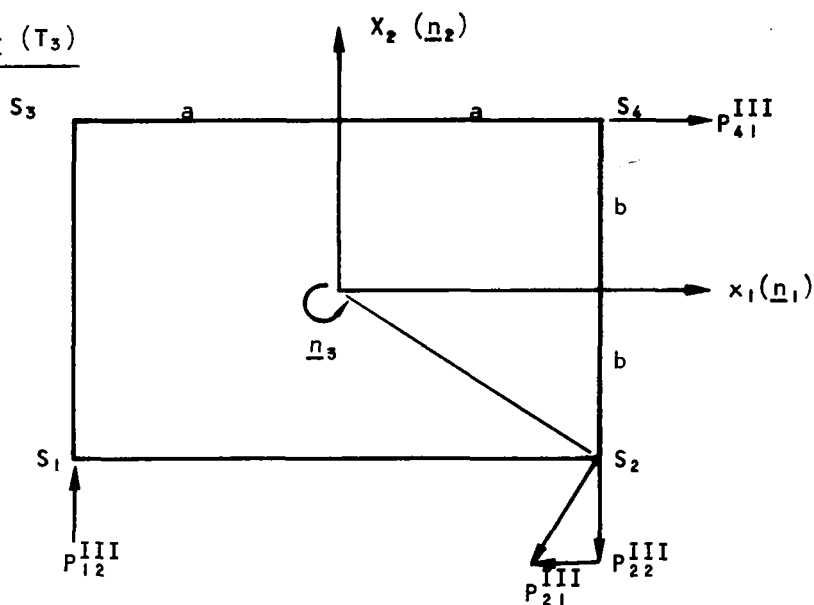
$$4aP_{23}^{II} = T_2$$

$$P_{23}^I = \frac{T_2}{4a} \tag{23}$$

5. Due to T_{II} (T_3)

Figure E-3

$$\left[\begin{cases} P^{III}_{41} = -P^{III}_{21} \\ P^{III}_{12} = -P^{III}_{22} \end{cases}\right] \tag{24}$$

$$2aP^{III}_{21} + 2bP^{III}_{41} = T_3 \tag{25}$$

$$\frac{P^{III}_{21}}{P^{III}_{22}} = \frac{b}{a} = \frac{P^{III}_{41}}{P^{III}_{12}} \tag{26}$$

$$\boxed{P^{III}_{41} = \left(\frac{b}{a}\right) P^{III}_{12}} \tag{27}$$

Substitute (27) into (25) and solve for P^{III}_{12},

$$2aP^{III}_{12} + 2b\left(\frac{b}{a}\right) P^{III}_{12} = T_3$$

$$2a\left(1 + \frac{b^2}{a^2}\right) P^{III}_{12} = T_3$$

$$\boxed{P^{III}_{12} = \frac{T_3}{2a\left(1 + \frac{b^2}{a^2}\right)}} \tag{28}$$

172

From Equations (19) ~ (28), we obtain

$$P_{12}^* = \frac{1}{2a(1 + \frac{b^2}{a^2})} T_3 = C_1 T_3 \tag{29}$$

$$P_{13}^* = \frac{T_1}{4b} - \frac{T_2}{4a} = C_2 T_1 - C_3 T_2$$

$$P_{21}^* = \frac{-(b/a)}{2a(1 + \frac{b^2}{a^2})} T_3 = C_4 T_3$$

$$P_{22}^* = -\frac{1}{2a(1 + \frac{b^2}{a^2})} T_3 = -C_1 T_3 = -P_{12}^* \tag{30}$$

$$P_{23}^* = \frac{T_1}{4b} + \frac{T_2}{4a} = C_2 T_1 + C_3 T_2$$

$$P_{33}^* = -(\frac{T_1}{4b} + \frac{T_2}{4a}) = -P_{23}^* \tag{31}$$

$$P_{41}^* = \frac{(b/a)}{2a(1 + \frac{b^2}{a^2})} T_3 = -P_{21}^* \tag{32}$$

$$P_{43}^* = \frac{T_2}{4a} - \frac{T_1}{4b} = -P_{13}^*$$

$$Q_{12} = P_{12} + P_{12}^*$$

$$Q_{13} = P_{13} + P_{13}^*$$

$$\left. \begin{array}{l} Q_{21} = P_{21} + P_{21}^* \\ Q_{22} = P_{22} + P_{22}^* \end{array} \right\} \quad Q_{2s} = \sqrt{Q_{21}^2 + Q_{22}^2}$$

$$Q_{23} = P_{23} + P_{23}^* \tag{33}$$

$$Q_{33} = P_{33} + P_{33}^*$$

$$Q_{41} = P_{41} + P_{41}^*$$

$$Q_{43} + P_{43} + P_{43}^*$$

173

LOAD CALCULATIONS

TABLE E-I

LOAD DATA

Name	Center of Mass	Mass	Estimated Maximum Weight, lb	X_1, in.	X_2, in.	X_3, in.
Core	B_1	M_1	400	0 (10.97)	0	0 (1.24)
High pressure inlet	B_2	M_2	31.1	7.75 (-1.12)	0	9.92 (-1.05)
High pressure outlet	B_3	M_3	44.8	-8.95 (0.5)	0	-8.40 (-1.1)
Low pressure inlet	B_4	M_4	28.6	4.00 (-0.53)	0	-8.80 (1.58)
Low pressure outlet	B_5	M_5	41.8	-4.23 -0.19	0 -4.95	12.62 1.90
High pressure in pipe	B_6	M_6	10	-1.52 -2.35	-39.50 0	15.20 -2.35
High pressure out pipe	B_7	M_7	5	-18.80 0.1	0 -4.45	-18.80 -1.07
Low pressure in pipe	B_8	M_8	15	0.80 -1.50	-35.60 -1.63	-8.55 -4.13
Low pressure out pipe	B_9	M_9	20	-12.00	-13.05	33.00

a. $F_{ij} = - M_i a_j$

$F_{11} = - M_1 a_1 = - m_1 g = - 400$

Therefore, F_{ij} are given as follows:

F_{ij}	$j = 1$	$j = 2$	$j = 3$
$i = 1$	-400	0	0
$i = 2$	-32	0	0
$i = 3$	-45	0	0
$i = 4$	-29	0	0
$i = 5$	-42	0	0
$i = 6$	-10	0	0
$i = 7$	-5	0	0
$i = 8$	-15	0	0
$i = 9$	-20	0	0

b. F_j and T_j $(j = 1, 2, 3)$

$F_1 = - \dfrac{598}{g} g = - 598 \text{ lb}$

$F_2 = 0$

$F_3 = 0$

$$T_1 = \sum_{i=1}^{9} [r_i F_{i3} - r_{i3} F_{i2}]$$

$r_{12}F_{13} - r_{13}F_{12} = 0$

$r_{22}F_{23} - r_{23}F_{22} = 0$

$r_{32}F_{33} - r_{33}F_{32} = 0$

$r_{42}F_{43} - r_{43}F_{42} = 0$

$r_{52}F_{53} - r_{53}F_{52} = 0$

$r_{62}F_{63} - r_{63}F_{62} = 0$

$$r_{72}F_{73} - r_{73}F_{72} = 0$$

$$r_{82}F_{83} - r_{83}F_{82} = 0$$

$$r_{92}F_{93} - r_{93}F_{92} = 0$$

$$\boxed{T_1 = 0}$$

$$T_2 = \sum_{i=1}^{9} \left[r_{i3}F_{i1} - r_{i1}F_{i3} \right]$$

$$r_{13}F_{11} - r_{11}F_{13} = 0$$

$$r_{23}F_{21} - r_{21}F_{23} = (9.92)(-32) = -317$$

$$r_{33}F_{31} - r_{31}F_{33} = (-8.4)(-45) = 378$$

$$r_{43}F_{41} - r_{41}F_{43} = (-8.8)(-29) = 255$$

$$r_{53}F_{51} - r_{51}F_{53} = (12.62)(-42) = -531$$

$$r_{63}F_{61} - r_{61}F_{63} = (15.12)(-10) = -152$$

$$r_{73}F_{71} - r_{71}F_{73} = (-18.8)(-5) = +94$$

$$r_{83}F_{81} - r_{81}F_{83} = (-8.55)(-15) = +128$$

$$r_{93}F_{91} - r_{91}F_{93} = (33)(-20) = -660$$

$$\boxed{T_2 = -805 \text{ lb-in.}}$$

$$T_3 = \sum_{i=1}^{9} \left[r_{i1}F_{i2} - r_{i2}F_{i1} \right]$$

$$r_{11}F_{12} - r_{12}F_{11} = 0$$

$$r_{21}F_{22} - r_{22}F_{21} = 0$$

$$r_{31}F_{32} - r_{32}F_{31} = 0$$

$$r_{41}F_{42} - r_{42}F_{41} = 0$$

$$r_{51}F_{52} - r_{52}F_{51} = 0$$

$$r_{61}F_{62} - r_{62}F_{61} = -(-39.5)(-10) = -395$$

$$r_{71}F_{72} - r_{72}F_{71} = 0$$

$$r_{81}F_{82} - r_{82}F_{81} = -(-35.16)(-15) = -534$$

$$r_{91}F_{92} - r_{92}F_{91} = -(-13.05)(-20) = -261$$

$$\longrightarrow \underline{T_3 = -1190 \text{ lb-in.}}$$

Take $\underline{a} = g\underline{n}_2$

$$a_1 = a_3 = 0$$

$$a_2 = g$$

a. $F_{ij} = -M_i a_j$

$F_{12} = -400$

$F_{22} = -32$

$F_{32} = -45$

$F_{42} = -29$

$F_{52} = -42$ $\qquad\qquad\qquad i = 1, \cdots, 9$

$F_{62} = -10$

$F_{72} = -5$

$F_{82} = -15$

$F_{92} = -20$

$F_{i1} = F_{i3} = 0$

b. F_j and T_j $(j = 1, 2, 3)$

$F_1 = 0$

$F_2 = -598$ lb

$F_3 = 0$

$$T_1 = -[r_{13}F_{12} + r_{23}F_{22} + r_{33}F_{32} + r_{43}F_{42} + r_{53}F_{52} + r_{63}F_{62}$$
$$+ r_{73}F_{72} + r_{83}F_{82} + r_{93}F_{92}]$$
$$= -[(0)(-400) + (9.92)(-32) + (-8.4)(-45) + (-8.8)(-29)$$
$$+ (12.62)(-42) + 1512(-10) + (-18.8)(-5)$$
$$+ (-8.55)(-15) + (33)(-20)]$$

$\underline{T_1 = 805 \ \text{lb-in.}}$

$\underline{T_2 = 0}$

$$T_3 = \sum_{i=1}^{9} [r_{i1}F_{i2} - r_{i2}F_{i1}]$$
$$= [r_{11}F_{12} + r_{21}F_{22} + r_{31}F_{32} + r_{41}F_{42} + r_{51}F_{52}$$
$$+ r_{61}F_{62} + r_{71}F_{72} + r_{81}F_{82} + r_{91}F_{92}]$$
$$= [(0)(-400) + (7.75)(-32) + (-8.95)(-45) + (4.0)(-29)$$
$$+ (-4.23)(-42) + (-1.52)(-10) + (-18.8)(-5)$$
$$+ (0.8)(-15) + (-12)(-20)]$$

$\underline{T_3 = +553.2 \ \text{lb-in.}}$

Take $\underline{a} = g\underline{n}_3$

$$a_1 = a_2 = 0$$
$$a_3 = g$$

a. $\quad F_{ij} = -M_i a_j$

$$F_{i2} = F_{i3} = 0$$

for $\ i = 1, \cdots, 9$

178

F_{ij} $j = 3, \ i = 1, \cdots, 9$

$F_{13} = -400$	$F_{63} = -10$
$F_{23} = -32$	$F_{73} = -5$
$F_{33} = -45$	$F_{83} = -15$
$F_{43} = -29$	$F_{93} = -20$
$F_{53} = -42$	

b. F_j and T_j $(j = 1, \cdots, 3)$

$F_1 = -Ma_1 = 0$

$F_2 = -Ma_2 = 0$

$F_3 = -Ma_3 = -598 \ lb$

$T_1 = \sum_{i=1}^{9} [r_{i2}F_{i3} - r_{i3}F_{i2}]$

$= [r_{12}F_{13} = r_{22}F_{23} + r_{32}F_{33} + r_{42}F_{43} + r_{52}F_{53}$

$+ r_{62}F_{63} + r_{72}F_{73} + r_{82}F_{83} + r_{92}F_{93}]$

$= [0 + 0 + 0 + 0 + 0 + (-39.5)(-10) + 0$

$+ (-35.6)(-15) + (-13.05)(-20)]$

$\underline{T_1 = 1190 \ lb\text{-}in.}$

$T_2 = \sum_{i=1}^{9} [r_{i3}F_{i1} - r_{i1}F_{i3}]$

$= - [r_{11}F_{13} + r_{21}F_{23} + r_{31}F_{33} + r_{41}F_{43} + r_{51}F_{53}$

$+ r_{61}F_{63} + r_{71}F_{73} + r_{81}F_{83} + r_{91}F_{93}]$

$= - [0 + 17.75)(-32) + (-8.95)(-45) + (4)(-29)$

$+ (-4.23)(-42) + (-1.52)(-10) + (-18.8)(-5)$

$+ (0.8)(-15) + (-12)(-20)]$

$\underline{T_2 = -553.2 \ lb\text{-}in.}$

$\underline{T_3 = 0}$

UNIT VECTOR FORCE AND MOMENT RESULTANTS AT REFERENCE CENTER

a_1	a_2	a	F_1	F_2	F_3	T_1	T_2	T_3
1g	0	0	-598	0	0	0	-805	-1190
0	1g	0	0	-598	0	805	0	553.2
0	0	1g	0	0	-598	1190	-553.2	0

$\underline{P_{ij}^{*}, \; P_{ij} \text{ for } \underline{a} = g\underline{n}_1}$

$$a = 0.9 \times 8 = 7.2 \text{ in.}$$

$$b = 2.9 \times 8 = 23.2 \text{ in.}$$

Compute

$$C_1 = \frac{1}{2a(1 + \frac{b^2}{a^2})} = \frac{1}{(2)(7.2)(1 + [\frac{23.2}{7.2}]^2)} = \frac{1}{164} = 0.61 \times 10^{-2} \text{ in.}^{-1}$$

$$C_2 = \frac{1}{4b} = \frac{1}{(4)(23.2)} = 1.08 \times 10^{-2} \text{ in.}^{-1}$$

$$C_3 = \frac{1}{4a} = \frac{1}{4(7.2)} = 3.47 \times 10^{-2} \text{ in.}^{-1}$$

$$C_4 = -(\frac{b}{a})C_1 = -(\frac{23.2}{7.2})C_1 = -1.96 \times 10^{-2} \text{ in.}^{-1}$$

Substitution of above values into Equations (29) ~ (32) leads to the following:

$$P_{12}^{*} = C_1 T_3 = (0.61 \times 10^{-2}) \times (-1190) = 7.27 \text{ lb}$$

$$P_{13}^{*} = C_2 T_1 - C_3 T_2 = -(3.47 \times 10^{-2})(-805) = +27.9 \text{ lb}$$

$$P_{21}^{*} = C_4 T_3 = (-1.96 \times 10^{-2})(-1190) = +23.3 \text{ lb}$$

$$P_{22}^{*} = -P_{12}^{*} = 7.27 \text{ lb}$$

$$P_{23}^{*} = C_2 T_1 + C_3 T_2 = -27.9 \text{ lb}$$

$$P_{33}^* = - P_{23}^* = + 27.9 \text{ lb}$$

$$P_{41}^* = - P_{21}^* = - 23.3 \text{ lb}$$

$$P_{43}^* = - P_{13}^* = - 27.9 \text{ lb}$$

$$P_{12} = - 1/2 \, F_2 = - 1/2 \, (0) = 0$$

$$P_{13} = - 1/4 F_3 = 0$$

$$P_{21} = - 1/2 F_1 = - 1/2(-598) = + 299 \text{ lb}$$

$$P_{22} = - 1/2 \, F_2 = 0$$

$$P_{23} = - 1/4 F_3 = 0$$

$$P_{33} = - 1/4 F_3 = 0$$

$$P_{41} = - 1/2 F_1 = + 299 \text{ lb}$$

$$P_{43} = - 1/4 F_3 = 0$$

$P_{ij}^*, \ P_{ij}$ for $\underline{a} = g\underline{n}_2$

$$P_{12}^* = C_1 T_3 = (0.61 \times 10^{-2})(553.2) = 3.37 \text{ lb}$$

$$P_{13}^* = C_2 T_1 - C_3 T_2 = (1.08 \times 10^{-2})(805) = 6.69 \text{ lb}$$

$$P_{21}^* = C_4 T_3 = (-1.96 \times 10^{-2})(553.2) = -10.85 \text{ lb}$$

$$P_{22}^* = - P_{12}^* = - 3.37 \text{ lb}$$

$$P_{23}^* = C_2 T_1 + C_3 T_2 = (1.08 \times 10^{-2})(805) = 8.69 \text{ lb}$$

$$P_{33}^* = - P_{23}^* = - 8.69 \text{ lb}$$

$$P_{41}^* = - P_{21}^* = + 10.85 \text{ lb}$$

$$P_{43}^* = - P_{13}^* = -8.69 \text{ lb}$$

$$P_{12} = - 1/2 F_2 = 299 \text{ lb}$$

$$P_{13} = - 1/4 F_3 = 0$$

$$P_{21} = 0$$

$$P_{22} = - 1/2 F_2 = 299 \text{ lb}$$

$$P_{23} = 0$$

$$P_{33} = 0$$

$$P_{41} = 0$$

$$P_{43} = 0$$

P^*_{ij}, P_{ij} for <u>a</u> <u>qn₃</u>

$$P^*_{12} = C_1 T_3 = 0$$

$$P^*_{13} = C_2 T_1 - C_3 T_2 = (1.08 \times 10^{-2})(1190) - (3.47 \times 10^{-2})(-553.2)$$

$$= 12.85 + 19.2 = 32.05 \text{ lb}$$

$$P^*_{21} = C_4 T_3 = (-1.96 \times 10^{-2})(0) = 0$$

$$P^*_{22} = - P^*_{12} = 0$$

$$P^*_{23} = C_2 T_1 + C_3 T_2 = (1.08 \times 10^{-2})(1190) + (3.47 \times 10^{-2})(-563.2)$$

$$= 12.85 - 19.2 = - 6.35 \text{ lb}$$

$$P^*_{33} = P^*_{23} = 6.35 \text{ lb}$$

$$P^*_{41} = - P^*_{21} = 0$$

$$P^*_{43} = - P^*_{13} = -32.05 \text{ lb}$$

$$P_{12} = 0$$

$$P_{13} = - 1/4 F_3 = - 1/4 (-598) = 149.5 \text{ lb}$$

$$P_{21} = 0$$

$$P_{22} = 0$$

$$P_{23} = - 1/4 F_3 = 149.5 \text{ lb}$$

$$P_{33} = - 1/4 F_3 = 149.5 \text{ lb}$$

$$P_{41} = 0$$

$$P_{43} = - 1/4 F_3 = 149.5 \text{ lb}$$

182

Q_{ii}

For $\underline{a} = gn_1$

$$Q_{12} = -7.27 + 0 = -7.27 \text{ lb}$$

$$Q_{13} = +27.90 + 0 = 27.90 \text{ lb}$$

$$Q_{21} = +23.30 + 299 = 322.30 \text{ lb}$$

$$Q_{22} = +7.27 + 0 = 7.27 \text{ lb}$$

$$Q_{23} = -27.90 + 0 = -27.90 \text{ lb}$$

$$Q_{33} = +27.90 + 0 = 27.90 \text{ lb}$$

$$Q_{41} = -23.30 + 299 = 275.70 \text{ lb}$$

$$Q_{43} = -27.90 + 0 \quad -27.90 \text{ lb}$$

For $\underline{a} = gn_2$

$$Q_{12} = 3.37 + 299 = 302.37 \text{ lb}$$

$$Q_{13} = 8.69 + 0 = 8.69 \text{ lb}$$

$$Q_{21} = 10.85 + 0 = -10.85 \text{ lb}$$

$$Q_{22} = -3.37 + 299 = 295.63 \text{ lb}$$

$$Q_{23} = 8.69 + 0 = 8.69 \text{ lb}$$

$$Q_{33} = -8.69 + 0 = -8.69 \text{ lb}$$

$$Q_{41} = 10.85 + 0 = 10.85 \text{ lb}$$

$$Q_{43} = -8.69 + 0 = -8.69 \text{ lb}$$

For $\underline{a} = gn_3$

$$Q_{12} = 0 + 0 = 0 \text{ lb}$$

$$Q_{13} = 32.05 + 149.5 = 181.55 \text{ lb}$$

$$Q_{21} = 0 + 0 = 0 \text{ lb}$$

$$Q_{22} = 0 + 0 = 0 \text{ lb}$$

$$Q_{23} = -6.35 + 149.5 = 142.15 \text{ lb}$$

$$Q_{33} = 6.35 + 149.5 = 155.85 \text{ lb}$$

$$Q_{41} = 0 + 0 = 0 \text{ lb}$$

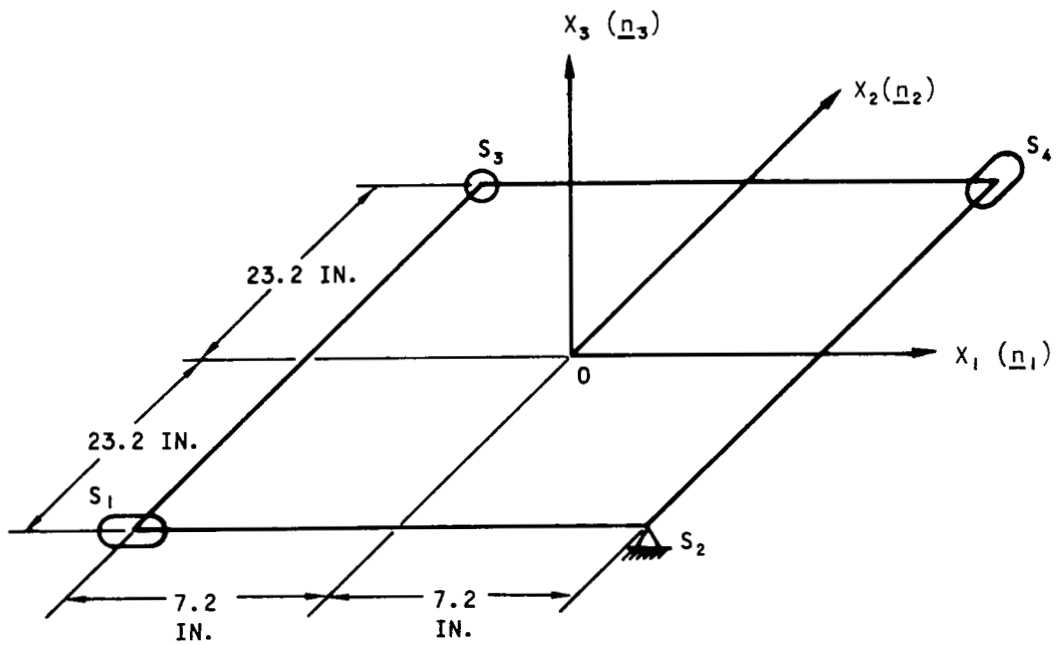$$Q_{43} = -32.05 + 149.5 = 117.45 \text{ lb}$$

Figure E-4.

REACTION FORCES AT SUPPORTS S_1, S_2, S_3, S_4
DUE TO UNIT G IN EACH DIRECTION

Load	$\underline{a}$			S_1, lb			S_2, lb			S_3, lb			S_4, lb		
	a_1	a_2	a_3	Q_{11}	Q_{12}	Q_{13}	Q_{21}	Q_{22}	Q_{23}	Q_{31}	Q_{32}	Q_{33}	Q_{41}	Q_{42}	Q_{43}
1	1g	0	0	0	-7.27	27.9	322.3	7.27	-27.9	0	0	27.9	275.7	0	-27.9
2	0	1g	0	0	302.37	8.69	-10.85	295.63	8.69	0	0	-8.69	10.85	0	-8.69
3	0	0	1g	0	0	181.55*	0	0	142.15	0	0	155.85	0	0	117.45

*Maximum

HORIZONTAL RESULTANT

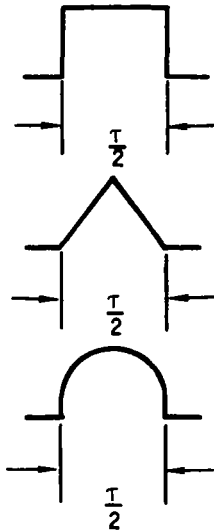| $\underline{a}$			S_1	S_2	S_3	S_4
a_1	a_2	a_3	$Q_S = [Q_{11}^2 + Q_{12}^2]^{\frac{1}{2}}$	$Q_S = [Q_{21}^2 + Q_{22}^2]^{\frac{1}{2}}$	$Q_S = [Q_{31}^2 + Q_{32}^2]^{\frac{1}{2}}$	$Q_S = [Q_{41}^2 + Q_{42}^2]^{\frac{1}{2}}$
1g	0	0	7.27	322.5*	0	275.7
0	1g	0	302.37	295.8	0	10.85
0	0	1g	0	0	0	0

*Maximum

DESIGN ANALYSIS OF BRACKETS FOR SHOCK AND VIBRATIONS

Design of Bracket Mounting

I. **Assumptions**

    1. Vibration Transmissibility = 2.5 (See Reference I)

    2. 10 cps Isolation System Shock Response (See Reference 2)

$$\frac{\tau}{2} = 0.005 \text{ sec} \qquad \tau = 0.01$$

$$\frac{\tau}{T} = \frac{0.01}{0.1} = 0.1$$

Shock Factor = 0.3

$$\tau = 0.01$$

$$\frac{\tau}{T} = 0.1$$

Shock Factor = 0.3

$$\tau = 0.008$$

$$\frac{\tau}{T} = 0.08$$

$$\text{Shock Factor} = \frac{4}{\pi}(0.25) \cong 0.3$$

2. **Total Load**

Vibratory, 2.5 x 6 = 15 g

Shock, 0.3 x 35 = 10.5g

Steady Acceleration   <u>5 g</u>

                      30.5g

Use 30g in $\underline{n}_3$ combined with another 30g in $\underline{n}_1$ or $\underline{n}_2$ direction.

3. **Reactions at S_i ($i = 1, .., 4$)**

         Case I $\underline{a} = 30g\underline{n}_1 + 30g\underline{n}_3$

         Case II $\underline{a} = 30g\underline{n}_2 + 30g\underline{n}_3$

Forces are shown on Table E-5 for these two load conditions.

4. **Structural Integrity (Figure E-5)**

     For 0.004 in. thick Fin, 20 Fins per in., 1 in. high specimen

$$A = 20 \times 0.004 = 0.08 \text{ in.}^2$$

$$E = 28 \times 10^6 \text{ psi}$$

$$\ell = 1.25 \text{ in. (length of the specimen)}$$

$$k_1 = \frac{AE}{\ell} = \frac{0.08}{1.25} \times 28 \times 10^6 = 1.79 \times 10^6 \text{ psi}$$

     From the test results of these fins (Reference 3)

$$k_2 = \frac{\sigma}{\epsilon} = \frac{\left(\frac{P}{A}\right)}{\left(\frac{\delta}{\ell}\right)} = \frac{\left(\frac{120}{1}\right)}{\left(\frac{10 \times 10^{-3}}{1.25}\right)} = 1.5 \times 10^4 \text{ psi}$$

Assume

$$k_2 = C\frac{AE}{\ell} = ck_1$$

$$C = \frac{k_2}{k_1} = \frac{1.5 \times 10^4}{1.79 \times 10^6} = 0.84 \times 10^{-2}$$

In the actual recuperator, the fin geometry is

     0.006 in. thick Fin, 16 Fins per in., $\ell = 5$ in.

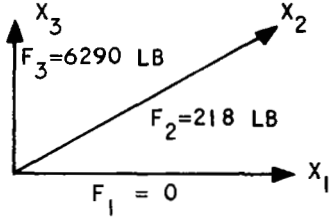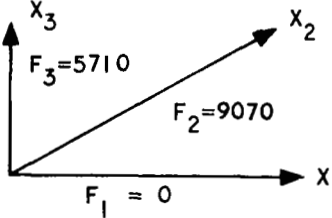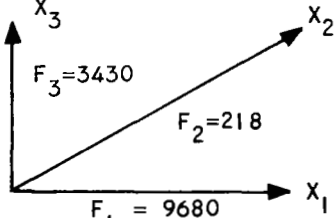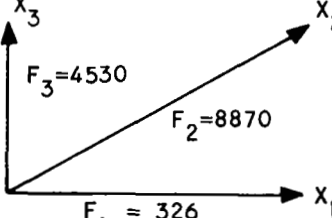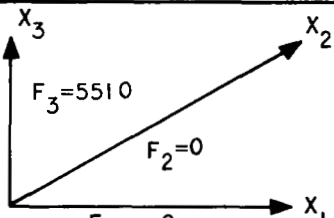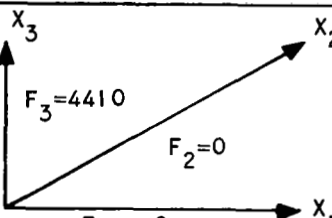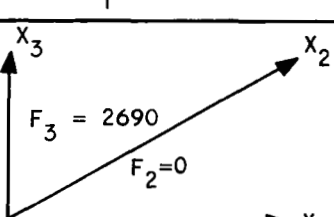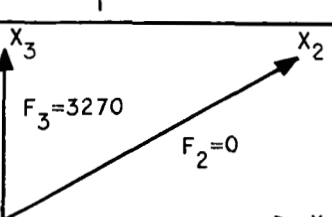$$A = 16 \times 0.006 = 0.0096 \text{ in.}^2 \text{ per in.}$$

$$E = 28 \times 10^6 \text{ psi}$$

$$\ell = 5 \text{ in.}$$

$$k = C\frac{AE}{\ell} = [0.84 \times 10^{-2}] \times \frac{0.096}{5} \times 28 \times 10^6$$

$$= 0.45 \times 10^4 \text{ psi}$$

Use $k = 0.45 \times 10^4$ psi

TABLE E-5

LOAD RESULTANTS

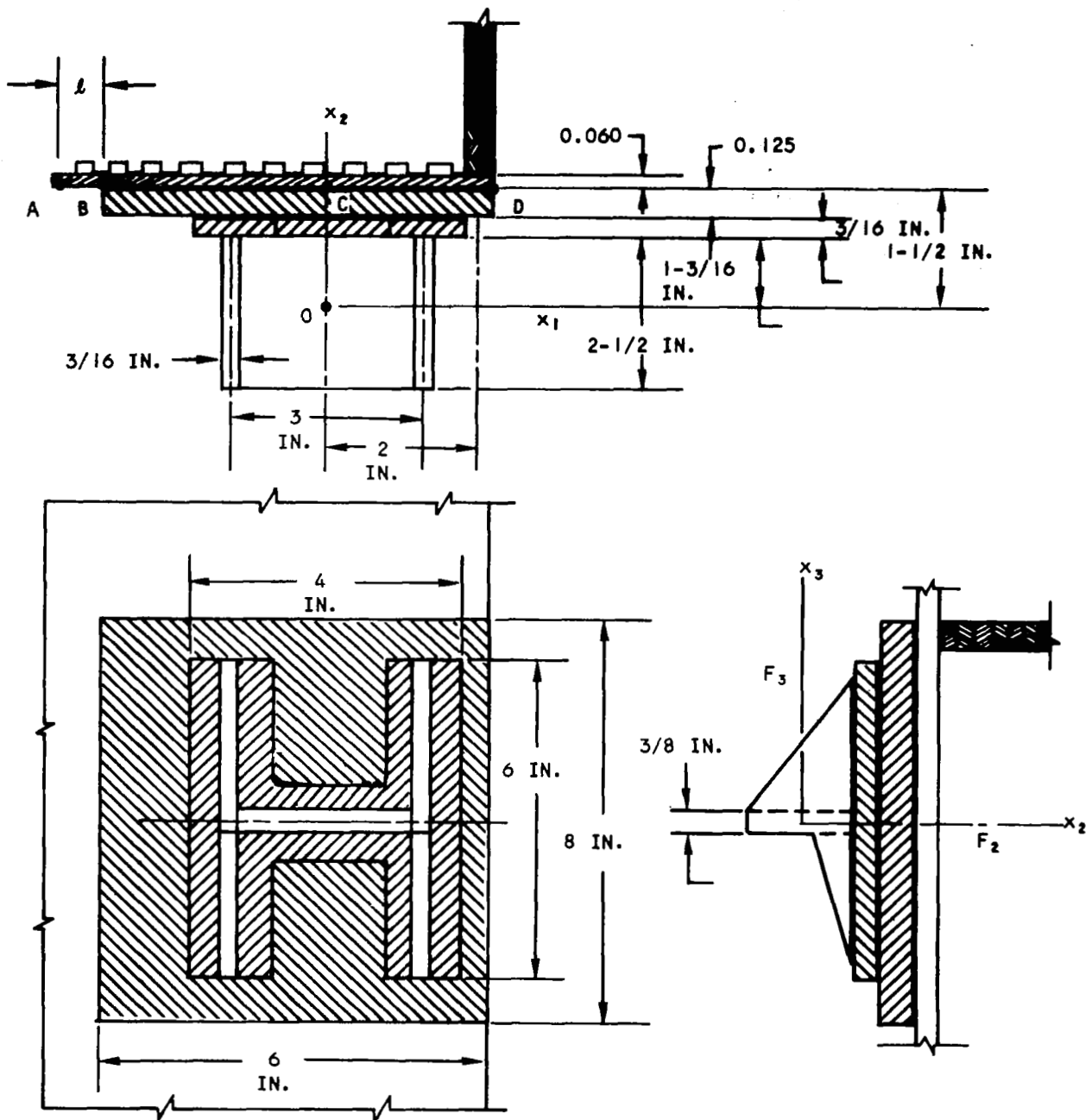| Support Station	CASE 1 30g LONG. + 30g IN X_1 AXIS	CASE 2 30g LONG. + 30g IN X_2 AXIS
S_1	X_3 X_2 $F_3 = 6290$ LB $F_2 = 218$ LB $F_1 = 0$ X_1	X_3 X_2 $F_3 = 5710$ $F_2 = 9070$ $F_1 = 0$ X_1
S_2	X_3 X_2 $F_3 = 3430$ $F_2 = 218$ $F_1 = 9680$ X_1	X_3 X_2 $F_3 = 4530$ $F_2 = 8870$ $F_1 = 326$ X_1
S_3	X_3 X_2 $F_3 = 5510$ $F_2 = 0$ $F_1 = 0$ X_1	X_3 X_2 $F_3 = 4410$ $F_2 = 0$ $F_1 = 0$ X_1
S_4	X_3 X_2 $F_3 = 2690$ $F_2 = 0$ $F_1 = 8260$ X_1	X_3 X_2 $F_3 = 3270$ $F_2 = 0$ $F_1 = 326$ X_1

Figure E-5.   Structural Integrity Analysis

Find λ (See Reference 4)

$$\lambda = 4\sqrt{\frac{k}{4EI}} \quad \text{(See P.4, of Reference 4)}$$

where

$$k = 0.45 \times 10^4 \text{ psi}$$

$$E = 28 \times 10^6 \text{ psi}$$

$$I = \frac{1}{12}(0.06)^3$$

$\therefore \lambda = 1.22$

$$\ell = \frac{3}{4}\frac{\pi}{\lambda} \quad \text{(See P. 11 of Reference 4)}$$

$$\ell = \frac{3}{4} \times \frac{\pi}{1.22} = 1.93 \text{ in.}$$

Load

$$\underline{F} = F_1\underline{n}_1 + F_2\underline{n}_2 + F_3\underline{n}_3$$

$$F_1 = 0$$

$$F_2 = 9,070 \text{ lb}$$
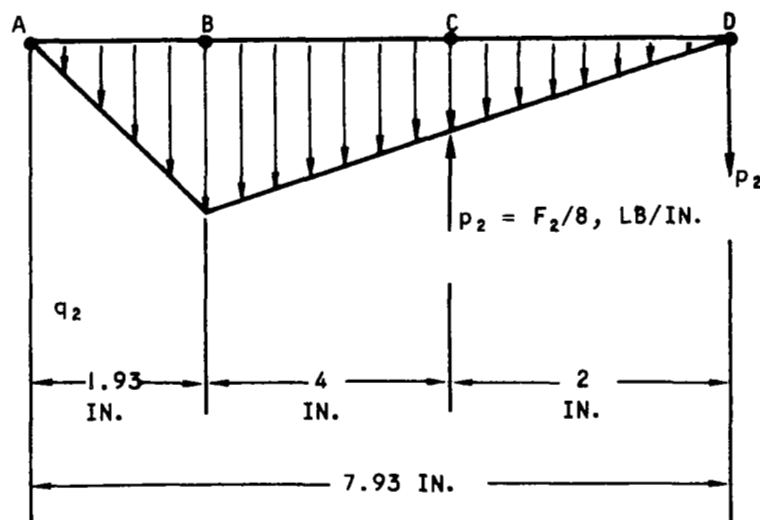
$$F_3 = 5,710 \text{ lb}$$

1. **Due to F_2**

Figure E-6

$P. = F_2/8 = 9070/8 = 1134$ lb per in.

$$\left(\frac{1}{2}\right)(6 \times q_2)(4) + \left(\frac{1}{2}\right)(1.93 \times q_2) \times \left(6 + \frac{1.93}{3}\right) = 1134 \times 2$$

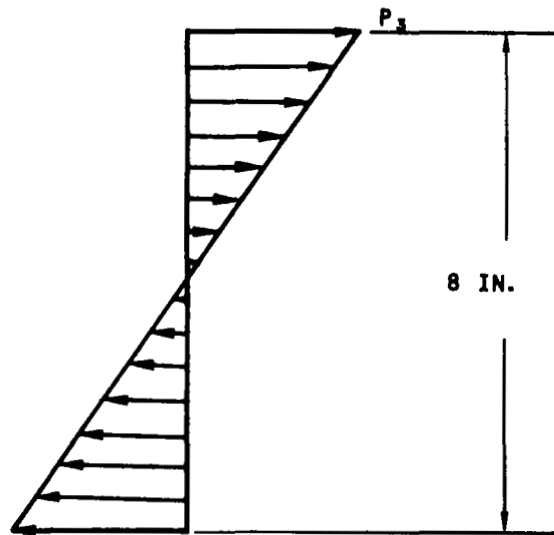$12q_2 + 6.43\ q_2 = 2 \times 1134$ lbs per in.

$18.43q_2 = 1134 \times 2$

$q_2 = \dfrac{1}{18.43} \times 1134 \times 2 = 0.108 \times 1134$

$ = 122.5$ psi

$\therefore\ q_2 = 122.5$ psi

2. Due to F_3

Reaction force distribution along the vertical line through Point C (see Figure E-5) is assumed as shown opposite and horizontal distribution is assumed the same as that in Figure E-6.

191

$$\frac{P_3}{2} (4)\left(\frac{2}{3}\right)(8) = (5710)(2) \qquad \text{(Assuming OC = 2 in.)}$$

$$P_3 = \frac{5710 \times 2 \times 2 \times 3}{4 \times 2 \times 8} = 1070 \text{ lb per in.}$$

$$q_3 = (0.108)(1070) = 115.5 \text{ psi}$$

$$q = q_2 + q_3 = 122.5 + 115.5 = 238 \text{ psi}$$

If F_3 is applied 1.5 in. away from the side plate of the core instead of 2 in.

$$\frac{1}{2} P_3 \times 4 \times \frac{2}{3} \times 8 = 5710 \times \frac{3}{2}$$

$$P_3 = \frac{5710 \times 3 \times 3 \times 2}{2 \times 4 \times 2 \times 8} = 8.5 \text{ lb per in.}$$

$$q_3 = (0.108) \times (805) = 87 \text{ psi} \quad \text{\textasciitilde}$$

$$^*q_{TOT} = q_2 + q_3 = 122.5 + 87 = 209.5 \text{ psi}$$

This is safe compared to estimated fin crushing load of 250 psi (based on results from Reference 3).

3. <u>Let OC be 1.5 in. Then</u>

$$q = 209.5 \text{ psi}$$

$$p_2 \text{ (p due } F_2\text{)} + \frac{1}{2} (7.93 \times 122.5) = 1134$$

$$p_2 = 1134 - 485$$

$$= 649 \text{ lb per in.}$$

$$p_3 = \frac{p_2}{p_2} p_3 = \frac{649}{1134} (805)$$

$$= 0.572 \times 805$$

$$= 460 \text{ lb per in.}$$

$$p = p_2 + p_3 = 649 + 460 = 1109 \text{ lb per in.}$$

<u>Desgin of Supporting Plate</u>

$$3 \times 3 \times q = 5710 \qquad \left(3 \times 3 \times \frac{3}{16}\right)$$

$$q = 635 \text{ psi}$$

If use $2\frac{1}{2}$ x 3 in.^{2} instead of 3 x 3 in.^{2}

$$3 \times \frac{5}{2} \times q \;=\; 5710$$

$$q \;=\; 760 \text{ psi}$$

From Timoshenko's "Theory of Plates and Shells" P.210, (Reference 5)

$$a \;=\; 3 \text{ in.}$$

$$b \;=\; 2.5 \text{ in.}$$

$$\frac{b}{a} \;=\; \frac{2.5}{3} \;=\; 0.833$$

From Table 39 on p. 210

At $x = \frac{a}{2}$ $y = b$ ($x = 1.5$ in, $y = 2.5$ in.)

$$M_x \;=\; (0.076)(qa^2)$$

$$=\; (0.076) \times (3)^2 \times (760)$$

$$=\; 520 \text{ in. lb}$$

At $x = \frac{a}{2}$, $y = 0$

$$M_y \;=\; 0.169 \times q \times b^2$$

$$=\; (0.169)(760)(2.5)^2$$

$$=\; 802 \text{ in. lb}$$

$$Z \;=\; \frac{h^2}{6} \;=\; \frac{1}{6} \times \left(\frac{3}{16}\right)^2, \; \frac{1}{z} \;=\; 1.7! \times 10^2$$

At D, ($x = 1.5$ in., $y = 0$)

$$\sigma_y' \;=\; (M_y)\left(\frac{1}{z}\right) \;=\; 802 \times 1.71 \times 10^2 \;=\; 13.7 \times 10^4 \text{ psi}$$

$$\sigma_y'' \;=\; \frac{9070}{3 \times \frac{3}{16}} \;=\; 16,100 \text{ psi}$$

$$\sigma_y \;=\; 137,000 + 16,100 \;=\; 153,100 \text{ psi}$$

At F $(x = \frac{a}{2}, \dot{y} = b)$

$M_x = 520$ in. lb

$\sigma_y' = 1.71 \times 10^2 \times 520 \approx 88,900$ psi

$\sigma_y = 88,900$ psi

If use $\frac{3}{8} \times 2.5 \times 3$ supporting plate

$\frac{1}{z} = \dfrac{6}{(\frac{3}{8})^2} = 42.7$

At D, $(x = 1.5$ in., $y = 0)$

$\sigma_y' = 802 \times 42.7 = 34,200$ psi

$\sigma_y'' = \dfrac{9070}{3 \times \frac{3}{8}} = 8060$ psi

$\sigma_y = 34,200 + 8060 = 42,260$ psi

At F $(x = 1.5$ in., $y = 2.5$ in.$)$

$\sigma_y = 520 \times 42.7 = 22,200$ psi

$2\frac{1}{2} \times 3 \times \frac{3}{8}$ supporting plate

$\sigma_{max} = 42,260$ psi

$6 \times 8 \times \frac{1}{8}$ Reinforcement Plate

$4 \times 6 \times \frac{3}{16}$ Base Plate of the Bracket

$2\frac{1}{2} \times 3 \times \frac{3}{8}$ Supporting Plate of the Bracket

$q = 209.5$ psi $\left.\rule{0pt}{20pt}\right\}$ Core

$p = 1109$ lb per in. $\left.\rule{0pt}{0pt}\right\rfloor$

$\sigma_{max} = 42,260$ psi - Supporting Plate

Design of the Bolts, (At S_1)

Use $\frac{5}{8}$ bolt

$$A = \frac{\pi}{4}\left(\frac{5}{8}\right)^2 = 0.306 \text{ in.}^2$$

1. **Tension**

$$\sigma_t = \frac{5710}{0.306} = 18,670 \text{ psi}$$

2. **Shear**

$$\sigma_b = \frac{9070}{0.306} = 29,600 \text{ psi}$$

3. **Principal Stresses**

$$\sigma_{nn} = \frac{\sigma_t}{2} + \sqrt{\left(\frac{\sigma_t}{2}\right)^2 + \sigma_b^2}$$

$$= \frac{18670}{2} + \sqrt{\left(\frac{18670}{2}\right)^2 + 29600^2}$$

$$= 9335 + 31100$$

$$\sigma_{nn} = 40,435 \text{ psi}$$

$$\sigma_{ss} = 31,100 \text{ psi}$$

4. **Compression at Contact Area**

$$\sigma_c = \frac{9070}{\left(\frac{3}{8}\right) \times \left(\frac{5}{8}\right)\left(\frac{1}{4}\right)} = 38,700 \text{ psi} \times 4 = 155,000 \text{ psi}$$

Use 5/8 bolts

$\frac{5}{8} \times 2 \times 10$ bolts

Thermal Expansion

$$\alpha = 6.5 \times 10^{-6} \ ^{\circ}F$$

$$\ell_1 = 2.3 \times 8 = 18.4 \text{ in. (in. } OX_1)$$

$$\ell_2 = 5.05 \times 8 = 40.4 \text{ in. (in. } OX_2)$$

$$T = 1200 \ ^{\circ}F$$

$$\delta_1 = \alpha \ell_1 T = 6.5 \times 10^{-6} \times 18.4 \times 1.2 \times 10^3$$

$$= 0.1434 \text{ in.}$$

$$\delta_2 = \delta_1 \times \frac{\ell_2}{\ell_1} = (0.1434)(40.4/(18.4)$$

$$= 0.315 \text{ in.}$$

The sizes of the slots are shown in Figure E-7.

ALLOWABLE LOADS AT DUCT FLANGE LOCATIONS

Assumptions

1. System start-up and operation does not coincide with launch and lift-off.

2. Pressure forces at flange points will be due to $\Delta p = 13$ psi max.

3. Interconnecting ducts will be self sufficient for launch and lift-off loads, i.e. The pipes and possibly valves must not be supported from the flanges.

4. Flexibility in the form of expansion joints or pipe expansion loops must be provided in the interconnecting ducts to control flange loads induced by thermal expansion.

5. The allowable loads determined here are limitations that the recuperator can withstand. If these loads are reflected back into the system, they may exceed the capability of other system components.
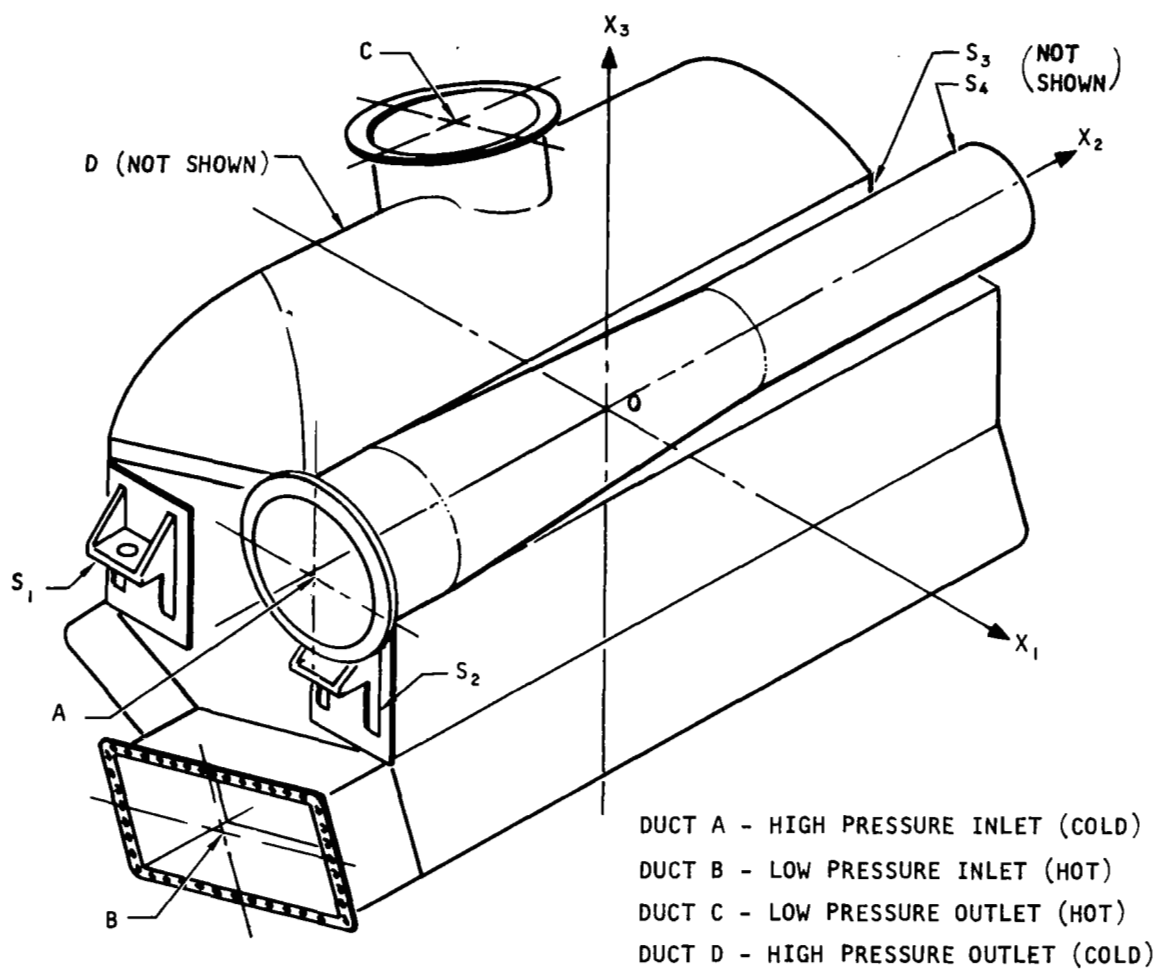
Duct and Support Locations

An isometric drawing of the recuperator is shown on Figure E-8.

196
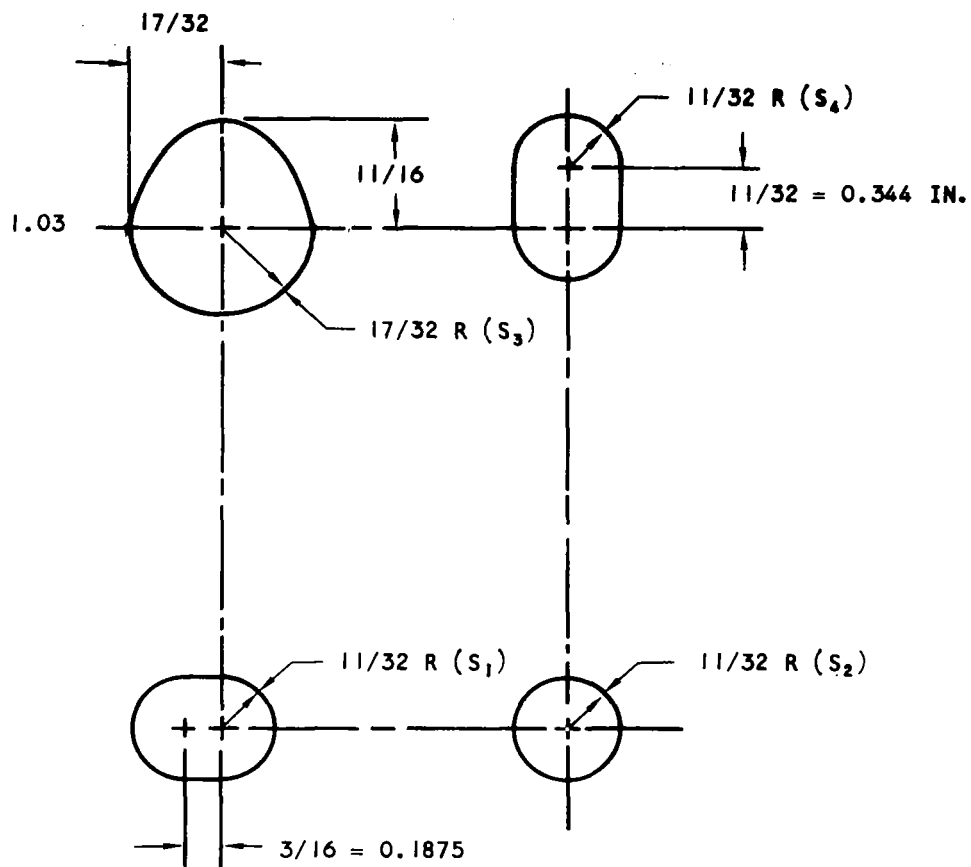
SUPPORTING PLATE FABRICATED FROM INCONEL 718
BOLTS ARE 5/8-IN. DIAMETER

Figure E-7. Mounting Bracket Slot Sizes

Figure E-8. Duct and Support Locations on Recuperator

DUCT A - HIGH PRESSURE INLET (COLD)

DUCT B - LOW PRESSURE INLET (HOT)

DUCT C - LOW PRESSURE OUTLET (HOT)

DUCT D - HIGH PRESSURE OUTLET (COLD)

A-24374-A

198

Duct and support co-ordinate locations are tabulated below.

	Support or Duct	Co-ordinate Locations Relative to Point 0		
		x_1	x_2	x_3
	S1	-7.2	-23.2	0
	S2	7.2	-23.2	0
	S3	-7.2	23.2	0
	S4	7.2	23.2	0
H.P. Inlet (Cold)	A	7.3	-25.0	8.1
L.P. Inlet (Hot)	B	3.8	-25.0	-10.0
L.P. Outlet (Hot)	C	-5.0	0	20.9
H.P. Outlet (Cold)	D	-13.8	0	-14.5

Allowable Stresses

Limit stress to $17,000/2 = 8500$ psi for No. 347 stainless steel 10,000 hr rupture strength with a safety factor 2 at $1200°F$.

Assume simultaneous bending and torsion. Let this be equally shared and assume maximum shear theory,

$$\sigma_{EQ.} = (\sigma_B^2 + 4t^2)^{1/2}$$

$$\sigma_B = 2t$$

$$\sigma_B \text{ ALL} = 8500/\sqrt{2} = 6000 \text{ psi}$$

$$t_{ALL} = 3000 \text{ psi}$$

Forces and Moments at Ducts A, B, C, D

1. **Duct A**

$$a = \pi r^2 = \pi (3)^2 = 28.3 \text{ in.}^2$$

$$\underline{F}_A = pa\underline{n}_2 = (13 \times 28.3) \underline{n}_2 = 368 \text{ lb } \underline{n}_2$$

Sectional modulus for bending, $z_b = (\pi \times 3^2)(0.03) = 0.85$ in.^{3}

Sectional modulus for torsion, $z_t = 2\pi r^2 t = 2z_b$

$$z_t = 2\pi(3^2)(0.03) = 1.70 \text{ in.}^3$$

Allowable moments; $M_b = M_t$

$$M_b = (6000)(0.85) = 5100 \text{ in. lb}$$

$$M_t = (3000)(1.70) = 5100 \text{ in. lb}$$

$$\underline{M}_A = \pm 5100 \, \underline{n}_1 \pm 5100 \, \underline{n}_2$$

2. Duct B

$$t = 0.03 \text{ in.}$$

$$a = (2 \times 6.75)(2 \times 4) = 108 \text{ in.}^2$$

$$\pi r^2_{eq.} = 108$$

$$r_{eq.} = 5.85 \text{ in.}$$

$$\underline{F}_B = (13)(108)\underline{n}_2 = 1400 \text{ lb } \underline{n}_2$$

$$z_b = \pi r^2 t = (\pi)(5.85)^2 (0.03) = 3.24 \text{ in.}^3$$

$$z_t = 2z_b = 6.48 \text{ in.}^3$$

$$M_b = M_t = (3.24)(6000) = 19450 \text{ in. lb}$$

$$\underline{M}_B = \pm 19450 \, \underline{n}_1 \pm 19450 \, \underline{n}_2$$

3. Duct C

$$t = 0.03 \text{ in.}$$

$$r = 4 \text{ in.}$$

$$a = \pi r^2 = 50.3 \text{ in.}^2$$

$$\underline{F}_c = -(13)(50.3)\,\underline{n}_3 = -653\text{ lb }\underline{n}_3$$

$$z_b = \frac{1}{2}\,z_t = \pi r^2 t = (\pi)(16)(0.03) = 1.51\text{ in.}^3$$

$$M_b = M_t = (1.51)(6000) = 9060\text{ in. lb}$$

$$\underline{M}_c = \pm 9060\,\underline{n}_2 \pm 9060\,\underline{n}_3$$

4. **Duct D**

$$t = 0.03\text{ in.}$$

$$r = 3\text{ in.}$$

$$a = \pi r^2 = 28.3\text{ in.}^2$$

$$\underline{F}_D = 13 \times 28.3\,(\cos 45\,\underline{r}_1 + \sin 45\,r_3)$$

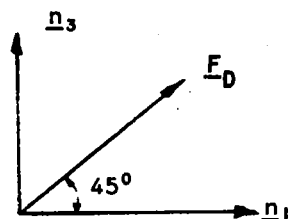$$\underline{F}_D = 260\text{ lb }\underline{n}_1 + 260\text{ lb }\underline{n}_3$$

$$z_b = \frac{1}{2}\,z_t = \pi r^2 t = (\pi)(3)^2(0.03) = 0.85\text{ in.}^3$$

$$M_b = M_t = (6000)(0.85) = 5100\text{ in. lb}$$

$$*\underline{M}_D = \pm 5100\,\underline{n}_2 \pm 5100\,(\sin 45^\circ\,\underline{n}_3 + \cos 45^\circ\,\underline{n}_1)$$

$$= \pm 3600\,\underline{n}_1 \pm 5100\,\underline{n}_2 \pm 3600\,\underline{n}_3$$

5. **Equivalent Force System at O**

$$F = \underline{F}_A + \underline{F}_B + \underline{F}_c + \underline{F}_D$$

$$= 368\,\underline{n}_2 + 1400\,\underline{n}_2 - 653\,\underline{n}_3 + 2600\,\underline{n}_1 + 260\,\underline{n}_3$$

$$= 260\,\underline{n}_1 + 1768\,\underline{n}_2 - 393\,\underline{n}_3 = \sum_{i=1}^{3} F_i\underline{n}_i$$

$$F_1 = 260\text{ lb}$$

$$F_2 = 1768\text{ lb}$$

$$F_3 = -393\text{ lb}$$

$$\underline{T} = \underline{M} + \underline{G}$$

$$\underline{M} = \underline{M}_A + \underline{M}_B + \underline{M}_c + \underline{M}_D$$

$$\underline{G} = \underline{r}_A \times \underline{F}_A + \underline{r}_B \times \underline{F}_B + \underline{r}_c \times \underline{F}_c + \underline{r}_b \times \underline{F}_b$$

where $\underline{r}_A$, $\underline{r}_B$, $\underline{r}_C$, $\underline{r}_D$ are position vectors of A, B, C, D. Respectively, and write

$$\underline{r}_A = \underline{r}_1 \qquad\qquad\qquad \underline{F}_A = \underline{F}_1$$

$$\underline{r}_B = \underline{r}_2 \qquad\qquad\qquad \underline{F}_B = \underline{F}_2$$

$$\underline{r}_C = \underline{r}_3 \qquad\qquad\qquad \underline{F}_C = \underline{F}_3$$

$$\underline{r}_D = \underline{r}_4 \qquad\qquad\qquad \underline{F}_b = \underline{F}_4$$

$$\underline{r}_i = \sum_{j=1}^{3} r_{ij}\,\underline{n}_j \qquad\qquad i = 1, 2, 3, 4$$

$$\underline{F}_i = \sum_{j=1}^{3} F_{ij}\,\underline{n}_j \qquad\qquad i = 1, 2, 3, 4$$

where r_{ij} $(i = 1, .., 4, j = 1, 2, 3)$

$$[r_{ij}] = \begin{matrix} 7.3 & -25.0 & 8.1 \\ 3.8 & -25.0 & -10.0 \\ -5.0 & 0.0 & 20.9 \\ -13.8 & 0.0 & -14.5 \end{matrix}$$

$$[F_{ij}] = \begin{matrix} 0.0 & 368.0 & 0.0 \\ 0.0 & 1400.0 & 0.0 \\ 0.0 & 0.0 & -653 \\ 260.0 & 0.0 & 260.0 \end{matrix}$$

From Equation (9)

$$\begin{aligned} G_1 &= (r_{12}F_{13} - r_{13}F_{12}) + (r_{22}F_{23} - r_{23}F_{22}) \\ &\quad + (r_{32}F_{33} - r_{33}F_{32}) + (r_{42}F_{43} - r_{43}F_{42}) \\ &= -(811)(368) - (-10)(1400) \\ &= 11020 \text{ in. lb} \end{aligned}$$

$$G_{12} = (r_{13}F_{11} - r_{11}F_{13}) + (r_{23}F_{21} - r_{21}F_{23})$$

$$+ (r_{33}F_{31} - r_{31}F_{33}) + (r_{43}F_{41} - r_{41}F_{43})$$

$$= -(-5)(-653) + (-14.5)(260) - (-13.8)(260)$$

$$= -3320 \text{ in. lb}$$

$$G_{13} = (r_{11}F_{12} - r_{12}F_{11}) + cr_{21}F_{22} - r_{22}F_{21})$$

$$+ (r_{31}F_{32} - r_{32}F_{31}) + cr_{41}F_{42} - r_{42}F_{41})$$

$$= (713)(368) + (3.8)(1400)$$

$$= 8010 \text{ in. lb}$$

Since $\underline{T}$ equals the vector sum of $\underline{M}$ and G, we have

$$\underline{T} = \underline{M} + G = \sum_{i=1}^{3} T_i \underline{n}_i$$

$$T_1 = M_1 + G_1 = G_1 + \sum_{i=1}^{4} M_{i1}$$

$$T_2 = M_2 + G_2 = G_2 + \sum_{i=1}^{4} M_{i2}$$

$$T_3 = M_3 + G_3 = G_3 + \sum_{i=1}^{4} M_{i3}$$

Choose the sign of M_{ij} ($i = 1, .., 4$, $j = 1, 2, 3$) such that the magnitude of T_j ($j = 1, 2, 3$) will be maximum. Therefore, we select

$$\underline{M}_1 = \underline{M}_A = 5100 \underline{n}_1 - 5100 \underline{n}_2 = \sum_{j=1}^{3} M_{1j} \underline{n}_j$$

$$\underline{M}_2 = \underline{M}_B = 19450 \underline{n}_1 - 19450 \underline{n}_2 = \sum_{j=1}^{3} M_{2j}\underline{n}_j$$

$$\underline{M}_3 = \underline{M}_C = -9060 \underline{n}_2 + 9060 \underline{n}_3 = \sum_{j=1}^{3} M_{3j} \underline{n}_j$$

$$\underline{M}_4 = \underline{M}_D = 3600 \underline{n}_1 - 5100 \underline{n}_2 + 3600 \underline{n}_3 = \sum_{j=1}^{3} M_{4j} \underline{n}_j$$

As the set to be combined with $\underline{G}$ then.

$$T_1 = M_{11} + M_{21} + M_{31} + M_{41} + G_1$$

$$= 5100 + 19450 + 3600 + 11020$$

$$= 39170 \text{ in. lb}$$

$$T_2 = M_{12} + M_{22} + M_{32} + M_{42} + G_2$$

$$= -(5100 + 19450 + 9060 + 5100 + 3320)$$

$$= -42030 \text{ in. lb}$$

$$T_3 = M_{33} + M_{43} + G_3$$

$$= 9060 + 3600 + 8010$$

$$= 20670 \text{ in. lb}$$

6. **Reaction Forces at S_1, S_2, S_3, S_4**

a. **Due to $\underline{F}$**

$$\underline{F} = F_1\underline{N}_1 + F_2\underline{n}_2 + F_3\underline{n}_3$$

$$= 260 \underline{n}_1 + 1768 \underline{n}_2 - 393\underline{n}_3$$

From Equation (18)

$$P_{21} = P_{41} = -\frac{1}{2} F_1 = -130 \text{ lb}$$

$$P_{12} = P_{22} = -\frac{1}{2} F_2 = -884 \text{ lb}$$

$$P_{13} = P_{23} = P_{33} = P_{43} = -\frac{1}{4} F_3 = 98 \text{ lb}$$

b. **Due to $\underline{T}$**

Use Equations (29) - (32) and note that

$$C_1 = 0.61 \times 10^{-2} \text{ in.}^{-1}$$

$$C_2 = 1.08 \times 10^{-2} \text{ in.}^{-1}$$

$$C_3 = 3.47 \times 10^{-2} \text{ in.}^{-1}$$

$$C_4 = 1.96 \times 10^{-2} \text{ in.}^{-1}$$

$$P_{12}^* = C_1 T_3 = (0.61) \times 10^{-2} \times (20670) = 126.2 \text{ lb}$$

$$P_{13}^* = C_2 T_1 - C_3 T_2 = (1.08 \times 10^{-2})(39170) - (3.47 \times 10^{-2})(-42030)$$

$$= 1883 \text{ lb}$$

$$P_{21}^* = C_4 T_3 = (-1.96 \times 10^{-2})(20670)$$

$$= 405 \text{ lb}$$

$$P_{22}^* = -P_{12}^* = -126.2 \text{ lb}$$

$$P_{23}^* = C_2 T_1 + C_3 T_2 = 423 - 1460 = -1037 \text{ lb}$$

$$P_{33}^* = -P_{23}^* = 1037 \text{ lb}$$

$$P_{41}^* = -P_{21}^* = -405 \text{ lb}$$

$$P_{43}^* = -P_{13}^* = -1883 \text{ lb}$$

c. **Reaction Forces under operation conditions**

From Equation (33), we have the following:

At S_1;

$$Q_{12} = P_{12} + P_{12}^* = 884 + 126.2 = -757.8 \text{ lb}$$

$$Q_{13} = P_B + P_{13}^* = 98 + 1883 = 1981 \text{ lb}$$

At S_2;

$$Q_{21} = P_{21} + P_{21}^* = -130 + 405 = 275 \text{ lb}$$

$$Q_{22} = P_{22} + P_{22} = -884 - 126.2 = -1010.2 \text{ lb}$$

$$Q_{23} = P_{23} + P_{23}^* = 98 - 1037 = -939 \text{ lb}$$

At S_3;

$$Q_{33} = P_{33} + P_{33}^* = 98 + 1037 = 1135 \text{ lb}$$

At S_4;

$$Q_{41} = P_{41} + P_{41}^* = -130 - 405 = -535 \text{ lb}$$

$$Q_{43} = P_{43} + P_{43}^* = 98 - 1883 = -1785 \text{ lb}$$

The loading we used to design the bracketry is

$$\underline{Q}_{DE} = 9070 \text{ lb } \underline{n}_2 + 5710 \text{ lb } \underline{n}_3$$

comparing this with the magnitudes of the reaction forces under operational condition, it is obvious that the bracketry designed from the lift-off condition is sufficient to guarantee a safe structural integrity under the most adverse operating condition.

REFERENCES

1. Contract NAS3-2793, Modification No. 5

2. Shock and Vibration Handbook, edited by C. M. Harris and C. E. Crede, Vol. I, Chapter 8 (Transient Response to Step and Pulse Functions, R. A. Ayre), McGraw-Hill Book Co.

3. Plate Fin Crushing Tests (Conducted by D. G. Bridgnell at AiResearch Manufacturing Company, Los Angeles, California).

4. Beams on Elastic Foundation, M. Hetenyi, The University of Michigan Press.

5. Theory of Plates and Shells, Timoshenko and Woinowsky-Krieger, McGraw-Hill, 1959, P 210.

206

PROGRAM

PARAMETRIC STUDY

(Sections 2 and 3, Appendices A, B and C)

PROBLEM STATEMENT

	COLD INLET	HOT INLET
Temperature, °R	801	1560
Pressure, psia	13.8	6.73
Argon Flow Rate, lb per min	36.69	36.69

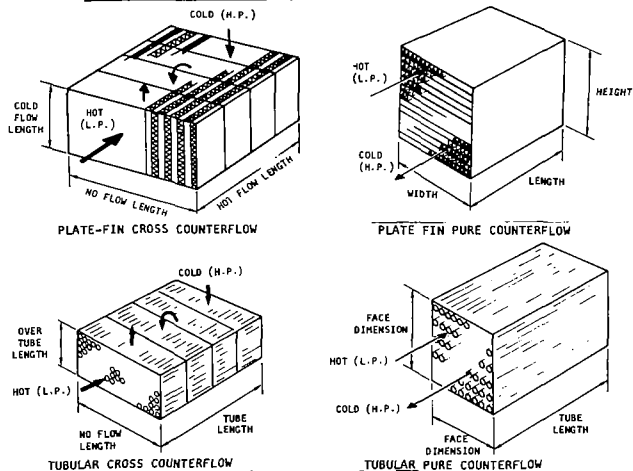### RANGE STUDIED

Temperature Effectiveness   0.75 to 0.95 percent
Overall Pressure Loss (ΔP/P)   0.5 to 8.0 percent

SELECTED CONDITION

Temperature Effectiveness = 0.9   Overall ΔP/P = 2.0 percent

HEAT EXCHANGER TYPES EXAMINED

PLATE-FIN CROSS COUNTERFLOW   PLATE FIN PURE COUNTERFLOW

TUBULAR CROSS COUNTERFLOW   TUBULAR PURE COUNTERFLOW

SPECIFIC STUDIES

Axial Conduction Effect, a mathematical analysis
Basic Data for Axial Flow Outside Tubes
Counterflow Tubular Heat Exchangers, a design computer program

SELECTED HEAT EXCHANGER

PURE COUNTERFLOW PLATE-FIN WITH TRIANGULAR END SECTIONS

ESTIMATED WEIGHT = 350 LB
Hastelloy C plates, 0.005 in. thick
Hollow header bars, Nickel fins
Plain rectangular fins in
both high and low pressure
triangular ends, 5 fins per in.

25.5 IN. FACE DIMENSION
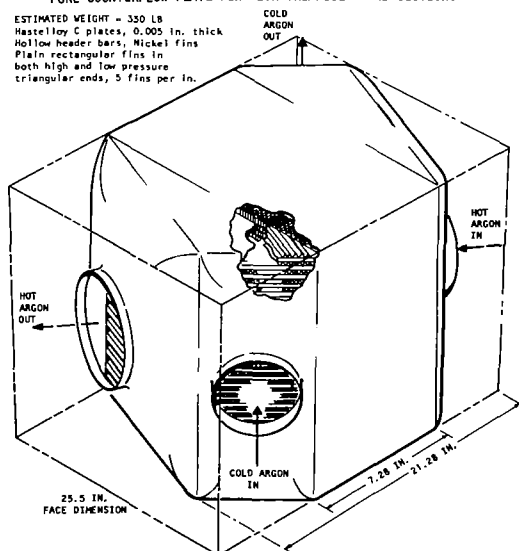
DEVELOPMENT PROGRAM

TRIANGULAR END SECTION DESIGN (Section 4 and Appendix D)

Triangular Ends - minimum weight and minimum pressure loss
Uniform Flow - requires non-symmetrical ends, therefore, ΔP/P
      increases to achieve heat transfer
End configuration selected for heat exchanger core with face
aspect ratio = 1.0
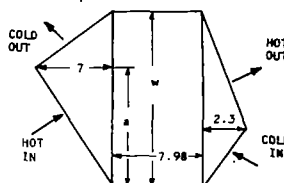
Ratio a/w = 0.7
ΔP/P Overall = 2.591

AXIAL CONDUCTION TESTING (Section 5)

Axial conduction reduces performance of high effectiveness
   heat exchangers.
Requires accurate knowledge of metal cross-sectional area to
   determine effect.
Tests determined effective metal cross section of offset fin
   matrix.

Result: Stainless steel fins instead of nickel (axial con-
      duction effect greater than fin effectiveness, lower
      conductivity preferred)

FLOW DISTRIBUTION (Section 6)

Determination of non-uniform flow very complex; testing re-
   quired.

Manifold Flow Distribution Tests

Design Goal: Maximum variation in flow 2 percent
From tests, the configuration to achieve this

ALL DIMENSIONS ARE APPROXIMATE
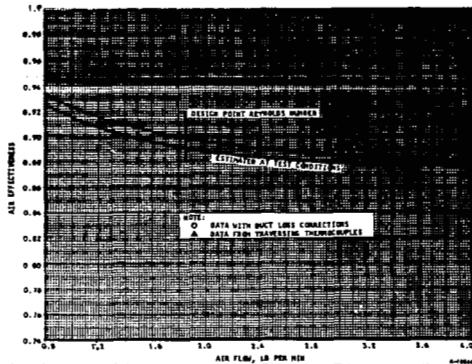ALL DIMENSIONS ARE INCHES
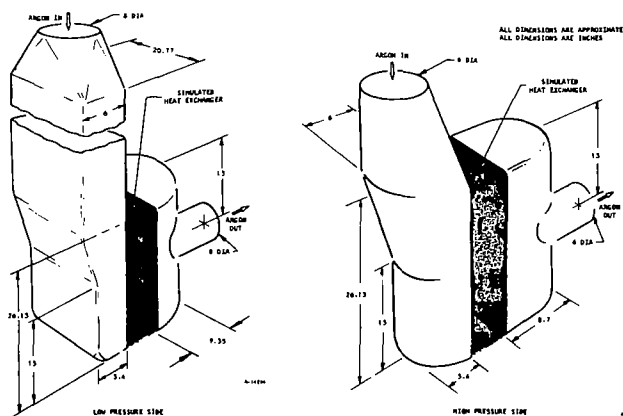
Heat Exchanger Flow Distribution

A heat exchanger with the configuration of the end section
design and a 2-in. stack height was tested.

Results: Effectiveness = 0.9 achieved
      ΔP/P Overall increased from 2.591 to 2.895 percent

	PREDICTED, PERCENT	TEST, PERCENT
HOT SIDE (LOW PRESS)		
COUNTERFLOW CORE	0.5	
TRIANGULAR END SECTIONS	0.422	
OVERALL CORE	0.922	1.245
COLD SIDE (HIGH PRESS)		
COUNTERFLOW CORE	0.202	
TRIANGULAR END SECTIONS	0.839	
OVERALL CORE	1.041	1.25
MANIFOLDS	0.028	0.4
OVERALL ΔP	2.591	2.895

COLD SIDE OVERALL CORE LOSSES INCREASE BY 1.2
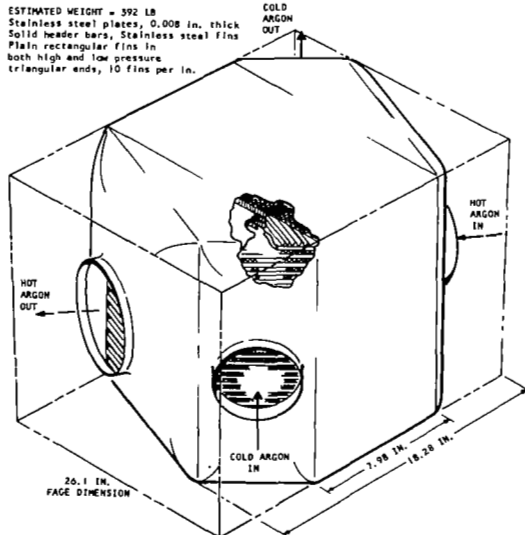HOT SIDE OVERALL CORE LOSSES INCREASE BY 1.35

208

SUMMARY

MECHANICAL DESIGN (Section 7 and Appendix E)

Coupled with above development studies, manufacturing and structural studies gave changed configuration.

ESTIMATED WEIGHT = 392 LB
Stainless steel plates, 0.008 in. thick
Solid header bars, Stainless steel fins
Plain rectangular fins in
both high and low pressure
triangular ends, 10 fins per in.

HOT ARGON OUT
HOT ARGON IN
COLD ARGON OUT
COLD ARGON IN
26.1 IN. FACE DIMENSION
7.98 IN. — 18.28 IN.

Stress analysis was conducted of recuperator and of the brackets and support structure necessary for system integration.

PRESSURE DROP REDUCTION (Section 8)

To reduce overall pressure loss of recuperator, changed face aspect ratios were studied.

Counter Flow Core Dimensions (Width x Stack Height x Flow Length) in.	Face Aspect Ratio	End Section Heights Hot	End Section Heights Cold	Degree of Pressure Drop Unbalance *	Effectiveness	Pressure Drop Predicted Percent	Pressure Drop Test** Percent	Weight lb
26.1 x 26.1 x 7.98	1.0	7.0	2.25	Approx 30%	0.9	2.591	2.805	392
26.1 x 26.1 x 7.98	1.0	4.0	2.0	Best	0.9(+)	2.836	3.214	359
17.6 x 39.6 x 7.98	2.25	5.0	2.05	Approx 30%	0.9	2.092	2.286	388
17.6 x 39.6 x 7.98	2.25	3.0	1.5	Best	0.9(+)	2.380	2.640	360
13.05 x 52.2 x 7.98	4.0	5.0	2.0	Approx 30%	0.9	1.863	1.994	381
13.05 x 52.2 x 7.98	4.0	3.5	1.6	Best	0.9(+)	1.951	2.117	360

*For flow distribution, end section pressure losses (hot to cold) should be balanced. Best, indicates the best balance which may be achieved. Approx. 30%, indicates the degree of unbalance accepted to reduce pressure drop.

**Based on results of both heat exchanger core and manifold tests.

(+) after effectiveness, indicates that with the better flow distribution (pressure drop balance) slightly higher effectiveness may be achieved.

Configuration 3 was selected for final design.

Pressure Losses of Selected Configuration

	Predicted Percent	Test* Percent
HOT SIDE (LOW PRESSURE)		
COUNTERFLOW CORE	0.5	
TRIANGULAR END SECTIONS	0.348	
OVERALL CORE	0.848	0.848	1.144
COLD SIDE (HIGH PRESSURE)		
COUNTERFLOW CORE	0.198	
TRIANGULAR END SECTIONS	0.419	
OVERALL CORE	0.617	0.617	0.742
MANIFOLDS	0.628	0.628	0.4
OVERALL HEAT EXCHANGER		2.093	2.286

*Change in pressure losses from predicted to test based on data from flow distribution test program discussed in Section 6.

FINAL DESIGN RECUPERATOR AND PERFORMANCE TEST (Sections 8 and 9)
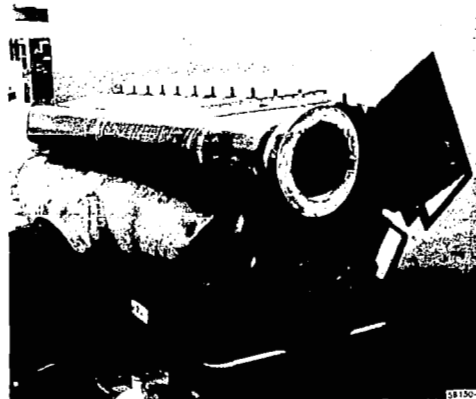
WEIGHT = 438 LB (WITH MOUNTING PROVISIONS)

A limited performance test was conducted on the final design configuration. Satisfactory heat transfer data was obtained, but pressure drop data was inconclusive. The effectiveness measured was 0.9 and the ΔP/P Overall was 5.45 percent. The reasons for not accepting this pressure loss data are explained in Section 9.

Final Performance

Temperature Effectiveness at Design Point = 0.9 (from 2-in. test core and final design)

Overall Pressure Loss (ΔP/P), percent = 2.286 (from 2-in. test core data only)

C-2398

66-0207

"The aeronautical and space activities of the United States shall be conducted so as to contribute . . . to the expansion of human knowledge of phenomena in the atmosphere and space. The Administration shall provide for the widest practicable and appropriate dissemination of information concerning its activities and the results thereof."

— NATIONAL AERONAUTICS AND SPACE ACT OF 1958

NASA SCIENTIFIC AND TECHNICAL PUBLICATIONS

TECHNICAL REPORTS: Scientific and technical information considered important, complete, and a lasting contribution to existing knowledge.

TECHNICAL NOTES: Information less broad in scope but nevertheless of importance as a contribution to existing knowledge.

TECHNICAL MEMORANDUMS: Information receiving limited distribution because of preliminary data, security classification, or other reasons.

CONTRACTOR REPORTS: Scientific and technical information generated under a NASA contract or grant and considered an important contribution to existing knowledge.

TECHNICAL TRANSLATIONS: Information published in a foreign language considered to merit NASA distribution in English.

SPECIAL PUBLICATIONS: Information derived from or of value to NASA activities. Publications include conference proceedings, monographs, data compilations, handbooks, sourcebooks, and special bibliographies.

TECHNOLOGY UTILIZATION PUBLICATIONS: Information on technology used by NASA that may be of particular interest in commercial and other non-aerospace applications. Publications include Tech Briefs, Technology Utilization Reports and Notes, and Technology Surveys.

Details on the availability of these publications may be obtained from:

SCIENTIFIC AND TECHNICAL INFORMATION DIVISION

NATIONAL AERONAUTICS AND SPACE ADMINISTRATION
Washington, D.C. 20546